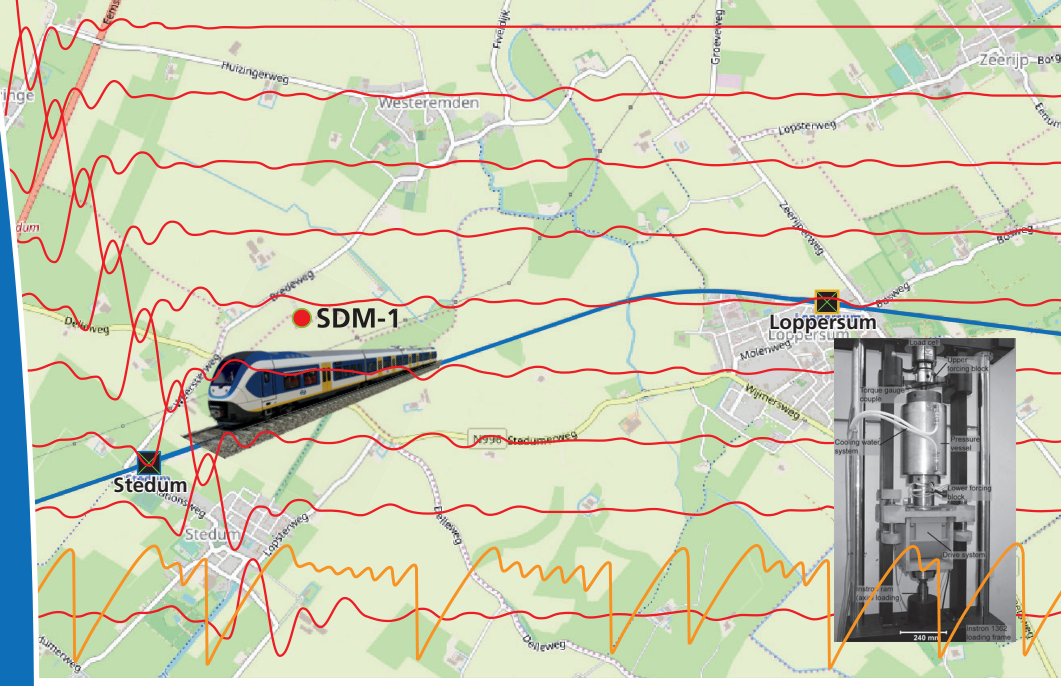

Investigating the Groningen gas reservoir

From passive seismic monitoring to experiments on effects of pore pressure on fault slip

Wen Zhou

215 UTRECHT STUDIES IN EARTH SCIENCES

Investigating the Groningen gas reservoir:

From passive seismic monitoring to experiments on effects of pore pressure on fault slip

PhD Thesis

Wen Zhou

UTRECHT STUDIES IN EARTH SCIENCES
No. 215

Members of the dissertation committee:

Prof. dr. L.G. Evers
Faculty of Civil Engineering and Geosciences
Technical University Delft
The Netherlands

Prof. dr. J.-M. Kendall
Department of Earth Sciences
University of Oxford
United Kingdom

Prof. dr. C. Thomas
Department of Physics, Institute of Geophysics
University of Münster
Germany

Prof. dr. E. Tinti
Department of Earth Sciences
Sapienza University of Rome
Italy

Prof. dr. J.A. Trampert
Department of Earth Sciences
Utrecht University
The Netherlands

The research reported in this thesis has been carried out at:
Department of Earth Sciences,
Faculty of Geosciences,
Utrecht University
Princetonlaan 8A, 3508 TC Utrecht,
The Netherlands

Cover design: Wen Zhou and Margot Stoete
Cover train image: Marielas

Printed by: Proefschriftmaken.nl

ISBN 978-90-6266-579-2

Investigating the Groningen gas reservoir:

From passive seismic monitoring to experiments on effects of pore pressure on fault slip

Onderzoek naar het Groningse gasreservoir:

Van passieve seismische monitoring tot experimenten naar de effecten van poriedruk op breukbeweging

(met een samenvatting in het Nederlands)

Proefschrift

ter verkrijging van de graad van doctor aan de
Universiteit Utrecht
op gezag van de rector magnificus, prof. dr. H.R.B.M. Kummeling,
ingevolge het besluit van het college voor promoties
in het openbaar te verdedigen op

woensdag 8 juli 2020 des middags te 4.15 uur

door

Wen Zhou

geboren op 18 september 1988
te Ningxiang, provincie Hunan, China

Promotor:
Prof. dr. C.J. Spiers

Copromotoren:
Dr. H. Paulssen
Dr. A.R. Niemeijer

The research reported in this thesis was funded by the European Union's Horizon 2020 research and innovation programme under the Marie Sklodowska-Curie grant agreement No 642029 - **ITN CREEP**.

To Qianqian

Contents

Summary

The Groningen gas field in the Netherlands is one of the largest onshore gas fields in the world. Since the start of production in 1963, the Groningen gas became an important source of energy and it contributed significantly to the Dutch economy. However, since the 1990s, there have been increasing issues with induced seismicity. Despite their relatively small magnitudes ($M_L \leq 3.6$), the earthquakes can cause damage to the mostly brick-built houses in the region due to their shallow depth and the soft sediments that are present in the shallow subsurface. The induced seismicity has led to considerable societal unrest and to the governmental decision to reduce gas production from 2015 and to end production by 2022.

The induced seismicity has been related to compaction of the reservoir rock caused by gas pressure depletion. Reservoir compaction leads to changes in normal and shear stresses along pre-existing faults which can lead to fault reactivation and seismic energy release, i.e. earthquakes. Thus, monitoring of compaction is of great importance to assess the seismic hazard in Groningen. Additionally, although elevated pore pressure is understood to reduce effective normal and thus promote slow fault slip over fast earthquake slip, limited studies exist that have addressed the question of how pore pressure affects slip behaviour at constant effective normal stress. Since pore pressures likely evolved in the faults of the Groningen field during the lifetime of the reservoir, it is important to understand the effects of pore pressure on slip behaviour.

In-situ monitoring of the seismic properties of the reservoir and the effect of pore pressure fault slip are the two aims addressed in this thesis.

Chapter 1 gives the motivation and scope of this thesis. Here, I introduce the background on the Groningen field, the induced seismicity, the seismic methods that are used and the basic concepts of laboratory simulation of fault slip.

In **Chapter 2**, I report results from an investigation on the seismic noise recorded by geophones located in a borehole at 3 km depth within the Groningen gas reservoir, and I search for potential noise sources which can be used for monitoring the reservoir. To do so, I first calculated sensor sensitivity and determined the orientations of the horizontal components of the geophones. The average noise power spectral density was then calculated to obtain the noise distribution in the frequency domain. Spectrograms in the time-frequency domain show abundant noise signals of anthropogenic origin such as trains, traffic, and other signals during working hours of which the sources can not be clearly identified. Besides abundant noise, I found occasional local and remote earthquake signals that can potentially be used

to image the reservoir.

Chapter 3 reports on a study of seismic interferometry using continuous noise. Noise interferometry has proven to be a powerful tool for imaging the seismic subsurface structure. In this chapter, I calculate the cross-correlations of the continuous noise data recorded by the borehole geophone array. The cross-correlations show that noise predominantly comes in from above and the daily and weekly variations further indicate that the noise has an anthropogenic origin. The P wave response for each pair of geophones emerges from the vertical component cross-correlations and the S wave response is retrieved from the horizontal components. The travel times of the direct P and S wave were used to determine the P and S velocity structure along the borehole and a very good agreement was found with the sonic log data. In addition, from the S-wave polarizations, I determined an azimuthal anisotropy with a fast direction of approximately N60°W and an estimated magnitude of ~4%. The fast polarization direction corresponds to the present direction of the maximum horizontal stress measured at nearby boreholes but is also similar to the estimated paleostress direction.

Chapter 4 presents the results of a study that uses the signals of nearby passing trains. It is shown that the P wave response between a pair of geophones can be retrieved with good signal-to-noise ratio by deconvolution interferometry using a single train signal. An even more accurate response of the direct P wave and the top and bottom reflections of the reservoir is obtained by stacking the responses of all train signals per day. The S wave response is retrieved from the horizontal components and is obtained from the P-to-S converted waves present in the train signals. The P and S velocity structure determined from the train noise data were found to have a smaller uncertainty than obtained from the continuous noise data. The results of train signal interferometry allowed time-lapse measurements of the direct P wave for the 10 month period in 2015 for which data were available. I observed a general decrease in travel time with a maximum magnitude of 40 ± 10 μs. This suggests that there is a P wave velocity increase in the reservoir that is caused by compaction, but the change is too small to allow a quantitative interpretation.

Whereas the reservoir along the geophone array can been monitored with interferometric techniques, there are no studies that enable monitoring of the overburden by deep borehole noise data. In **Chapter 5**, I introduce a method that is similar to the conventional receiver-function method which, in this setting, allows imaging of the reservoir overburden. The method uses sources at the surface and receivers at depth and is called HZdecon, an abbreviation for horizontal-vertical component deconvolution for a single receiver. The method detects P-to-S converted waves that are generated at interfaces with strong impedance contrasts. I tested the method with synthetic data and demonstrated that the arrivals present in the HZdecon results represent P-to-S converted waves from overburden interfaces. I applied the method to check-shot data and train signals and identified P-to-S converted waves from several major lithological contrasts. Time-lapse measurements were made using the train noise data from 2015, but no major time-lapse changes in the overburden were detected.

In **Chapter 6** I investigate the origin of a significant, but temporary, P wave travel time anomaly that is reported in chapter 4 and a simultaneous anomaly of P-to-S

converted waves that is reported in chapter 5. I present additional observations of a decrease in noise level below the gas-water contact (GWC) that accompanies these observations. All observations suggest a temporary elevation of the GWC in the reservoir. The timing is related to drilling activities at 4.5 km distance from the geophone array. It is inferred that the GWC was elevated due to a pressure increase in the water section of the reservoir sandstone. This implies pressure communication between the well bottom and the surrounding reservoir during drilling. The 3.5 day time delay between drilling activities in the reservoir and their response at the observation well indicates fast propagation of the pressure front, potentially requiring propagation along a highly permeable fault damage zone.

Chapter 7 is an experimental study of fault slip stability under different pore pressure conditions. Here, I report on simulated fault slip, with quartz gouge, at 60 MPa effective normal stress and 6 μm/s loading velocity using the hydrothermal ring shear apparatus at Utrecht University. Results from four experiments are reported under dry, wet, fluid pressure 10 MPa and fluid pressure 150 MPa conditions, respectively. Shear stress and acoustic emission are recorded continuously at 5 MHz sampling rate.

Transitions from stable to slow slip to fast stick slip and reverse transitions are found in all 4 experiments, which is explained to be due to the continuous evolution of localization and delocalization of deformation. Moreover, I observe inter-seismic slow slip events which occur at the end of each interseismic period and gradually grow to fast slip events. The four experiments all exhibit both fast and slow slip events during the experiments, but a high pore pressure promotes slow slip and lower slip rate in the fast slip regime. I explain these effects to be mainly a result of shear stiffness increase with increasing fluid pressure. Dynamic weakening might be damped at high pore pressure which would also slow down fast slip.

The amplitudes of acoustic emissions are found to generally increase with stress drop consistent with previous studies. At the same time, significant variations with displacement have been found. Fast slip occurring shortly after a transition (stable) period are mostly only with low frequency signals, which suggests a similar mechanism as very low frequency earthquakes (VLFEs) discovered at the up-dip seismogenic regime in subduction zone. Inter-seismic slow slip at large displacement are capable of triggering small acoustic emissions, which indicates that these slow slip events are accompanied with small scale localized slip. This phenomenon is similar to episodic slow slip and tremors which have been discovered at the down-dip end of the seismogenic zone within subduction zones.

In **Chapter 8**, I draw general conclusions of the seismological and experimental observations. Suggestions for future research are given to improve our understanding of the subsurface response to gas extraction in the Groningen field.

Chapter 1

Introduction

1.1 Scope of this study

Earthquakes impose hazard to society and therefore it is of great importance to understand the occurrence of earthquakes and earthquake related processes. Despite the major advancements that have been achieved in the past century, for example on the statistics of earthquakes (e.g., frequency-magnitude relation, Omori's law), on earthquake source representation (seismic moments, source time function), on the stress redistribution after an earthquakes and on the mechanical description of faulting (e.g., Coulomb failure, rate-and-state friction), there are still many aspects of earthquakes that are far from being properly understood.

In the Groningen region of the Netherlands, earthquakes have been recorded since 1991. It is generally accepted that these earthquakes are induced by gas extraction and it has been shown that compaction plays a major role (Bourne et al., 2014; Pijnenburg et al., 2019). Surface subsidence and (limited) measurements of reservoir compaction give some insight into the geomechanical response of the Groningen reservoir. However, time-lapse monitoring of the subsurface and in-situ measurements of seismic velocity variations may help to improve our understanding of the Groningen subsurface response to gas extraction and earthquake slip.

Even though earthquakes in Groningen are mainly the result of stress changes due to compaction of the reservoir, the changing pore fluid pressure within faults may have an effect on slip behaviour and fault reactivation. Since the discovery of episodic slow slip by Dragert et al. (2001) in the Cascadia subduction zone, a wide spectrum of slip rates have been discovered. However, the underlying mechanism is still not well understood, despite many mechanisms that have been suggested on the basis of numerical and experimental studies. Among all observations of conditions favorable for the occurrence of slow slip, a high pore fluid pressure has been widely supported. The current understanding is limited to the mechanical effect of pore fluid pressure in reducing the fault effective normal stress or through co-seismic dilatancy (i.e., fault volume dilation causing a transient increase of effective normal stress). Although no slow slips have been observed in Groningen up to now, an investigation of pore pressure effects on fault slip would improve our understanding of slip and stress transfer and by extension of induced earthquakes.

Thus, in this dissertation, I address the issue of induced seismicity in the Groningen gas field through in-situ seismic monitoring and friction experiments with varying pore pressure.

For seismic monitoring, I use noise data recorded by a deep borehole geophone array in the reservoir. Firstly, I show that these data can be used to determine the seismic structure of the reservoir. Then, I describe methods to measure time-lapse changes in the reservoir and overburden. I further show that reservoir drilling can cause pore pressure variations at several kilometers distance.

In order to investigate the effects of pore pressure on fault slip, I conduct rotary shear experiments on quartz gouge under constant boundary conditions but with variable pore fluid (pressure) conditions. The behavior of the simulated fault is observed through both mechanical and seismic (acoustic) data to provide a better view of the effect of pore pressure on slow slip.

1.2 The Groningen gas field

The Groningen gas field was discovered in 1959 with the Slochteren-1 well. The importance of the discovery only became clear in 1960 when another well, Delfzijl-1, at 20 km distance appeared to have gas of similar composition and pressure, and it was realized that both could be part of a single gas field (De Jager & Visser, 2017; Stauble & Milius, 1970). Indeed, the Groningen gas field (Fig. 1.1) is one of the largest onshore reservoirs of the world with originally recoverable gas reserves of ~2900 billion m^3 (De Jager & Visser, 2017). Production started in 1963 and the first recorded earthquake occurred in 1991. The level of induced seismicity stayed low with about 5 earthquakes ($1.5 \leq M_L \leq 2.7$) per year in the next 10 years. However, in 2003 the number of events and their magnitudes started to increase (Van Thienen-Visser & Breunese, 2015). The Huizinge earthquake of 2012, the largest earthquake to date (M_L=3.6), caused considerable damage and a large amount of public concern. After the Zeerijp (M_L=3.4) earthquake of 2018, the Dutch government decided to cut production completely in 2030, and a year later it was decided to stop production already in 2022.

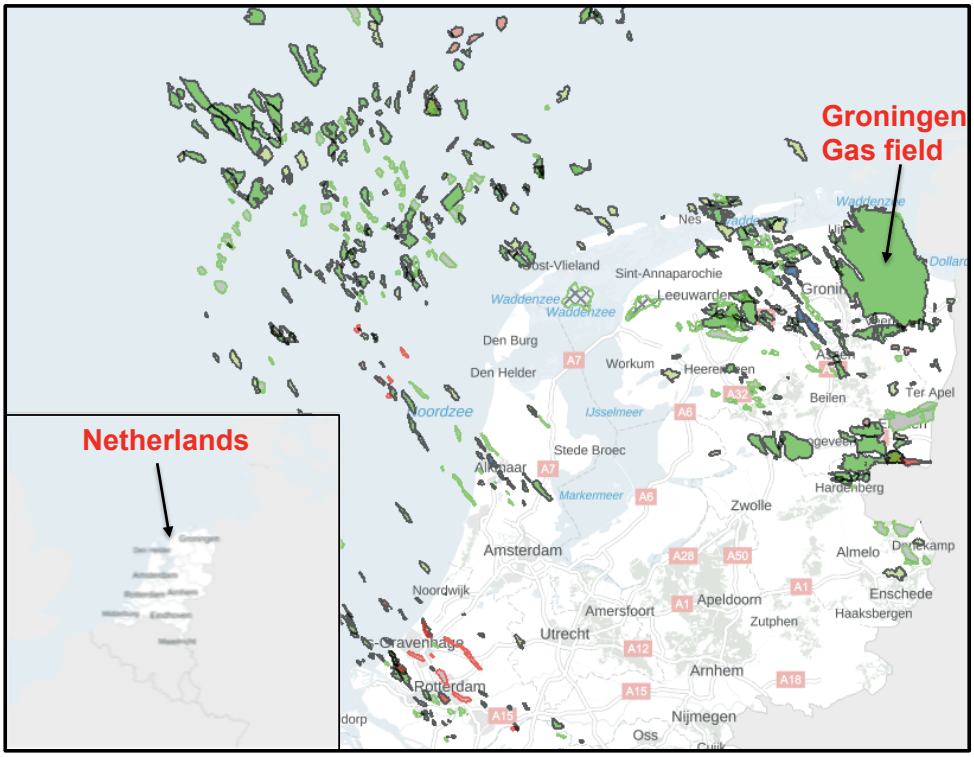

Figure 1.1: Location of the Groningen gas field (modified from DINOloket, 2020).

The reservoir in Groningen is the Upper Permian Rotliegend sandstone. This is a formation that hosts a large number of gas fields in northwestern Europe, extending

from the North Sea in the west to Poland in the east (De Jager & Visser, 2017). The gas mostly comes from the coal-bearing part of the Upper Carboniferous, which acts as the source rock, whereas the overlaying Zechstein rocksalt provides the seal that prevents the gas to escape from the sandstone.

The Groningen field has been extensively surveyed by 3D seismics since the 1980s, and the structure is imaged in great detail (Romijn, 2017). The main faults have a NNW-SSE trend, whereas other faults have a strike that is closer to E-W or N-S (Kortekaas & Jaarsma, 2017).

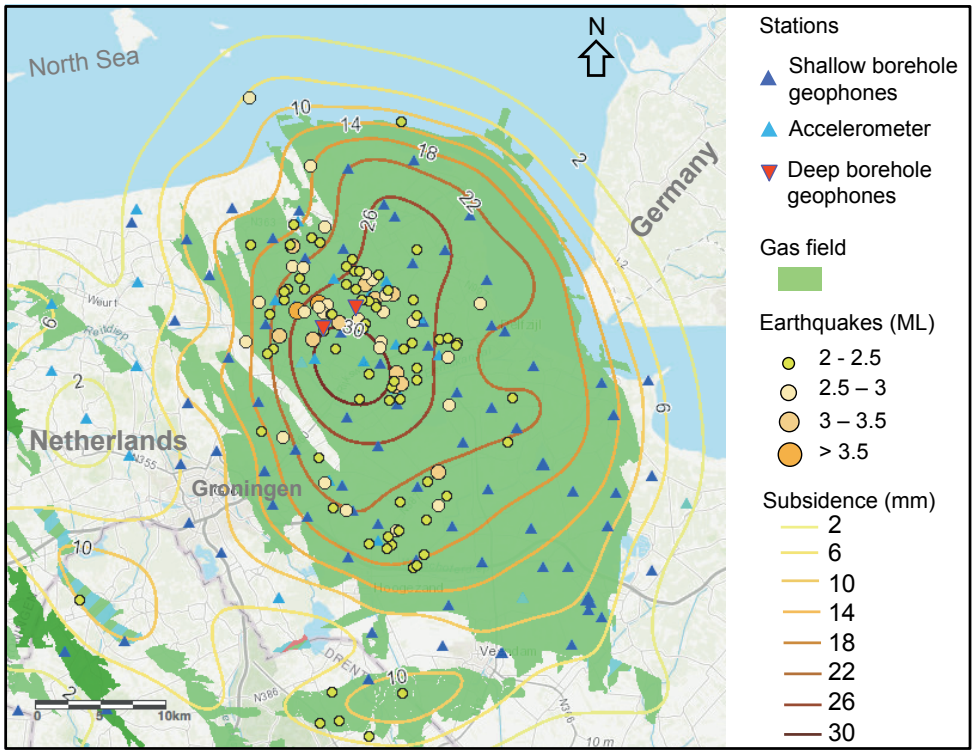

Figure 1.2: Seismicity, subsidence and seismic networks in the Groningen field (modified from NAM, 2020b). Earthquakes (1991 - 2019, M_L>2) are retrieved from the KNMI catalog (KNMI, 2020). Surface subsidence is obtained from levelling measurements between 1972 and 2013 (NAM, 2018). The locations of the two deep boreholes used in this thesis are marked with red triangles.

1.3 Seismic monitoring networks

After the Huizinge (M_L=3.6) earthquake of 2012, research on Groningen seismicity developed and increased in various fields. Furthermore, earthquake monitoring improved considerably due to the deployment of a dense shallow (0 - 200 m) borehole monitoring network that was installed in a few years (Dost et al., 2017; Fig. 1.2).

In addition, Nederlandse Aardolie Maatschappij (NAM) installed geophone arrays at reservoir level in two deep boreholes (NAM, 2019a; NAM, 2019b; Fig. 1.2). The shallow and deep borehole data recorded by these networks have been mainly used for earthquake localization, providing earthquake catalogs of the entire field (KNMI, 2020) and of (micro-)earthquakes close to the observation wells (NAM, 2020a). The data of the shallow borehole network have further been used in various other types of studies (Fokker & Ruigrok, 2019; Hofman et al., 2017; Spica et al., 2018). Except for a cross-well correlation study by Spica et al. (2018), the data of the deep geophone arrays have only been used for earthquake location and source inversion (Willacy et al., 2019; Willacy et al., 2018). The work presented in this thesis demonstrates that noise that is passively recorded by a deep borehole geophone array can be used for in-situ monitoring of the seismic properties of the reservoir.

1.4 Seismic methods to detect medium changes

Previous studies found a correlation between seismicity and gas production for the Groningen field (De Waal et al., 2015; Van Thienen-Visser & Breunese, 2015), and it was shown that reservoir compaction plays a crucial role (Bourne et al., 2014). The link between pressure depletion and sandstone compaction is also demonstrated in laboratory experiments (Hol et al., 2018; Pijnenburg et al., 2018; Pijnenburg et al., 2019). For the Groningen reservoir, compaction is mainly inferred from surface subsidence because there are only few direct measurements of reservoir compaction (Cannon & Kole, 2018; Kole, 2015). Therefore, it would be useful to determine compaction from seismic data. However, it is not known whether it is feasible to detect such changes with the methods and data that are currently available.

Traditionally, seismologists use earthquakes to image the Earth's interior. Large earthquakes generate seismic waves that can travel through the entire Earth and are suitable for global imaging. In seismic exploration, active sources like air guns, explosions or vibrator trucks are used to image the subsurface up to a depth of a few km. In the past two decades, there has been a large increase in the number of studies that used ambient noise to investigate subsurface structure. For regions that are densely sampled by seismic sensors, techniques of noise interferometry can perform better than the more traditional source-receiver imaging methods. The research presented in this thesis uses seismic interferometry of passively recorded borehole data and it employs the receiver function technique that is adopted from global seismology.

1.4.1 Seismic interferometry

Seismic interferometry is based on the idea that the response of the medium between two receivers can be retrieved from the ambient noise field. The method allows seismologists to use signals that were previously unused and treated as noise, such as microseismic noise, anthropogenic noise, or coda of earthquake seismograms.

The first contributions to seismic interferometry were by Aki (1957) who used ambient noise to extract surface waves and Claerbout (1968) who showed that the reflection response at a station can be obtained from the auto-correlation of a seis-

mogram. The basic concept of seismic interferometry is well introduced by Wapenaar et al. (2010). For the simple case of a 1D medium it is easily shown that the cross-correlation of random noise recorded by two stations gives a pulse at the propagation time between the two stations. This is similar to the situation of having a source at one station and a receiver at the other. Extensions to 2D and 3D media require additional conditions such as a uniform distribution of sources surrounding the two stations. The main contribution to the cross-correlation then comes from the sources that produce the stationary-phase wave field between the two stations. More information about the history, the development and applications of this technique is given in the tutorial by Wapenaar et al. (2010), the review by Snieder & Larose (2013), and the textbook by Schuster (2009) for applications in seismic exploration.

Seismic interferometry has also proven to be successful in detecting time-lapse changes in the medium. For instance, Brenguier et al. (2008) and Wegler & Sens-Schönfelder (2007) found seismic velocity changes in the shallow subsurface that are associated to earthquakes. They used surface wave responses that were retrieved from microseismic noise. Co-seismic velocity changes in an underground mine were also detected by Olivier et al. (2015) using ambient noise data. Behm (2016) and Hillers et al. (2015) further showed that fluid injection can change seismic velocity. However, there are no interferometric studies of time-lapse effects caused by reservoir compaction. In this thesis, I investigate the feasibility to retrieve the body wave response between borehole geophones from noise data, and study their potential to detect time-lapse changes caused by reservoir compaction in the Groningen gas field.

1.4.2 Receiver function

The receiver function method (e.g., Langston, 1979) reveals near receiver P-to-S converted waves that arrive in the coda of the direct P wave (or S-to-P converted waves that arrive as precursors to the direct S wave). A P wave with near vertical incidence is mainly recorded on the vertical component of a seismic station whereas the converted S waves are mainly recorded on the horizontal components. A receiver function is obtained by deconvolving the horizontal component of a seismogram by the vertical component. It is a function that yields the P-to-S converted waves at their time delays with respect to the direct P wave.

In global seismology, receiver functions are normally obtained from P waves of teleseismic earthquakes, because of their near vertical incidence, and the receiver function method has been widely used to image interfaces with large impedance contrasts, such as the Moho, upper mantle discontinuities and subducting slabs.

In this thesis, I apply the approach to noise signals that are generated at the surface and are recorded by borehole geophones at depth, thus reversing the conventional receiver function configuration. For this local setting I name the horizontal-to-vertical deconvolution HZdecon, and I will apply it to train noise data for shallow subsurface monitoring.

1.5 Fault stability in friction experiments

Since 1991, we have seen a increasing number of earthquakes in the Groningen field, as a result of pressure depletion in the reservoir. However, beside the effect of pressure depletion on sandstone compaction, there are only scattered studies on the isolated effect of pore pressure on fault stability, i.e. the effect of pore pressure at constant effective normal stress. I address this question using an experimental study of fault sliding behaviour.

Stick-slip frictional behavior is seen as the laboratory equivalent of earthquakes (Brace & Byerlee, 1966), which can be simulated with a simple spring-slider model (Fig. 1.3a).

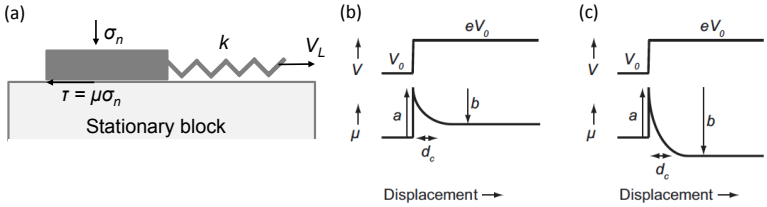

Figure 1.3: (a) diagram of a spring-slider, (b,c) Schematic representation (after Den Hartog (2013)) of the friction evolution in response to a step velocity increase (from V_0 to $V = eV_0$) and RSF parameters. (b) velocity strengthening, (c) velocity weakening

The mechanical mechanism in stick-slip behaviour has been experimentally studied, which has inspired the development of empirical relations of frictional slip and velocity such as the rate and state friction (RSF) equations which describe the evolution of friction upon an instantaneous change in load-point velocity (Dieterich, 1979; Ruina, 1983).

$$\mu = \mu_0 + aln(\frac{V}{V_0}) + bln(\frac{V_0\theta}{d_c}) \tag{1.1}$$

Where d_c is a critical slip distance, μ_0 is the friction at steady-state at a reference velocity V_0, a is a dimensionless parameter that quantifies the instantaneous change in frictional strength (direct effect) and b represents the subsequent change in friction to a new steady state (evolution effect). The state variable θ is governed by a differential equation which evolves with time or slip:

$$\frac{d\theta}{dt} = 1 - \frac{V\theta}{d_c} \tag{1.2}$$

At steady state, $d\theta/dt = 0$ and the equations reduce to

$$(a-b) = \frac{\Delta\mu}{ln(V/V_0)} \tag{1.3}$$

For $(a–b)$ (i.e $d\mu/dV) > 0$, the simulated fault is velocity strengthening (Fig. 1.3b) and accelerating slip cannot nucleate. Unstable slip can only nucleate when $(a - b)$

< 0 and the behaviour is velocity weakening (Fig. 1.3c). In addition to a velocity weakening property, the breakdown in fault strength has to occur more rapidly than the elastic unloading in order for an instability to nucleate. This is captured in the stability criterion, derived for a single-degree of freedom spring slider model Ruina (1983):

$$k_c = \frac{\sigma_n^{eff}(b-a)}{d_c} \tag{1.4}$$

Accelerating slip can only nucleate if this critical stiffness k_c is larger than the system stiffness. This general macroscopic relation is important for understanding the mechanical process of earthquake nucleation, but does not describe the micro-scale process of fault slip. The intrinsic effects of pore pressure on fault slip, beyond its effect on effective normal stress, might include important micro-scale physical and chemical processes but have barely been studied. We therefore conduct experiments on simulated fault gouges with variable pore pressure conditions to investigate the effect of pore pressure on frictional slip and slip stability.

1.6 Aims and thesis outline

The first aim of this thesis is to investigate if passive seismic methods can be used for reservoir monitoring with deep borehole geophone data, and to explore if these methods can be used to detect temporal changes in seismic velocity (chapters 2, 3, 4, 5 and 6). The second aim is to investigate earthquake frictional slip, its relation with pore pressure and its signal characteristics (chapter 7).

The seismological research is presented in chapters 2 to 6. In chapter 2, I analyze the continuous borehole data and I search for signals and noise that can be used to image the seismic structure of the reservoir. The application of ambient noise interferometry by cross-correlation is introduced in chapter 3. The feasibility of the method for imaging the P and S velocity structure is discussed as well as the potential for time-lapse monitoring. In chapter 4, I use train noise to image the P and S wave velocities in the reservoir. Time-lapse measurements are made to determine velocity changes caused by reservoir compaction. The method of horizontal-to-vertical component deconvolution (HZdecon) is presented in chapter 5. I test the feasibility of this technique with synthetic and explosion data and apply it to train noise. In chapter 6, I examine the time-lapse changes in P wave travel time and in P-to-S conversion delay time that were found in the previous chapters. I discuss the relation between the seismic observations and drilling activities at 4.5 km distance.

Chapter 7 reports results of an experimental study of fault slip with variable pore pressure. I investigate how changes in pore fluid conditions affect slip and slip stability. In addition to the mechanical data obtained on more than 500 slip events per experiment, I also investigate the acoustic (elastic energy release at audible and ultrasonic frequency) emission (AE).

General conclusions and suggestions for future research are given in chapter 8.

Chapter 2

Recordings of a geophone array in the Groningen gas reservoir

2.1 Introduction

In recent years, geophone strings in boreholes are frequently used to monitor seismicity induced by fluid injection (Maxwell, 2011), induced seismicity in gas/oil reservoirs (NAM, 2016) or earthquake activity on an active fault (Lin et al., 2012). These deep borehole tools are adopted from traditional vertical seismic profile (VSP) instruments such as the widely used OMNI-2400 sensor, a 3-component 15 Hz geophone. Although the instrumentation is relatively mature for VSP exploration, long term monitoring at a depth of 3 km requires equipment that can withstand the conditions of constant high temperature and high pressure. Thus, continuous monitoring with deep borehole geophones at such large depths is rare.

In the Groningen gas field, NAM intermittently deployed geophone strings in deep boreholes (NAM, 2020). The main purpose was to detect and locate induced earthquakes in the Groningen reservoir, in particular to constrain the depths of the events with a higher resolution than can be obtained from surface seismic stations. Events that are located with the deep borehole data are listed in Willacy et al. (2019) and can be found on the NAM website (https://www.nam.nl/feiten-en-cijfers/diepte-van-aardbevingen.html).

Apart from monitoring seismicity, deep geophone array data can also be used to determine the local velocity structure without active sources by the technique of seismic interferometry (Behm, 2016; Grechka & Zhao, 2012; Miyazawa et al., 2008; Vaezi & van der Baan, 2015). Moreover, Behm (2016) and Hillers et al. (2014) demonstrated the potential of measuring velocity changes using borehole noise data. In this thesis, the feasibility of noise interferometry applied to the geophone array data in Groningen is investigated with the aim to determine the velocity structure and to detect potential velocity changes caused by compaction.

We start this chapter by analyzing the character of the noise field. This is because noise interferometry uses ambient noise as the source to retrieve seismic response between stations. We first calibrate the data by removal of the instrument response, and we determine the orientation of the horizontal components. The overall seismic noise distribution is then analysed in the frequency domain by the power spectrum density of the ground motion. After that, the raw data are analysed using spectrograms which give the power spectral density as a function of time and frequency.

A manual search over the spectrograms revealed multiple interesting signals. These signals are of anthropogenic nature, such those as generated by trains and machines, or from natural sources such as local earthquakes or deep focus earthquake from the Fiji Islands region. In addition, fluid waves along the borehole were identified. We suggest that most of these noise signals can be used to determine the subsurface structure with interferometric techniques.

2.2 Deep borehole geophone strings

As mentioned before, NAM completed several deployments of geophone strings in deep boreholes in the Loppersum area, the seismically most active region of the Groningen gas field (Fig. 1.2). The geophone strings were deployed in observation

wells SDM-1 and ZRP-1,2,3 (Fig. 2.1). Borehole SDM-1 was drilled in 1965, and ZRP-1 10 years later, in 1975. The deviating wells ZRP-2 and ZRP-3, from 2014 and 2015, respectively, were not only drilled as observation wells, but also to collect new reservoir cores. In this thesis, we focus on the deployments of the geophone string in SDM-1 with 10 geophones. The string deployed in the wells ZRP-1 and ZRP-2 is equipped with 7 geophones. The geophones along the string are clamped to the steel casing of the borehole by a shoe pushing to the opposite side of the casing. They measure 3 orthogonal components of ground motion (**X-Y-Z**) where **Z** is the near-vertical component along the well. The data are recorded at 2000 samples per second.

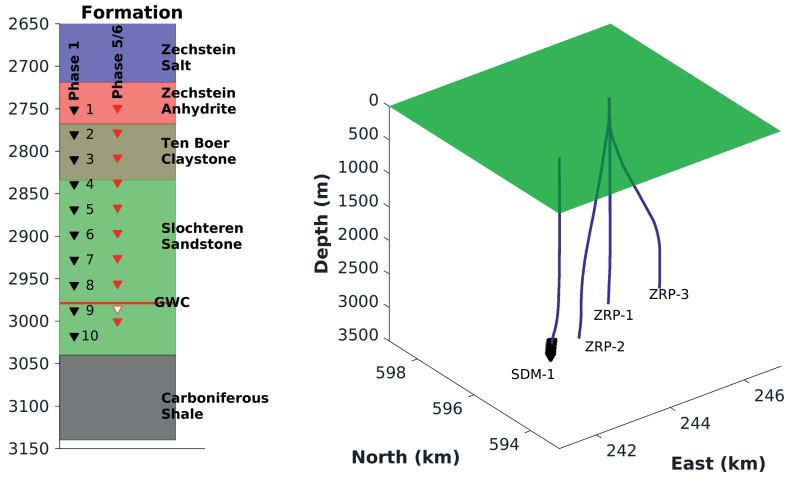

Figure 2.1: Left: Lithostratigraphy around the sandstone reservoir and geophone locations in SDM-1. GWC = Gas-water contact. Right: Location of the SDM and ZRP wells and of geophone array SDM-1. Coordinates are given within the Dutch National Triangulation Grid.

Table 2.1: Periods of deployment of the deep borehole geophone strings used in this thesis.

Well	Phase 1 (2013)	Phase 5 (2015)	Phase 6 (2015)
SDM-1	09 Oct - 23 Dec	23 Jan - 29 Jun	03 Jul - 01 Dec
ZRP-1	21 Nov - 23 Dec		

In this thesis, data are analyzed from three separate geophone deployments in boreholes SDM-1 and ZRP-1 (see Table 2.1). For a complete description of the data the reader is referred to NAM (2016). The first deployment in SDM-1 overlaps in time with the first deployment in ZRP-1 at the end of 2013 and is called Phase 1. The 5th and 6th geophone deployments in SDM-1, named Phase 5 and 6, covered most of 2015. The 10 geophones of SDM-1 are located from top to bottom (see Fig. 2.1): in the Zechstein anhydrite layer (geophone 1), in the Ten Boer claystone (geophones 2 and 3), and in the Slochteren sandstone (geophones 4 - 10). Note that the geophone locations do not exactly match between deployments, and that

the configuration is slightly different between Phase 1 in 2013, and Phase 5 and 6 in 2015 (Fig. 2.1). Furthermore, it should noted that there were occasional data losses in all acquisitions.

Noise analysis and noise interferometry have been carried out both for the data of SDM-1 and ZRP-1, but only results for SDM-1 are presented in this thesis because this well had a larger number of geophones and had a better coverage of the sandstone reservoir. Cross-well interferometry between SDM-1 and ZRP-1 has been attempted, but is out of the scope of this thesis. For this topic the reader is referred to Spica et al. (2018).

2.3 Correction for instrument response

Signals that are recorded by seismic instruments are a function of the time dependence of the source, the wave propagation response of the medium and the response of the instrument. Thus, to obtain wave propagation or source effects, correction for the instrument response is needed.

The 15 Hz OMNI-2400 sensors, which are employed in the geophone strings, have documented properties that were used to derive the frequency dependent instrument response. A short overview of seismic instrumentation and a description of the instrument response of the OMNI-2400 sensor is given in Appendix 2.11. After correction for instrument response, the recordings are converted to ground motion velocity.

2.4 Orientations of the geophone components

Apart from correction for the instrument response, determination of the orientations of the three components of each geophone is required when using the data. The geophones are fixed along a hanging cable that cannot exert a torque to orient or level the geophones. Due to the elongated shape of the geophones, the **Z**-components are assumed to be parallel to the borehole. Thus, the **Z**-components are nearly vertically oriented in borehole SDM-1 with a maximum dip angle of 15°.

The orientations of the horizontal components can be random. I determined the horizontal geophone orientations of SDM-1 for phase 1, 5 and 6 by combining P-wave arrival data from check shots (performed by NAM) with data from earthquakes in the Groningen area that were located by the KNMI (Royal Netherlands Meteorological Institute). For this we used the method that is described in Appendix 2.12. The horizontal motion of the first manually picked P-wave lobe is assumed to be along the horizontal radial direction, defined as positive away from the source. The checkshots, with a frequency content of a few Hz to ~100 Hz, have downgoing P waves with a first lobe of ~0.01 s duration. The earthquakes, with a frequency content of a few to tens of Hz, have upgoing P waves with a duration of the first lobe of ~0.1 s.

Individual results from the checkshots show large inconsistencies of more than 40° (see Table 2.4). The absolute directions are therefore difficult to determine with check shots. On the other hand, the variations in horizontal orientations between the

geophones for the various checkshots are relatively small, with a standard deviation of 3.3° - 7.4° (see Table 2.5). This suggests that the structure between the checkshot at the surface and the geophones at depth changes the P-wave propagation out of the vertical plane between source and receivers due to dipping layers or other types of heterogeneity.

In contrast to the checkshots, there is a larger consistency of the directions obtained from the earthquakes. The lower frequency earthquake signals may be less affected by the potentially smaller heterogeneity at deeper crustal levels. However, because there is smaller azimuthal coverage by earthquakes than the checkshots, it is difficult to verify this.

2.5 Noise distribution in frequency domain

Before imaging the Groningen reservoir with noise interferometry, we first investigated the noise distribution in the frequency domain. After removal of the instrument response, we calculated the power spectral density (PSD) for the vertical component data of the 10 geophones. We used a 2-hour time span (from 02:56 to 04:59 UTC on 29 Nov 2013) for which PSDs were calculated for consecutive time segments of 120 s duration. The averages of these PSDs are shown in Figure 2.2 together with the New High-Noise Model (NHNM) and the New Low-Noise Model (NLNM) by Peterson (1993).

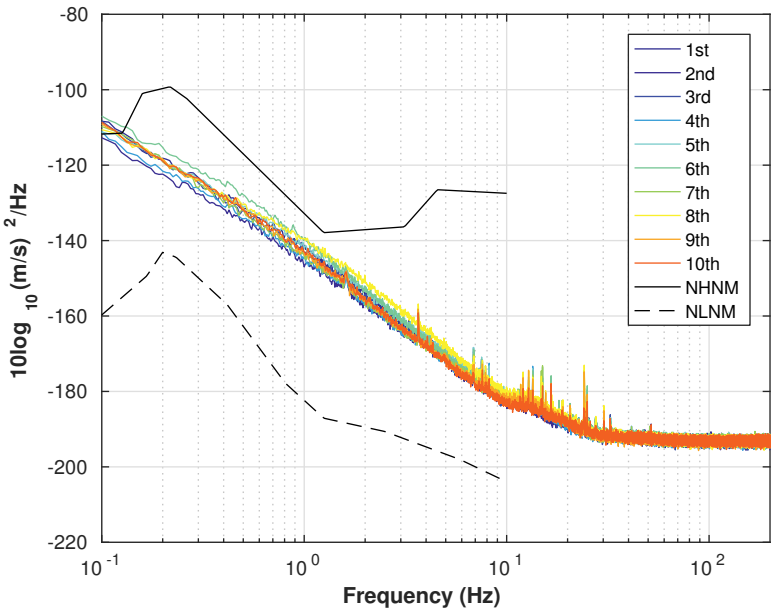

Figure 2.2: Colored curves show the PSDs of the vertical component noise data recorded by the 10 geophones in SDM-1. The PSDs are obtained as averages from individual PDFs for 2 minute segments (2013/11/29; 02:56-04:59 UTC). Solid and dashed black lines indicate the high- and low-noise models of Peterson (1993), respectively.

At frequencies between 0.1 to 10 Hz, the noise is below the NHNM and above the NLNM. Note that the 10 geophones have different noise levels for this low frequency range. This can be due to variations in instrument damping (with a nominal damping constant $h = 0.57 \pm 0.12$, see Appendix 2.11, Table 2.2), or due to variations in electrical noise at each geophone. Thus, although the PSD curves largely fit the trend of noise models, they may represent predominantly instrument noise rather than true seismic noise below 10 Hz. Additional evidence for this is that the geophone noise decreases exponentially from 0.1 to 0.2 Hz (and beyond), whereas the NLNM and NHNM noise levels show an increase of ~10 dB in this frequency band.

The noise data show multiple peaks between 1 and 40 Hz and they seem to exist for all 10 geophones, which suggests they represent true seismic noise. The peak at ~1.6 Hz was also identified at shallow borehole stations in Groningen by Jagt (2017). Researches by Jagt (2017) and Van Der Vleut (2019) suggested that this signal originates from wind turbines at the northeastern coast of Groningen. Most likely it is produced by the largest wind turbine, named 'David', that is ~16 km from SDM-1 (Jagt, 2017). Other signals, especially at frequencies larger than 10 Hz, are still poorly understood. In the next section, time-frequency analysis is carried out to investigate those signals.

2.6 General noise distribution in spectrograms

In order to investigate the noise characteristics in more detail, time-frequency spectrograms were calculated. A spectrogram of the vertical component noise recorded by geophone 10 on a working day (Friday, 29 Nov 2013) is presented in Figure 2.3. The spectrogram is obtained from PSDs for sliding time windows of 3 seconds with a 2 second overlap. On the seismogram itself (Fig. 2.3b), only one clearly distinguishable signal can be identified, indicated by (9). It is from a small induced earthquake with a peak amplitude of 15 nm/s. The spectrogram of Figure 2.3a, on the other hand, shows abundant signals that contribute to the noise. Signal (1) is one of many signals that are repeatedly observed between 04:39 and 00:15 (5:39 and 1:15 local time) the next day. These signals, that are identified at regular (mostly half hour) time intervals, are generated by trains, as will be explained in the next section. Signal (2) of Figure 2.3a is a harmonic signal with a frequency between ~17 and ~20 Hz of varying amplitude. The origin of this signal could not be identified. Signals (3) - (6) are signals with multiple isolated frequencies from 8 to 30 Hz. Their timing is clearly correlated with human activity. For instance, signal (3) starts at 6:25 (7:25 local time) and stops at 8:32 (9:32). Then there is a 25 minute (coffee?) break after which signal (4) starts at 08:57 (9:57) and continues till 11:00 (12:00). After a break of nearly an hour (lunch?), signal (5) lasts from 11:53 to 14:04 (12:53 to 15:04). After another break, signal (6) starts at 14:35 (15:35) and stops at 16:00 (17:00). After that, similar signals do not reoccur anymore during that day. Signal (7) has a dominant frequency of around 68 Hz and is observed only during working hours. The appearance of this signal seems to be related to passing trains. Furthermore, there is a very weak signal (8) with a small increase PSD amplitude at frequencies between 5 to 13 Hz; it is hardly visible in Fig. 2.3a. Similar signals occur close to but after train signals, which suggests that they are related to train

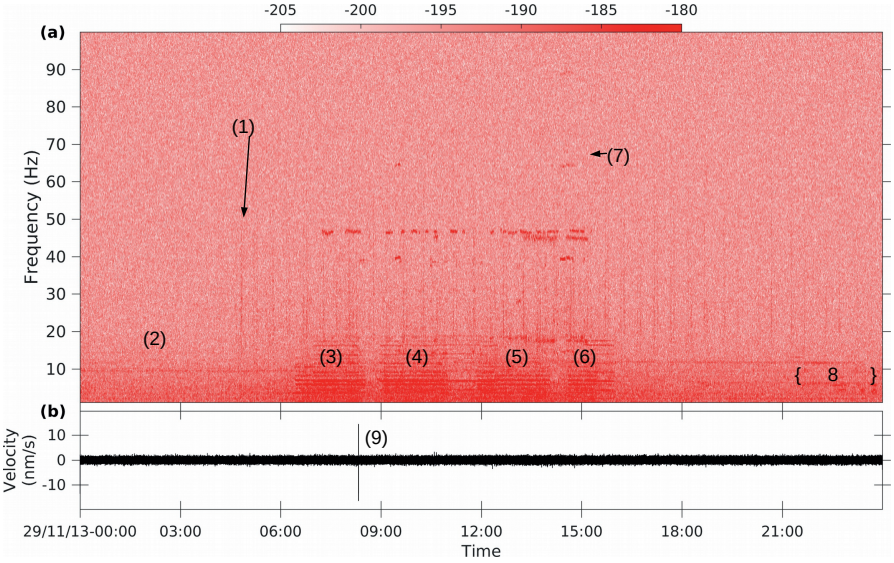

Figure 2.3: (a) Vertical component spectrogram of geophone number 10 for Friday 29 Nov 2013. Different types of signals are indicated with numbers. The PSD scale bar is shown at the top, with unit $10log_{10}m^2/s^2/Hz$. (b) Vertical component seismogram filtered between 1 and 100 Hz.

activity. Lastly, it is noteworthy to mention that the noise band from 1 to 20 Hz generally has a smaller amplitude from 00:00 to 4:00 compared to other times of the day. In summary, we can identify plenty signals from the spectrogram at 1 to 100 Hz, and most of these signals have a clear pattern related to human activity.

2.7 Trains

Figure 2.3a shows signals with frequencies of 20 to 80 Hz (sometimes up to 100 Hz) that occur at very regular intervals after 4:39 UTC. Borehole SDM-1 is located just 500 m from the railroad between Stedum and Loppersum and is 1 km away from station Stedum (Fig. 2.4). The regular intervals at which the signals are observed were found to match the train schedule of nearby station Stedum. The train schedule shows that the first train from Stedum to Loppersum runs at 5:38 local time (4:38 UTC), which agrees with signal (1) in Figure 2.3a. According to the schedule, a train leaves from Stedum to Loppersum at 8 and 38 minutes after the hour and the train in the other direction, from Loppersum to Stedum, departs from Loppersum at 13 and 43 minutes after the hour at daytime. A more detailed plot is presented in Figure 2.5 with 6 insets that show zoom-ins of train-signal spectrograms for 3-minute intervals for the frequency range of 1 to 100 Hz. The figure confirms that the twice-per-hour schedule changes to a once-per-hour schedule after 19:00 UTC.

Figure 2.5 shows that the train signals are of ~2-minute duration, with several

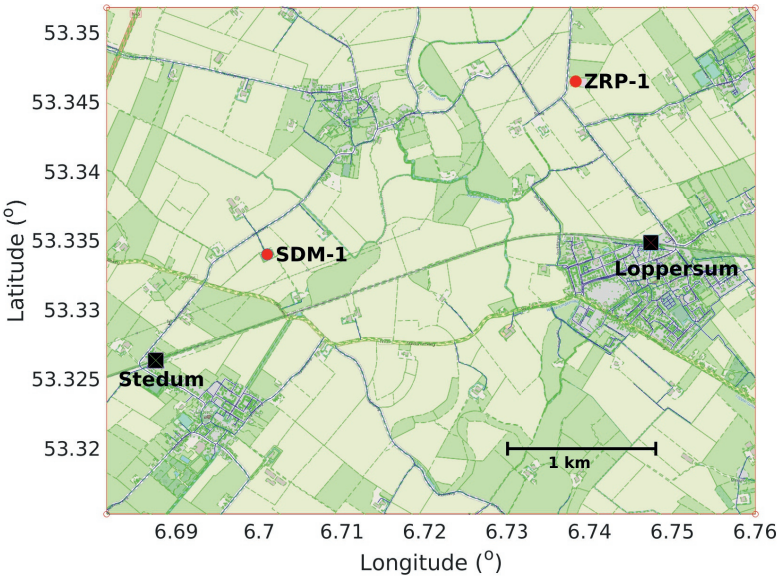

Figure 2.4: Map with the locations of boreholes SDM-1 and ZRP-1 as well as the stations Stedum and Loppersum with the railroad connecting the two.

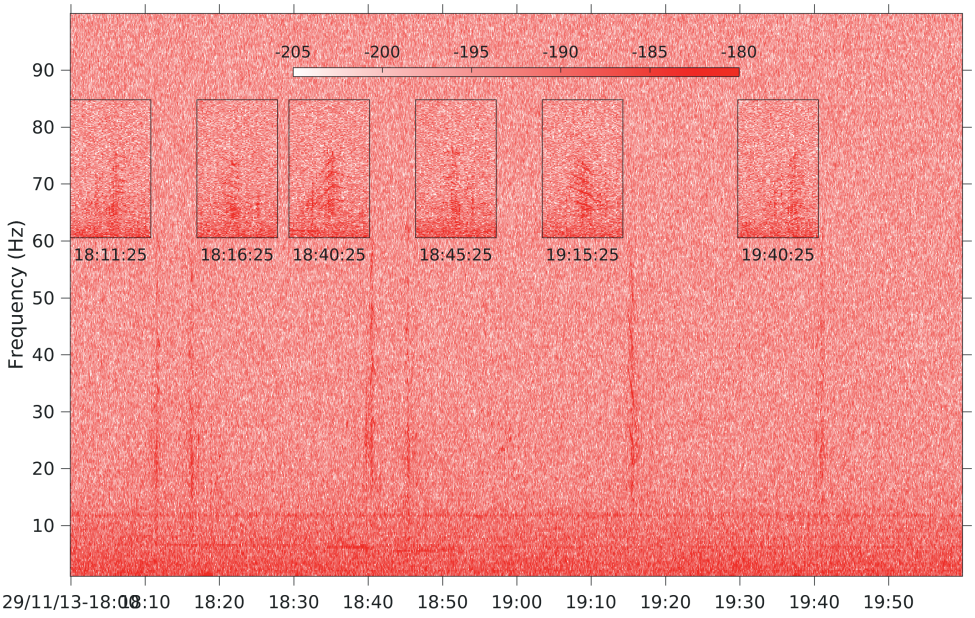

Figure 2.5: Spectrogram (geophone 10, vertical component) of 29 Nov 2013, 18:00-20:00 UTC. Insets show zoom-ins of train-signal spectrograms for 3-minute time windows with indicated starting times for the frequency range from 1 to 100 Hz along the vertical axis.

higher-amplitude frequencies. The first signal from 18:11:25 shows increasing frequencies up to the time where the train passes the borehole (largest amplitudes). In contrast, the signal from 18:16:25 shows a decreasing frequency trend. Similar patterns are found for the other signals. The 18:11:25 signal corresponds to a train from Stedum to Loppersum, whereas the 18:16:25 signal is from a train from Loppersum to Stedum. Since borehole SDM-1 is close to Stedum station (see Fig. 2.4), the variations in frequency are explained by train acceleration or deceleration: increasing frequencies for accelerating trains leaving from Stedum station, and decreasing frequencies for trains arriving at Stedum. In addition, there appears to be a Doppler effect (increasing frequency followed by decreasing frequency) that is most clear for the trains leaving Stedum (18:11:25 and 18:40:25). Seismic train signals have also been analyzed in other studies (e.g., Chen et al., 2004; Fuchs & Bokelmann, 2018; Quiros et al., 2016), and the reader is referred to those for more background, as this is not subject of this thesis.

2.8 Fluid wave in the borehole

Occasionally, a distinct high-frequency (15 - 1000 Hz), high-amplitude (>0.004 mm/s) signal is observed that propagates downward (Fig. 2.6). The signal is tremor-like (without a clear onset) and has an apparent velocity of ~1500 m/s, approximately the speed of an acoustic wave in water.

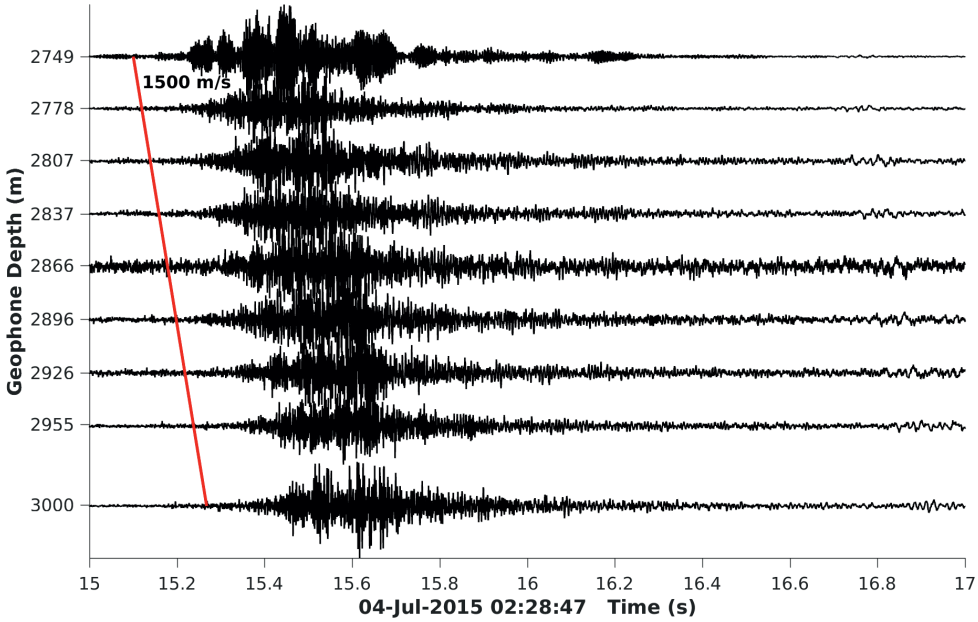

Figure 2.6: Example of a high frequency fluid wave.

The source of this wave is not clear. However, its characteristics, with the propagation speed close to that of an acoustic wave in water, the high frequency content

and the absence of dispersion, suggest that it is an acoustic wave that travels within the fluid of the borehole. It is therefore not related to the rock formation around the borehole. Because of the low speed (and independence of the formation around the borehole which may be affected by compaction) time-lapse differences in the inter-geophone travel times can be used to detect potential geophone displacements over time.

2.9 Earthquakes

With the geophone string of SDM-1 earthquakes with $M_L \geq 1$ from the entire Groningen gas field can be detected. However, large and nearby events are often clipped (Fig. 2.7). Smaller magnitude micro-earthquakes close to the borehole have a high-frequency signal that is well recorded by the geophones due to the flat instrument response above 15 Hz, the high resolution (52 V/m/s) and the high sampling rate of 2000 Hz.

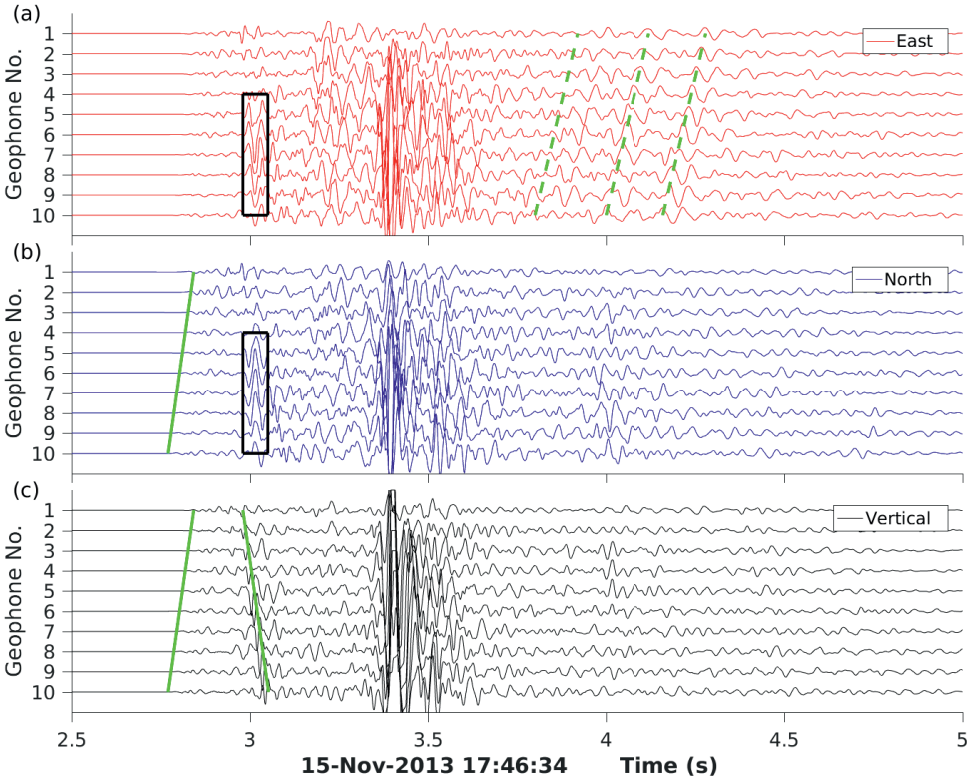

Figure 2.7: Recordings of the Stedum M_L 1.6 earthquake of 2013-11-15 17:46:36 (KNMI, 2020) by the SDM-1 geophone string. Horizontal recordings have been rotated to North and East directions. The instrument response is not removed because the signal is clipped. The green solid lines have slopes of up- and downward propagating P waves, the dashed lines have slopes of upgoing S waves.

Figure 2.7 shows the recordings of a M_L 1.6 earthquake in Stedum (as listed in the KNMI earthquake catalog: `https://www.knmi.nl/kennis-en-datacentrum/dataset/aardbevingscatalogus`) at a distance of ~2 km southeast of SDM-1. The signal starts with an upgoing P wave at ~2.8 s that is most clearly visible on the North and vertical components (green solid lines with positive slope). At ~3 s, a clear downgoing P wave appears on the vertical components (green solid line with negative slope). This downward propagating P wave suggests the presence of a reflecting interface above the geophone string. At the same time, at ~3 s, the East and North components are dominated by a near horizontal propagating wave that arrives at geophones 5 to 10 at approximately the same time (black box). It is interpreted as a trapped P wave within the low-velocity reservoir, also because geophones 6 and 7, at the level with lowest P velocity, have largest amplitudes (Willacy et al., 2019). The opposite signs on East and North components suggest a near northwest-southeast propagating P wave, which is consistent with the earthquake location of the KNMI catalog. At ~3.4 s, another near horizontal propagating wave can be recognized, which is interpreted as a trapped S wave (Willacy et al., 2019). The largest amplitude is observed on the vertical component, which suggests a normal faulting focal mechanism because of the larger (vertical) SV amplitude compared to the (horizontal) SH amplitude. After 3.8 s, upgoing S waves can be observed in the coda of the East component, suggesting that there are strong impedance contrasts at larger depths.

Although there is abundant information contained in the waveforms of local events like Figure 2.7, it is clear that the wave propagation is complex. Thus, a very detailed velocity model and comprehensive waveform modeling are needed in order to use this information to determine the earthquake source parameters and focal mechanism (Willacy et al., 2019) or to investigate the medium. Nakata & Snieder (2011) used median distance range (100 - 1000 km) earthquakes with near vertical incidence to investigate seismic velocity and time-lapse changes with seismic interferometry. A similar strategy can be applied to the Groningen borehole data to monitor subsurface structure. Figure 2.8 shows data from a median distance range event in Germany, listed in the GFZ catalog (2013-11-30 18:09:57, 50.37°N, 7.32°E, 7 km depth, $=_L$=2.5; GFZ (2020)). It is an event 330 km south of SDM-1. The seismograms, with a first arrival at ~45 s, have a duration of over 50 seconds. The first part is dominated by an upgoing P wave with its coda (black box in Fig. 2.8c). It has largest amplitudes on the vertical components. The second part, from 80 to 120 s, has larger amplitudes on the horizontal components (black box in Fig. 2.8a,b). This part is dominated by an upgoing S wave and its coda (Fig. 2.8d,e). An event like this can be used to investigate 1D P and S velocity structure around the borehole by interferometry or receiver function methods, because the waves travel near vertically. Such median range earthquakes would theoretically be close-to-ideal sources to investigate the time-lapse changes in velocity structure. However, they occur relatively rare around the Netherlands and will therefore not provide high time resolution.

Compared to the median distance range earthquakes, large global earthquakes might be an alternative if they are recorded sufficiently well. To find out, I manually searched through the data at the very low-frequency end of instrument sensitivity, at few Hz. I discovered clear signals of up- and downgoing P waves, for instance

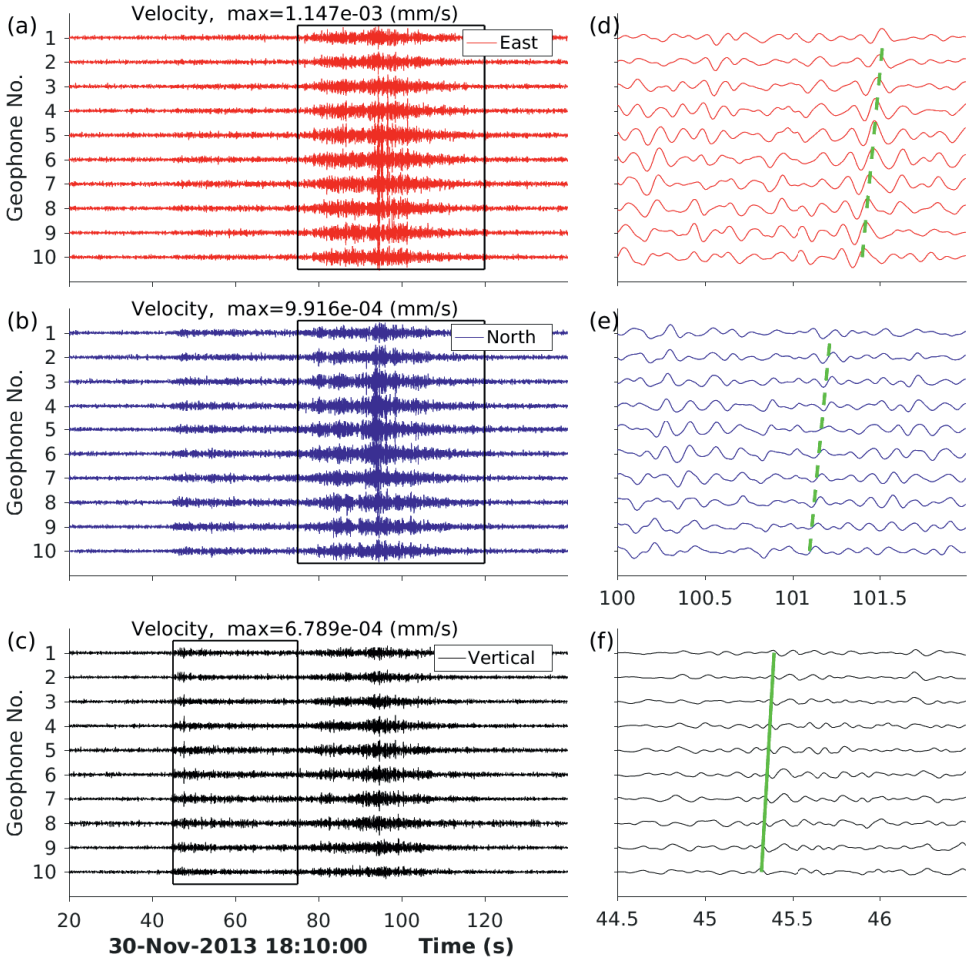

Figure 2.8: Seismograms of the Germany, M_L 2.5, earthquake of 2013-11-30 18:09:57 (50.37°N 7.32°E, 7 km). Horizontals are rotated to North and East, and the instrument response is removed before a high pass filter of 5 Hz. Solid and dashed green lines have the slopes of upgoing P and S waves, respectively.

as shown in Figure 2.9. In this figure, the upgoing P wave starts at 5.5 s and the downgoing P wave at 7.5 s. In addition, a weaker downgoing coda wave can be seen from 8.7 to 9.7 s. The time difference between the two dominant up- and downgoing P waves is 1.9 s, which corresponds to the vertical two-way travel time from the reservoir to the surface.

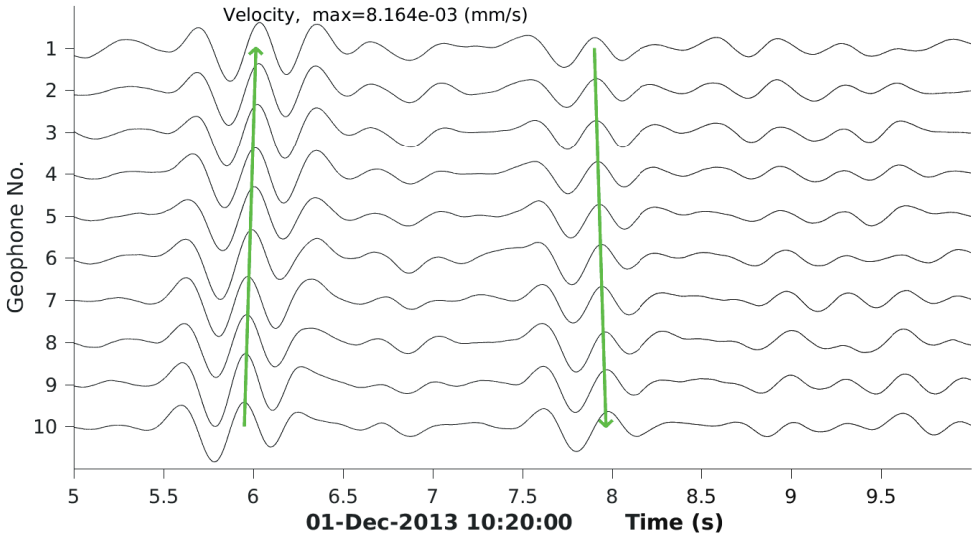

Figure 2.9: Low frequency vertical component seismograms from a magnitude 5.4 event in Fiji Islands Region (2013-12-01, 10:01:32, -17.5737°N -178.2609°E, 536 km). The instrument response has been removed, and then a high pass filter of 2 Hz is applied. Green arrows indicate the upgoing PKP wave and its surface reflection.

The source of these signals was found to be the m_b 5.4 earthquake in the Fiji Islands region (2013-12-01, 10:01:31.81, -17.574°N -178.261°E, at 535 km depth; International Seismological Centre (2020)), which is at a distance of 144.102° from SDM-1. The travel time of the PKP phase is 1113.34 s (18 min + 33.34 s), as calculated with the travel time toolkit TauP (Crotwell et al., 1999). Thus, the expected arrival time is 10:20:05.15 which fits the onset time of our recorded signal at ~10:20:05.4 very well (Fig. 2.9). The reason that this moderately large earthquake has been recorded at such a large distance by 15 Hz geophones may be due to the fact that it is a deep focus earthquake that strongly excited high frequencies. The 2 Hz signal is apparently not completely attenuated along its path and can be detected at 3 km depth because of the low seismic noise level. Signals from sources like this, traveling vertically up from the reservoir to the surface and reflecting back may be used to measure the travel time from the reservoir to the surface. Here I just showed one example, but the abundance of deep focus earthquakes in the Tonga-Fiji region may potentially allow time-lapse monitoring to detect travel time changes related to subsidence, or near surface velocity changes caused by precipitation, earthquakes or other effects.

2.10 Conclusions

In this chapter, recordings by the geophone string in borehole SDM-1 were analyzed. Various types of noise and earthquake signals were recognized. The noise field at 1 - 100 Hz appears to be dominated by different anthropogenic noise sources. Signals generated by trains were identified by their regular appearance. Signals with increasing frequency with time match accelerating trains whereas decelerating trains show decreasing frequencies. In addition, there is some evidence for a Doppler effect. Their regular appearance and their wide frequency band make these train signals suitable not only for determining the velocity structure around the borehole, but also for time-lapse monitoring of the Groningen reservoir.

Furthermore, high-frequency P waves traveling with the acoustic velocity of water were found. Although the source of these waves remains unclear, it is clear that they travel within the fluid of the borehole. Contrary to other types of noise sources, they are insensitive to the rock formation around the borehole. These signals can therefore be used to independently measure inter-geophone travel times, for instance to detect potential geophone displacements.

Earthquakes from different distances are briefly investigated. Induced earthquakes from the Groningen field at local distances (< 30 km) are recorded at SDM-1 with complex interfering wavefields. This means that comprehensive modeling is required to use these events for imaging purposes. The P and S wavefields of median range events (300 - 1000 km) are better separated. These events can potentially be used to investigate the seismic structure of the Groningen field. P wave signals of deep-focus earthquakes at distances larger than 140° and with magnitudes as low as 5.4 are clearly identified at low frequencies, and their surface-reflected wave can also be identified. The abundance of deep focus earthquakes in the Tonga-Fiji region may allow time-lapse monitoring of the vertical two-way travel times from the surface to the reservoir.

2.11 Appendix I - Seismometer frequency response

A general description of seismic instrumentation and the response of a seismometer is given in Havskov & Alguacil (2004). Here I give a brief outline based on their work and I provide the frequency dependent instrument response of the borehole geophones.

A mechanical seismometer can be described as a damped spring-mass system. There are two motions involved in the seismometer system. One is the ground motion $u(t)$ and the other is the displacement of the mass relative to the ground $z(t)$, both are taken positive upwards. There are two forces acting on the mass m. One is from the spring with spring constant k, giving a force $(-kz)$. The other one is due to damping with a friction constant D, giving a force $(-D\dot{z})$. The sum of forces is equal to the mass times the acceleration

$$-kz - D\dot{z} = m(\ddot{u} + \ddot{z}) \tag{2.1}$$

The mass and spring constant determine the seismometer's natural frequency: $\omega_0 = \sqrt{k/m}$. By defining the damping constant $h = \frac{D}{2m\omega_0}$ and substitution of ω_0, the equation of motion becomes

$$\ddot{z} + 2h\omega_0\dot{z} + w_0^2 z = -\ddot{u} \tag{2.2}$$

Theoretically, it is possible to solve (2.2) for every sample in time domain if h and w_0 are known. But we would like to have an equation in frequency domain to understand the performance of the seismometer. Since an arbitrary signal can be described as a superposition of harmonics (Fourier series), we use

$$u(t) = U(\omega)e^{i\omega t} \; ; \; z(t) = Z(\omega)e^{i\omega t} \tag{2.3}$$

where $U(\omega)$ is the amplitude of the ground motion and $Z(\omega)$ is the amplitude of the mass relative to the ground at frequency ω. In the frequency domain, the displacement response of the seismometer to input ground displacement, $S_d^d(\omega)$, is given by the ratio of $Z(\omega)$ to $U(\omega)$:

$$S_d^d(\omega) = \frac{Z(\omega)}{U(\omega)} = \frac{\omega^2}{-\omega^2 + i2h\omega_0\omega + \omega_0^2} \tag{2.4}$$

Conventional seismometers or geophones are velocity transducers that record motion by a moving coil in a magnetic field. In this case, the output induction voltage is proportional to the velocity of the mass relative to the ground. The generator constant, G (in V/ms^{-1}), relates the velocity of ground motion to the output voltage of the coil. The coil resistance, R_g, damps the system. With an additional external resistor, R_e, the effective generator constant G_e of the system becomes $G_e = G\frac{R_e}{R_e+R_g}$. This implies that the frequency dependent output voltage of the sensor is proportional to the velocity of the mass relative to the ground multiplied by G_e, giving a sensor response to displacement

$$S_d^v(\omega) = \frac{i\omega Z(\omega)\; G_e}{U(\omega)} = \frac{i\omega^3 G_e}{-\omega^2 + i2h\omega_0\omega + \omega_0^2} \tag{2.5}$$

and a response to ground velocity

$$S_v^v(\omega) = \frac{i\omega Z(\omega)\, G_e}{i\omega U(\omega)} = \frac{\omega^2 G_e}{-\omega^2 + i2h\omega_0\omega + \omega_0^2} \tag{2.6}$$

The next stage of the seismometer system is the analog-to-digital (A/D) converter which converts the output voltage of the sensor to digital counts by a constant c. The constant c is determined by the signal range divided by the recording resolution (e.g., 12, 14, 18 or 24 bit). Thus, the total instrument response to input ground velocity is given by

$$T_v^v(\omega) = \frac{\omega^2 c\, G_e}{-\omega^2 + i2h\omega_0\omega + \omega_0^2} \tag{2.7}$$

The geophones that were used in this study are the OMNI-2400 15 Hz geophones manufactured by Geospace Technologies. The parameters of these geophones are given in Table 2.2:

Table 2.2: OMNI-2400 15 Hz geophone system

Natural frequency (f_0)	15 Hz
Mass (m)	7.8 gram
Damping constant (h)	0.57 ± 0.12
Effective generator constant (G_e)	52 V/ms^{-1}
A/D conversion (c)	1.3351e-08 V/count

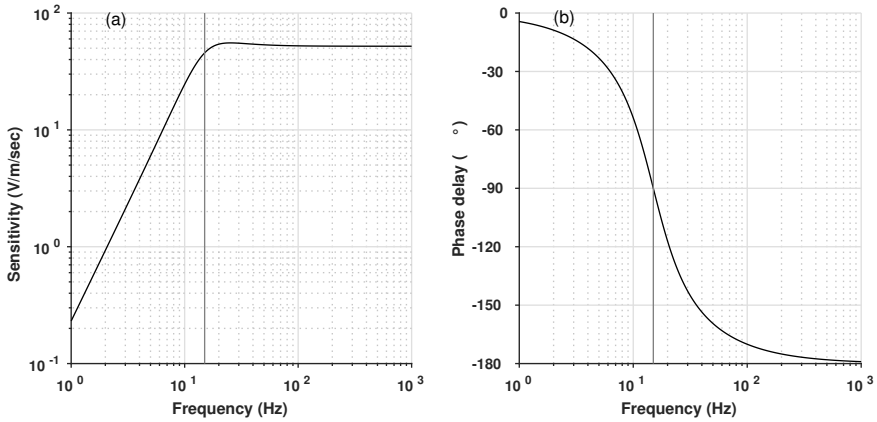

Figure 2.10: Amplitude (a) and phase (b) response of the geophone as a function of frequency. The gray vertical line indicates the natural frequency of 15 Hz.

The theoretical response $S_v^v(\omega)$ of the geophone is calculated from these parameters. Fig. 2.10a shows the amplitude response. The sensitivity increases with ω^2 from 1 to 15 Hz, and above that remains constant at 52 V/m/s. The phase response is shown in Fig. 2.10b. We can see that the phase response theoretically varies from

$0°$ at 0 Hz to $180°$ at very high frequency Hz. The frequency dependent variations of the phase response emphasizes the importance of removing the instrument response from raw data.

2.12 Appendix II - Determination of the orientation of the horizontal components

Data recorded by the horizontal components **X** and **Y** are denoted by the vector $\mathbf{d}_{xy}(t)=[d_x(t), d_y(t)]^T$. In the East-West North-South coordinate system these data, $\mathbf{d}_{en}(t)=[d_e(t), d_n(t)]^T$, are obtained by a rotation matrix $\mathbf{R}_{en}^{xy}$ over an angle ϕ:

$$\mathbf{d}_{en}(t) = \mathbf{R}_{xy}^{en}\, \mathbf{d}_{xy}(t) \tag{2.8}$$

with

$$\mathbf{R}_{xy}^{en} = \begin{bmatrix} \cos\phi & \sin\phi \\ -\sin\phi & \cos\phi \end{bmatrix}. \tag{2.9}$$

To determine the unknown angle ϕ, the particle motion of first incoming direct P waves is used. This particle motion is assumed to be in the radial direction, the horizontal direction between source and receiver that is positive away from the source. For a given source location $S=(S_e, S_n)$ and a receiver location at $R=(R_e, R_n)$ the azimuth α, defined as the angle with North (positive towards East), is:

$$\alpha = \arctan \frac{R_e - S_e}{R_n - S_n} \quad \text{for} \;\; R_n - S_n > 0, \tag{2.10}$$

or

$$\alpha = \arctan \frac{R_e - S_e}{R_n - S_n} + 180° \quad \text{for} \;\; R_n - S_n < 0. \tag{2.11}$$

For a given azimuth α, the radial and transverse components $\mathbf{d}_{rt}(t)=[d_r(t), d_t(t)]^T$ are obtained by the rotation matrix $\mathbf{R}_{en}^{rt}$:

$$\mathbf{d}_{rt}(t) = \mathbf{R}_{en}^{rt}\, \mathbf{d}_{en}(t) \tag{2.12}$$

with

$$\mathbf{R}_{en}^{rt} = \begin{bmatrix} \cos\alpha & \sin\alpha \\ -\sin\alpha & \cos\alpha \end{bmatrix}. \tag{2.13}$$

In short, the radial and transverse components can directly be obtained from the **X** and **Y** component data:

$$\mathbf{d}_{rt}(t) = \mathbf{R}_{en}^{rt}\, \mathbf{R}_{xy}^{en}\, \mathbf{d}_{xy}(t). \tag{2.14}$$

For each source an estimate of the angle ϕ is obtained by minimizing the P-wave energy on the transverse component. For this, the average squared amplitude is determined within a manually picked small time window that includes the first lobe of the P wave. For the high-frequency check shots the duration of this window is typically ~0.01 s (Fig. 2.11), for the earthquakes it is ~0.05 - 0.1 s (Fig. 2.12).

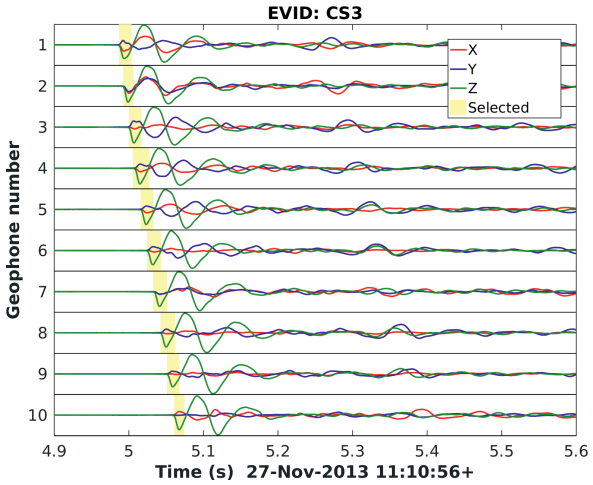

Figure 2.11: Raw data of check shot CS3 (Table 2.3) with a downgoing P wave onset.

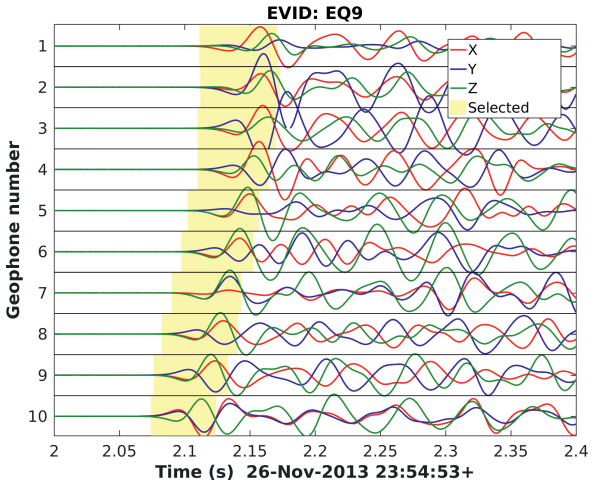

Figure 2.12: Raw data of earthquake EQ9 (Table 2.3) with an upgoing P wave onset.

Minimization of the energy on the transverse component still gives an ambiguity of 180° (ϕ or ϕ + 180°). The polarity of the P wave can be used to distinguish between the two. A downgoing P wave from a check shot will have a first motion that is downward (negative) and in the positive radial direction. Opposite to check shots, regional earthquakes with incidence from below will either have a first motion up (positive) combined with a horizontal motion in the positive radial direction, or a first motion down and in the negative radial direction. This information is used to determine the azimuth ϕ of the horizontal component for each source. The results for each of the geophones are presented in Appendix 2.13 (phase 1, 9 Oct -23 Dec 2013), 2.14 (phase 5, 23 Jan - 29 Jun 2015) and 2.15 (phase 6, 3 Jul - 1 Dec 2015).

2.13 Appendix III - Orientation of horizontal components for SDM-1, phase 1

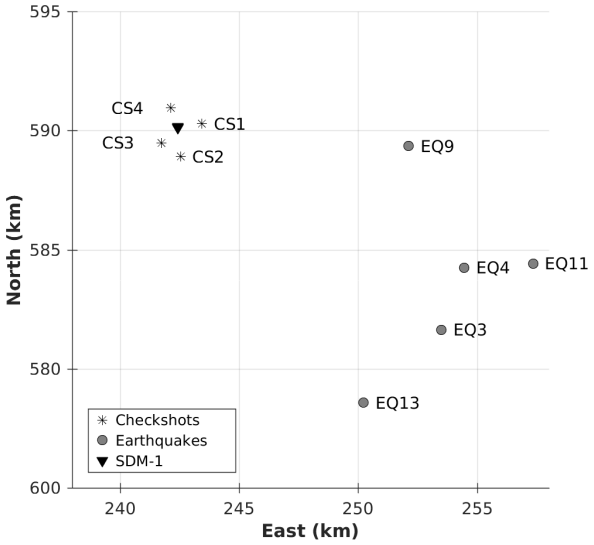

Figure 2.13: Location of the checkshots (CS) and earthquakes (EQ) (see Table 2.3) which are used to determine the orientation of the horizontal components of the geophones of SDM-1 for phase 1. Coordinates are given in the Dutch National Triangulation Grid (Rijksdriehoekstelsel).

Table 2.3: Check shots (CS) and earthquakes (EQ) which are used to determine the azimuth of the horizontal components for phase 1.

	Time	East (m)	North (m)
CS1	27-Nov-2013 11:42:56	243444	595285
CS2	27-Nov-2013 11:28:56	242542	593911
CS3	27-Nov-2013 11:10:56	241745	594480
CS4	27-Nov-2013 11:54:56	242139	595946
EQ3	23-Oct-2013 23:57:37	253505	586636
EQ4	07-Nov-2013 01:23:00	254452	589250
EQ9	26-Nov-2013 23:54:53	252127	594345
EQ11	08-Dec-2013 03:32:48	257344	589422
EQ13	22-Dec-2013 21:51:44	250228	583576

The azimuths of the **X** components for phase 1 (9 Oct - 23 Dec 2013) are presented in Table 2.4 as angle ϕ with respect to North (positive clockwise towards East). The **Y** components are $90°$ anticlockwise from **X**, so their azimuth is $\phi - 90°$. Table 2.5 gives the difference in angle ϕ between the lower geophones and the top geophone

(GP01).

Table 2.4: Azimuth of **X** component [$\phi(^\circ)$], Phase 1 (9 Oct - 23 Dec 2013), SDM-1.

	CS1	**CS2**	**CS3**	**CS4**	**EQ3**	**EQ4**	**EQ9**	**EQ11**	**EQ13**	**Mean**	**SD**
GP01	-61.2	-85.1	-106.3	-73.0	-70.1	-68.0	-75.4	-70.6	-70.1	-75.5	13.2
GP02	-136.1	-160.3	-172.4	-149.8	-145.4	-145.8	-153.3	-146.1	-146.1	-150.6	10.5
GP03	-12.0	-43.7	-53.6	-28.3	-22.5	-23.6	-31.3	-24.1	-25.5	-29.4	12.4
GP04	-36.1	-65.1	-81.8	-55.3	-50.1	-48.4	-56.1	-50.0	-53.7	-55.2	12.6
GP05	-43.7	-74.0	-89.7	-62.1	-68.8	-70.4	-73.0	-67.6	-67.1	-68.5	12.1
GP06	-20.1	-46.9	-62.6	-38.7	-46.1	-44.1	-50.2	-50.5	-42.6	-44.6	11.4
GP07	-138.4	-159.4	-178.2	-158.4	-160.5	-160.1	-165.6	-159.1	-157.5	-159.7	10.2
GP08	-23.2	-38.7	-60.0	-41.7	-40.9	-40.3	-46.1	-41.6	-37.8	-41.1	9.5
GP09	-14.2	-25.8	-51.4	-37.3	-30.3	-29.1	-35.2	-30.2	-28.6	-31.3	10.0
GP10	75.0	62.9	47.0	57.1	62.4	63.5	57.8	61.7	64.2	61.3	7.4

Table 2.5: Azimuth difference of the **X** component with that of geophone 1 in degrees.

	CS1	CS2	CS3	CS4	EQ3	EQ4	EQ9	EQ11	EQ13	Mean	SD
GP01	-136.2	-148.0	-153.3	-130.1	-132.5	-131.5	-133.2	-132.3	-134.3	-136.8	8.1
GP02	148.9	136.8	140.6	153.1	152.2	150.7	148.9	152.2	149.7	148.1	5.6
GP03	-87.0	-106.6	-100.6	-85.4	-84.9	-87.1	-89.1	-85.8	-89.7	-90.7	7.6
GP04	-111.1	-128.0	-128.8	-112.4	-112.5	-111.9	-113.9	-111.7	-117.9	-116.5	7.1
GP05	-118.7	-136.9	-136.7	-119.2	-131.2	-133.9	-130.8	-129.3	-131.3	-129.8	6.7
GP06	-95.1	-109.8	-109.6	-95.8	-108.5	-107.6	-108.0	-112.2	-106.8	-105.9	6.1
GP07	146.6	137.7	134.8	144.5	137.1	136.4	136.6	139.2	138.3	139.0	3.9
GP08	-98.2	-101.6	-107.0	-98.8	-103.3	-103.8	-103.9	-103.3	-102.0	-102.4	2.7
GP09	-89.2	-88.7	-98.4	-94.4	-92.7	-92.6	-93.0	-91.9	-92.8	-92.6	2.8
GP10	0.0	0.0	0.0	0.0	0.0	0.0	0.0	0.0	0.0	0.0	0.0

2.14 Appendix IV - Orientation of horizontal components for SDM-1, phase 5

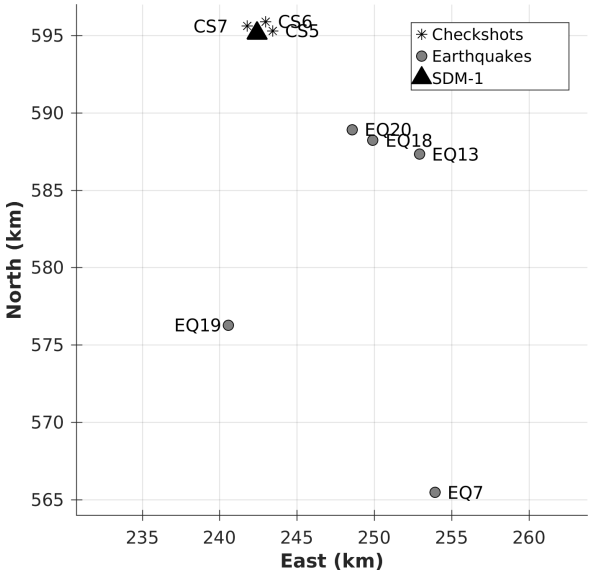

Figure 2.14: Location of the checkshots (CS) and earthquakes (EQ) (see Table 2.6) which are used to determine the orientation of the horizontal components of the geophones of SDM-1 for phase 5. Coordinates are given in the Dutch National Triangulation Grid (Rijksdriehoekstelsel).

	Time	East (m)	North (m)
CS5	20-Feb-2015 12:22:56	243444	595285
CS6	20-Feb-2015 12:59:56	242987	595882
CS7	20-Feb-2015 14:19:56	241802	595596
EQ7	03-Feb-2015 00:02:22	253939	565473
EQ13	22-Feb-2015 06:08:50	252937	587326
EQ18	01-Mar-2015 10:16:30	249916	588212
EQ19	14-Mar-2015 19:26:59	240566	576270
EQ20	16-Mar-2015 23:57:29	248568	588909

Table 2.6: Check shots (CS) and earthquakes (EQ) which are used to determine the azimuth of the horizontal components for phase 5.

During phase 5 (23 Jan - 29 Jun 2015) geophones 1, 8 and 9 had one horizontal component out of order, so their orientations could not be determined. Three checkshots were operated by NAM on 2 Feb 2015 and 5 earthquakes (Fig. 2.14 and

Table 2.6) were used to obtain estimations of geophone orientations for geophones 2, 3, 4, 5, 6, 7 and 10. The results are presented in Table 2.7. There appears to be an inconsistency for the azimuth obtained for the third checkshot (CSP7) compared to those of the other checkshots and earthquakes. Because of the larger variations in the angles obtained by the checkshots, it was decided to determine the average angle from the earthquake data only.

	CS5	CS6	CS7	EQ7	EQ13	EQ18	EQ19	EQ20	Mean	SD
GP02	-97.8	-80.6	85.0	-160.9	-155.5	-159.4	-161.2	-158.7	-159.1	2.3
GP03	15.6	29.5	-166.3	-57.4	-44.7	-47.7	-51.7	-46.7	-49.6	5.0
GP04	23.0	38.3	-155.9	-51.5	-39.4	-40.8	-41.8	-36.7	-42.0	5.6
GP05	-127.4	-107.8	52.0	164.5	166.6	163.1	169.6	171.0	167.0	3.3
GP06	-134.0	-116.3	49.5	158.5	160.7	155.9	161.8	159.8	159.3	2.3
GP07	-122.6	-101.9	60.4	173.6	175.8	173.3	178.6	-179.4	176.4	3.2
GP10	-81.6	-56.9	106.5	-136.0	-132.4	-134.8	-132.3	-131.5	-133.4	1.9

Table 2.7: Azimuth of **X** component [$\phi(^\circ)$], Phase 5 (23 Jan - 29 Jun 2015), SDM-1.

Table 2.8 gives the difference in angle ϕ of each of the geophones with geophone 10. It shows that this relative difference is obtained very consistently with a standard deviation of maximal 4°.

	CS5	CS6	CS7	EQ7	EQ13	EQ18	EQ19	EQ20	Mean	SD
GP02	-16.2	-23.7	-21.5	-24.9	-23.1	-24.6	-28.9	-27.2	-23.8	3.8
GP03	97.2	86.4	87.2	78.6	87.7	87.1	80.6	84.8	86.2	5.6
GP04	104.6	95.2	97.6	84.5	93.0	94.0	90.5	94.8	94.3	5.7
GP05	-45.8	-50.9	-54.5	-59.5	-61.0	-62.1	-58.1	-57.5	-56.2	5.5
GP06	-52.4	-59.4	-57.0	-65.5	-66.9	-69.3	-65.9	-68.7	-63.1	6.1
GP07	-41.0	-45.0	-46.1	-50.4	-51.8	-51.9	-49.1	-47.9	-47.9	3.7
GP10	0.0	0.0	0.0	0.0	0.0	0.0	0.0	0.0	0.0	0.0

Table 2.8: Azimuth difference of the component with that of geophone 10 in degrees.

2.15 Appendix V - Orientation of horizontal components for SDM-1, phase 6.

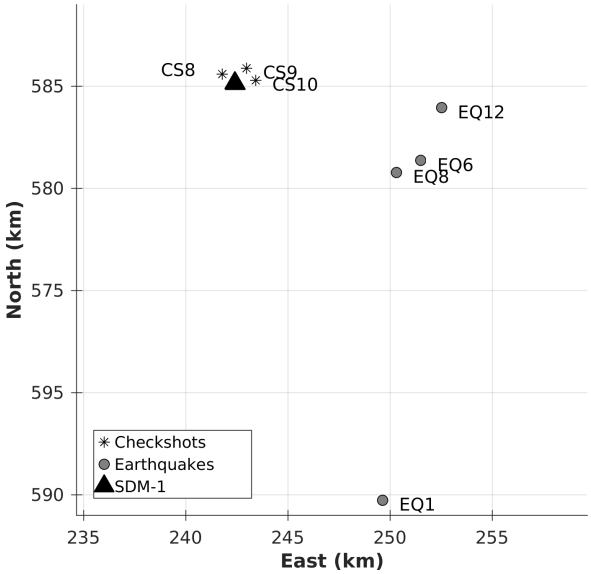

Figure 2.15: Location of the checkshots (CS) and earthquakes (EQ) (see Table 2.9) which are used to determine the orientation of the horizontal components of the geophones of SDM-1 for phase 6. Coordinates are given in the Dutch National Triangulation Grid (Rijksdriehoeksstelsel).

	Time	East (m)	North (m)
CS8	16-Jul-2015 08:25:56	241801	595596
CS9	16-Jul-2015 08:58:19	242987	595882
CS10	16-Jul-2015 09:06:19	243444	595285
EQ1	04-Jul-2015 04:18:02	249647	574737
EQ6	08-Jul-2015 02:47:32	251521	591361
EQ8	16-Jul-2015 02:27:14	250332	590780
EQ12	19-Jul-2015 20:06:44	252536	593941

Table 2.9: Check shots (CS) and earthquakes (EQ) which are used to determine the azimuth of the horizontal components for phase 6.

During the 6th geophone deployment in SDM-1 (phase 6: 3 Jul - 1 Dec 2015), 3 checkshots were operated on 16 Jul 2015. The same process was applied as described in Appendix II for geophone 1, 2, 4, 6, 7, 8, 9 and 10. Geophone 3 and 5 had one horizontal component that did not work. For geophone 4, we had to swap

the **X** and **Y** data to obtain consistent results. We suspect that the connections were interchanged at the AD converter.

	CS8	CS9	CS10	EQ1	EQ6	EQ8	EQ12	Mean	SD
GP01	-52.3	-57.2	-12.7	-37.1	-33.7	-37.0	-36.7	-36.1	1.6
GP02	-125.0	-143.8	-98.8	-114.6	-113.0	-118.1	-115.3	-115.2	2.1
GP04	-161.8	-165.6	-122.6	-154.4	-143.0	-142.4	-144.9	-146.2	5.6
GP06	-56.8	-66.0	-22.0	-47.3	-50.5	-56.8	-59.7	-53.6	5.7
GP07	-112.3	-111.0	-64.8	-93.7	-73.9	-127.0	-88.1	-95.7	22.5
GP08	-140.4	-152.7	-108.3	-124.0	-133.0	-134.8	-128.4	-130.0	4.9
GP09	-157.5	-169.6	-125.2	-142.2	-144.8	-149.2	-144.7	-145.2	2.9
GP10	-10.9	-17.2	27.4	10.2	9.2	5.6	6.9	8.0	2.1

Table 2.10: Azimuth of **X** component [$\phi(^\circ)$], Phase 6 (3 Jul - 1 Dec 2015), SDM-1.

	CS8	CS9	CS10	EQ1	EQ6	EQ8	EQ12	Mean	SD
GP01	-41.4	-40.0	-40.1	-47.3	-42.9	-42.6	-43.6	-42.6	2.5
GP02	-114.1	-126.6	-126.2	-124.8	-122.2	-123.7	-122.2	-122.8	4.2
GP04	-150.9	-148.4	-150.0	-164.6	-152.2	-148.0	-151.8	-152.3	5.7
GP06	-45.9	-48.8	-49.4	-57.5	-59.7	-62.4	-66.6	-55.8	7.8
GP07	-101.4	-93.8	-92.2	-103.9	-83.1	-132.6	-95.0	-100.3	15.8
GP08	-129.5	-135.5	-135.7	-134.2	-142.2	-140.4	-135.3	-136.1	4.2
GP09	-146.6	-152.4	-152.6	-152.4	-154.0	-154.8	-151.6	-152.1	2.6
GP10	0.0	0.0	0.0	0.0	0.0	0.0	0.0	0.0	0.0

Table 2.11: Azimuth difference of the **X** component with that of geophone 10 in degrees.

Chapter 3

P and S velocity structure in the Groningen gas reservoir from noise interferometry

This chapter is based on the following publication: Zhou & Paulssen, 2017

Zhou, W. & H. Paulssen (2017), P and S velocity structure in the Groningen gas reservoir from noise interferometry, *Geophysical Research Letters*, vol. 44, no. 23.

3.1 Introduction

The Groningen gas field (Fig. 3.1a) in the Netherlands is one of the world's largest onshore gas fields and has been producing since 1963 (Van Thienen-Visser & Breunese, 2015). As a result of gas extraction, subsidence and induced seismicity occur, causing damage and concern in the area.

In 2013, the year with the highest level of induced seismicity, two geophone strings were placed in two boreholes that were originally used as production wells, to monitor seismicity in the reservoir (NAM, 2016). A string of 10 geophones was positioned in borehole SDM-1 and a string of 7 geophones in borehole ZRP-1 (Fig. 3.1b). In this study we used the data of SDM-1 to demonstrate that it is possible to accurately determine the P- and S-wave velocity structure along a borehole at 3 km depth, as well as S-wave anisotropy, from anthropogenic noise at the surface using seismic interferometry.

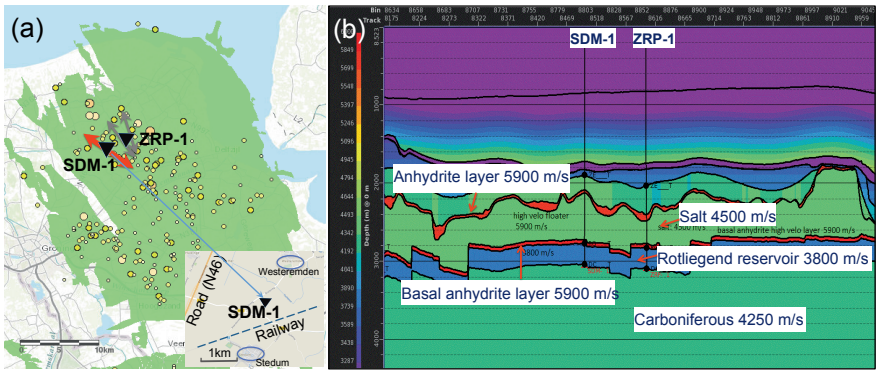

Figure 3.1: (a) The Groningen gas field (green) with seismicity (M_L 0.1-3.5; 2013-2014) and the borehole locations SDM-1 and ZRP-1(black inverted triangles). The grey arrows indicate the maximum horizontal stress directions in boreholes ZRP-2 and ZRP-3 from breakout tests (Van Eijs, 2015). The red arrow indicates the fast S wave polarization direction obtained for SDM-1 in this study. Inset shows the location of borehole SDM-1 with the village of Westeremden, the railway, and the road N46. (b) Cross-section (length ~20 km, depth 4.4 km) through a P wave velocity model with boreholes SDM-1, and ZRP-1. The velocity scale bar ranges from 3287 to 6000 m/s. (Source: Nederlandse Aardolie Maatschappij, NAM).

The technique of seismic interferometry is well established. A number of studies has shown that the Green's function between two receivers can be extracted from noise cross-correlations (e.g., Bakulin & Calvert, 2006; Snieder, 2004; Wapenaar & Fokkema, 2006; Weaver & Lobkis, 2005). Some conditions apply, such as an isotropic distribution of noise sources, although in practice noise sources within the receiver–receiver Fresnel zones suffice (Snieder & Larose, 2013). The technique has been used widely: to retrieve surface waves for imaging crustal and upper mantle structure (e.g., Galetti et al., 2017; Lin et al., 2011; Shapiro et al., 2005), to detect body waves travelling through the mantle and core (e.g., Gerstoft et al., 2008; Poli et al., 2012; Wang et al., 2015), in exploration settings (e.g., Draganov et al.,

2009; Vasconcelos et al., 2010) and to image time dependent variations of the velocity field (e.g., Brenguier et al., 2008; Draganov et al., 2012; Hillers et al., 2015; Ridder et al., 2014; Wegler & Sens-Schönfelder, 2007). An extensive review of the literature is given in Snieder & Larose (2013).

Some studies obtained the velocity structure between borehole sensors using earthquake data (Hofman et al., 2017; Nakata & Snieder, 2012; Trampert et al., 1993), while recent studies have shown that borehole body wave propagation can also be retrieved from noise data. Miyazawa et al. (2008) extracted direct downgoing P and S waves up to 370 m depth in the frequency band 10-55 Hz from industrial noise at the surface. Grechka & Zhao (2012) summarized several applications of downhole seismic interferometry. They obtained a downgoing P wave with frequencies up to 50 Hz at nearly 2 km depth, and also found horizontally propagating S waves between two boreholes. Vaezi & van der Baan (2015) investigated the effects of geophone clamping to the borehole. They retrieved downgoing P waves at 1800 m depth, and in some cases also more weakly upgoing P waves at frequencies lower than 60 Hz. Recently, Behm (2016) found downgoing P and S waves up to 50 Hz at around 1000 m depth, and suggested that velocity changes may be monitored from the high-frequency (> 50 Hz) part of the cross-correlations.

In this study, noise interferometry was applied to the three component recordings measured in borehole SDM-1. The P and S wave velocity structure within the reservoir was determined with high accuracy and azimuthal anisotropy was detected from the obtained S-wave polarizations.

3.2 Data and processing

We used 33 days of data (21 November to 23 December 2013) from the 10 15-Hz geophones in borehole SDM-1 positioned at depths from 2750 m to 3017 m with a geophone spacing of 30 m. The data were continuously recorded with a sampling rate of 2000 Hz. The data from the original sensor directions were rotated to East, South and Down, using the information provided by check shots.

To obtain the cross-correlations, we followed the processing scheme of Bensen et al. (2007), using 1-bit normalization to remove amplitude bias in the time domain. Spectral whitening with a smoothed version of the amplitude spectrum was applied to remove frequency bias. After that the data was filtered from 3 to 400 Hz. We deliberately used a wide band pass filter to allow potential additional filtering at later stages. We tested that there is only little difference in filtering before or after cross-correlation (see Fig. S1 in the supporting information).

Normalized cross-correlations $C_{rs}(t)$ were calculated for each geophone pair:

$$C_{rs}(t) = \frac{\int_{-T/2}^{T/2} r(\tau)s(\tau+t)d\tau}{\parallel r(t) \parallel \parallel s(t) \parallel}$$

where $s(t)$ is the processed record at the reference geophone (i.e. virtual source), and $r(t)$ is processed record at one of the other (receiver) geophones. T is the duration of the segmented records, and $\parallel\parallel$ denotes the L^2 norm of the signal. The cross-correlations were calculated for 6 second segments ($T = 6$ s) with $2/3$ overlap,

and then they were stacked per hour. Further processing was based on these hourly stacks.

3.3 Cross-correlations

The cross-correlations obtained from 24 hours of stacked data with the top geophone as virtual source are displayed in Figure 3.2. The causal parts of the cross-correlations between the vertical components (Fig. 3.2a) show a strong signal with an apparent velocity of about 3700 m/s, similar to the average P wave velocity of the (Rotliegend) reservoir (see Fig. 3.1b). It is therefore interpreted as the direct downgoing P wave. The cross-correlations between the East components show a signal with an apparent velocity of about 2400 m/s (Fig. 3.2b). This velocity is similar to the average S velocity in the reservoir (courtesy Nederlandse Aardolie Maatschappij, NAM; see Fig. 3.4) and is therefore interpreted as the downgoing S wave. Full sets of cross-correlations between all components can be found in Figures S2 and S3 of the supporting information, for the top and bottom geophone as virtual sources, respectively. The P wave has its largest amplitude on the vertical component cross-correlations, whereas the East and North component cross-correlations have their strongest amplitude at the arrival time of the S wave (where the vertical component has near-zero amplitude). This is consistent with the polarization of vertical P and S wave propagation along the borehole, respectively. The strong signals for the downgoing waves compared to the upgoing ones indicate that the dominant noise comes from above.

The power spectra (Fig. 3.2c, d) show that the vertical component cross-correlations contain signal with frequencies up to 80 Hz whereas the horizontal component cross-correlations only contain signal up to 50 Hz.

Apart from the direct P and S waves, the horizontal and vertical component cross-correlations seem to contain an additional signal with an apparent velocity of ~4500 m/s. It is most clearly seen on the horizontal components, but can also be identified as a small precursory onset to the P wave on the vertical component cross-correlations. We interpret this signal as a P wave that comes in at an inclined angle, because its apparent velocity is higher than the P velocity of the medium and also because it is observed on the vertical and horizontal cross-correlations. We also identify high-frequency arrivals at 0 s delay time on all cross-correlations. Here they are most clearly visible on the East component cross-correlations, but their signature can also be identified in the spectra at around 250 Hz. Such signals have been identified before and were then attributed to tiny time calibration pulses superposed on the recordings by the data logger (Takagi et al., 2015).

Figures 3.3a and c show the causal parts of the hourly cross-correlations as a function of day and time over the entire period of 33 days for the vertical and East component, respectively. The top geophone is used as virtual source and the bottom geophone as receiver. Diurnal and weekly variations of the cross-correlations can be identified, revealing that the downward propagating noise is of anthropogenic origin. A zoom-in of this figure for a single day is given in Figure S4 of the supporting information.

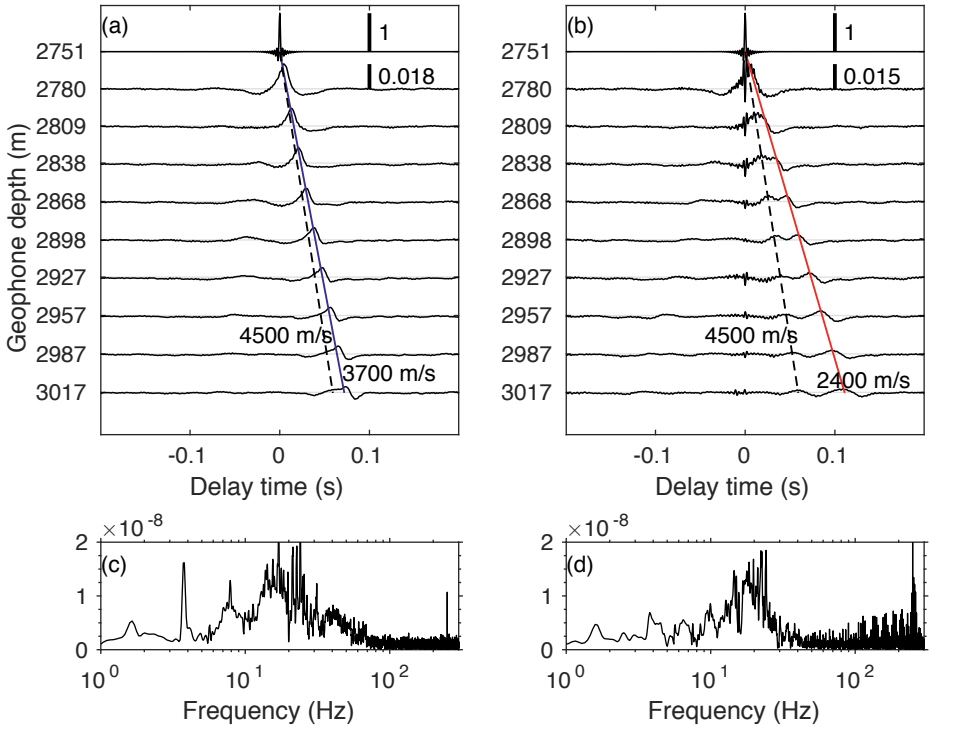

Figure 3.2: (a) Vertical (Z-Z) component cross-correlations and (b) East (E-E) component cross-correlations for the 24-hour stacks of 21 November 2013. The top geophone was used as virtual source. The vertical bars indicate the scaling of the top trace (with value 1), and the other traces (with 0.018 and 0.015, respectively). Panels (c) and (d) represent the power spectra of the vertical and East component cross-correlations for the lowermost geophone, respectively.

3.4 Travel time estimation and velocity profile

To obtain a single accurate apparent P wave travel time per geophone pair, the time of maximum vertical component cross-correlation was measured for each of the hourly stacks (Fig. 3.3a). With 33 days and 24 hours per day, we obtained 33*24 P wave travel times for each geophone pair. The histogram of travel times for Figure 3.3a is shown in Figure 3.3b (blue distribution). Because the travel time distribution is skewed, we used a kernel density estimation (Botev et al., 2010) to obtain its probability density function (PDF) (Fig. 3b, red curve). The maximum likelihood value obtained from this PDF is then used as estimate of the travel time for this geophone pair. In a similar way, using each of the geophones as a virtual source and the others as receiver, in total 45 independent source-receiver travel times were obtained. The total travel time for each virtual source-receiver pair can be written as the summation of interval travel times between neighboring pairs of geophones. A linear least squares method was used to the 45 source-receiver travel times (equations) to determine the 9 interval travel times (unknowns). Estimates

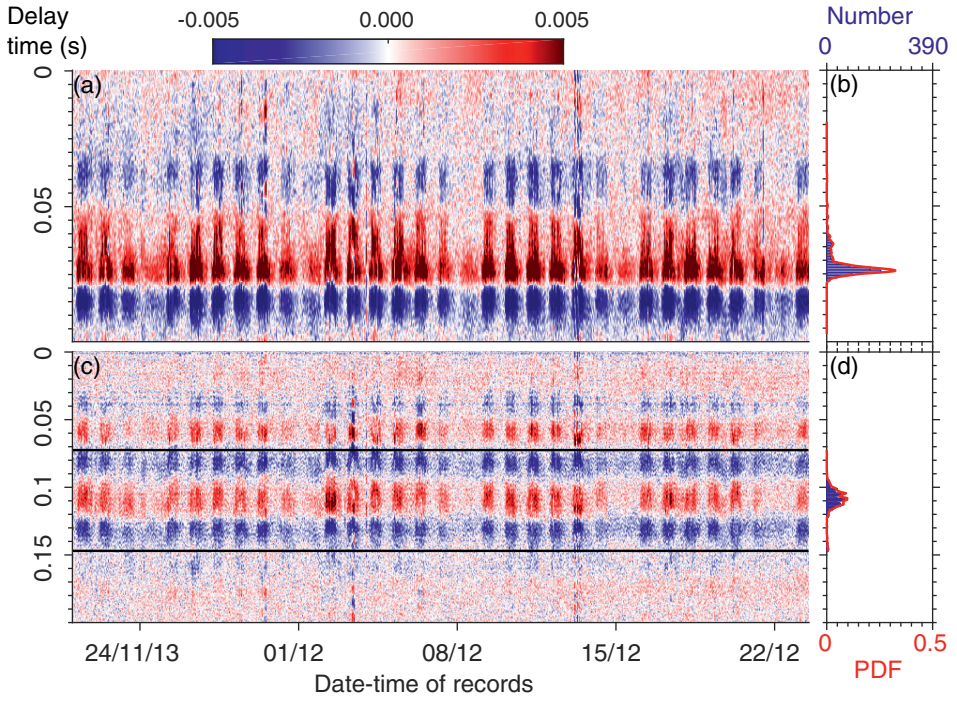

Figure 3.3: (a) Causal parts of the vertical component cross-correlations with the top geophone as virtual source and the bottom geophone as receiver. (b) Histogram of the number of apparent P wave arrival times (blue) with its PDF (red) in the same figure. (c) Similar to (a) for East component cross-correlations with the black lines indicating timing thresholds. (d) Similar to (b) for S wave arrival times.

of the errors in the interval travel times were obtained from the diagonal elements of the model covariance matrix. The velocities between the geophones (with their errors) were directly calculated from the interval travel times (with their errors) using the inter-geophone distance of 30 m.

The same approach was used for the East components to obtain the S wave velocities. However, in order to reduce the influence from the earlier P wave arrival, we set timing thresholds with apparent velocities of 1500 m/s and 3500 m/s for S wave picking. Furthermore, not all timings could be used due to interference with this earlier arrival (Fig. 3.2b). Therefore only geophones with distances larger than 90 m to the virtual source were used.

The inferred P and S Velocity profiles are shown in Figure 3.4. We find a good agreement between our estimated P velocity structure and the velocity structure from acoustic logging (courtesy NAM) with lower velocities in the middle of the the reservoir. The top geophone is located in an anhydrite layer and the corresponding high velocity is recovered in our model. The S-velocity structure shows a sharp decrease at the top, but the velocity structure within the reservoir is more poorly

resolved. However, there is a good agreement with the average S velocity of the reservoir sandstone as provided by the NAM.

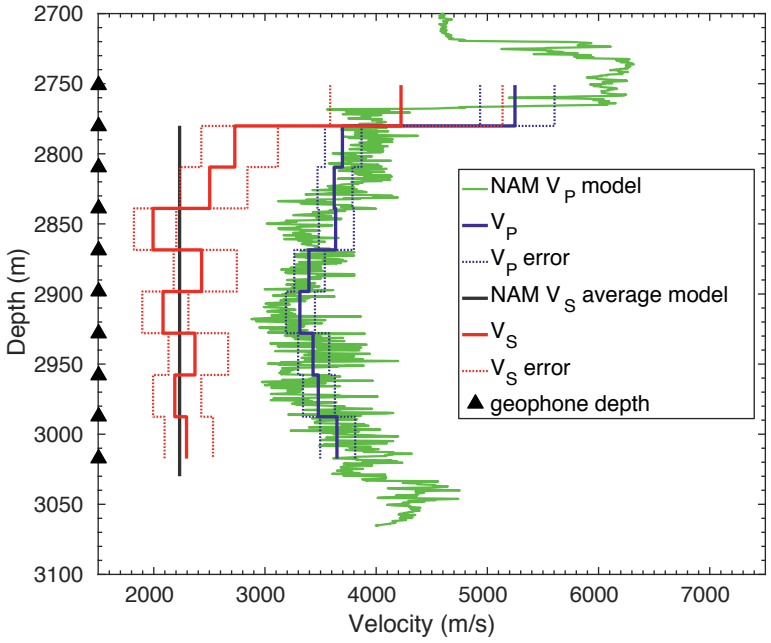

Figure 3.4: Inferred P velocity profile (blue) and S velocity profile (red) with errors (dashed). The P velocity from well log data is shown in green and the average reservoir S velocity in black (data provided by NAM). Geophone depths are indicated by triangles.

3.5 Shear wave anisotropy

Shear wave anisotropy can be used to detect preferred alignment in materials, such as oriented cracks caused by the local stress situation. Miyazawa et al. (2008) successfully retrieved shear wave anisotropy in a borehole by comparing time shifts of the cross-correlations for different azimuths. In this study, we followed a similar approach to determine polarization anisotropy within the reservoir sandstone. We used data from the reservoir only, that is, from the 3rd to the 10th geophone (2809 - 3017 m), and stacked the cross-correlations over the entire period of 33 days. The horizontal components were rotated over 90° with 5° increments to obtain cross-correlation traces for 37 azimuths between -90° (West-West cross-correlations) and 90° (East-East cross-correlations). The data were band pass filtered between 3 and 100 Hz to eliminate high-frequency noise. For each of the azimuths, the shear wave velocity was obtained from the optimum stacking velocity along the 8 cross-correlation traces. The optimum stacking velocity is the velocity that best aligns the S wave arrivals, giving the largest amplitude on the summed trace. The process was

applied using each of the geophones as a virtual source. Fig. 3.5a shows the shear wave velocity as a function of azimuth for each of the virtual sources (indicated by different symbols). For each azimuth the average shear wave velocity with its standard deviation is obtained from these data. Clearly, the data are suggestive of shear wave splitting showing a 2-ψ dependence with a 90° difference between the fast and slow polarization directions. The average shear velocity V_S as a function of azimuth ψ is thus fitted as

$$V_S(\psi) = V_{S_0}\left[1 + \frac{1}{2}M\cos(2(\psi - \phi))\right] \tag{3.1}$$

where V_{S_0} is the azimuth independent shear wave velocity of 2225 m/s, ϕ the fast polarization direction and M the magnitude of shear wave anisotropy defined as $(V_{S_{fast}} - V_{S_{slow}})/V_{S_0}$. We carried out a grid search for ϕ and M to find the optimum parameters using a χ^2 misfit

$$\chi^2 = \frac{1}{N}\sum_{i=1}^{N}\frac{(d_i^{obs} - d_i^{calc})^2}{\sigma_i^2}$$

where the observed data d_i^{obs} is $V_S(\psi_i)$ with its standard deviation σ_i shown in Fig. 3.5a, and d_i^{calc} is obtained from eq. (1). Figure 3.5b shows that the optimum value is obtained for a magnitude of 4% and a fast polarization direction of -65° (N65°W). The uncertainties are inferred from the χ^2=1 contour, giving a magnitude of the anisotropy of (4±2)% with a fast polarization direction of N65°W±18°. This direction is not only consistent with the NW-SE paleostress directions found for the Groningen reservoir (Gent et al., 2009), but also with the current maximum horizontal stress directions determined at two nearby boreholes (Van Eijs (2015); see Fig. 3.1a). Figure 3.5c shows the cross-correlations for the fast and slow directions using the geophone at 2809 m depth as virtual source.

3.6 Discussion and conclusions

In this study, we analyzed noise data from 10 geophones located at ~3 km depth in the Groningen gas reservoir in the Netherlands. Vertical component cross-correlations for 33 days of continuous recording clearly show direct P arrivals in 3-80 Hz band, whereas the horizontal components yield S arrivals at 3-50 Hz (Fig. 3.2). We observe that the cross-correlations are dominated by noise from above and show both diurnal and weekly variations (Fig. 3.3). This indicates that the fluctuations are due to variations in anthropogenic noise. Previous studies by Grechka & Zhao (2012), Vaezi & van der Baan (2015) and Behm (2016) have shown that surface activity can indeed be the dominant noise source up to 2 km depth. Our results confirm their observation, extending it to a depth of 3 km. Traffic can be an important source of noise; it has been employed in other interferometry studies (Behm et al., 2014; Nakata et al., 2011; Quiros et al., 2016). The effects of traffic, from the national road N46 and the railroad (Fig. 3.1), also seem to dominate our noise recordings at depth. Analyzing the noise spectra as a function of time, we found that relatively high frequency noise was generated at regular times corresponding to the train schedule (Fig. S5 in supporting information), suggesting that the train signal

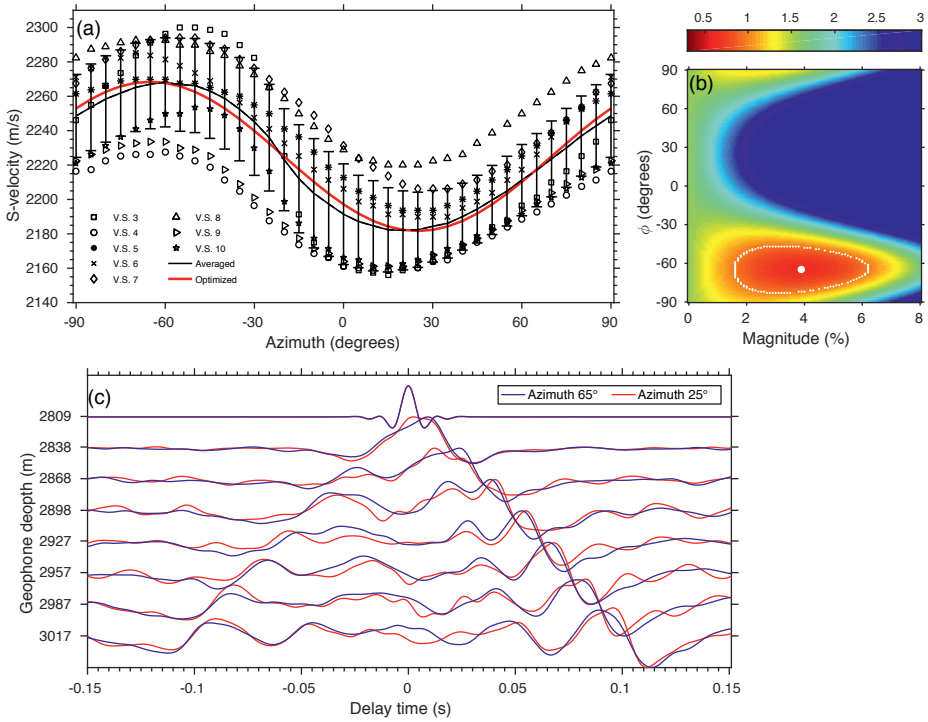

Figure 3.5: (a) Shear velocity as a function of azimuth for the 8 virtual sources (various symbols). The average is represented by the black solid curve and the standard deviations are indicated by the vertical bars. The optimum fit to the data (M=4%, ϕ=-65°) is shown by the red curve. (b) χ^2 misfit as a function of azimuth of the fast direction and magnitude. The white line represents the χ^2=1 contour. (c) Horizontal component cross-correlations for azimuth N65°W (fast, blue) and N25°E (slow, red) for a virtual source at 2809 m.

is an important source of high-frequency noise. Traffic along the road N46 is another likely noise source as revealed by the precursory P wave signal on the horizontal and vertical cross-correlations (Fig. 3.2). Assuming wave propagation along a straight line from the road at ~1800 m distance to the borehole at 3 km depth, we find that the signal would come in at an angle of 31° with the vertical. Using a P wave velocity of 3700 m/s in the medium, this would give an apparent velocity of 4300 m/s, very close to the 4500 m/s observed for the precursory arrival. It may seem surprising that we obtained strong P and S wave cross-correlation peaks at the 'correct' travel times corresponding to downward propagation along the borehole, considering that traffic noise is generated at some horizontal distance. We note, however, that subsurface scattering likely plays an important role and that constructive interference from randomly distributed noise sources is maximum in the stationary phase region (Snieder, 2004; Snieder & Larose, 2013), that is along the borehole in this case.

In this study we obtained the P and S wave travel times between each geophone pair, we used the 33(days)*24(hours) travel times picked from hourly stacked cross-correlations and determined the most likely travel times from the measurement distribution. The difference between this measurement and the maximum cross-correlation time obtained for the entire 33-day stack is within one sample (0.5 ms).

We also found evidence for shear wave anisotropy, estimating the average shear velocity within the reservoir as a function of polarization direction. The anisotropy amounts to (4±2)% with a fast direction of N65°W±18°. The orientation is roughly similar to the NW-SE paleostress direction as well as directions of maximum horizontal stress determined at nearby boreholes, so the origin of the anisotropy remains ambiguous. Although magnitudes of shear wave anisotropy and stress anisotropy cannot directly be related, we note that the magnitude of anisotropy (~4%) and the difference between the maximum and minimum horizontal stress at nearby wells (~3%) (Van Eijs, 2015) are both small.

This study has shown that the correlation of anthropogenic noise with frequencies up to 80 Hz can be used to determine the velocity structure along a borehole at 3 km depth. The scattered wavefield produced by traffic on a nearby road and railroad likely allowed the accurate construction of the velocity profile. This opens perspectives for other (former production) boreholes with similar noise settings for which the velocity structure or anisotropy is insufficiently known. We did not succeed to identify temporal variations of the medium within the 33 day time span because the cross-correlations appeared to be dominated by fluctuations in anthropogenic noise (Fig. 3 and Fig. S4 in supporting information). Nevertheless, it should be possible to identify temporal medium variations at locations with more stable noise environments, as shown by Behm, 2016.

3.7 Supporting information

3.7.1 Figure S1

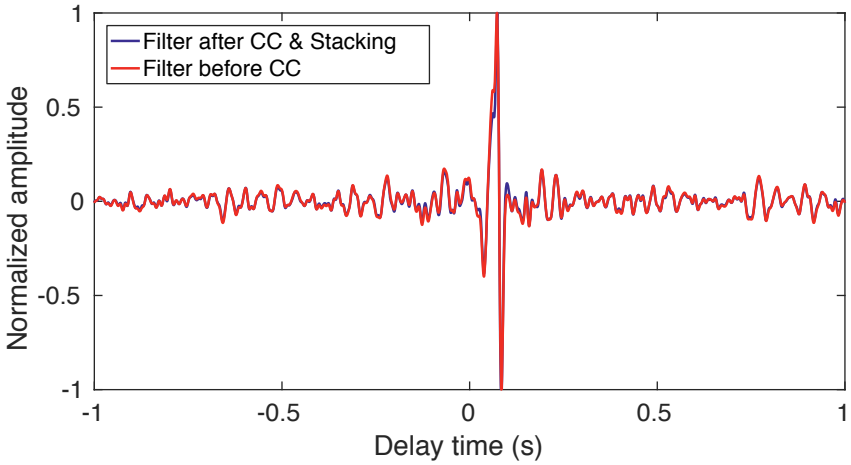

Cross-correlations for 24 hours of vertical component stacked data (21-11-2013) with the 1st geophone as virtual source and the 10th geophone as receiver. The red curve shows the result when a 3-100 Hz filter was applied before the cross-correlation while the blue curve shows the result when this filter was only applied after cross-correlation and stacking the data.
The maximum amplitudes of the two cross-correlations were normalized to 1.

3.7.2 Figure S2

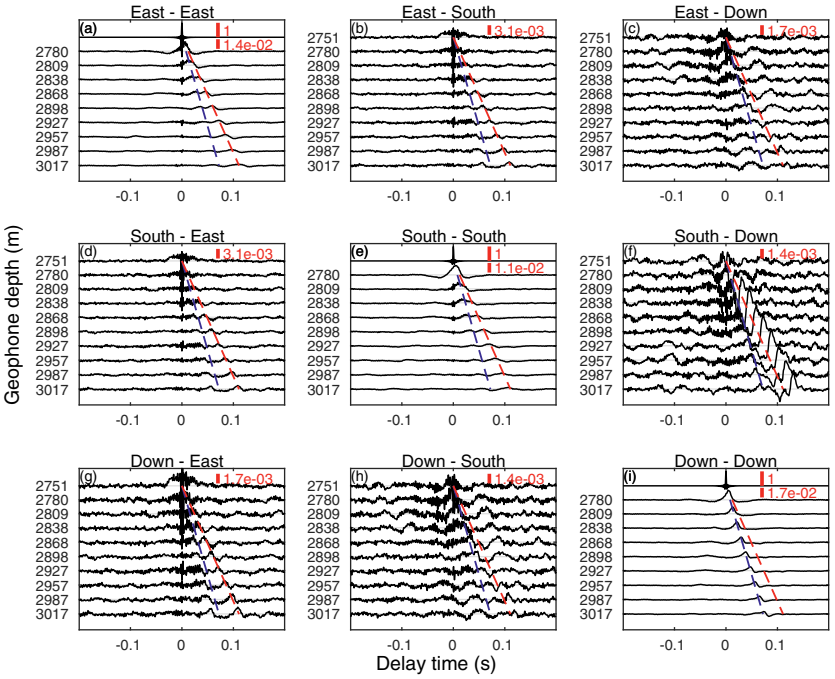

The 9 component cross-correlations with the 1st geophone as a virtual source. The vertical short red bars in each panel indicate the scales. Note that the auto-correlations have a different scale bar compared to the others. The blue dashed lines indicate the downgoing P wave inferred from the peaks of vertical-vertical component cross-correlations (i). The red dashed lines represent the downgoing S wave identified from the East-East component cross-correlations (a).

3.7.3 Figure S3

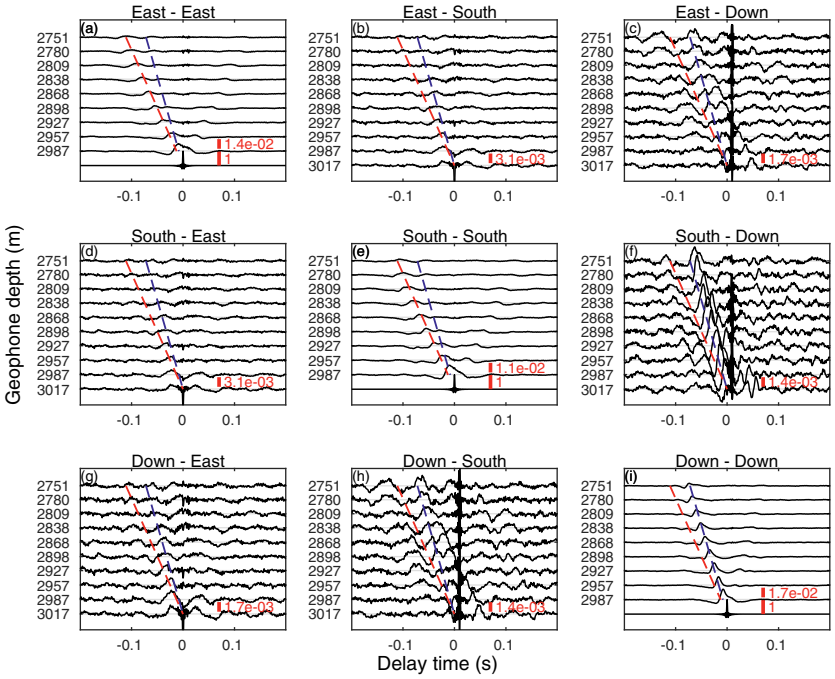

Similar to Figure S2, but with the bottom geophone as virtual source.

3.7.4 Figure S4

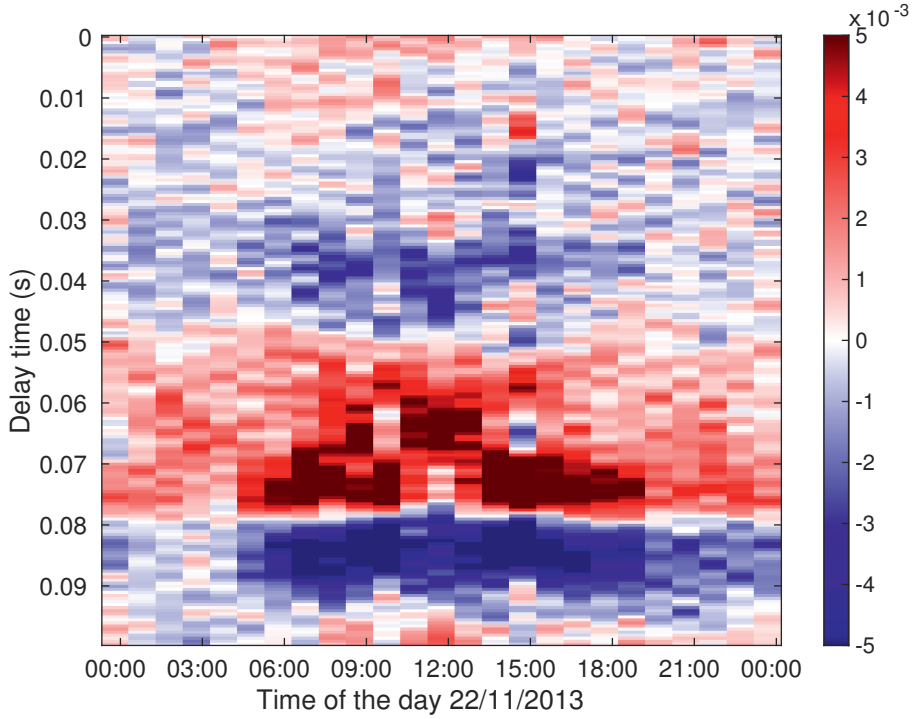

Variations of the hourly cross-correlation stacks for a working day (Friday, 22-11-2013). It is a zoom-in of Fig. 3a in the paper: the causal part of the vertical cross-correlations with the virtual source at the top geophone and the receiver at the bottom.

3.7.5 Figure S5

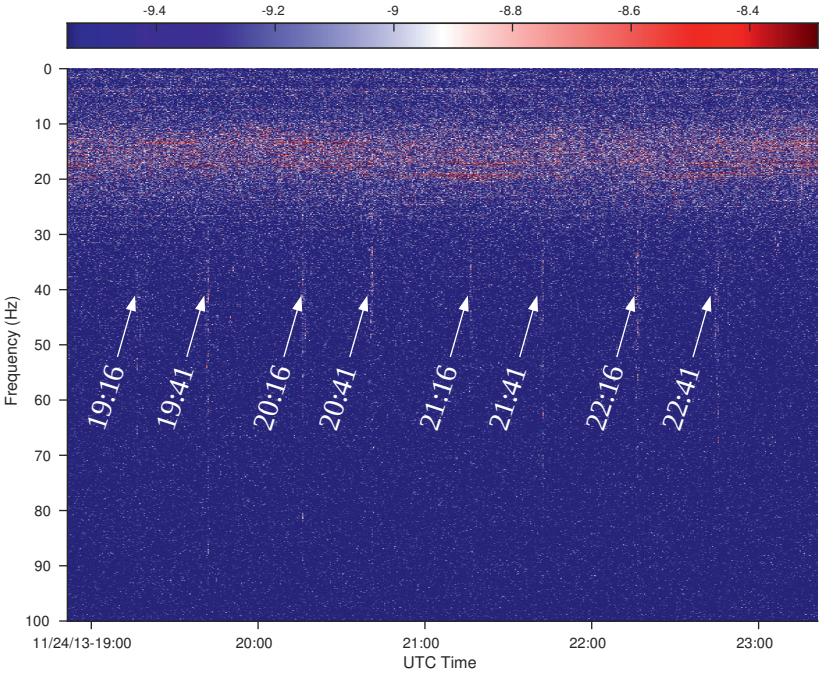

Spectrograms of vertical component noise recorded at the top geophone on 24-Nov-2013 for 30 second time segments. The higher frequency (30 - 80 Hz) noise appears at regular times corresponding to the train schedule, it is present in 1 or 2 segments. The signals at 16 minutes past the hour correspond to trains traveling in southwesterly direction, those at 41 min to trains going in the opposite direction.

Chapter 4

Monitoring the P and S velocity in the Groningen gas field using train noise

This chapter is based on:

Zhou, W. & H. Paulssen (2019), Travel time changes in the Groningen gas reservoir by train noise interferometry of borehole data, in: *Extended abstracts of 81th EAGE Conference and Exhibition 2019*, European Association of Geoscientists & Engineers, pp. 1–5, DOI: 10.3997/2214-4609.201900671.

Zhou, W. & H. Paulssen (2020), Compaction of the Groningen gas reservoir investigated with train noise, *Manuscript submitted for publication*.

4.1 Introduction

Seismic waves that travel through the earth are sensitive to the properties along their wave paths. If the properties of the medium change, wave propagation will change, implying that there will be changes in travel time, signal amplitude and potentially of the ray path. Monitoring changes of the seismic wave field thus is of great importance for imaging changes in subsurface conditions, for instance to detect stress changes surrounding a fault (Niu et al., 2008), to infer near-surface weakening due to an earthquake (Nakata & Snieder, 2011), or to determine stress or strain changes caused by oil or gas production (Hatchell & Bourne, 2005), mining (Olivier et al., 2015) or CO_2 storage (Boait et al., 2012). With advanced researches on the coda of ambient noise auto- or cross-correlations seismic velocity changes have been detected due to the solid-earth tides (Sens-Schönfelder & Eulenfeld, 2019) and earthquake damage in shallow layers (Brenguier et al., 2008; Wegler & Sens-Schönfelder, 2007). Despite the large accuracy in relative velocity that can be achieved in such studies of coda-wave interferometry ($dv/v < 0.1\%$), their disadvantage is the inability to localize the detected changes. Therefore, it is difficult to link the observations to changes in the earth, although there have been studies to solve this problem (Larose et al., 2010; Obermann et al., 2019). Compared to studies that employ coda wave interferometry, interferometric studies that identify variations in the direct P or S wave response have a better spatial resolution.

The Groningen gas field in the Netherlands is one of the largest onshore gas fields in the world. Production started in 1963, causing induced seismicity with damage to houses especially in the last two decades (NAM, 2016). Although the triggering mechanism of the earthquakes is complex, it is suggested that reservoir compaction as a result of gas depletion plays a dominant role (Bourne et al., 2014; Candela et al., 2018; Dempsey & Suckale, 2017). Monitoring the temporal variations of the reservoir is essential to calibrate geomechanical models that relate compaction and subsidence to the extraction of gas. In Groningen, in-situ measurements of compaction are obtained from downhole radioactive markers (Kole, 2015) and distributed strain sensing (DSS) (Cannon & Kole, 2018). However, seismological methods have not been used. Conventionally, temporal variations of seismic velocity in reservoirs are inferred indirectly from 4D seismic surveys (Hatchell & Bourne, 2005; MacBeth et al., 2018). Alternatively, as suggested by Behm (2017), it should be possible to measure temporal in-situ velocity variations from passive data with noise interferometry. Here we investigate the feasibility to detect time-lapse changes in P and S wave velocity from geophone data in a deep borehole.

In 2013, two monitoring wells in the Groningen gas field in the Netherlands were equipped with geophone strings in the reservoir at 3 km depth. Zhou & Paulssen (2017) (Chapter 3) showed that it was possible to determine the P- and S-wave velocity structure in the reservoir along one of these boreholes (SDM-1) using noise interferometry by cross-correlation. However, it was also clear that diurnal variations in anthropogenic noise had a strong impact on the interferograms, impeding the detection of travel time variations caused by changes in the medium. In chapter 2, it was shown that there are regular and repetitive noise signals in the continuous geophone recordings of SDM-1 that are generated by passing trains along a

railroad at ~500 m distance from the well. Zhou & Paulssen (2017) (Chapter 3) suggested that this train noise dominantly contributes to the high-frequency part of cross-correlations, which would allow a higher time resolution than can be obtained from the lower-frequency ambient noise.

Trains are well-known sources of vibrations, especially for generating Rayleigh waves. Their signals have been analyzed and modeled to determine soil characteristics for engineering purposes (e.g., Yang et al., 2003). Various studies have focussed on the character of train signals (e.g., Chen et al., 2004; Fuchs & Bokelmann, 2018). Inbal et al. (2018) were able to determine attenuation in the shallow crust from Rayleigh waves generated by trains. Some studies employed seismic interferometry of train signals. Quiros et al. (2016) used the signals recorded by an array of geophones parallel to a railway and retrieved strong Rayleigh waves and weak P waves. Zhang et al. (2019) addressed the problems of train-signal interferometry that are associated by the movement of the source and were able to obtain direct P waves. Brenguier et al. (2019) designed a dense array in southern California to retrieve P waves by interferometry of freight-train noise and showed the potential for monitoring seismic velocity changes associated to seismicity of active faults.

In this study, we detect and isolate train signals from the downhole geophone recordings in borehole SDM-1. Noise interferometry is applied to the high-frequency train signals to retrieve the P- and S-wave response within the reservoir and to obtain time-lapse measurements. To our knowledge, this is the first study that employs train noise in deep-borehole data.

4.2 Borehole data and train signals

The data that are used in this chapter are from two 5-month geophone deployments in 2015 in well SDM-1 (phase 5 and 6: Table 2.1, Figs. 2.1 and 1.2). The well is located in the Loppersum area of the Groningen gas field, a region of high seismcity and compaction (Bourne et al., 2014). Three-component 15-Hz geophones were positioned at depths from 2750 m to 3000 m, with inter-geophone spacings of 30 m from the top geophone (GP01) to the 9^{th} geophone (GP09) and 15 m between GP09 and lowest geophone (GP10). The geophones are positioned at the same depths for the two deployments and there is a only a small time gap of 4 days between the two deployment periods. A detailed description of the deployments and sensor parameters is given chapter 2 and appendix 2.11.

Fig. 4.1 shows a map of the region with the single track railway which links the two towns Stedum and Loppersum and borehole SDM-1 at 500 m distance. Fig. 4.2 presents the vertical component recordings of the borehole geophones (filtered between 30 and 120 Hz) for a train from Stedum to Loppersum (Fig. 4.2c) and from Loppersum to Stedum (Fig. 4.2d). The spectrograms of the recordings by the bottom geophone (GP10 at 3000 m depth) are presented in Figs. 4.2a and b. These spectrograms are obtained from the amplitude spectra for sliding time windows of 2 s duration with 1.9 s overlap.

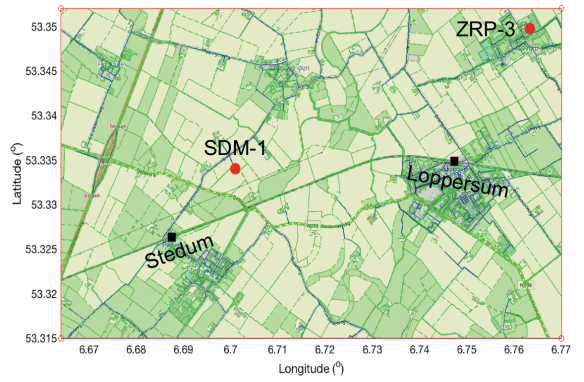

Figure 4.1: Location of borehole SDM-1 and the railway track with stations Stedum and Loppersum. The distance from SDM-1 to the railway is ~500 m.

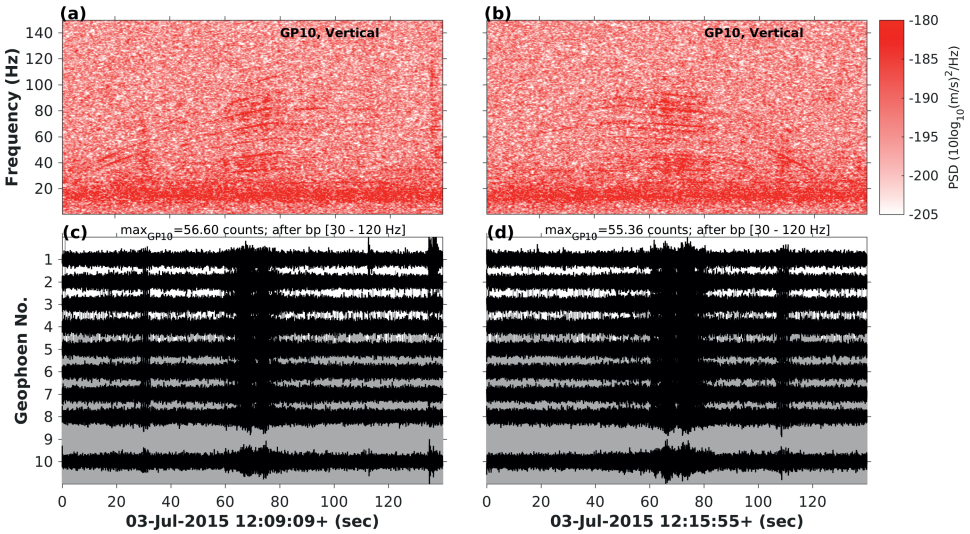

Figure 4.2: (c-d): Filtered (30 - 120 Hz) vertical component geophone recordings at SDM-1 of a train departing from Stedum station to Loppersum (c), and a train approaching Stedum station from Loppersum (d). The vertical component of geophone 9 was out of order during this deployment. (a-b): Spectrograms of the recordings by geophone 10.

Despite the large depth of the geophone array (3 km), train signals can be clearly distinguished in the spectrograms (Fig. 4.2a,b). In the time domain, the signals can not be recognized in the unfiltered data, but they can be identified after band pass filtering from 30 to 120 Hz (Fig. 4.2c,d). The spectrogram of Fig. 4.2a shows that the characteristic frequencies increase from ~20 s to ~80 s (after 12:09:09 on 3 July 2015) with maximum amplitudes between 60 and 80 s when the train is close to the borehole. The timing fits the train schedule which says that trains in the direction to Loppersum should depart from Stedum station at 12:08. The increasing frequencies

are likely produced by train acceleration. Note that preceding the dominant wavetrain, there is a smaller amplitude signal at ~30 s in Fig. 4.2a,c. The spectrogram of the next train is shown in Fig. 4.2b (starting at 12:15:55). In this case the dominant signal begins with high frequencies which gradually decrease, probably due to the deceleration of a train approaching Stedum from Loppersum. The timing agrees with the train schedule: trains from Loppersum should arrive at Stedum at 12:17. The secondary arrival is now observed after the dominant train signal, at ~110 s in Fig. 4.2b. The timing of the secondary wavetrains with respect to the dominant signal for trains in opposite directions suggests excitation approximately halfway between Stedum station and SDM-1 along the railway. A satellite image shows that there is a switch at this location from the single track to a double track at Stedum station which likely excites the secondary arrivals.

4.3 Train signal detection and deconvolution

Unlike previous studies which use trains signals buried in continuous noise (Brenguier et al., 2019; Quiros et al., 2016; Zhang et al., 2019), we use isolated train signals to exclude other types of noise and strong signals (for instance caused by traffic, earthquakes or anthropogenic noise from machine vibrations; see Fig. 2.3). So before we can calculate the interferograms, we first need to detect the train signals.

As shown in Fig. 4.2a-b, train signals are tremor-like (lacking a clear onset) with an amplitude that is slightly higher than the noise in the 30-120 Hz frequency band. Their duration can be up to 100 seconds. A first quick-and-dirty detection is obtained from the 30-120 Hz continuous, vertical component data of geophone 2: when the average of the (absolute) amplitude of a 30 s moving time window is above a certain threshold. Then, the spectrogram around each potential event is obtained. For each spectrum (as a function of time) the total power within the 30-90 Hz frequency band is calculated. This time-dependent signal is then smoothed to allow clear identification of the main and the secondary signals (usually their time difference is 30 to 40 s). When the secondary signal arrives before the dominant signal, the event is identified as a train from Stedum to Loppersum, if the order is reversed it is identified as a train in the opposite direction. In this way, out of the roughly 9000 detected trains for each 5-month period, the travel direction of approximately 7000 trains could be determined. Finally, a 20 s time window is determined around the maximum of the main signal. The choice of 20 s is based on the observation that the dominant signal often has this duration (from 60 to 80 s in Fig. 4.2).

The P and S wave response can be obtained by interferometry using cross-correlation or deconvolution (Snieder et al., 2006; Snieder et al., 2009). Rather than applying cross-correlation as in Zhou & Paulssen (2017) (Chapter 3), deconvolution was chosen in this study because of its ability to preserve the high frequencies while eliminating the train signal source. The study by Akbar et al. (2018) suggests that for strong and stable noise sources, the deconvolution method performs well for the geophone data of SDM-1.

In the frequency domain, the deconvolution of the j^{th} component of geophone R

(R^j) by the i^{th} component of geophone S (S^i) is given by

$$D_{RS}^{ji}(\omega) = \frac{R^j(\omega)}{S^i(\omega)} \tag{4.1}$$

where D_{RS}^{ji} may be interpreted as an estimate of the Green's function response of a virtual source at the location of S acting in the i-direction recorded by a receiver at the location of R in the j-direction. In practice, to preserve stability of the deconvolution, a water level is applied and the deconvolution is approximated by:

$$D_{RS}^{ji}(\omega) \approx \frac{R^j(\omega)S^{i*}(\omega)}{\Phi^i(\omega)} \tag{4.2}$$

where $S^{i*}(\omega)$ is the complex conjugate of $S^i(\omega)$, and $\Phi^i(\omega)$ is its auto-correlation with a waterlevel:

$$\Phi^i(\omega) = max\{S^i(\omega)S^{i*}(\omega),\ c \cdot max\{S^i(\omega)S^{i*}(\omega)\}. \tag{4.3}$$

The water level is taken as 0.01% of the maximum spectral power of the auto-correlation ($c = 0.0001$). If the auto-correlation for a certain frequency has a value below this water level it is replaced by it.

The deconvolutions are calculated for 30-90 Hz bandpass filtered data to avoid influence from other types of (higher amplitude) noise at frequencies below 30 Hz. Moreover, train signals are strongest in the 30-90 Hz frequency band (Fig. 4.2a,b).

4.4 P and S wave response in the reservoir

By applying inter-geophone deconvolutions we were able to retrieve P wave and S wave responses. The P wave response is retrieved from the vertical component deconvolutions. In the following, we illustrate the method for the data of phase 6 (3 Jul - 1 Dec 2015). Fig. 4.3b presents the vertical component deconvolutions of a single train with the data of the top geophone ($D_{RS}^{ZZ}(t)$, with S=GP01, R=GP01-GP10). It shows that a stable deconvolution response can already be obtained for a single train signal. The direct downgoing P wave from GP01 is retrieved robustly, despite the slight oscillations that are present after the main peak. By averaging over 60 trains (approximately the number of identified trains per day), we obtained stable deconvolutions that are nearly identical to the ~9000-train average for the entire deployment period (Fig. 4.3c). By stacking, incoherent oscillations are significantly reduced and reflections from the bottom and the top of the reservoir can be distinguished. Although the P wave coda is determined with sufficient accuracy to allow a more detailed investigation, we focus here on the direct P wave only because it has a higher amplitude and is more stable. Coda wave analysis of the deconvolved data looks promising but would require comprehensive waveform modeling.

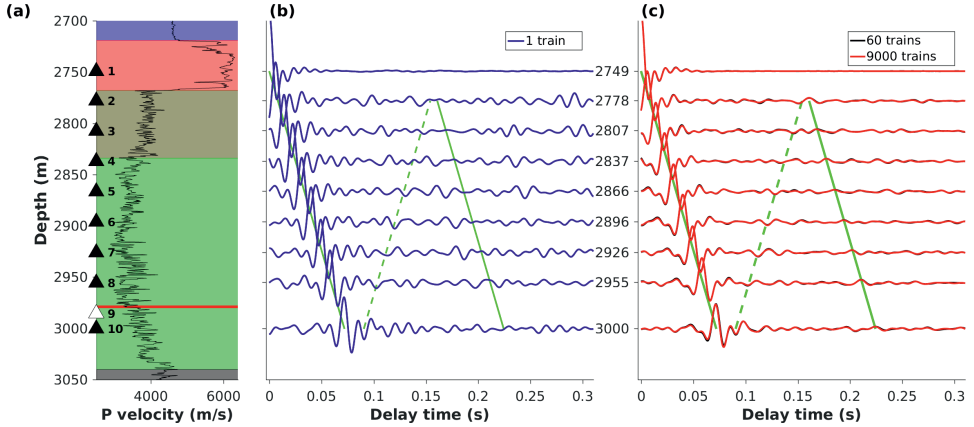

Figure 4.3: (a) Geophone locations (triangles), P-wave velocity from well-log data (black line) and rock type. Colors represent from top to bottom: rock salt (purple), anhydrite (pink), claystone (brown), sandstone (green) and shale (grey). The red line marks the gas-water contact. (b) Vertical component deconvolutions for a single train using the data of the top geophone. (c) Stacked deconvolutions for 60 trains (black) and 9000 trains (red, on top). Solid and dashed green lines represent down- and upgoing P waves with a velocity of 3500 m/s. The deconvolutions are obtained for the data of phase 6 (3 Jul - 1 Dec 2015).

Our previous study, which used cross-correlation interferometry of ambient noise, showed that the P wave response of SDM-1 could be retrieved from the horizontal component geophone recordings (Zhou & Paulssen, 2017: Chapter 3). Previous train noise interferometric studies only retrieved the P wave response (Brenguier et al., 2019; Zhang et al., 2019; Zhou & Paulssen, 2019). Here we show that the S wave response can also be obtained from train signals.

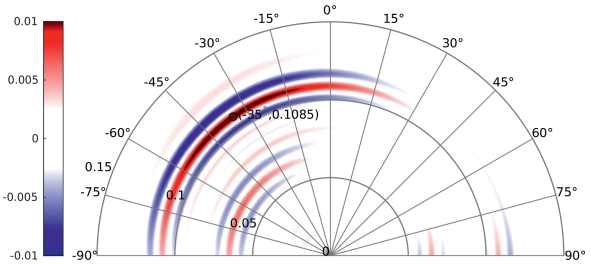

Figure 4.4: Horizontal component deconvolutions of geophone 10 with geophone 2 as a function of azimuth. The time scale is 0 to 0.15 s along the radial direction. The largest amplitude is found for an azimuth of -35° at 0.108 s, the inter-geophone S wave travel time.

In order to obtain the S wave response with the highest signal-to-noise ratio, we first searched for the direction that gives strongest S wave amplitude. To find this direction, we performed horizontal component deconvolutions for all azimuths for the geophone pair GP02-GP10 (which covers the largest distance in the reservoir). The horizontal component pairs were rotated from west (-90°) to east (90°) to find

the largest amplitude. Fig. 4.4 shows that the largest amplitude is obtained at ~0.11 s for an azimuth of -35° (35° west from north), or, alternatively, 145° (145° east from north). The timing matches the expected P-wave travel time for the velocity model of Zhou & Paulssen (2017) (Chapter 3). Considering the uncertainty in the azimuth and the uncertainty in the orientations of the horizontal components (Appendix 2.15), it is likely that the azimuth of -35° roughly agrees with the direction from SDM-1 to the railway. If the S waves were excited by horizontal movement of the train on the railway track, the maximum S wave polarization would be parallel to the railway. Instead, the obtained direction is roughly perpendicular. It is therefore likely that the incident S waves recorded by the geophone array are generated by conversion from P waves in the overburden of the reservoir. This implies that they predominantly have an SV-type polarization. Because the relative orientations of the horizontal components (with respect to each other) are fairly well constrained (Appendix 2.14 and 2.15), the horizontal components of all geophones were rotated to 145° and 55°. We found that the train signal deconvolutions between the geophone pairs for the 145° direction indeed produced clear S wave responses.

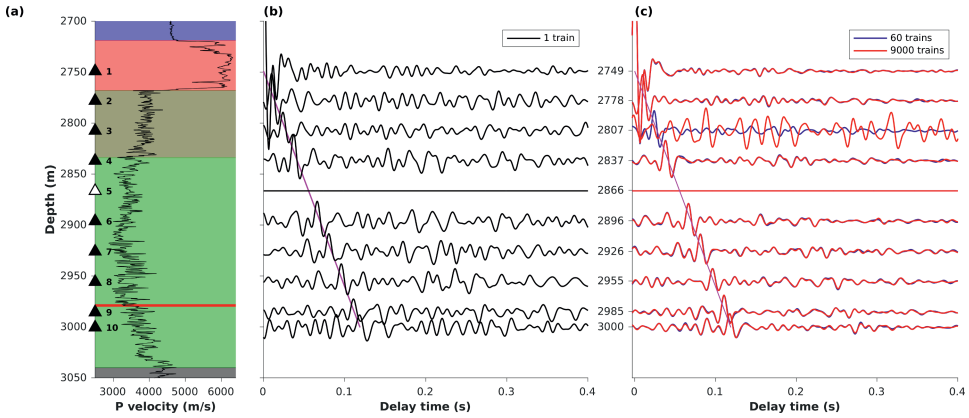

Figure 4.5: (a) Geophone locations and rock formation as in Fig. 4.3a. (b) Horizontal component deconvolutions for a single train for an azimuth of 145°. (c) Stacked deconvolutions for 60 trains (blue) and ~9000 trains (red, on top). The magenta line indicates a the downgoing S wave with a velocity of 2100 m/s. (GP05 had one horizontal component out of order. GP03 was working in the beginning but broke down after ~10 days.)

Fig. 4.5b shows that for the azmuth of 145° the downgoing direct S wave can be obtained from a single train deconvolution with an average velocity of 2100 m/s. Similar to the P wave response, the S-wave stack of 60 trains gives nearly identical results to the one of ~9000 trains (Fig. 4.5c).

4.5 P and S velocity in the reservoir

In the previous section, it was shown how inter-geophone P and S wave responses can be retrieved from deconvolutions of train signals. Thus, the P and S wave travel

times for all possible geophone pairs can be obtained from the peaks of the downgoing direct waves. The velocity structure can then be calculated from the travel time data.

The timing of the peaks of the arrivals times is limited by the 0.5 ms sample interval. To obtain a more accurate estimate, quadratic 3-point interpolation around the maximum is performed (Silver et al., 2007).

Similar to Zhou & Paulssen (2017) (section 3.4), a kernel density estimation (Botev et al., 2010) is used to obtain the probability density function of the measured travel times for each geophone pair and its maximum likelihood value is taken as the inter-geophone travel time. The travel times from all geophone combinations are then used in a linear least squares inversion to obtain the P and S wave travel times between neighboring geophones with uncertainty. Subsequently, the P and S wave velocity profiles are calculated. Fig. 4.6 presents the P and S velocity profiles obtained from the two data sets for 2015 (phase 5 and 6). The difference in the P velocity profiles inferred from trains in the two opposite directions was found to be negligible (see also Zhou & Paulssen, 2019).

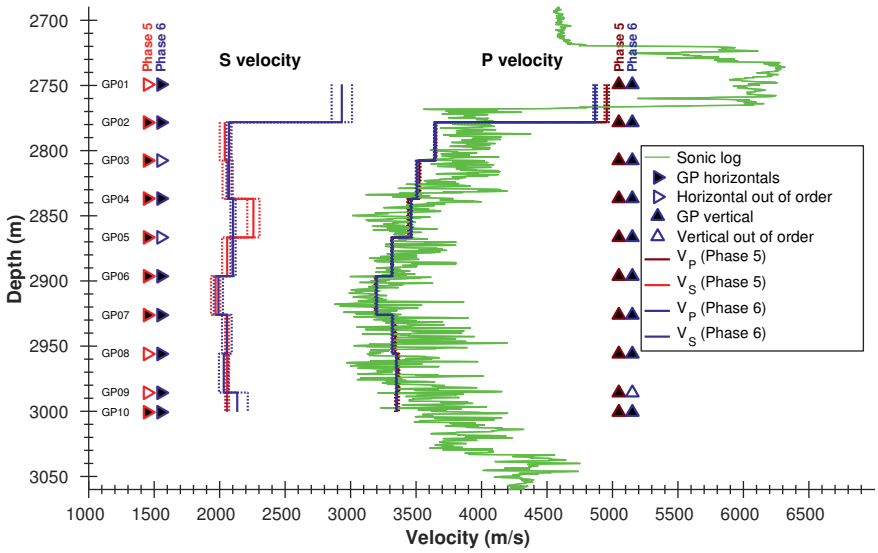

Figure 4.6: P and S velocity profiles (solid) by train-signal deconvolution obtained for two subsequent deployments: phase 5 (23 Jan - 29 Jun 2015, red) and phase 6 (3 Jul - 1 Dec 2015, blue). The errors are indicated by the dashed lines. Triangles represent geophone positions: filled when the components were operational during the entire deployment (left for horizontals, right for vertical). The sonic log in green is provided by NAM.

The P-velocity structure obtained by train-noise interferometry matches the sonic log that was measured in 1963 very well. However, we observe that our average P wave velocity for the Ten Boer claystone (GP02-GP04) is lower than the P velocity of the sonic log provided by NAM. This was also found for the P velocity profile obtained by ambient noise cross-correlation (Zhou & Paulssen, 2017: Chapter 3).

but here, with the higher frequency content of the train signals, the uncertainty is significantly smaller. The cause of the smaller P velocity in the claystone obtained from our data is not clear. Rather than an underestimate of the true velocity, it is expected to find an overestimate of the (apparent) velocity by interferometry. This will occur if the dominant wavefield is inclined to the array of geophones. It is also unlikely that the velocity in the claystone has decreased over the past 50 years, for instance by the opening of cracks associated to earthquakes, because we do not observe a travel time increase for 2015 in the time lapse data, as will be presented later. Potentially, there is an effect caused by the difference in scale lengths. The sonic log measurements typically use a 10 kHz signal corresponding to a wavelength of ~0.4 m, whereas our measurements have frequencies from 30 to 90 Hz corresponding to wavelengths of 40-120 m. This implies that our data are sensitive to a wide area outside the borehole. The fault map from the NAM shows the presence of a fault (with an offset of 40 m) at a distance of 50 m from the borehole. We speculate that heterogeneity in the vicinity of the borehole, potentially related to faulting (and related damage zones), may explain the discrepancy between our results and the sonic log data.

Note that the S velocity from GP02 to GP04 is also low, and lower than the results from the cross-correlation noise study using East-component data (Fig. 3.4). However, we find that the S-velocity profiles from the two studies are overall in good agreement, considering potential effects of heterogeneity and anisotropy (~4%, section 3.5).

4.6 Temporal changes of P wave travel times

As was discussed in the introduction, seismic velocity changes have been observed and linked to reservoir compaction (Hatchell & Bourne, 2005; MacBeth et al., 2018) and earthquakes (Niu et al., 2008). One of the main goals of this research is to investigate potential seismic velocity changes in the Groningen reservoir. In the previous section, we used isolated train signals to retrieve inter-geophone P and S wave travel times and velocities. Here we show that the measurements can also be used to determine temporal changes.

To obtain inter-geophone travel time measurements with a higher accuracy than single train measurements, we stacked the deconvolutions of 30 consecutive trains travelling in the same direction. Travel times of the direct P waves are then measured from the 30-train stacks. Since there are typically about 30 identified train signals per direction per day, this approximately corresponds to one measurement per day for each direction. By using all data for 2015, this allows analysis of temporal variations over the year.

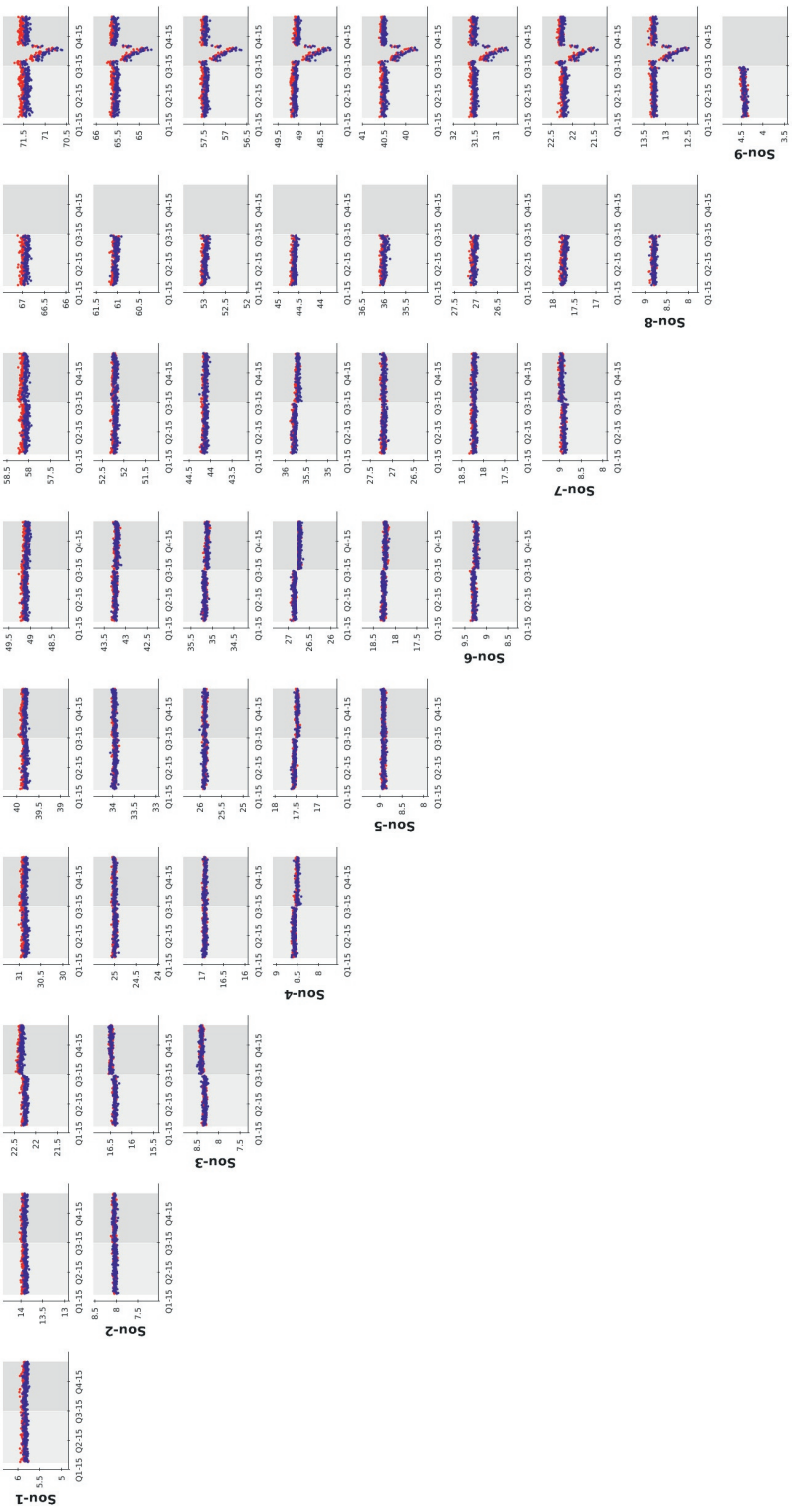

Figure 4.7: P wave travel times as a function of time from the stacked deconvolutions for all geophone combinations. Rows show diagrams for geophones acting as virtual source, columns those for geophones acting as virtual receiver. Deployment phase 5 (23 Jan - 29 Jun 2015) has a light-grey background, phase 6 (3 Jul - 1 Dec 2015) is in darker grey. P wave travel times obtained for trains from Stedum to Loppersum are in blue, for Loppersum to Stedum they are in red. Travel times along the vertical axis are in ms.

Fig. 4.7 gives an overview of all P wave travel time measurements. Each row shows the travel time diagrams obtained from the stacked vertical-component deconvolutions with, from top to bottom, the signal of geophone GP01 to GP10 (i.e. the denominator in the frequency representation of the deconvolution). These geophones can be interpreted as the virtual sources. The columns represent the virtual receivers, the signal which is deconvolved. Within each diagram, the background indicates the deployment period: light grey for phase 5 (23 Jan - Jun 29 2015), darker grey for phase 6 (3 Jul - 1 Dec 2015). The travel time measurements for trains from Stedum to Loppersum are in blue and those for the opposite direction are in red.

Most of the data do not show obvious trends as a function of time, except for the travel time data to geophone 10 during the first months of phase 6 (last column of Fig. 4.7). This outstanding travel time anomaly is probably related to drilling of a deep borehole and will be discussed in chapter 6. Some diagrams show distinct steps in travel time from the first deployment to the next, for instance for the geophone pairs that have geophone 4 as virtual source or receiver. These are probably caused by small changes in geophone position between the two deployments.

To investigate potential changes in the medium associated to earthquakes, we analyzed the travel time data around the occurrence of two local earthquakes: a M_L 0.9 earthquake at 2.4 km distance and a M_L 3.1 event at approximately 14 km. We did not observe significant travel time variations for the days around these earthquakes. This implies that the travel time changes at SDM-1 associated to these earthquakes are smaller than can be measured, that is smaller than the standard deviation of 30 - 40 μs. Furthermore, it should be noted that the time resolution is limited because we only have a single measurement per day.

To investigate the long-term travel time changes that might be related to reservoir compaction, we applied linear fits to the travel time data. We did this per deployment for each geophone pair and obtained independent estimates for trains from Stedum to Loppersum and the opposite direction. The travel time changes over the entire deployment period are then estimated from the linear fits. Fig. 4.8 shows examples for the geophone pair GP01→GP02 across anhydrite-claystone interface (Fig. 4.8a) and for geophone pair GP02→GP08 along the reservoir (Fig. 4.8b). Compilations of all travel time changes per 5-month deployment period are presented in Tables 4.1 and 4.2. To assess the reliability of the results, we not only calculated the travel time changes for the deconvolutions with the virtual source above the virtual receiver (data above the diagonal in Tables 4.1 and 4.2), but also for the virtual source below the virtual receiver (data below the diagonal). It can be verified that most of the measurements are in agreement within the error.

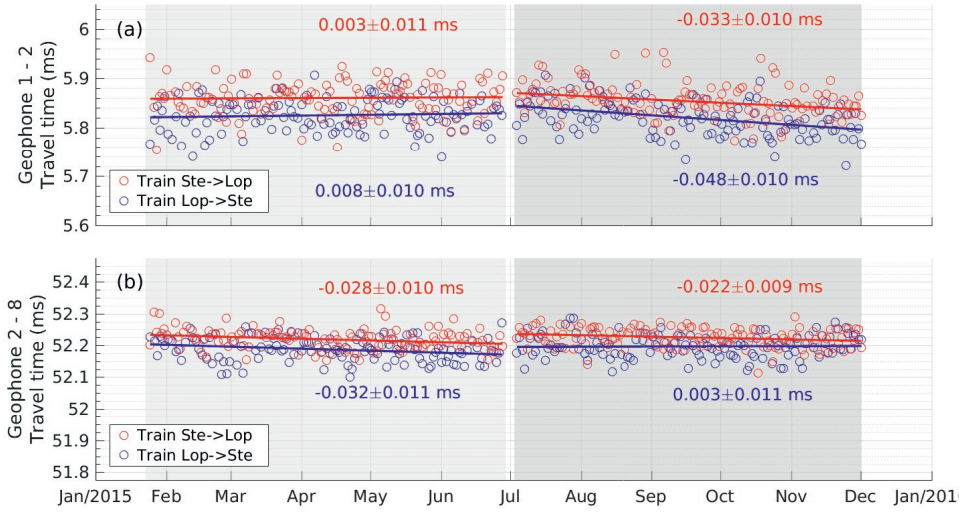

Figure 4.8: (a) P-wave travel times from GP01 to GP02 and (b) from GP02 to GP08. The measurements are obtained from stacked deconvolutions for trains from Stedum to Loppersum (red) and from Loppersum to Stedum (blue). The two deployments are indicated by their gray scale background. Linear fits are applied to the data and the accumulated travel time change per deployment period (with standard deviation) is noted.

The tables show that most inter-geophone travel times decreased a few or a few tens of microseconds per 5-month deployment period. The one-standard deviation uncertainties are typically around 10 μs. Since the travel time changes are generally smaller or just slightly bigger than the uncertainty, it is difficult to draw hard conclusions. However, the general pattern of decreasing travel times (negative values in Tables 4.1 and 4.2) is in agreement with an increase of medium velocity caused by compaction.

Notably, there are a few striking patterns in the observations. For phase 5, most geophone pairs that include GP09 have travel time changes of tens of microseconds: the combinations of GP01 up to GP07 (all above GP09) with GP09 all show a travel time decrease (of -46 μs, on average), the geophone pair GP08-GP09 has a travel time change close to zero, and the geophone combination GP09-GP10 has a travel time increase of several 10s of μs. (Table 4.1). A somewhat similar behavior is found for the geophone pairs involving GP08: combinations of GP01 to GP05 with GP08 give a travel time decrease (on average -20 μs), geophone pairs GP06-GP08, GP07-GP08 and GP08-GP10 have small travel time changes, whereas the travel time change of pair GPO8-GP10 is positive. Lastly, the combinations with GP06 show an analogous pattern: GP01 to GP04 with GP06 have a negative travel time change (of 28 μs, on average), the travel time change of GP05-GP06 is close to zero, and that of GP06-GP07 is positive. The simplest explanation is an instrumentation artifact, such as an upward movement of geophones GP06, GP08 and G09. For instance, a 20 μs travel time change corresponds to a geophone displacement of approximately 7 cm. Recently, we found out that the geophones with these large travel time changes are located close to perforations in the borehole casing. We speculate that the perfora-

tions may have influenced the measurements, for instance by poor geophone clamping, or by fluid flow and/or pressure variations through the perforations. Borehole fluid may have leaked into the surrounding rock, changing its medium properties.

The data of GP08 for the second deployment in 2015 (phase 6) show the same trend as described for the first deployment, but the data of GP06 do not (Table 4.2). The vertical component data of GP09 were out of order. For this second deployment, we found that the travel times that involve GP01 show a consistent decrease of on average $-38\mu s$. This may be explained by a downward movement of GP01 by ~19 cm.

	Rec01	Rec02	Rec03	Rec04	Rec05	Rec06	Rec07	Rec08	Rec09	Rec10
Sou01	-	3 ± 11 8 ± 10	1 ± 9 11 ± 9	-14 ± 10 -4 ± 11	-3 ± 11 9 ± 11	-17 ± 11 -13 ± 12	-3 ± 12 11 ± 12	-27 ± 11 -40 ± 13	-30 ± 13 -54 ± 13	-10 ± 14 -9 ± 15
Sou02	14 ± 11 7 ± 12	-	-7 ± 7 13 ± 9	-6 ± 8 9 ± 9	-5 ± 9 -9 ± 10	-29 ± 8 -20 ± 11	-5 ± 11 6 ± 9	-28 ± 10 -32 ± 11	-57 ± 12 -53 ± 13	-5 ± 11 -30 ± 11
Sou03	14 ± 9 -0 ± 10	4 ± 7 6 ± 8	-	-0 ± 9 3 ± 9	-15 ± 8 -8 ± 9	-38 ± 9 -26 ± 11	-7 ± 9 15 ± 10	-34 ± 10 -27 ± 10	-70 ± 11 -59 ± 11	-3 ± 10 -24 ± 11
Sou04	3 ± 10 1 ± 10	-12 ± 7 -1 ± 8	-8 ± 7 -8 ± 9	-	-2 ± 8 -9 ± 9	-25 ± 7 -34 ± 8	-9 ± 8 -2 ± 10	-22 ± 8 -24 ± 11	-65 ± 10 -47 ± 11	-4 ± 9 -17 ± 10
Sou05	4 ± 11 -21 ± 12	-13 ± 8 2 ± 9	-13 ± 8 -8 ± 9	-2 ± 8 -1 ± 8	-	-9 ± 8 -5 ± 9	-13 ± 8 0 ± 10	-19 ± 9 -16 ± 10	-55 ± 11 -45 ± 14	-0 ± 9 -31 ± 11
Sou06	-22 ± 10 -25 ± 11	-36 ± 9 -28 ± 9	-40 ± 9 -32 ± 9	-40 ± 8 -29 ± 8	-14 ± 8 -23 ± 9	-	24 ± 9 39 ± 10	5 ± 9 -1 ± 9	-35 ± 11 -48 ± 11	26 ± 11 5 ± 11
Sou07	14 ± 11 -2 ± 10	-10 ± 9 -8 ± 9	-4 ± 8 -20 ± 10	-11 ± 7 -6 ± 9	-11 ± 8 -20 ± 9	26 ± 9 19 ± 9	-	-24 ± 9 2 ± 8	-45 ± 12 -63 ± 12	-12 ± 11 -13 ± 10
Sou08	-1 ± 12 -64 ± 13	-36 ± 10 -36 ± 9	-28 ± 9 -39 ± 9	-14 ± 8 -28 ± 10	-31 ± 9 -24 ± 9	-1 ± 9 -17 ± 9	-13 ± 9 -6 ± 9	-	0 ± 12 -9 ± 12	30 ± 11 6 ± 10
Sou09	-5 ± 14 -10 ± 17	-44 ± 10 -39 ± 9	-63 ± 11 -52 ± 10	-47 ± 11 -32 ± 11	-40 ± 10 -24 ± 12	-30 ± 12 -16 ± 12	-51 ± 12 -45 ± 10	-5 ± 11 3 ± 11	-	69 ± 11 51 ± 10
Sou10	17 ± 15 -10 ± 16	-3 ± 11 -33 ± 11	-10 ± 11 -39 ± 10	-7 ± 10 -18 ± 10	-12 ± 10 -32 ± 10	26 ± 11 2 ± 12	12 ± 12 -41 ± 11	32 ± 12 -0 ± 10	73 ± 10 45 ± 11	-

Table 4.1: P wave travel time changes for phase 5 (23 Jan - 29 Jun 2015) in microseconds. Values for trains from Stedum to Loppersum are shown in red (top) and those for Loppersum to Stedum in blue (bottom).

	Rec01	Rec02	Rec03	Rec04	Rec05	Rec06	Rec07	Rec08
Sou01	-	-33 ± 10 -48 ± 10	-26 ± 8 -33 ± 9	-28 ± 9 -41 ± 10	-37 ± 10 -38 ± 10	-31 ± 10 -38 ± 10	-47 ± 10 -44 ± 11	-53 ± 11 -39 ± 11
Sou02	-33 ± 9 -56 ± 11	-	8 ± 8 9 ± 8	-6 ± 8 4 ± 8	-14 ± 8 8 ± 8	-5 ± 8 23 ± 10	-14 ± 10 -0 ± 10	-22 ± 9 3 ± 11
Sou03	-27 ± 10 -41 ± 11	-3 ± 7 5 ± 8	-	-8 ± 8 -11 ± 9	-7 ± 8 -7 ± 8	-23 ± 9 -7 ± 9	-15 ± 9 8 ± 8	-30 ± 9 -16 ± 10
Sou04	-14 ± 10 -67 ± 12	-5 ± 7 -14 ± 7	-11 ± 8 -21 ± 9	-	-11 ± 8 6 ± 9	-7 ± 8 12 ± 8	-12 ± 7 1 ± 10	-30 ± 8 20 ± 10
Sou05	-44 ± 10 -54 ± 12	-24 ± 7 6 ± 9	-11 ± 7 -2 ± 8	-2 ± 9 -8 ± 9	-	4 ± 8 -1 ± 8	-13 ± 9 -6 ± 9	-23 ± 10 -13 ± 9
Sou06	-29 ± 9 -32 ± 11	-11 ± 8 26 ± 9	0 ± 8 5 ± 8	4 ± 8 7 ± 9	1 ± 8 7 ± 8	-	-9 ± 8 -8 ± 9	-15 ± 8 -17 ± 9
Sou07	-17 ± 11 -67 ± 14	-4 ± 9 6 ± 9	-10 ± 8 -12 ± 9	3 ± 8 -4 ± 10	6 ± 8 -2 ± 9	-10 ± 9 -21 ± 8	-	-6 ± 9 1 ± 9
Sou08	-41 ± 12 -48 ± 14	-29 ± 9 15 ± 11	-24 ± 9 -8 ± 10	-16 ± 9 5 ± 10	-19 ± 9 -1 ± 10	-22 ± 8 -17 ± 10	-14 ± 8 11 ± 9	-

Table 4.2: P wave travel time changes for phase 6 (3 Jul - 1 Dec 2015) in microseconds. Values for trains from Stedum to Loppersum are shown in red at the top and those for Loppersum to Stedum in blue at the bottom. The vertical component of geophone 9 was out of order. Results for the data of geophone 10 are not presented because of the large travel time anomaly (Fig. 4.7).

To investigate potential movements of the geophones, we analysed independent data from fluid waves that travel within the borehole. The analysis is presented in

section 4.8.

Among all the travel time measurements, the most striking are those for the geophone pairs that include GP10 during phase 6 (Fig. 4.7). They show a large travel time decrease of up to 0.7 ms that is limited to the period between July and September 2015. We found that this anomaly is associated to the drilling of a new well at 4.5 km distance. A detailed analysis of the observation can be found in chapter 6.

4.7 Temporal changes of P wave amplitude

In the previous section, we investigated temporal variations of the travel time response of the reservoir. Most geophone pairs showed a small (albeit mostly not significant) travel time decrease per deployment period, suggesting that there might be some effect of compaction. Compaction would likely also affect the amplitudes of the deconvolutions. The advantage of deconvolution interferometry over cross-correlation interferometry is that it eliminates the source signal. Amplitude variations of the deconvolutions can therefore reflect medium changes.

The (maximum) amplitude of the direct P wave was measured from the stacked train deconvolutions. An overview of all the data is presented in Fig. 4.9. Generally, there are only small amplitude variations during the first half of 2015, whereas all geophone combinations show a gradual amplitude increase during the second half of 2015. During this period, the amplitude typically increases from ~0.04 to ~0.045, corresponding to a 12% increase. It might be tempting to explain the amplitude increase by compaction, but the absence of such a trend during the first half of 2015 suggests that this interpretation is not warranted.

Apart from the long-term trends, we observe a significant amplitude anomaly from mid July to early September for all deconvolutions that include geophone 10 (last column of Fig. 4.9). The timing of this anomaly is consistent with the travel time anomaly of Fig. 4.7, which suggests that it is related to the drilling of a new well as will be discussed in chapter 6. Another anomaly is measured for geophone pairs that include GP04 as virtual source. The amplitude anomaly starts on Jul 27 and returns to the reference level on August 24. The timing of the anomaly is within the period of drilling, suggesting that this is a related effect.

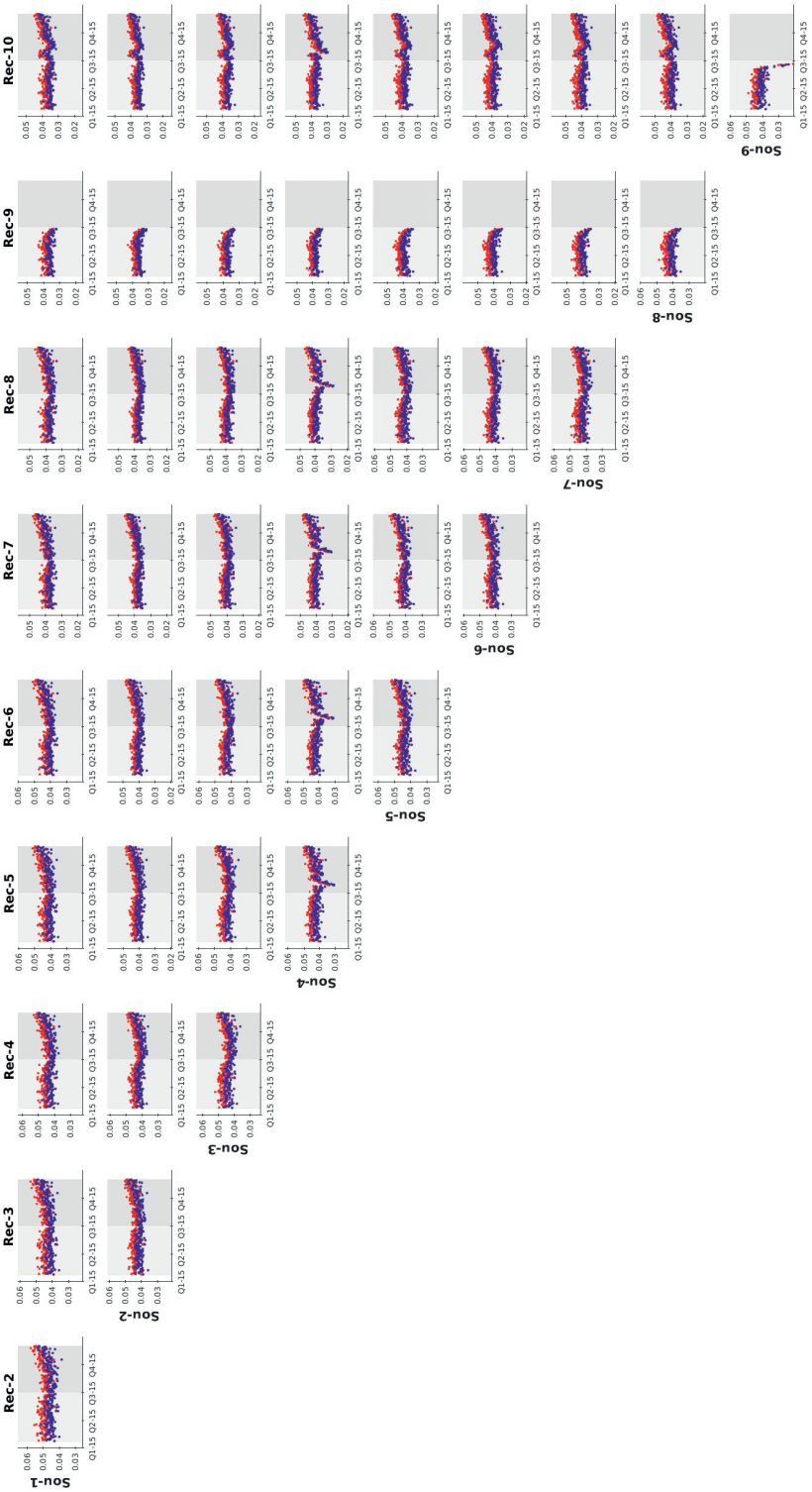

Figure 4.9: Amplitude measurements of the direct P wave from the stacked deconvolutions as a function of time. Rows show diagrams with geophones acting as virtual source, columns those for geophones acting as virtual receiver. Deployment phase 5 (23 Jan - 29 Jun 2015) has a light-grey background, phase 6 (3 Jul - 1 Dec 2015) is in darker grey. Amplitudes obtained for trains from Stedum to Loppersum are in blue, for Loppersum to Stedum they are in red.

4.8 Temporal changes of the fluid wave response

To verify that our measured travel time changes are due to medium changes and not caused by displacement of the geophones or other artificial effects, we carried out independent measurements using fluid wave events (section 2.8). The physical source of the observed fluid wave signals (see Fig. 2.6) is not known, but they are characterized by a high frequency content (up to 1000 Hz) and a propagation speed of ~1500 m/s, the speed of sound in water. Thus, it is assumed that they predominantly travel within the water (or actually brine) column of the borehole and that there are little to no effects from the surrounding rock. Note that, for simplicity, we use the term fluid wave both for the original fluid wave signal as for the fluid wave response obtained by interferometry. Fluid waves along a borehole have been identified in a previous study interferometric study by Vaezi & van der Baan (2015) where they were called tube waves.

We used the vertical component spectrograms to detect the fluid wave events. Fluid wave signals were identified when the average power spectral density of all geophones in the 100-500 Hz frequency band was larger than a certain threshold. In addition, only signals with an apparent downward velocity between 1450 and 1550 m/s were selected to exclude signals from high-frequency micro-earthquakes.

We found that the number of detected fluid wave events decreased over time, starting with tens of events per day in the beginning of 2015 while later they became less frequent. During the first deployment, there were 115 days with at least one fluid wave event, whereas there were only 67 days with detected fluid wave events during the second deployment.

Because the fluid wave signals are tremor-like in character, i.e. without clear onsets or phase peaks (Fig. 2.6), we applied deconvolution interferometry to retrieve their travel times along the borehole. The deconvolution (Eq. 4.2) is calculated on band pass filtered fluid wave signals (100 - 300 Hz), with a water level parameter c of 0.01% (Eq. 4.3). After that a 200 Hz low-pass filter is applied. Lastly, the responses were stacked per day to improve the signal-to-noise ratio. Fig. 4.10 shows the stacked fluid wave responses for a day at the beginning and a day at the end of the first deployment in 2015, where the signal of the top geophone is used for deconvolution. The direct downgoing fluid wave has an average speed of 1510 m/s and there are also clear reflections from ~7 m below the bottom geophone and the level of the top geophone.

Fig. 4.10 shows that there are time shifts between the stacked fluid wave responses of February 6 (in black) and those of June 2 2015 (in red). The time shifts are especially clear for the multiply reflected waves, with those of June 2 is being delayed. This suggests that the propagation speed of the fluid wave decreases with time.

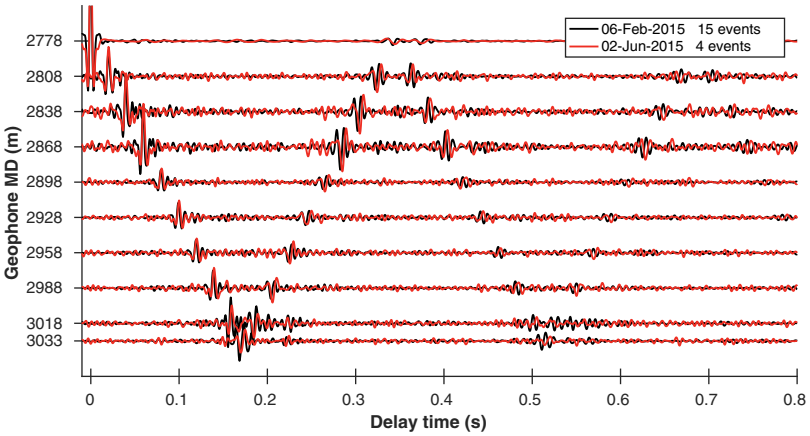

Figure 4.10: Stacked fluid wave deconvolutions using the signal of the top geophone. MD is the depth measured along the well.

To investigate this in more detail, we measured the travel times of the direct downgoing fluid waves from the daily stacked deconvolutions. Note that the signal-to-noise ratio of these stacks depends on the (varying) amplitudes of the original fluid wave signals as well as on the number of fluid wave events that were identified per day. This means that the accuracy varies. Fig. 4.11 gives an overview of all inter-geophone fluid wave travel times for 2015, generally showing an increase over the year.

It is unlikely that these travel time changes are caused by geophone displacements, because this would require that all inter-geophone distances increase with time. This is inconsistent with the time-lapse variations found for the P waves (section 4.6). Furthermore, the estimated displacements would be too large. For example, the fluid wave travel time change from geophone 1 to 10 is 1.8 ms for the first 5 month deployment. Translating the relative travel time change (dt/t) of 1.1% to a relative change in distance (dz/z) would yield a 2.7 m elongation of the geophone string. This is not only unlikely, such an elongation would also have been detected by the P-wave travel time data. Thus, it is more likely that there was a change in the properties of the borehole fluid with time. This may be related to a temperature increase caused by heating from the geophones as found by Cannon & Kole (2018), or by a gradual change in composition of the borehole fluid. The exact mechanism is still unclear.

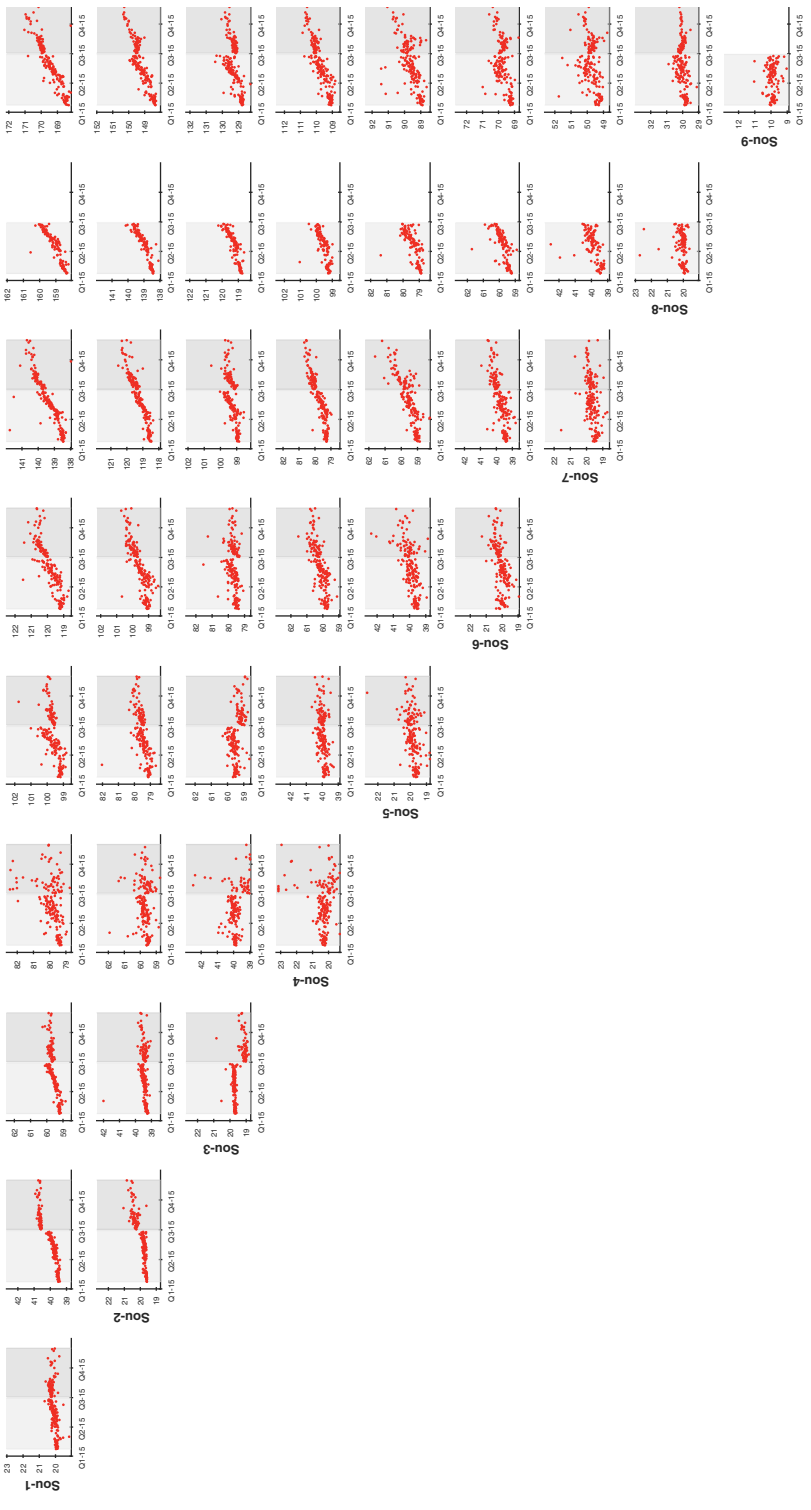

Figure 4.11: Time-lapse measurements of inter-geophone travel times of the fluid wave for phase 5 (light-grey background) and phase 6 (dark-gray background) in 2015. The travel times along the vertical axis are in ms.

4.9 Discussion

This study showed that it is feasible to very accurately obtain the P and S velocity structure along the geophone array of borehole SDM-1 by interferometry of train noise. The inter-geophone travel times obtained by train signal deconvolution resulted in a P wave velocity profile with a maximum uncertainty of 20 m/s (0.4 %). The uncertainty in the retrieved S wave profile varied between 30 and 80 m/s (1-3%). We found that the P velocity profile is in agreement with the sonic log data, except within the Ten Boer claystone formation where our data yield a smaller velocity. It is difficult to explain this difference because interferometric methods are more likely to give an overestimation of the true velocity. The discrepancy may be due to the difference in scale length between the acoustic measurements and our data, with our data being sensitive to an area of potentially tens of meters around the borehole. Thus, it could be an effect of heterogeneity outside the borehole. Furthermore, we found that the S velocity profile obtained from train noise is generally in good agreement with that obtained from our earlier study using ambient noise (Chapter 3). The largest difference is again obtained for the Ten Boer claystone section, where the current study yields a lower velocity than obtained from ambient noise. There are two effects that can play a role. The ambient noise data were obtained for lower frequencies and might therefore be more strongly affected by the overlying high velocity anhydrite layer. Secondly, there can be an effect of anisotropy. The S wave anisotropy over the entire (mostly sandstone) reservoir was found to be approximately 4% (section 3.5) and it may be larger in the claystone. In the presence of anisotropy, the difference in inferred S velocity may be caused by the difference in horizontal direction that was used for the two studies.

Temporal variations of the P wave response obtained from the repetitive, high-frequency train signals were also investigated. Measurements of inter-geophone P travel times and amplitudes did not show clear changes related to local earthquakes. However, a general trend of travel time decrease with time was obtained for the two deployments in 2015. This is in line with an interpretation of reservoir compaction increasing the P wave velocity. Unfortunately, our measured travel time changes were generally too small to be significant. The uncertainty in the travel time change is ~10 μs per deployment period of 5 months, and the estimated travel time decrease due to compaction over the reservoir is considered to be of the same order (Fig. 4.8b). Our roughly estimated travel time decrease, of the order of 10 μs over 5 months, is much smaller than values that have been reported for studies of 4D seismics. These vary between 0.1 and 1.5 ms per year for various sandstone reservoirs, although reservoir slowdown has also been observed (MacBeth et al., 2019). However, the time-lapse from 4D seismics includes the effects of reservoir thinning which may partly explain the discrepancy with our results.

Potential effects of reservoir compaction were further investigated by measuring the amplitudes of the P waves obtained from the train-signal deconvolutions. These data show a general trend of increasing amplitude with time for the second half of 2015. This observation would be in line with reservoir compaction, but a similar trend is not observed for the first half of 2015. Thus, it is unclear if the amplitude data reflect effects of compaction.

The most notable feature in the P-wave travel time data is a clear anomaly of up to 0.7 ms for all geophone combinations that include geophone 10 (Fig. 4.7). The time span of this anomaly, from July to September 2015, corresponds to reservoir drilling of a well at 4.5 km distance. The interpretation of this anomaly will be further discussed in chapter 6.

Similar to the P wave analysis, time-lapse analysis of S wave travel times has also been attempted. This was not successful because of the relatively poor signal-no-noise ratio of the S wave responses (see Fig. 4.5).

Deconvolution interferometry of fluid waves that travel within the borehole was performed to verify that our P wave time-lapse measurements reflect variations of the medium surrounding the borehole rather than geophone artifacts. However, we found that the ~1% travel time increase along the array over a 10 month time span is most likely caused by a change of the borehole fluid. We did not find evidence for artifacts associated with geophones which could bias the time-lapse measurements of the P waves.

4.10 Conclusions

We applied train-noise interferometry on borehole geophone array data to monitor the Groningen gas reservoir. The transient train signals recorded at depths of around 3 km contain higher frequencies than other types of anthropogenic noise. Thus, deconvolution interferometry of train signals allowed more accurate travel time measurements than were obtained by cross-correlation of ambient noise.

We determined the average P and S velocity between the 30-m spaced geophones with an uncertainty of less than 0.4% for P and less than 3% for S velocity. Furthermore, with approximately 60 trains per day, it was possible to determine time-lapse measurements. We found that travel time decreases associated with reservoir compaction are small, 0-30 μs for the two 5-month deployments. These values are of the same order as the uncertainty (~10 μs), so it is difficult to assess potential effects of compaction. However, it is relevant to mention that our estimated travel time decreases are much smaller than values that have been reported in the literature for similar settings, and that this study has shown that it is feasible to measure travel time changes from passive data that are smaller than obtained from 4D seismics.

A separate analysis is carried out on fluid waves that propagate within the borehole with the velocity of sound in water. Temporal variations of their inter-geophone travel times show that the velocity of the borehole fluid decreased by ~1% over a 10 month period. This suggests a change in borehole fluid, for instance caused by increased temperature from heat release by the geophones or a change in composition. The analysis shows that high-frequency fluid waves can be used for borehole fluid monitoring.

Chapter 5

Monitoring the Groningen gas reservoir and overburden by PS conversions

5.1 Introduction

Production from the Groningen gas field in the Netherlands, one of the largest onshore gas fields in the world, is currently under strict regulation because of the notable seismicity caused by compaction of the reservoir sandstone. Several studies have suggested that most of the events occur in the gas reservoir along existing faults (Jagt et al., 2017; Spetzler & Dost, 2017; Willacy et al., 2019). However, a small portion of the events seems to be located in the overburden, potentially in the anhydrite layer within the Zechstein salt formation, a few hundred meter above the reservoir (Spetzler & Dost, 2017; Van Weers, 2019). Although the number of events above the reservoir is relatively small, they indicate that the overburden is deforming by unstable slip. Moreover, experimental work by Hunfeld et al. (2017) on anhydrite samples from the Groningen subsurface shows that they exhibit a velocity-weakening behavior (i.e. decreasing frictional resistance with increasing sliding velocity), implying that anhydrite is capable of nucleating earthquakes. For the seismic hazard assessment in Groningen it is therefore important to monitor the deformation of the overburden.

Surface subsidence and reservoir compaction are measured for the Groningen gas field, but there are currently no studies that monitor the behavior of the 3 km thick overburden. Commonly, temporal changes of the overburden and underburden of oil or gas reservoirs are determined from time-lapse seismic surveys, usually in offshore settings. Such 4D surveys have shown that for a compacting reservoir the overburden and underburden often exhibit slowdown corresponding to extension (e.g., Hatchell & Bourne, 2005; a good overview is given by MacBeth et al., 2019).

In this chapter we present a method to monitor the reservoir overburden using passive data from a geophone array deployed at reservoir level. The method relies on P-to-S converted waves (PS waves) generated at layer interfaces for sources located at the surface. It is based on the deconvolution of the horizontal component signal with the vertical component and is similar to receiver function approach which is traditionally used for seismic stations at the surface (e.g., Langston, 1979). Here we name the method HZdecon (stands for horizontal vertical deconvolution) because it is applied to borehole data from surface sources.

The method is first tested on synthetic data calculated for a model obtained based on well-log data of borehole SDM-1 in the Groningen reservoir. Then it is applied to the recorded check shot data recorded by the geophone array in this borehole. The comparison between synthetic and observed HZdecons illustrates the feasibility of the approach and allows an interpretation of the HZdecons in terms of overburden layers. Finally, the method is applied to train noise to monitor temporal changes of the reservoir overburden.

5.2 P-to-S conversions and Horizontal-Vertical deconvolution

A plane P wave incident on a interface between two solid layers with a strong impedance contrast will not only generate a transmitted P wave but also a trans-

mitted S wave (for non-normal incidence). If both waves are subsequently recorded by a single receiver, their difference in arrival time is a function of the P and S velocity of the second medium, the distance from the interface to receiver and the incidence angle of the incident P wave. Conversely, the presence of a PS wave indicates the presence of an impedance contrast and its time difference with the direct P wave is a measure of the distance of the interface to the receiver. For a horizontally layered medium and near vertical incidence the particle motion of the P wave is predominantly in the vertical direction whereas it is mostly in the horizontal (radial) direction for the PS wave. The receiver function method exploits this time difference between the direct P wave and its PS conversion(s) as well as the difference in polarization direction. A receiver function is the deconvolution of the horizontal component by the vertical component for a time window that includes the P wave and its coda with the converted waves (e.g., Bath & Stefánsson, 1966; Langston, 1979; Phinney, 1964; Rondenay et al., 2008). It thereby removes the source wavelet of the incoming wave and the common travel time to the interface at which conversion takes place.

In the seismological community, the receiver function method has been widely used to image subsurface discontinuities such as the Moho (e.g., Langston, 1979; Xu et al., 2007), mantle discontinuities (e.g., Huang et al., 2014; Vinnik, 1977) and a subducting slab interface (e.g., Cheng et al., 2017; Paulssen & De Vos, 2017), usually employing incident P waves from teleseismic earthquakes. The receiver function method is not, or least not commonly, used by the exploration seismology community. Sheley & Schuster (2003) migrated PS conversions of vertical seismic profile (VSP) data from active surface sources and were able to image structures that were located above the geophone array. The benefits of PS migration for imaging complex subsurface structures were further illustrated by Xiao et al. (2006). Ruigrok et al. (2012) compared the performance of the receiver function method with cross-correlation interferometry.

Our data are obtained from an array borehole geophones located in the Groningen reservoir at a depth of around 3 km. The instrumentation and the various types of noise and signals that are recorded by these geophones noise are described in chapter 2. Contrary to the standard receiver function setting with P wave incidence from below (from teleseismic earthquakes) and a receiver at the surface, in the current setting we have (anthropogenic) sources at the surface that are recorded by a vertical geophone array at depth. For nearby surface sources, the direct P waves are mainly recorded by the vertical component whereas their P-to-S converted waves from interfaces above the geophone array are mainly recorded in the horizontal direction. Here, we follow the classical receiver function approach (e.g., Langston, 1979) to obtain what we call Horizontal-Vertical deconvolution, or HZdecon. The time domain deconvolution of a horizontal component time segment, $H(t)$, by its vertical component, $Z(t)$, becomes a division in the frequency domain. Similar to the previous chapter we include a water-level stabilization, but here, in addition, a low-pass Gaussian filter is applied:

$$HZ(\omega) = \frac{H(\omega)}{Z(\omega)} \approx \frac{H(\omega)Z^*(\omega)}{\Phi(\omega)} G(\omega) \tag{5.1}$$

where $\Phi(\omega)$ is the vertical component auto-correlation with a water level

$$\Phi(\omega) = max\{Z(\omega)Z^*(\omega),\ c \cdot max\{Z(\omega)Z^*(\omega)\} \tag{5.2}$$

and $G(\omega)$ is the Gaussian low-pass filter,

$$G(\omega) = e^{\frac{-\omega^2}{4\alpha^2}}. \tag{5.3}$$

where the frequency band is determined by α. In the following section we illustrate the HZdecon approach with synthetics calculated for a 1-D model based on well log data obtained for the borehole.

5.3 HZdecon synthetic test

To test the feasibility of the method, we first applied the method to synthetic data. The sonic log data of well SDM-1, provided by NAM, were smoothed by harmonic averaging over a 60 m sliding window to obtain a realistic, yet relatively smooth, P velocity model from the surface down to the gas reservoir. Then, the relations between S velocity and density with P velocity for the various lithologies as given by Romijn (2017) were used to calculate the S and density profiles.

The model is shown in Fig. 5.1 together with the interpreted stratigraphic layers (after Romijn, 2017 and DINOloket, 2020). The North Sea group is a 700 m thick layer of Quaternary and Tertiary sediments and has a P velocity of around 2 km/s. The Chalk group below is of Late Cretaceous age and mainly consists of carbonate rocks with a P velocity between 2.5 and 4 km/s. Below the Chalk group is a sequence of various thinner sedimentary layers consisting of the Early Cretaceous Rijnland group, the Jurassic Altena group and the Triassic Germanic group (R+A+G). The average P velocity of this sequence is relatively low, around 3 km/s. The Zechstein group consists mainly of rocksalt with a near constant P velocity of 4.5 km/s, but it also includes two anhydrite layers, one near the top (anhydrite floater) and the other at the very bottom (basal anhydrite), both with a high P velocity of nearly 6 km/s. The Zechstein acts as the caprock of the late Permian Rotliegend reservoir, a porous sandstone with an average P velocity of 3.7 km/s. The model below the reservoir at 3.1 km depth, the maximum depth of the sonic log data, has been given gradually increasing P and S velocities while the density is kept constant.

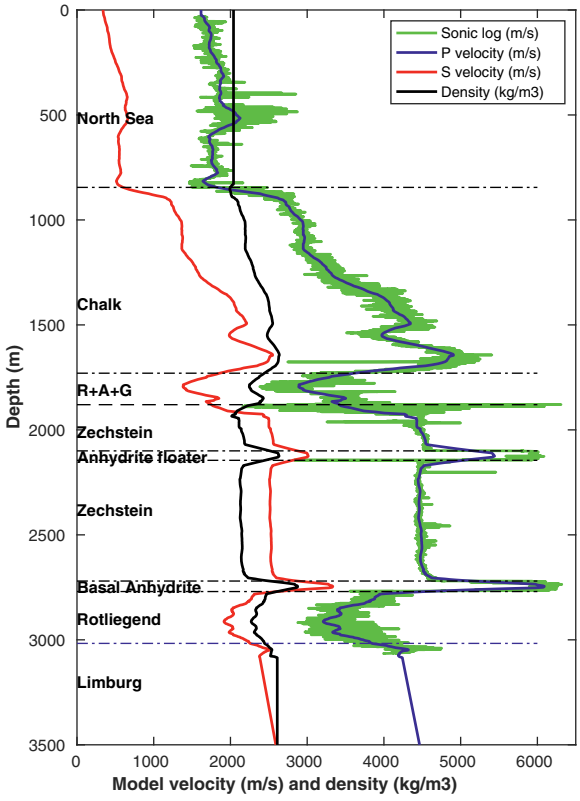

Figure 5.1: Seismic velocity and density model derived from the sonic log data of SDM-1 (green). Nomenclature of stratigraphic layers is adopted from Romijn (2017) and DINOloket (2020).

Synthetic seismograms were calculated with the spectral element code SPECFEM2D (e.g., Komatitsch et al., 2002; Komatitsch et al., 2010; Tromp et al., 2008). We simulated 2D elastic wave propagation from an explosive source ($Mxx = 1, Mzz = 1, Mxz = 0, M_0 = 5 \times 10^8$ Nm) at 20 m depth for the 1D model shown in Fig. 5.1. The horizontal grid spacing of the model was 5 m, and the vertical grid spacing was 5 m outside the reservoir and 2.5 m in the reservoir. Horizontal and vertical component synthetics were obtained for two vertical arrays of sensors from the surface to 3130 m depth (with 10 m depth spacing) at 500 and 790 m distance from the source. The source time function was a Ricker wavelet with a dominant frequency of 20 Hz. The vertical and horizontal (positive towards source) component synthetics for the array at 500 m distance are shown in Fig. 5.2 and 5.3, respectively.

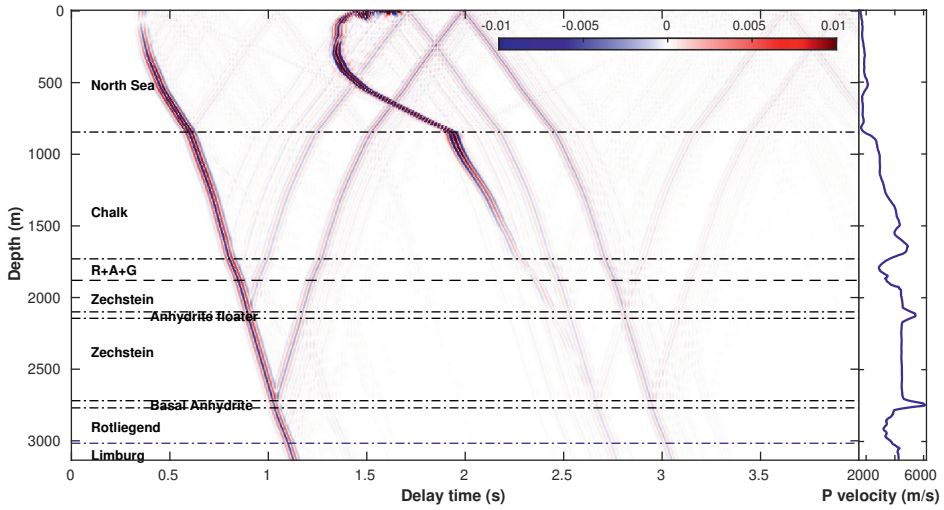

Figure 5.2: Vertical component velocity seismograms for the model of Fig. 5.1 for an explosive source at a distance of 500 m from a vertical array of receivers plotted as a function of depth. The colour scale is velocity in m/s.

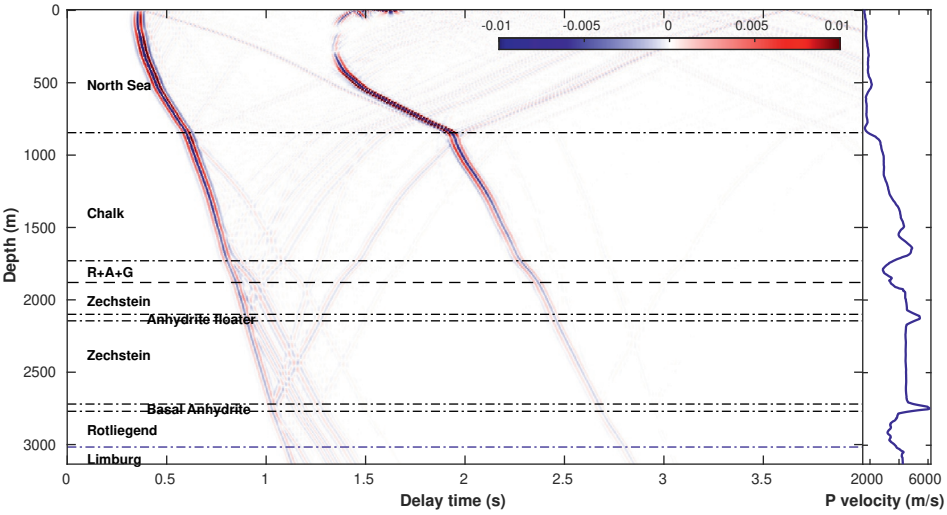

Figure 5.3: Similar to Fig. 5.2, but for horizontal component (positive towards source).

The first arrival in Fig. 5.2 and 5.3 is the direct downgoing P wave. Reflected and transmitted P waves are most clear on the vertical component seismograms, whereas reflected or transmitted PS waves are more prominent on the horizontal component. Taking the synthetic seismograms from 0 to 4 seconds, we calculated HZdecons using a water level $c = 0.002$ and a Gaussian filter with $\alpha = 150$ rad/s. Fig. 5.4 shows the first 0.6 seconds of the HZdecons. The direct P wave in HZdecon

is present at 0 s and the reflected and transmitted PS waves arrive at positive delay times.

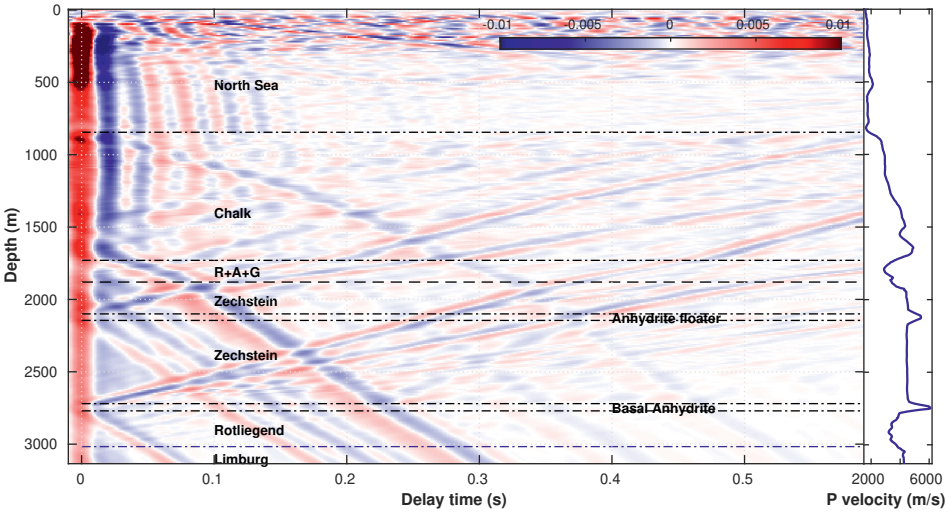

Figure 5.4: HZdecon for the synthetic seismograms of Fig. 5.2 and 5.3.

For receivers within the Rotliegend (2765 - 3017 m), the synthetic HZdecons mainly include downgoing PS waves from interfaces below the North Sea group within the first ~0.5 s. The bottom and top of the basal anhydrite layer both generate PS waves which arrive at 3000 m depth at ~0.04 s (positive, red) and ~0.06 s (negative, blue), respectively. The anhydrite floater, the top of the Zechstein salt and the interface between the Chalk and the Rijnland-Altena-Germanic (R+A+G) group all generate strong PS waves that show up between 0.15 s and 0.3 s in the HZdecon at 3000 m depth. Beyond 0.3 s the signals become weaker because there are mostly gradual velocity variations within the Chalk group. However, at ~0.43 s there is a secondary PS wave generated as an upward reflected P wave from the basal anhydrite layer that is subsequently downward reflected and converted to an S wave at the anhydrite floater. The PS arrival from the base of the North Sea group arrives at ~0.52 s. The synthetic HZdecons of Fig. 5.4 are useful for the interpretation of the observed HZdecons from the reservoir that will be presented in the next sections.

5.4 HZdecon for an explosive source

For each geophone deployment in well SDM-1 several check shots were fired to determine the orientation of horizontal components. Ideally, an explosion is only a source of P waves, and therefore any recorded S wave signal must have been converted from a P wave. We first apply HZdecon to the data of one of the check shots: CS8 of the phase 6 deployment. This check shot was located 790 m northwest of borehole SDM-1 (Fig. 2.15 and Table 2.9 of the Appendix).

The components of the geophones were first rotated to the North-East-Up coordinate system using the information of Appendix 2.15. Then, the horizontals were further rotated to the (negative) radial and transverse directions using the back-azimuth of the source to the well SDM-1.

A 10 second time window containing the entire wave train of the check shot was taken to calculate the HZdecon with a water level constant c=0.002 and a Gaussian filter with α=150 rad/s (low pass with -3 dB at 40 Hz). The radial component HZdecon results for 7 geophones are presented in Fig. 5.5 (GP03, GP05, and GP09 had one or more components out of order). Synthetic HZdecon results for a source at 790 m are shown in the background. The PS waves from the top and bottom of the basal anhydrite (0.04 - 0.06 s at 3000 m) are clear, and there is good agreement with the synthetic HZdecons. The next downward propagating PS wave (with positive sign) arrives at 0.18 s at 3000 m, which is 0.02 s later than the PS wave from the bottom of the anhydrite floater in the synthetics, suggesting that in reality the interface is somewhat higher than our 1D model. This signal is followed by several PS waves that originate from the top of the Zechstein and velocity contrasts within Rijnland-Altena-Germanic group. The last arrival of this sequence is a clear PS wave (with negative sign) from the base of the Chalk group which arrives at ~0.29 s at 3000 m depth. Beyond 0.3 s the signals are weak, although some of them can be traced along the receiver array.

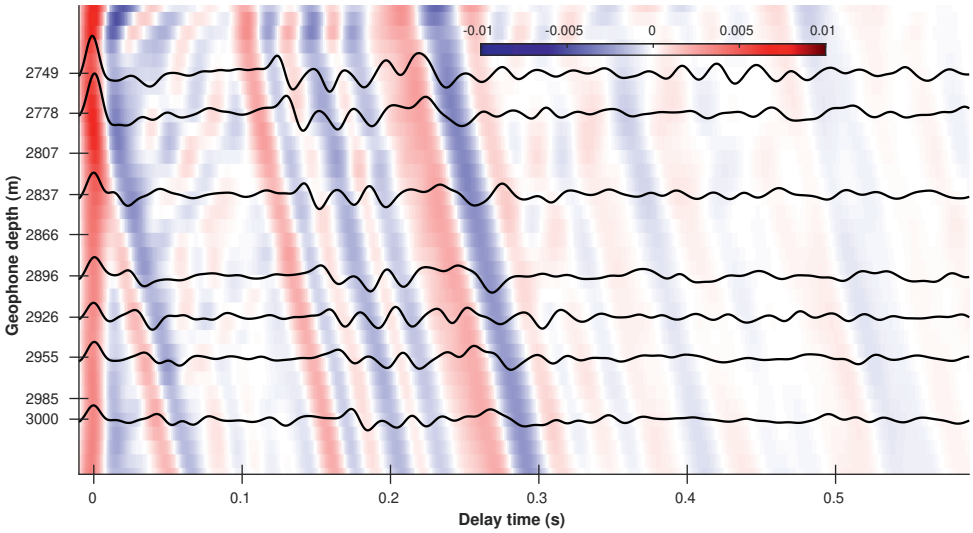

Figure 5.5: Radial component HZdecons for check shot CS8 (black lines). The synthetic HZdecons in the background are obtained for an explosive source at 790 m distance.

5.5 HZdecon of train signals

In the previous chapter it was shown that P and S wave responses in the reservoir can be retrieved from inter-geophone deconvolutions of train noise (Fig. 4.3 and 4.5).

A high signal-to-noise ratio was obtained for the stacked response of all detected train signals. In this section we apply the HZdecon method to the train signals and analyse the stacked results. In the following section we will present the results of time-lapse HZdecon.

For the HZdecon analysis, we used the same 20 second time windows of train noise as in the previous chapter. A 4th order butterworth filter (30 - 90 Hz) was first applied to the data to capture the highest amplitudes and to eliminate other types of (lower frequency) noise. Then, the data were deconvolved with a water level constant $c = 0.01$ and a Gaussian filter with $\alpha = 450$ rad/s (low pass with -3 dB at 120 Hz). HZdecon was first performed on east (E/Z) and north (N/Z) components, and the resulting stacks for all of the ~9000 detected trains between July 3 and December 1, 2015 are shown in Fig. 5.6. The synthetic HZdecons for a source at a distance of 500 m, the distance of borehole SDM-1 to the railway, are shown in the background for comparison.

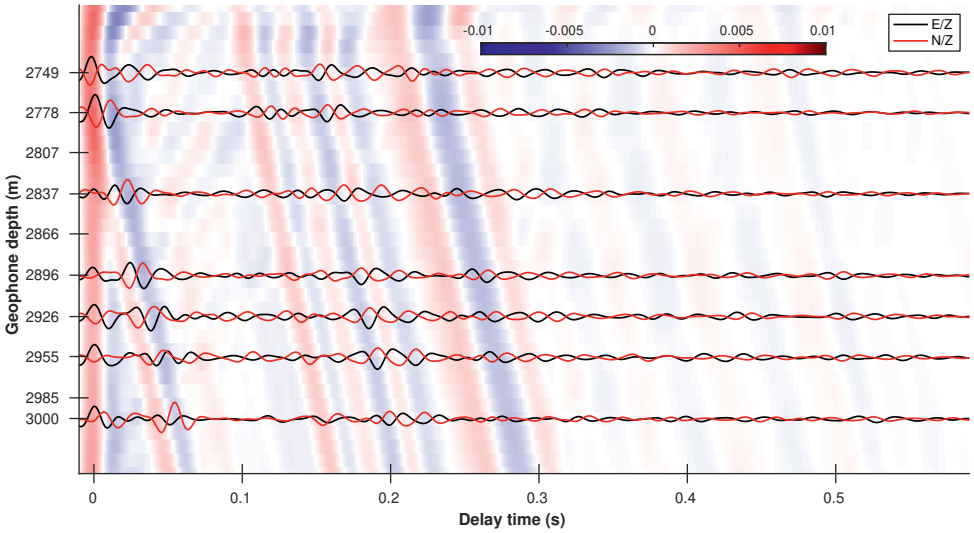

Figure 5.6: Stacked HZdecon results for ~9000 train signals from July 23 to Dec 1, 2015. East component HZdecons are in black, north component HZdecons are in in red. Synthetic HZdecons for an explosive source at 500 m distance are shown in the background.

Although we know that the trains travel southeast from SDM-1, trains are moving sources. Therefore, we can not define the radial component for the train sources in an unambiguous way. Thus, we rotated the horizontal components to find the direction which gives the largest amplitude PS waves in the HZdecons. Fig. 5.7 illustrates the results for the top geophone. We found that the maximum amplitudes of the PS waves (for all 7 geophones) were obtained for azimuths between 128° and 153° and chose the median azimuth of 131° as the radial direction.

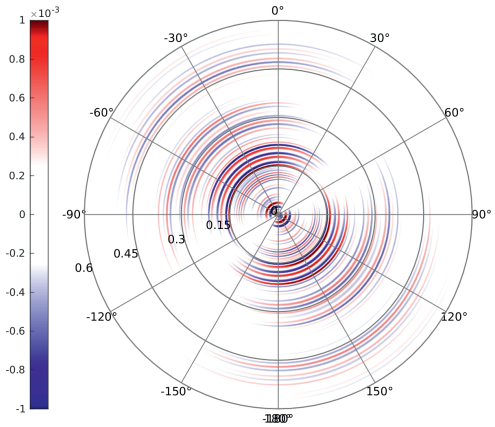

Figure 5.7: Stacked HZdecons of GP01 as a function of azimuth (data from Jul 3 to Dec 1, 2015). Radial axis represents HZdecon delay time (0 - 0.6 s).

The stacked HZdecons for the azimuth of 131° (Fig. 5.8) show several downgoing PS waves. The first, and also the largest, is the conversion from the basal anhydrite (0.05 s at 3000 m). The PS wave from the floater anhydrite (~0.15 s at 3000 m) can be identified, although is not very strong. Contrary to the check shot data of CS8 presented in the previous section, its timing matches that of the synthetics. The top of the Zechstein rocksalt has generated a significant PS wave (~0.2 s at 3000 m), and the PS wave from the base of the Chalk group can also be recognized (~0.28 s at 3000 m). Lastly, at ~0.53 s (at 3000 m) the PS conversion from the base of the North Sea group is faintly visible.

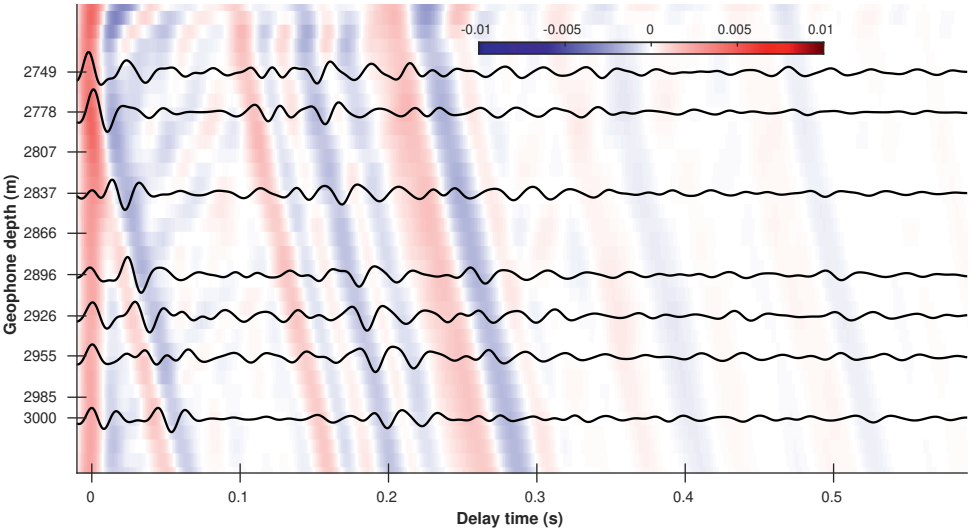

Figure 5.8: Stacked HZdecons for an azimuth of 131°. Synthetic HZdecons for an explosive source at 500 m distance are shown in the background.

5.6 Time-lapse HZdecon of train signals

In the previous sections it was shown that the HZdecon method can be applied to the geophone data of borehole SDM-1 for surface sources such as check shots and (stacked) train signals. The HZdecons are sensitive to interfaces within the overburden, in particular those with large velocity contrasts such as those associated with the two anhydrite layers, the top of the Zechstein and the base of the Chalk group. In this section we investigate the feasibility of time-lapse monitoring with HZdecon using repetitive train signals. Delay time variations, if present, can then be related to changes in structure above the geophones.

Individual HZdecons were calculated for an azimuth of 131°, the estimated direction of maximum amplitude of the PS waves obtained in the previous section. The HZdecons retrieved for trains traveling in the two opposite directions were then stacked per day (~30 trains) to improve the signal-to-noise ratio. Fig. 5.9 shows the results of the time-lapse analysis for GP02 for trains from Stedum to Loppersum. The HZdecons from 0 to 0.6 s appear to be nearly stable. Unfortunately, we could not detect significant long-term variations that are related to extension of the overburden, so-called overburden slowdown, as has been observed for various reservoirs with 4D seismics (MacBeth et al., 2019).

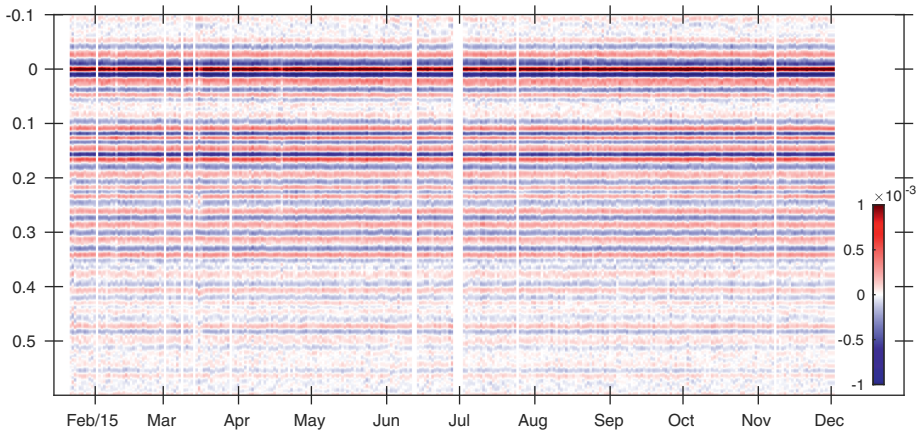

Figure 5.9: Daily stacked HZdecons of GP02 for trains from Stedum to Loppersum.

Although there is no evidence for long-term travel time shifts in the HZdecons, small short-term variations can be observed, for instance for March 15 and April 19 (Fig. 5.9). We analyzed the individual (unstacked) HZdecons and found that a few anomalous HZdecons caused the deviations in the stacks.

Whereas most of the data did not show significant travel time shifts, a large travel-time change was found for GP10 for the period from mid July to the beginning of September. It can be observed as the small shift in the daily stacked HZdecons in Fig. 5.10(a). We cross-correlated each of the (daily stacked) HZdecons with the

average HZdecon for that deployment period to quantify the travel time shift. We did this for a 0.07 second time window with a dominant contribution of the PS wave from the basal anhydrite layer (red segment in Fig. 5.10(b)). The time shift is then retrieved as the time of maximum cross-correlation. The cross-correlation analysis was performed for both train directions separately to assess the consistency of the results and to obtain an indication of the uncertainty of the measurements.

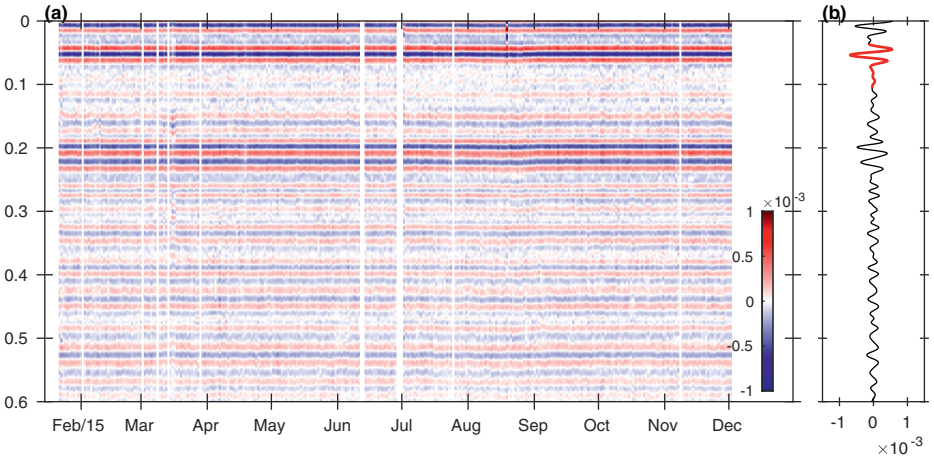

Figure 5.10: (a) Daily stacked HZdecons of GP10 for trains from Stedum to Loppersum. (b) Average HZdecon for July-November with time window used for cross-correlatation shown in red.

Figure 5.11 shows a near zero time shift with a scatter of ±0.25 ms for the first deployment period. For the second deployment (July -December) an increasing time shift from mid July to the beginning of September is found. It is independently retrieved for the two data sets with opposite train directions. The maximum of the travel time shift, on the 20st of August, is approximately 1 ms and is clearly larger than the data scatter. Note that the cross-correlation values, displayed in blue in Fig. 5.11, are consistently high, indicating a pure travel time shift rather than waveform distortion. It is remarkable that the time span of the anomaly corresponds to that of the inter-geophone P wave travel time anomalies observed for geophone pairs with GP10 in chapter 4 (Fig. 4.7). Here, the anomaly is only observed for GP10, which suggests that it is caused by a local change in the medium around GP10. The increase in delay time ($t_{PS} - t_P$) suggests that it is caused by an increase in P velocity or a decrease in S velocity (or a combination of both). The interpretation of this anomaly will be presented in chapter 6.

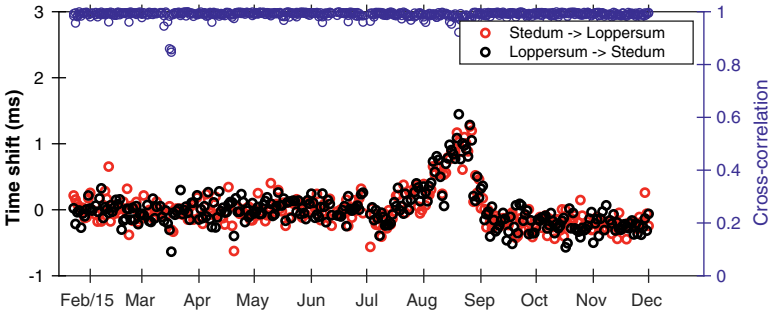

Figure 5.11: Travel-time shifts (red and black) of GP10 retrieved by cross-correlation. Cross-correlation values are in blue.

5.7 Discussion and conclusions

We applied a method that is similar to the receiver function method in global seismology to data from a borehole geophone array at 3 km depth in the Groningen gas reservoir. The method is based on the deconvolution of the horizontal component by the vertical component of each receiver (HZdecon) and is applied to near vertical incident wave fields that originally had a P wave origin. The deconvolution result for each receiver is a time signal which is (ideally) independent of the source time function and shows P-to-S converted waves as delayed arrivals with respect to the direct P wave. The time delay of a PS wave (with respect to the direct P wave) is a measure of the distance between the point of wave type conversion and the location of the receiver; it can be used to identify the interface at which conversion took place.

We first applied the method to synthetic data obtained for a 1D structure based on the sonic log data of borehole SDM-1, the borehole for which we had the continuous geophone array data. HZdecon responses were obtained for hypothetical receivers from the surface down to depth of the actual geophone array. These synthetic HZdecon responses provided insight into the various PS arrivals and allowed them to be interpreted in terms of the velocity structure of the reservoir overburden. After the synthetic test, the method was applied to explosion data and to signals produced by passing trains. The HZdecon results for the observed data showed good agreement with the synthetics, and PS arrivals from strong lithological contrasts at depths larger than 1500 m could be identified, such as the base of the Chalk group, the top of the Zechstein and the two anhydrite layers in the Zechstein rocksalt. A difference in the delay time of the PS arrival from the anhydrite floater between the synthetics and the data from a check shot suggests that this floater is shallower towards the northwest of the borehole.

The success of the HZdecon method implied that it should be feasible to perform time-lapse measurements with repetitive train signals in order to investigate overburden deformation. Although overburden extension has been detected for a large number of reservoirs, with time shifts typically of 1 ms per year (MacBeth et al.,

2019), we did not observe significant long term (permanent) changes of PS arrivals below the North Sea group (800 - 2700 m). Note that a time shift of 0.5 ms per 5 month deployment period would have been detected (see Fig. 5.11). Whereas we could not detect long term overburden variations within the 10 month period of our recordings, we did detect a clear temporary time-shift of the PS arrivals recorded by the lowermost geophone. The time span of this anomaly corresponds to the drilling of a new borehole at 4.5 km distance and an interpretation of the data will be presented in the next chapter.

In conclusion, we have shown that high quality PS wave responses from the overburden can be obtained by horizontal-to-vertical deconvolution of data recorded by a geophone array at 3 km depth using different types of surface sources. We named the technique HZdecon to distinguish it from the traditional receiver function method because it not only retrieves the PS waves converted near the receivers, but from all lithological interfaces with sharp impedance contrasts that are present from the surface down to the receiver array. Moreover, application of the HZdecon method to a vertical receiver array allows identification (and separation, see Akbar et al., 2018) of the up- and downgoing PS converted wave fields. Furthermore, we have shown that with this method it is feasible to monitor temporal subsurface variations using repetitive surface sources such as passing trains.

Chapter 6

Seismic footprints of reservoir drilling in the Groningen gas field

6.1 Introduction

In chapter 4 (sections 4.6 and 4.7) and chapter 5 (section 5.6) temporal variations of inter-geophone responses and responses of PS converted waves were investigated using repetitive train signals recorded by a geophone array in a 3 km deep well in the Groningen reservoir. We found that these responses should have sufficient resolution to detect realistic changes in the seismic properties associated with reservoir compaction or changes in the overburden, but we did not measure significant time-lapse changes during two 5-month geophone deployments in 2015. We also did not find evidence for seismic velocity variations related to a M_L 0.9 earthquake at 2.4 km distance and a M_L 3.1 earthquake at 14 km distance. Our observations suggest that changes due to reservoir compaction, overburden extension, or earthquakes are likely small. However, P wave inter-geophone travel times (and amplitudes) and PS converted waves showed a strong anomaly in the period from mid July to the beginning of September of 2015. The anomaly was always associated with data of GP10, the lowermost geophone. In the previous chapters, we suggested that the anomalous observations may be related to the drilling of a new well at 4.5 km distance, but we did not explain any of the details. In this chapter, we interpret our observations and address the seismic foot print of drilling through the effects of pore pressure diffusion. The setting is presented in Fig. 6.1, with the locations of borehole SDM-1 with the geophone array and borehole ZRP-3 which was drilled in 2015.

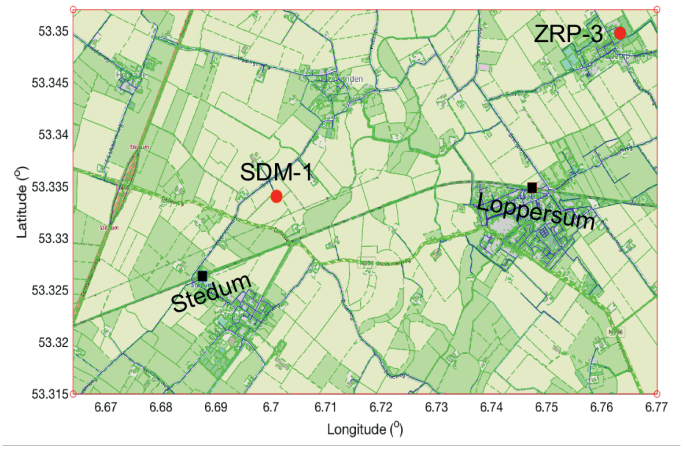

Figure 6.1: Map of the Loppersum area with borehole locations SDM-1 and ZRP-3 and the railway line with the villages Stedum and Loppersum.

6.2 Seismic observations

In this section we present previous and new seismic evidence of medium changes near the bottom of borehole SDM-1 when the reservoir at ZRP-3 was drilled.

6.2.1 Travel time changes of direct P waves

In chapter 4, we retrieved P wave responses between the geophones in borehole SDM-1 from train signals using deconvolution interferometry. The deconvolutions of high frequency (30 - 90 Hz) train signals allowed very accurate measurements of inter-geophone P wave travel times, and the large number of passing trains provided a large amount of temporal measurements. The P wave travel times (t_P) to the bottom geophone (geophone 10) all showed a large travel time deviation (Δt_P) of up to 0.7 ms from mid July to the beginning of September 2015 (Fig. 4.7, last column). These data were obtained from stacked deconvolutions (of 30 trains, approximately a day), but the pattern is also retrieved from single train deconvolutions as shown in Fig. 6.2 for the travel times between geophone 8 and 10.

It is unlikely that the observed travel time shift is caused by a movement of the lowermost geophone, because it would correspond to a displacement of 2.6 m followed by a return to its original position in September. Furthermore, the fluid waves within the borehole do not show a similar pattern (see section 4.8 in chapter 4). We suspected that the observation might be related to changes in the medium in the vicinity of geophone 10. In particular, we realized that geophone 10 is the only geophone beneath the gas-water contact (GWC) (see Fig. 6.2; geophone 9 was out of order). An upward movement of the GWC would produce a travel time decrease to geophone 10 by the replacement of gas by water in the porous sandstone, increasing the P velocity and decreasing the inter-geophone travel times. If the GWC would move back to its original level, the travel times would also obtain their normal values again.

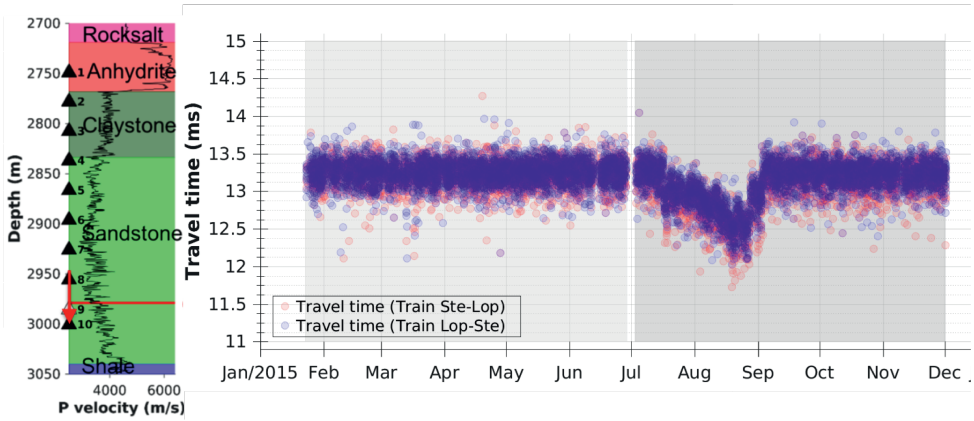

Figure 6.2: Left panel: Depths of geophones and lithology. The red line above geophone 9 indicates the gas-water contact. Right panel: P wave travel times from geophone 8 to geophone 10 from individual train signals; red circles for trains from Stedum to Loppersum, blue circles for trains from Loppersum to Stedum.

To obtain a better insight into the details of the anomaly, the data of Fig. 6.2 are shown again in Fig. 6.3a for the period from July 5 to September 10, 2015. The P wave travel times for the single train deconvolutions are indicated by the blue and

red circles and their daily average (~60 trains per day) by the black circles with an error bar of two standard deviations. It is clear that the travel time anomaly starts on July 17 and returns to the original level on September 3. It was realized that this time span overlapped with the drilling of the well ZRP-3 at 4.5 km distance (Fig. 6.1), and that there might be a relation between the two.

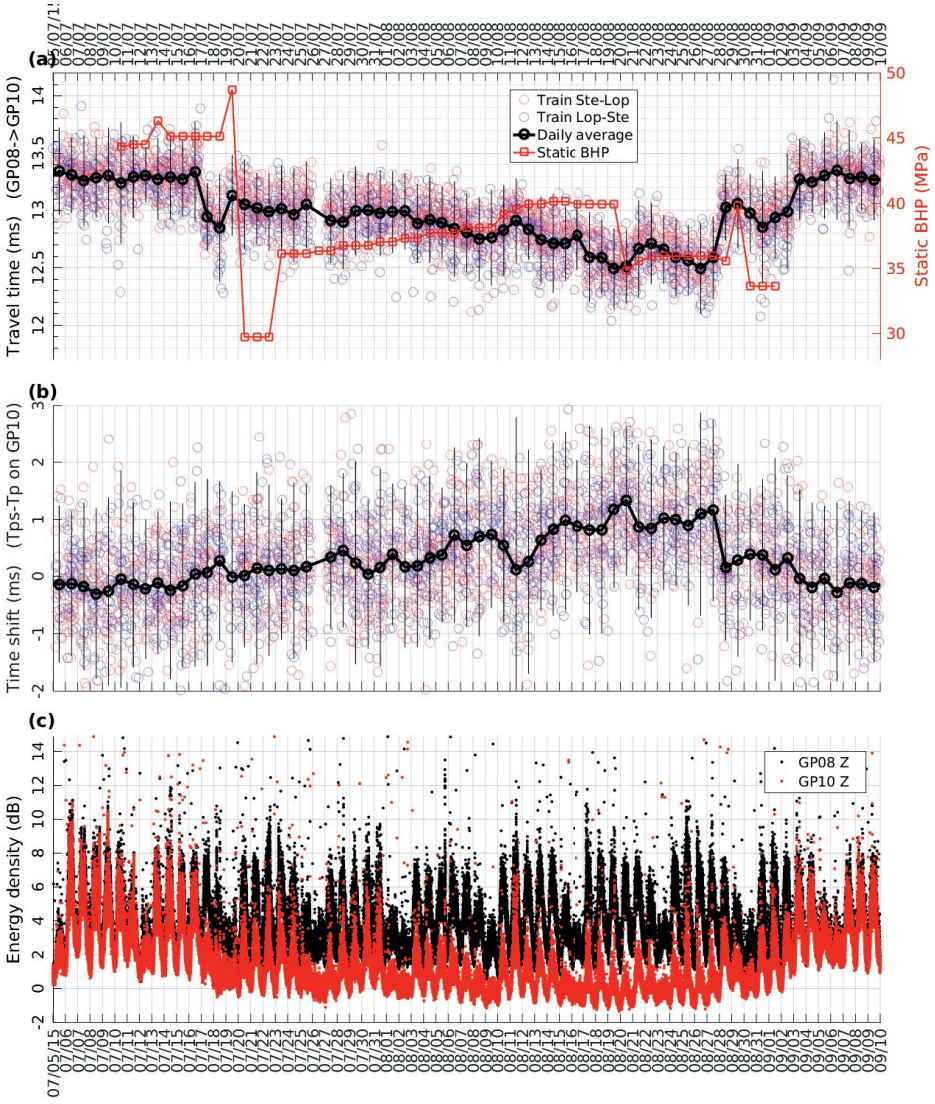

Figure 6.3: (a) Travel times from geophone 8 to geophone 10 from single train deconvolutions (red en blue circles) and their daily average (black). The error bar is twice the standard deviation. The red squares indicate the static bottom-hole pressure at ZRP-3 (courtesy NAM). (b) Time shift in $t_{PS} - t_P$ delay time for geophone 10. (c) Average power density (5 - 30 Hz) in dB for geophone 8 (black) and 10 (red).

6.2.2 Travel time changes of P-to-S converted waves

In chapter 5, we used horizontal-to-vertical component deconvolution (HZdecon) to retrieve responses of P-to-S converted waves as delayed arrivals with respect to the direct P wave. The observed arrivals from surface sources (check shots and trains) could be identified as PS waves generated at lithological contrasts of the overburden of the reservoir.

From the repetitive train signals, we retrieved time-dependent (daily stacked) HZdecon responses. The responses of geophone 10 showed a time shift from mid July to the beginning of September (Fig. 5.10). To quantify the time shift ($\Delta(t_{PS} - t_P)$) as a function of time, we cross-correlated the (daily stacked) HZdecon responses with the average signal for the time window of the PS wave from the Basal anhydrite layer (Fig. 5.11). The data showed a positive time shift of up to ~1 ms. Here we show that the same pattern is retrieved from the HZdecons for individual trains, albeit with a large scatter in the data (Fig. 6.4).

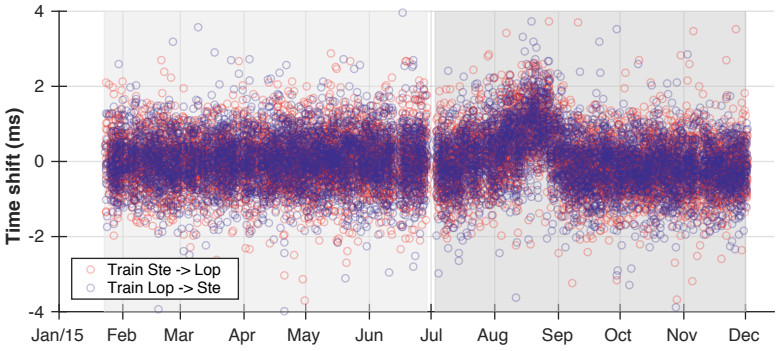

Figure 6.4: Time shifts of HZdecon responses at geophone 10 for individual train signals.

The data of Fig. 6.4 are also presented in Fig. 6.3b together with their daily average and twice the standard deviation. This figure shows that the time shifts observed for the HZdecons of geophone 10 occur in exactly the same span as the travel time anomalies of the direct P waves to geophone 10 and that both types of data appear to be anticorrelated. Thus, upward displacement of the geophone is further ruled out, because it would lead to a decrease of the $t_{PS} - t_P$ times, whereas the opposite is observed.

The observed 0.7 ms decrease in P wave travel time from geophone 8 to 10 together with the to ~1 ms increase in the delay time of the PS converted waves imply a P wave travel time decrease of 0.7 ms accompanied by a small S wave travel time increase. It should be noted, however, that these numbers are indicative, because their uncertainties are large, particularly for the PS delay time shift (see Fig. 6.3a-b). The observations support the hypothesis of a rise of the gas-water contact, because the substitution of gas by water in the porous sandstone would increase the P velocity and slightly decrease the S velocity (e.g., Adam et al., 2006; Smith et al., 2003).

6.2.3 Changes in noise level and an associated micro-earthquake

The changes in the train signal responses at geophone 10 presented in the previous two subsections prompted a more thorough analysis of the noise recorded at geophone 10. Continuous noise spectrograms were investigated, and we found a striking decrease of the low frequency anthropogenic noise level (not associated to trains, see section 2.6) for the same period as the anomalous inter-geophone P wave travel times and the delay times of the PS waves measured from train signals.

We calculated the average power density of the noise in the frequency band between 5 and 30 Hz. Fig. 6.3c shows the measurements for the vertical component data of geophone 8 and 10 for every 30 seconds. Daily and weekly patterns of the noise level are evident while large amplitude data (> 20 dB) are mostly associated with local earthquakes. Apart from those variations, we observe a discrepancy in the noise levels between geophone 8 and 10 for the time span between July 17 and September 2, where the noise level of geophone 10 is clearly lower (with a minimum in August). Noise level comparisons have also been made with other geophones and for the horizontal components. We found that only the vertical component data of geophone 10 show this temporary decrease in noise level. The noise level data allowed accurate timing of the beginning (July 17, 00h) and the end (September 2, 19h) of the anomalous time span (Fig. 6.5a-b).

While checking the spectrograms around the onset time, we detected a weak earthquake signal (Fig. 6.5). The signal has a duration of ~0.2 s and back azimuth close to the North-South direction as can be inferred from the strongest onset on the North component. The signal was too weak to be localized and is not listed in the catalogue of earthquakes determined from the deep borehole arrays in the Loppersum area (NAM, 2020a).

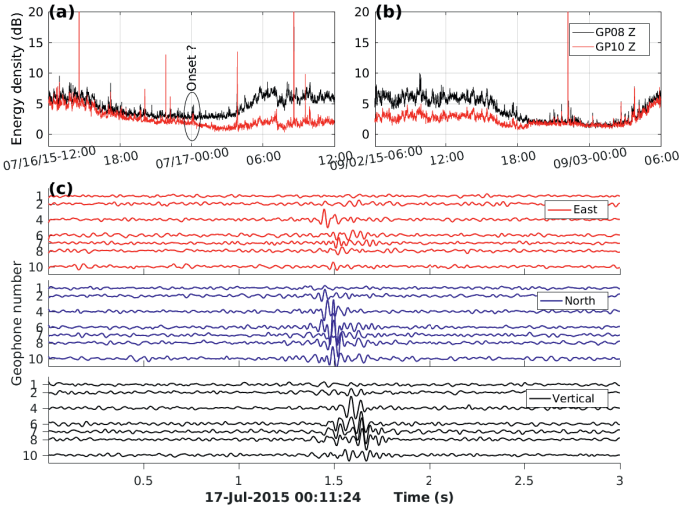

Figure 6.5: (a) and (b) Vertical component noise level of geophone 8 (black) and 10 (red) for the frequency band from 5 to 30 Hz. (c) Recordings of a weak earthquake at the start of the noise level decrease of geophone 10.

6.3 Interpretation

6.3.1 Elevation of the GWC from seismic observations

The seismic observations of the previous section showed anomalous responses of geophone 10 between July 17 and September 3, 2015. As mentioned before, the temporary decrease in P wave travel time to geophone 10 (Δt_P) of up to 0.7 ms and the increase in the delay time of the PS waves ($\Delta(t_{PS} - t_P)$) of ~1 ms might be explained by a temporary upward movement of the gas-water contact (GWC). Here we analyse this interpretation in more detail.

The change in seismic velocities due to the substitution of gas by water in a porous sandstone can be calculated with the Gassmann (1951) model of fluid subsititution (e.g., Adam et al., 2006; Smith et al., 2003). It gives the effective medium properties derived from its individual components. The bulk modulus of a fluid saturated rock is related to the porosity and to the bulk moduli of the mineral matrix, the pore fluid and the rock frame. The bulk modulus of the fluid will increase in case of gas-water substitution, and this will increase the effective bulk modulus of the rock, and consequently also the P velocity. The shear modulus, on the other hand, will not change as it is mainly dependent on the solid frame of the rock. However, due to the small increase in density, a slight decrease in S velocity is expected.

To obtain a quantitative estimate of the change in the level of the GWC using Gassmann's model, we would need accurate values of the bulk and shear moduli of the matrix, fluids (gas and brine) and rock frame for the local rock. Because these are unknown to us and rough estimates would have very large uncertainties, we took a more practical approach. We estimated the average P velocity above and below the GWC from the sonic log data and found P velocities of 3321 m/s and 3688 m/s, respectively (Fig. 6.6). Assuming these values, a 0.7 ms P wave travel time decrease would correspond to an elevation of the GWC by 23 m. We further checked if this elevation of the GWC could also explain the increase in PS delay time. Assuming a 23 m shift of the GWC, an S wave travel time increase of 0.3 ms ($\Delta(t_{PS}-t_P)-\Delta t_P$ = 1.0 - 0.7 ms), vertical propagation and an S velocity of 2000 m/s for the sandstone with gas (Fig. 4.6 in chapter 4), we find that an S wave velocity decrease of only 52 m/s (2.6%) is required. This decrease would be solely the effect of the density increase on the shear velocity caused by the replacement of gas by water. Although the values appear realistic, it should be noted that all uncertainties are large and that 23 m should only be interpreted as an indication of GWC elevation inferred from our measurements.

The third piece of evidence is the rapid decrease in the noise level, as well as its rapid return to the normal level, observed for geophone 10 (Fig. 6.5). Such rapid changes can be accomplished by changes in the level of the GWC. However, it is not entirely clear how this would reduce the 5-30 Hz noise level. The sandstone-with-water column above geophone 10 would increase by an elevation of the GWC. Because the noise consists mostly of vertically propagating P waves (Zhou & Paulssen, 2017, see chapter 3) it would imply that P waves are effectively more attenuated in the water-bearing sandstone.

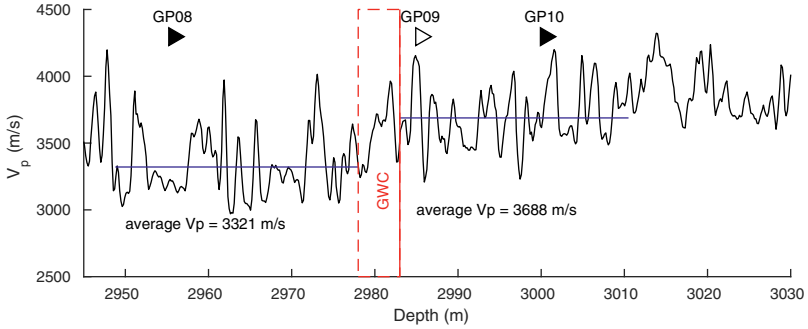

Figure 6.6: Determination of average P velocity from sonic log data.

6.3.2 GWC elevation at SDM-1 and borehole operations at ZRP-3

We found that an elevation of the GWC can explain the three types of seismic observations. The question then rises what caused the elevation of the GWC. Since the timing of the anomaly appeared to be related to the drilling of borehole ZRP-3 at 4.5 km distance, we investigated the detailed drilling report which was provided to us by NAM.

Drilling started on May 23 (2015) and Table 6.1 gives an overview of operations of potential relevance to our seismic observations. Note that on most days no actual drilling took place. Other activities were, for instance, pull out of hole (POOH) of bottom hole assembly (BHA) or drill pipe (DP), run in hole (RIH) of liner, cementing or well logging. A brief summary is given below.

The reservoir was reached by drilling into the Ten Boer claystone on July 13. Downhole losses of the drilling mud (11 m^3) occurred on July 18 and the first hours of July 19. Drilling took place mostly on single days between July 23 and August 21, when the maximum depth of 3284 m (or 3885 m MD, measured depth along borehole) was reached. The (undisturbed) level of the GWC (depth 2980 m) was reached on July 31, and the Carboniferous was drilled on August 11. Cementing of the borehole took place on August 28-29, and the borehole was left on August 30 after cement hardening.

The first conclusion is that there is no correlation between our observations and times of actual drilling. Thus, drilling noise does not explain the anomalous observations. A more likely cause is related to pore pressure variations caused by drilling. NAM kindly provided us with data of the static bottom hole pressure, calculated from the borehole depth (h), the drilling mud density (ρ) and the gravitational acceleration (g) ($BHP_s = \rho g h$). The data are shown in Fig. 6.3a. Note that the static bottom hole pressure represents only part of the total pressure at the well head because dynamic pressure effects are not included. The static bottom hole pressure data of Fig. 6.3a show strong changes between July 18 and 23 that are related to the mud losses and subsequent actions to fix this. From July 23 to August 19, when drilling depths increased from 3521 to 3868 m MD (2919 m to 3267 m true depth) there is a gradual increase in static bottom hole pressure from 36 to 39 MPa. This

Table 6.1: Selections from ZRP-3 drilling report

Time	Drilling report
13/Jul 07:45 - 17:00	Drilling 3429 - 3502 m, Ten Boer at 3475 m (230-250 bar)
13/Jul 17:00 - 18/Jul 04:30	POOH BHA, logging, RIH liner
18/Jul 07:30 - 19/Jul 02:30	Pumping (105 bar), attempt to start rotation. Pressure drop to 85 bar. Mud losses, ~3.5 m^3 in 10 minutes.
18/Jul 16:30 - 17:00	Pumping (64 bar)
18/Jul 22:15 - 19/Jul 02:30	Cementing (series of pumping of cement). Total mud loss was 11 m^3
23/Jul 19:15 - 20:00	Drilling 3502 - 3503 m (122 bar)
23/Jul 20:30 - 24:00	Drilling to 3521 m (123 bar)
28/Jul 20:15 - 22:15	Drilling to 3557 m (172-182 bar)
31/Jul 04:15 - 06:00	Drilling to 3581 m (190 bar)
02/Aug 13:00 - 16:00	Drilling to 3611 m (210 bar)
04/Aug 18:15 - 21:00	Drilling to 3641 m (205-210 bar)
07/Aug 04:15 - 07:15	Drilling to 3671 m (206-212 bar)
10/Aug 04:45 - 24:00	Drilling 3671 - 3756 m (142-145 bar)
11/Aug 00:00 - 22:00	Drilling 3756 - 3811 m, Carboniferous at 3754 m (145-149 bar)
12/Aug 00:00 - 02:30	Drilling 3811 - 3818 m (145-147 bar)
14/Aug 10:00 - 12:30	Drilling 3819 - 3837 m (170 bar)
16/Aug 14:30 - 19:15	Drilling 3837 - 3868m (220-230 bar)
21/Aug 07:00 - 12:15	Drilling 3868 - 3885 m (94 bar)
29/Aug 00:00 - 02:15	Performed cement job
29/Aug 02:15 - 02:45	Bled off to 0 bar
29/Aug 13:15 - 24:00	Wait on cement
30/Aug 00:00 - 07:30	Wait on cement
30/Aug 14:00	Released rig on well

Drilling depths are measured along hole (not true depths)
Pressures in bar are measured at the pump at the surface
POOH = pull out of hole
BHA = bottom hole assembly
RIH = run in hole

trend is anti-correlated with the P wave travel time decrease from geophone 8 to 10 and is correlated with the increase in PS delay time of geophone 10 (Fig. 6.3a,b).

If we assume that the bottom hole pressure at well ZRP-3 is related to our anomalous observations at SDM-1, then it is likely that they are linked through changes in pore pressure. Pore pressure variations at the bottom of the borehole can cause changes in the level of the GWC because the well is perforated (at depths between 2965 and 2995) and the well is not closed at the top, the pressure of a high density brine column in the well prevents the gas from flowing in through the perforations at the bottom. An elevation of the GWC of ~23 m then corresponds to a local increase of the pore pressure in the water bearing part of the sandstone of ~0.23 MPa ($\Delta P = \rho g \Delta h$).

By linking the beginning and the end of the drilling operations in the reservoir to the beginning and the end of our anomalous observations, we can calculate the time that the pressure front took to propagate from ZRP-3 to SDM-1. Drilling into the Ten Boer claystone took place on July 13, between 7:45 and 17:00, while the anomalous observations started on July 17 at ~00:00 (Fig. 6.5a). This gives a time delay of 3 days and 7 - 16 hours. A similar calculation can be made for the end of the anomalous period. The hardening of the cement at ZRP-3 took place on August 30 (00:00 - 07:30). After cement hardening the well is sealed and there is no influence from the borehole anymore on the pore pressure of the reservoir. Combining this to the end of the anomaly at SDM-1 on September 2 at 19:00 (Fig. 6.5b) gives a time

delay of 3 days and 11.5 - 19 hours.

6.3.3 Pore pressure diffusion

From our seismic observations and their correlation with the static bottom hole pressure at ZRP-3, we have concluded that pore pressure variations may have triggered changes in the level of the GWC in SDM-1 at 4.5 km distance. Next, we need to verify that the process of pore pressure diffusion can indeed explain the delayed time response at SDM-1 caused by pressure variations at ZRP-3.

For isotropic and spherical diffusion, Shapiro et al. (2002) showed that the hydraulic diffusivity (D) associated to pore pressure diffusion in a fluid bearing porous medium can be estimated from the time (t) it takes the pressure front to reach a certain distance (r)

$$r = \sqrt{4\pi D t} \tag{6.1}$$

Given the time delays of 3 days and 7 - 16 hours (beginning) and 3 days and 11.5 - 19 hours (end), we can estimate the pore pressure diffusivity from the inferred propagation time of the pressure front. The largest (3 days and 19 hours) and smallest (3 days and 7 hours) time delays give diffusivities of 4.9 m^2/s and 5.7 m^2/s, respectively.

Our hydraulic diffusivity of roughly 5 m^2/s compares well with diffusivity values inferred from more than 90 case histories of induced seismicity associated water reservoir impoundment, fluid injection and seasonal precipitation changes by Talwani et al. (2007). Nearly all their calculated diffusivities range between 0.1 and 10 m^2/s (although they assume 1D pore pressure diffusion and omit the factor π in Eq. 6.1).

A completely independent estimate of the hydraulic diffusivity is obtained from the material properties using the relation between the diffusivity tensor $\mathbf{D}$ and the permeability tensor $\mathbf{K}$ (Shapiro et al., 2002)

$$\mathbf{D} = \frac{N\mathbf{K}}{\eta} \tag{6.2}$$

where η is the pore fluid dynamic viscosity and N is a poroelastic modulus defined as

$$N = MP_d/H$$

$$M = (\phi/K_f + (\alpha - \phi)/K_g)^{-1}$$

$$H = P_d + \alpha^2 M$$

$$\alpha = 1 - K_d/K_g$$

$$P_d = K_d + (4/3)\mu_d$$

where $K_{f,d,g}$ are the bulk moduli of the fluid (f), dry rock frame (d) and solid grain material (g), μ_d is the shear modulus of the frame and ϕ is the porosity.

The hydraulic diffusivity D is estimated by simplifying Eq. 6.2 to a scalar equation and adopting an average permeability (k) of 120 mD for the Groningen sandstone reservoir (Hettema et al., 2017). The following values were also obtained from

the literature: the porosity of the Groningen reservoir ϕ = 0.15 (Pijnenburg et al., 2018); the bulk modulus of quartz K_g = 37 GPa (Smith et al., 2003); the bulk modulus of water K_f = 2 GPa; the pore fluid dynamic viscosity of water at 100°C η = 2.8 10^{-4} Pa.s (The Engineering Toolbox, 2020). The bulk modulus and shear modulus of the dry rock frame were derived from the average seismic velocities of the gas saturated sandstone (Vp=3300 m/s, Vs=2100 m/s, see Chapter 5) and a density of 2200 kg/m^3 obtained from the well log data. We found K_d= 11 GPa and μ_d= 9.7 GPa. With these values a pressure diffusivity of 3.9 m^2/s was obtained, which is somewhat smaller than our previously estimated diffusivity of 4.9 - 5.7 m^2/s. To obtain a diffusivity within the range of our observations, a permeability k = 151 - 176 mD is required, which is still within the wide range of the measurements (1 - 1000 mD) given by De Jager & Visser (2017).

6.3.4 Other evidence

Although there are clear effects in the seismic data at SDM-1 that can be associated to a change in the level of the GWC caused by drilling of borehole ZRP-3 at 4.5 km distance, no such effects were detected at SDM-1 in the period of drilling of borehole ZRP-2 (de Jong, 2020, personal communication). This is surprising, because the distance from ZRP-2 to SDM-1 is 1.8 km, which is much smaller than the distance between ZRP-3 and SDM-1 (Fig. 6.7).

The discrepancy between the findings for ZRP-2 and ZRP-3 suggest that pore pressure diffusion is not homogeneous in the Groningen reservoir. Indeed, the reservoir is highly faulted and faults may either act as barriers or as efficient conduits of pore pressure. The fast and strong response of the GWC level at SDM-1 to pressure variations at ZRP-3 suggests that there may be a fault with high diffusivity between the two locations. The NAM fault map for the top of the reservoir (Fig. 6.7) does not show a fault that links the two locations, but there is a (long) ENE-WSW striking fault approximately 300 m north of SDM-1 that seems to continue east of ZRP-3. These two fault segments are potentially connected beneath the reservoir. If this is the case, the damage zone of this fault, which would have a high porosity and permeability (Yehya et al., 2018), would likely act as a conduit for fast pressure diffusion. Whereas the (anisotropic) diffusivity is high in the direction along the damage zone of the fault, it is low for across the fault (Yehya et al., 2018). If ZRP-2 is located outside or across the damage zone of the fault, pressure diffusion would be less effective, potentially explaining why no anomalies are observed during the drilling of ZRP-2. It is realized that this interpretation is highly speculative. However, it is clear that the reservoir is highly heterogeneous, which could locally permit efficient pore pressure diffusion (for structures with high permeability) or the opposite.

6.4 Discussion

This study has shown that drilling operations can have a large effect on the fluid pressure of the reservoir. We found a temporary decrease of the P wave travel time and an increase in PS-P delay time for the lowermost geophone in borehole SDM-1. Both observations, requiring a P velocity increase and an S velocity decrease, can be

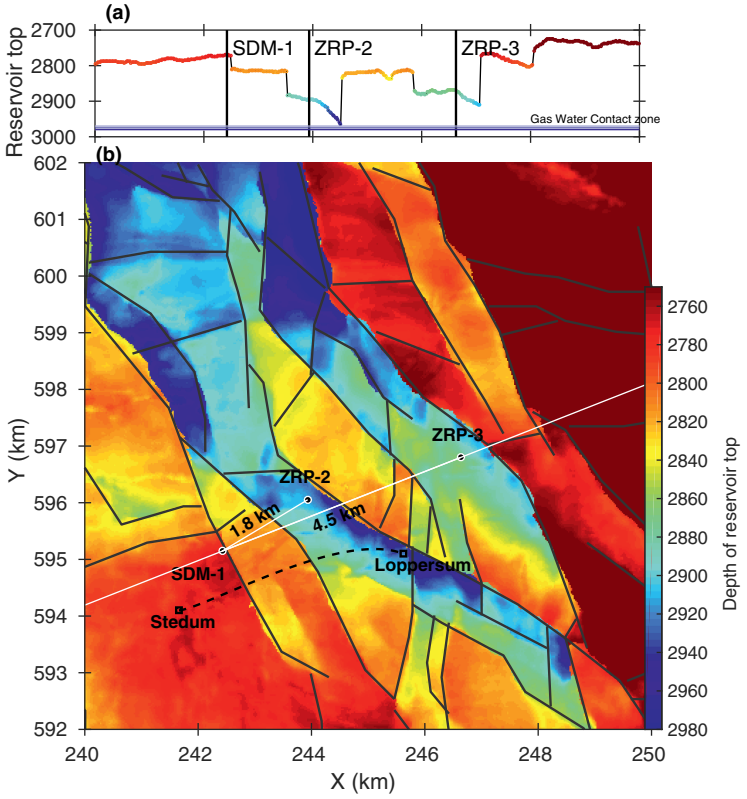

Figure 6.7: (b) Topography of the top of the reservoir with faults in black and the locations of boreholes SDM-1, ZRP-2 and ZRP-3. The railway from Stedum to Loppersum is indicated by the dashed line. (a) Depth of the top of the reservoir for the cross-section through SDM-1 and ZRP-3 (white line in b).

explained by a temporary rise of the GWC of roughly 23 m. The rise of the GWC is caused by a local change in pore pressure that could be linked to an increase of bottom hole pressure at borehole ZRP-3.

The pore pressure diffusivity was estimated from the time delays from the beginning and the end of pressurization at ZRP-3 and their seismic response at 4.5 km distance. The obtained diffusivity (4.9 - 5.7 m^2/s) is only somewhat higher than estimated from the material properties and falls within the range inferred from temporal and spatial patterns of seismicity associated with fluid diffusion (Talwani et al., 2007). Remarkably, there were no significant earthquakes in the KNMI catalog (KNMI, 2020) that could be linked to the drilling of ZRP-3. However, a nearby micro-earthquake was detected at the onset of the seismic anomaly at SDM-1 (Fig. 6.5) which could be indicative of a small pressure change.

Our observations further show that mud losses are not a necessary condition for pore pressurization at a large distance. Mud losses at ZRP-3 were reported on July 18 02:30 (Table 6.1), which is one day after the start of the seismic anomaly on

July 17 00:00 (Fig. 6.5). We did not find significant seismic changes in the seismic observations that could be related to the mud losses (Fig. 6.3).

Although there is no evidence for significant seismicity that is associated to drilling of borehole ZRP-3, there is a case of drilling related seismicity in the Groningen area that is likely associated to mud losses. Dost et al. (2012) reported an earthquake swarm of 41 events ($M_L < 1.4$) near Midlaren (now municipality Noordlaren) between February 22 and March 22, 2009. They suggested that the swarm is related to an experiment carried out by NAM, which is the drilling of borehole HGZ-1 at 4-5 km distance from the events. We revisited the Midlaren earthquake swarm and compared it to the drilling report (NLOG, 2020). It states for February 21: " ... Suffered from downhole losses. Waited for mud. Spotted 3x LCM[1]." The mud losses occurred in the Lower Triassic Rogenstein member (claystone with oolite layers) while drilling at 3198 m MD (2590 m true depth) and losses were reported until March 8. The first triggered event occurred on February 22 at 11:56:26 (KNMI, 2020), approximately one day after the first losses. If the first earthquake is related to the first mud losses, a pore pressure diffusivity of roughly 18.7 m^2/s is obtained (t = 24 hours and r = 4.5 km in Eq. 6.1). This would correspond to a permeability of 500 mD using the parameters of section 6.3.3. Such high diffusivity and permeability values would require fast pore pressure diffusion along a fault (or faults). It is likely that this was the case, as Fig. 6.8 shows that first mud losses were reported close to an E-W striking fault and the earthquake swarm occurred close to a connecting ENE-WSW striking fault.

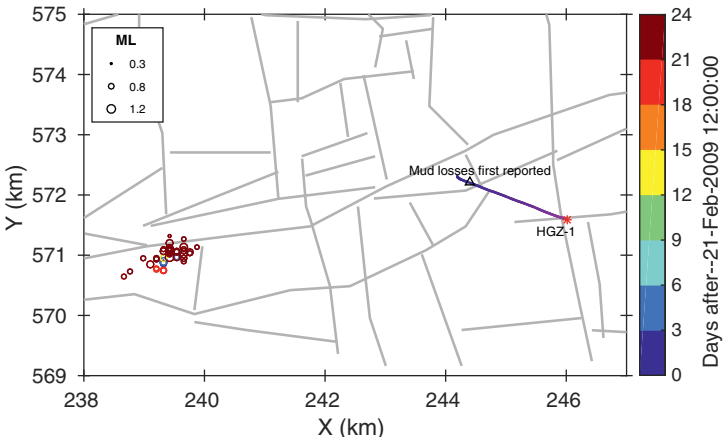

Figure 6.8: Midlaren earthquake swarm of February 22 to March 22, 2009, with timing of the event represented by the colour scale. Gray lines indicate faults. The well path of HGZ-1 is shown in plan view with colour indicating well depth; the star marks the surface location, the triangle the location of reported mud losses.

[1]LCM = lost circulation material

6.5 Conclusions

We used train noise data from a deep geophone array in the Groningen reservoir to investigate time-lapse variations of the reservoir. We found a temporal anomaly of approximately 1.5 month duration for the inter-geophone P wave travel times to the geophone located beneath the GWC, and, in the same period and for the same geophone, an anomaly in the time delay between the direct P wave and a PS converted wave. These data, together with a change in noise level, are best explained by a temporary elevation of the GWC of roughly 23 m.

The time span of anomalous observations could be linked to the drilling of borehole ZRP-3 at 4.5 km distance. The qualitative (anti-)correlation of the seismic anomalies at SDM-1 with the bottom hole pressure at borehole ZRP-3 revealed an effect of pore pressure diffusion. From the time delays of drilling into the reservoir and the end of the operations at ZRP-3 on one hand, and the seismic response at SDM-1 on the other, we estimated a pore pressure diffusivity of 4.9 - 5.7 m^2/s and a permeability of approximately 151 - 176 mD. The diffusivity and permeability estimates are somewhat high, but within acceptable ranges given in the literature.

The absence of similar seismic anomalies during the drilling of another well, ZRP-2, suggests that pore pressure diffusion in the Groningen reservoir is complex and that faults may play an important role. Additional support for the role of faults in efficient pore pressure diffusion comes from the Midlaren earthquake swarm of 2009 which is associated to the drilling of well HGZ-1. The fault map shows a link between the location of first mud losses and the location of the earthquake swarm. The time difference of only a day between first mud losses and the first earthquakes at 4 - 5 km distance gives a pressure diffusivity of 19 m^2/s corresponding to a permeability of 500 mD. These values are significantly higher than for the pore pressure diffusion between ZRP-3 and SDM-1.

We conclude that small pressure variations caused by drilling operations can have a fast and distant effects by pore pressure diffusion along faults. Proper fault zone monitoring is therefore of crucial importance to limit the seismic hazard associated to drilling.

Chapter 7

Effect of pore pressure on fault slip stability: Experiments on simulated quartz gouges

7.1 Introduction

It has long been thought that faults fail through either catastrophic earthquakes or through stable, aseismic sliding or creep (Reid, 1910). However, in the last few decades, advances in seismological and geodetic technologies have led to the discovery of transient slip phenomena (silent earthquakes) such as slow slip event (SSE), episodic slow slip and tremor (ETS), low-frequency earthquakes (LFE) and very-low-frequency earthquakes(vLFE) (see e.g. Wang & Tréhu (2016) and Beroza & Ide (2011) for reviews).

The occurrence of even limited acceleration during slow slip events (SSE) inevitably leads to stress changes on the fault which might trigger or delay seismicity. In the case of the 2011 M9.0 Tohoku earthquake, a SSE observed about one month before the earthquake was inferred to have increased shear stress in the hypocenter area (Ito et al., 2013). Clearly, then, understanding the mechanisms of slow slip and tremor and how these are related to regular earthquakes could make a major contribution to improving seismic hazard evaluation.

Slow slip events were first observed from strain meter data by Linde et al. (1996) at shallow depth (< 4 km) on the San Andreas fault, and by Hirose et al. (1999) at more than 40 km depth along the subducting slab in southwest Japan, using GPS measurements. Dragert et al. (2001) reported slow slip on the Cascadia subduction zone from GPS data. Subsequent research in Cascadia by Rogers & Dragert (2003) showed that slow slip events and deep tremor signals are temporally and spatially coupled. Later, Obara et al. (2004) found similar episodic behaviour at the Nankai Through in the Southwest Japan region, overlapping with previously discovered tremors on seismographs (Obara, 2002). Shelly et al. (2007) reported that a portion of the coherent signal in tremors are in fact low frequency earthquakes (LFE) which can be located, with high accuracy, at depths above but parallel to the intraplate seismicity of the subducting Nankai slab, in southwest Japan. Furthermore, the authors suggested that the LFEs occur at the interface between the subducting oceanic plate and the overriding plate. Tomography maps presented by Shelly et al. (2007) show that the depths of LFEs are in a region of high Vp/Vs ratio, which might potentially be linked to porosity and high pore pressure. In Cascadia, images from Receiver functions by Audet et al. (2009) similarly show high Vp/Vs ratio around the deep subduction interface at 25 - 45 km. Coherent LFEs have also been found in tremors in the Cascadia subduction zone by (e.g., Bostock et al., 2012; Plourde et al., 2015), with event location also suggested to be around the plate interface.These consistent observations strongly suggest that slow slip events are occurring in a high pore pressure region accompanied by low frequency tremor.

For induced fault slip in the upper crust by anthropogenic activities, Guglielmi et al. (2015) and Wei et al. (2015) reported aseismic slip and slip induced seismicity at a geothermal field and in fluid injection experiments on natural faults, which suggest that slip behaviour can exhibit a wide spectrum of slip rates at the reservoir scale. Das & Zoback (2013) attempted to detect low frequency energy associated with slow slip events, but later studies suggest that this signal was the result of regional earthquakes (e.g. Caffagni et al., 2015; Zecevic et al., 2016). To date, to the best of my knowledge, no episodic slow slip events have been observed in human-induced

slip.

Experimental frictional sliding of bare rock-on-rock surfaces and using simulated fault gouges (e.g., Dieterich, 1978; Scholz & Engelder, 1976) have inspired the development of a set of empirical equations that are capable of producing the full spectrum of fault slip, from aseismic slip to slow slip to earthquakes. These rate and state friction equations (Dieterich, 1979; Ruina, 1983), describe the evolution of friction from an instantaneous change in velocity(V_0) to a new velocity(V):

$$\mu = \mu_0 + aln(\frac{V}{V_0}) + bln(\frac{V_0\theta}{d_c}) \tag{7.1}$$

where d_c is a critical or characteristic slip distance, μ_0 is the friction for steady-state slip at a reference velocity V_0. The state variable θ is governed by a differential equation ("ageing law") as suggested by Dieterich (1979):

$$\frac{d\theta}{dt} = 1 - \frac{V\theta}{d_c} \tag{7.2}$$

where θ evolves linearly with time for $V = 0$, or by a "slip law" as suggested by (Ruina, 1983):

$$\frac{d\theta}{dt} = -\frac{V\theta}{d_c} ln(\frac{V\theta}{d_c}) \tag{7.3}$$

where θ evolution occurs only for non-zero slip velocities.

Stability analyses of a spring-slider system with a single degree of freedom governed by equations 7.1,7.2 and 7.3 (e.g., Gu et al., 1984) indicate that if $d\mu/dV>0$, the fault is velocity strengthening and is not capable of nucleating an instability. Unstable slip can only nucleate when $d\mu/dV<0$, i.e. when the simulated fault is velocity weakening. In addition to a negative value of $d\mu/dV$, in order for a fault to be able to accelerate, the critical stiffness k_c of the system must be larger than the stiffness k of the fault surroundings. Only if both conditions are met (i.e. $d\mu/dV<0$ and $k_c > k$) accelerating slip can nucleate on the fault. The critical stiffness (Ruina, 1983) is related to the Terzaghi effective normal stress, which is normal stress σ_n minus pore fluid pressure Pf ($\sigma_n^{eff} = \sigma_n - Pf$) and the RSF parameters via:

$$k_c = \frac{\sigma_n^{eff}(b-a)}{d_c} \tag{7.4}$$

If $k_c > k$ but close to k, it is possible to nucleate slow slip events that do not accelerate further to seismic slip velocities. A k_c close to k can be obtained if $d\mu/dV$ (i.e. $(a-b)$) is negative and close to zero or if effective normal stress is small or if d_c is large. Since d_c is generally found to be small in experimental studies (Leeman et al., 2016; Marone & Kilgore, 1993; Scuderi et al., 2017), this suggest that the occurrence of slow slip is promoted in regions of elevated fluid pressures (low effective normal stress) or at depths where the frictional properties change from velocity-weakening to velocity-strengthening (i.e. from negative to positive $(a-b)$ values). In the latter case, this has been shown experimentally to correspond to the thermally controlled down-dip and up-dip limits of the seismogenic zone at least

along megathrust faults (Den Hartog et al., 2012). Interestingly, a transition from velocity weakening to strengthening also occurred with increasing sliding velocity at constant temperature in hydrothermal friction experiments on a variety of fault gouge materials. (e.g., Blanpied et al., 1995; Boulton et al., 2014; Chester, 1994; Niemeijer et al., 2016). Such an effect of slip velocity on $(a - b)$ is yet another mechanism by which slow slip transients can be produced, because the maximum slip velocity should be limited by the velocity-strengthening property occurring at larger velocity.

One mechanism of producing high pore fluid pressures and thus low effective normal stresses and a value of k_c close to k in subduction settings, is the dehydration of serpentine minerals (e.g., Peacock & Wang, 1999). Liu & Rice (2007) suggested that low effective normal stress could be an explanation for seismic observations of short recurrence time (Rogers & Dragert, 2003) and the triggering of tremors (e.g., Gomberg et al., 2008; Rubinstein et al., 2008; Thomas et al., 2009), on the basis of numerical models. As an alternative mechanism, based mainly on numerical modeling, (Segall et al., 2010) invokes strengthening upon acceleration due to a transient decrease of pore pressure as a result of dilation of a gouge layer. This dilatancy strengthening or hardening mechanism has been studied experimentally by Ougier-Simonin & Zhu (e.g., 2013), Samuelson et al. (2009), and Xing et al. (2019).

The complete spectrum of slip behaviour predicted by RSF theory was recently reported in room-temperature friction experiments using fine-grained quartz gouge at 100% humidity conditions (Leeman et al., 2016; Scuderi et al., 2017). The evolution from stable slip to slow slip to regular stick-slips (earthquakes) was reproduced by varying the ratio of k/k_c:

$$K \equiv k/k_c = \frac{kd_c}{\sigma_n^{eff}(b-a)} \tag{7.5}$$

The results of their experiments suggest that the regime for slow to silent slip covered the range $0.9 < K < 1$, whereas fast audible unstable slip occurred at K<0.7. Without involving pore pressure, the transition from fast to slow slip was reproduced by performing experiments at decreasing effective normal stress, thereby increasing K. In addition, a full transition from slow to fast slip could be observed as a function of sliding displacement, despite an observed increase in k, caused by shear-enhanced compaction (Leeman et al., 2016; Scuderi et al., 2017). Alongside the observed increase in k, a decrease in both $(a - b)$ and d_c was observed, which outweighed the increase in k. Slow slip events have been reported in numerous other experimental friction studies (e.g., Kaproth & Marone, 2013; Okazaki & Katayama, 2015).

As explained above, pore pressure is believed to play a key role in promoting slow slip and tremor along subduction zone interfaces (Rogers & Dragert, 2003), by decreasing effective normal stress on the fault surface (Liu & Rice, 2005) or through other effects such as dilatancy strengthening (Segall et al., 2010). However, to investigate the effect of pore pressure independent from that of effective stress, experiments have to be designed at constant effective normal stress but varying pore pressure. Such experiments were recently implemented by Xing et al. (2019), using gouges of antigorite, olivine, quartz and chrysotile sandwiched between sandstone

forcing blocks. They found that high pore pressure stabilizes fault slip and suggest a dilatancy strengthening mechanism. Their data showed clear increases in $(a-b)$ with fluid pressure in antigorite gouge, but the observed in $(a-b)$ in quartz gouge were small and with large uncertainty. Furthermore, in these experiments, only limited slip was possible and no transitions from slow sliding to fast stick-slips were observed within an individual experiment. This leaves the following question(s) open: does pore pressure stabilize fault slip in quartz gouge? Is the change in $(a-b)$ significant enough to explain the change in slip behaviour? Are there any other parameters which could change due to changes in pore pressure that could influence slip behaviour?

Here, I used a unique hydrothermal ring shear apparatus in the High Pressure and Temperature (HPT) laboratory at Utrecht University, to perform a series of experiment to investigate the influence of pore pressure on the evolution of slip within a fine-grained quartz layer over a large displacement $x > 40$ mm.

Furthermore, despite the fact that LFE and tremor are strongly related in space and time to slow slip events, Obara (2002) originally suggested that the movement of fluid was a source mechanism for tremor, without considering the coupling with slow slip. In contrast, later studies suggested shearing deformation as the source of tremor/LFE (Obara et al., 2004; Rogers & Dragert, 2003; Shelly et al., 2007, e.g.,) because of the dominantly recorded S wave signal of LFEs. Numerical simulations by Shapiro et al. (2018) recently showed that near horizontal fluid motion as single force source can produce similar S wave pattern. Thus, whether LFE/tremor are the result of direct elastic energy release of shear deformation or fluid motion similar to volcano tremor, is still an important unresolved question. Thus, in an attempt to better understand the coupling between slow slip and tremor and mechanisms of tremor, I record elastic waves generated in the gouge by a broad band piezoelectric sensor that has sensitivity (not calibrated) from 100s Hz to ~ 2 MHz.

7.2 Experimental method

The hydrothermal ring shear apparatus (Niemeijer et al., 2008) in the HPT laboratory is designed for the application of large shear strains ($\gamma > 50$) to gouge samples. Moreover, the pressure compensated loading piston (Fig. 7.1b) ensures that variations in fluid pressure do not affect the effective normal stress acting on the gouge layer(σ_n^{eff}). By directly controlling the effective normal stress ($\sigma_n^{eff} = \sigma_n - P_f$) instead of normal stress (σ_n), this machine enabled me to investigate how pore pressure affects friction and sliding behaviour.

7.2.1 Sample material and initial handling

The sample in the experiments is a simulated gouge consisting of a commercially available fine-grained pure quartz powder (U.S. Silica Company, product Sil-co-Sil 49) which has 95% of the grains smaller than <49 μm (Fig. 7.20) . About ~0.6 gram of material was used to yield a gouge layer with an initial thickness of ~1.5 mm for three experiments performed at dry, wet (i.e. flooded with water maintained at atmospheric pressure) and using a pore water pressure P_f of 150 MPa, A fourth

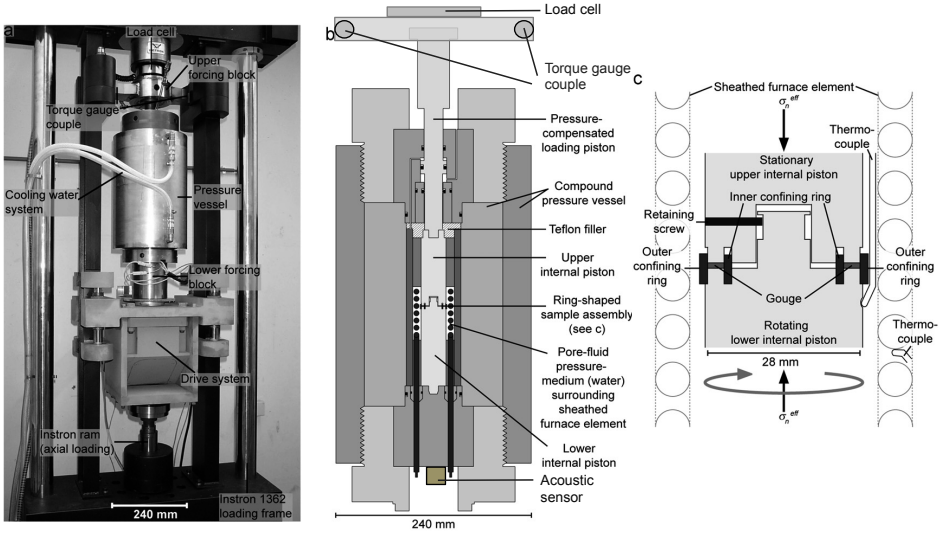

Figure 7.1: Hydrothermal ring shear apparatus. Figure modified from Den Hartog et al. (2012) and Niemeijer et al. (2008). (a) Overview of the machine, the rotary-shear-drive system and pressure vessel mounted inside the Instron loading frame. (b) Simplified schematic cross section of the pressure vessel and piston-sample assembly. (c) Schematic cross section of the sample assembly. σ_n^{eff} =effective normal stress.

experiment performed using a pore water pressure of 10 MPa and using 0.4 gram of sample material yielded an initial gouge thickness of ~1 mm. All samples had an initial porosity of ~ 35% (before axial loading).

Four experiments are reported in this thesis (Table.7.1), all performed at an effective normal stress (σ_n^{eff}) of 60 MPa, a driving velocity (V_0) of 6 $\mu m/s$ and at room temperature (~20°C). For simplicity, I name these experiments according to their pore fluid conditions, and use that through this chapter.

Table 7.1: Experiment parameters

Exp name	Exp ID	P_f (MPa)	σ_n^{eff} (MPa)	V_0 ($\mu m/s$)	Weight (gram)	Displacement (mm)	μ_{ss}
Dry	u802	- (room air)	60	6	0.6	43	0.53
Wet	u803	1 atm (filled with water)	60	6	0.6	43	0.5
Pf10	u812	10	60	6	0.4	55	0.54
Pf150	u804	150	60	6	0.6	43	0.67

$\mu_{ss} = \tau/\sigma_n^{eff}$, obtained from displacement of 3 mm (Fig. 7.3a)
atm, atmosphere pressure

In setting up each experiment, the powder sample is placed in a ring-shaped area (outer edge ⌀ 28 mm and inner edge ⌀ 22 mm) (Fig. 7.1c) between the upper and lower Remanit 316 stainless steel pistons, which were machined with teeth of 0.2 mm height, 0.3-0.4 mm width and spacing of 0.5 mm to grip the sample. Inner and outer Ni-alloy rings, sprayed with a low friction MoS_2 (Molykote) coating,

confine the sample, although some sample extrusion does occur. The piston-sample assembly is installed inside the pressure vessel (Fig. 7.1b, c) and then saturated with water, expect in one experiment which was performed under room-dry conditions. The initial fluid used in experiments performed wet and with pore fluid pressure is demineralized water.

7.2.2 Apparatus and data acquisition

Application of normal (axial) stress to the sample within the hydrothermal ring shear machine is achieved using an Instron testing machine with the loading ram situated below the rotating table and pressure vessel, as shown in Fig. 7.1a. A load cell, located directly above the upper piston assembly and torque cell arm, measures axial loading force. This is servo-controlled to be constant within ~0.01 kN at 14.137 kN (or 60 MPa effective normal stress on the sample),

Fluid pressure is applied to the pressure vessel and sample using a servo-controlled pump. The rotary or ring shear drive (Fig. 7.1a) features a constant voltage electromotor connected to a gear box (1:100) which is in turn connected to the rotating base plate and attached pressure vessel through an angled gear box (1:100). Rotation of the top piston is prevented by an arm within the Instron frame (Fig. 7.1a, c), thus imposing shear on the sample. Due to the finite width (3 mm) of the sample ring area, the chosen constant rotation speed of 6.0 μm/s, defined in the center of the ring, produces a small velocity gradient from 5.3 to 6.7 μm/s from the inner edge to the outer edge.

Two load cells (torque gauge couple in Fig. 7.1b) are located between the frame and the upper loading block for measuring torque generated on the upper piston and sample during shearing of the sample. The torque values from both cells are added and converted to shear stress (τ) on the sample, defined at the centre of the ring (i.e. at 12.5 mm radius). Shear stress is corrected for fluid pressure dependent, normal stress dependent and displacement dependent seal friction using calibrated values obtained previously by Den Hartog & Spiers (2013). The measurement of shear stress is also used for inferring slip displacement and velocity during accelerating slip events, by assuming a constant loading system stiffness.

Mechanical data signals recorded consisted of the externally measured torque, rotary shear/angular displacement (potentiometer, digital resolution ±0.4 μm located above the drive system in Fig. 7.1a), pore pressure (±0.005 MPa), temperature (±1 $^{\circ}C$, close to the sample, Fig. 7.1c), normal loading force (±0.05 kN, the load cell on the very top of Fig. 7.1b), vertical position of Instron ram (±0.05 μm, beneath the table in Fig.1.1a) and relative displacement of the top piston to the pressure vessel (measurement error ~0.004 μm - on the right-hand side of the drive system in Fig. 7.1a) .

Besides mechanical data, I also record acoustic emissions (AE) with a 1 MHz and a 4 kHz piezoelectric sensor on the bottom of the vessel(Fig. 7.1b). The two AE sensors are spring-loaded (Fig. 7.2), with one directly underneath the bottom piston and one ~20 mm to the side. Silica gel is used for increasing coupling. Eventually, I find that the 1 MHz sensor also has good sensitivity at frequencies as low as 1 kHz, thus, for simplicity, I only present data from the 1 MHz sensor.

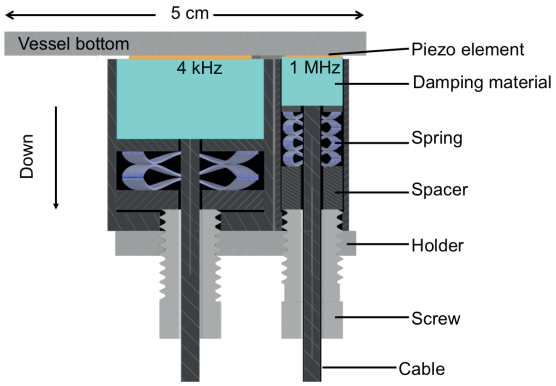

Figure 7.2: Assembly of acoustic sensors, mounted at the bottom of the vessel.

During the experiments, I use a fast and high accuracy recording system to record the torque load cell couple and the two AE sensors at 16 bit accuracy and 5 MHz sampling rate, with a cut-off at ±2.5 Volts for AE. At the same time, a slower recording system records at 18 bit accuracy and 10 to 100 Hz for all mechanical data signals.

7.2.3 Sample particle size measurement

After each experiment, the sample assembly was carefully disassembled. In all experiments, the sample was barely cohesive and only small (~5 mm) pieces could be recovered, often not covering the entire thickness of the sample. The sample pieces recovered were preserved under dry condition in a desiccator. In order to investigate the potential role of grain size reduction, pieces of samples from the four experiments were randomly selected and gently disaggregated using a pestle and mortar, and dispersed in deionized water for a laser diffraction particle size analysis. For each sample, between 6 to 13 repeat measurements were done for each experiment, which gives mostly stable and consistent results (only one measurement out of 30 is considered to be unstable and thus not included in the statistical analysis).

7.3 Results: Mechanical data and analysis

7.3.1 General aspects

In all four experiments performed, sliding causes shear stress to increase to a peak or apparent yield stress value, after which it stabilizes at a near constant level over displacements of 2 - 6 mm (Fig. 7.3a). The shear stress supported (i.e. shear strength) during this stable shear regime (bold font numbers in Fig. 7.3a) varies between 30 to 40 MPa for the four experiments. Moving from dry to wet (unpressurized) conditions, the shear stress supported decreases slightly, from ~32 MPa to ~30 MPa, or in terms of apparent friction coefficient, μ ($=\tau/\sigma_n^{eff}$, ignoring cohesion), from 0.53 to 0.50. With increasing pore fluid pressure (Pf), shear stress increases from the 30 MPa measured wet at atmospheric pressure to ~32 MPa (Pf10) to ~40 MPa (Pf150),

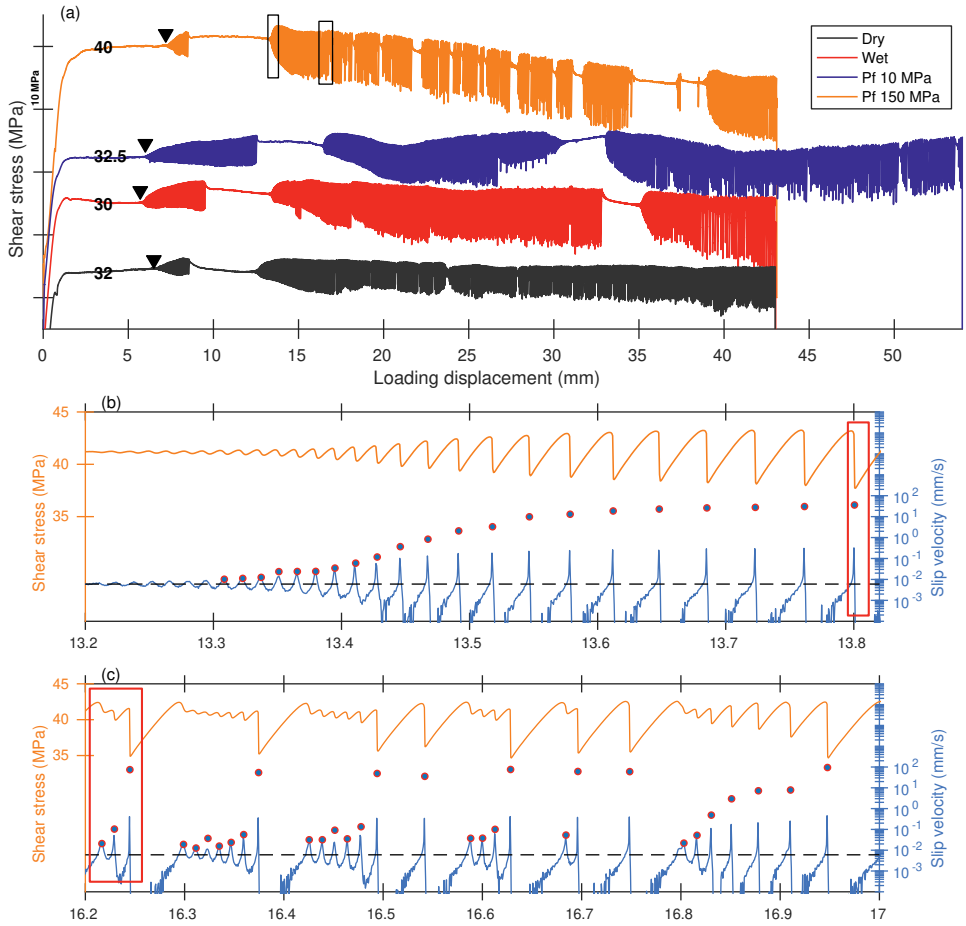

Figure 7.3: (a) Shear stress vs. load point displacement for all four experiments. NOTE: Curves are offset for visualization, and bold numbers indicates shear stress supported at a displacement of 3 mm. Inverted triangles indicate the first occurrence of oscillations in shear stress, i.e. accelerating slip. (b, c) Stress drop events and slip velocity variations during a portion of sliding for experiment Pf150. A continuous slip velocity curve is calculated from decimated data (10 Hz sampling rate). A maximum slip velocity (dots) of each stress drop is calculated from the original data after a pre-conditioning filter (see Appendix II). The grey dashed line indicates the load-point velocity of 6 $\mu m/s$. The red rectangle marks stress drop events that will be described in section 7.4.

or in terms of μ from 0.5 to 0.54 to 0.67. The strength of dry gouge (32 MPa) is thus similar to that of wet gouge with 10 MPa pore pressure. No repeat experiments were performed, so there is no constraint on the reproducibility of these values.

Further shearing of the samples results in the development of quasi-periodic oscillations in shear stress, whose amplitudes and recurrence time grow with displacement until reaching a nearly-constant level. Similar behaviour was reported in experiments by Leeman et al. (2016) and Scuderi et al. (2017). Here I define these as 'transitional slow slip events'. The displacement at which shear stress oscillations first occur (indicated with inverted triangles in Fig. 7.3a) increases with increasing fluid pressure. The displacement corresponding to the first appearance of shear stress oscillations in the dry experiment is larger than the wet and Pf10 experiments (6.5 mm vs. 5.7 mm and 6.0 mm), but smaller than the Pf150 experiment (7.2 mm).

In all experiments, with ongoing slip, several episodes of stable sliding occur, without clear systematic. After each stable sequence, the emergence of instability shows a similar pattern as in the initial case, that is, initially slow and small stress drops become faster and larger with accumulated displacement, as shown in Fig. 7.3b.

Besides transitional slow slip, I observe another type of slow slip event (Fig. 7.3d), which often occurs at the end of interseismic periods and gradually evolve into fast slip events. Due to the fact that these slow slip events appear shortly before fast slip events and their slip rates are small (within the same order of magnitude as the load-point velocity, Fig. 7.3d), I name this behavior interseismic slow slip, in contrast to the previously defined transitional slow slip events. I also observed precursory creep or slow slip before most individual fast slip events, but these are not further discussed in this chapter due to their complexity.

In order to compare quantitatively the slip velocities occurring during the periodic oscillations and stick slips, I calculate the rate of change of stress ($d\tau/dt$) by taking the time derivative of the shear stress records which I then convert to slip velocity by dividing an assumed constant system stiffness(k):

$$V = \frac{d\tau}{kdt} + V_0 \tag{7.6}$$

where V_0=6 $\mu m/s$ is the loading velocity. Applying Eq.7.6 to the decimated (10 samples/second) stress-time/displacement curves, I obtained a low-pass filtered slip velocity curve, such as the light blue curves for run Pf150 in Fig. 7.3b and c, for each experiment. However, due to the large variation in slip velocity (several orders of magnitude), a low pass filtered stress curve can not capture the character of fast slip event. At the same time, I can not use the high frequency signal for the small and slow slip events, because high frequency noise would introduce serious over estimation. Therefore, I developed a routine that first determines the signal frequency content and compares this with the frequency content of the background noise for each stress drop event. On the basis of the frequency content obtained, a low-pass filtering is performed. Maximum slip velocities (V_{max}) for each stress drop is presented with blue dots for experiment Pf150 in Fig. 7.3b, c. See appendix II for details on determining signal frequency content.

In Fig. 7.3c, I present a zoom-in of shear stress vs. displacement for experiment

Pf150, which shows the irregularity of the stick-slips. Small and slow stress drops are sometimes present during the stick periods and seem to delay the occurrence of fast slips, with a growing magnitude towards each fast slip.

7.3.2 Stress drop detection and system shear stiffness

As embodied in equation 7.6, the stress rate ($d\tau/dt$) is linearly related to slip velocity for a constant system stiffness. Therefore, we use the stress rate data to detect stress drop events. As shown in panel (a) of Figures 7.4 to 7.7, the stress rate is calculate using decimated (10 Hz) stress data. Negative values in the stress rate curve represent stress drops. Positive values means shear stress increases with time, which occurs during the 'stick phase' equivalent to inter-seismic period.

For detecting stress drops, I look at the negative part of the stress rate data, and apply a threshold of -0.5 MPa/s (i.e., $d\tau/dt$ < -0.5 MPa/s), which allows events with a slip rate as small as ~10 μm/s to be detected. Detected events are indicated with gray dots in panel a) in Figs.7.4 - 7.7)

To calculate system shear stiffness from inter-seismic period, I select time intervals in the stress rate curve with $d\tau/dt$>0 and the second derivative $d^2\tau/dt^2$ close to zero. Then, apparent shear stiffness is calculated from stress rate $d\tau/dt$ over dividing by the loading point velocity V_0:

$$k = -\frac{d\tau}{V_0 dt} \tag{7.7}$$

I refer to this as the "apparent" shear stiffness because the aseismic creep sometimes occurs during the "stick phase", particularly for slow oscillating stress drops.

In panel b) of Figs.7.4 - 7.7, I present an evaluation of shear stiffness data as a function of displacement. The calculated shear stiffness at each data point is an apparent stiffness, which indicates how much stress has accumulated per mm of load-point displacement. During stable sliding, apparent stiffness and $d\tau/dt$ are expected to be zero. I do, however, observe some intervals with positive k values, which indicate that very small oscillations exist even during stable sliding periods in our experiments. The apparent stiffness at stable sliding period generally starts from 0 MPa/mm and gradually increases until a visible oscillation appears.

During the transitional period between stable sliding and fast stick slip, the apparent stiffness (panel b in Figs.7.4 - 7.7) increases gradually indicating that the sample is becoming more 'sticky' (i.e. with less creep) during the quasi-stick phase. In large stick-slip regions (i.e. during long displacement periods of stick slip behaviour), the values of apparent stiffness are concentrated near a band (for instance 140±20 MPa in Fig. 7.4b). Scatter beneath this band is from the quasi-stick phases of slow slip events.

To avoid the influence of stable and slow slip on shear stiffness estimation, a probability density function (PDF) of measured apparent shear stiffness was calculated for each experiment instead of simple averaging. The PDF gives an estimate of loading shear stiffness from the maximum point for each experiment (panel c in Figs.7.4-7.7).

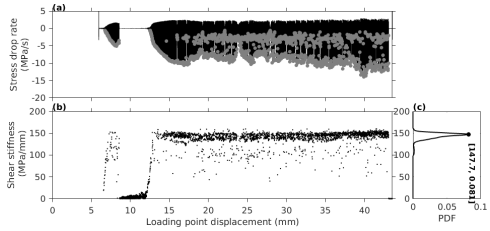

Figure 7.4: u802 Dry

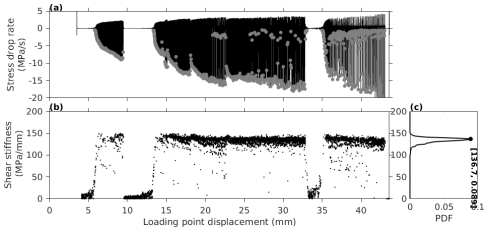

Figure 7.5: u803 Wet

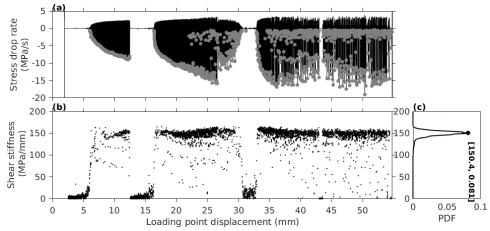

Figure 7.6: u812 Pf10

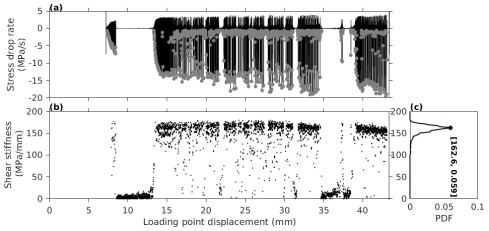

Figure 7.7: u804 Pf150

Figures 7.4 - 7.7: (a) shear stress rate from the derivative of 10 Hz decimated shear stress recording. Gray dots are automatically detected stress drop events. (b) Apparent shear stiffness, obtained from stress increase intervals and Eq.7.7. And (c) the distribution of apparent shear stiffness.

7.3.3 Effect of pore pressure on stress drop and slip velocity

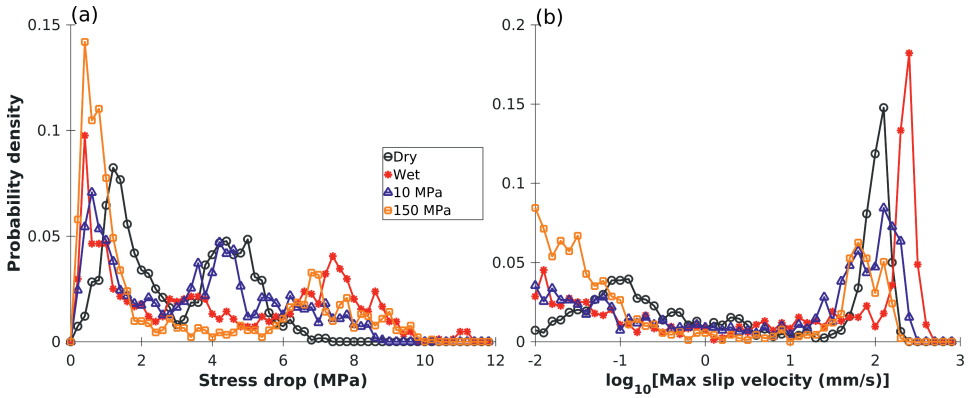

Figure 7.8: The probability density functions of events on (a) stress drop and (b) maximum slip velocity of 4 experiments

After detecting shear stress drops and determining the magnitude of these drops, I obtained a PDF of stress drop values for each experiment (Fig. 7.8a). All experiments are dominated by two peaks, with peak positions and values differing amongst the 4 experiments. The dry experiment shows stress drops ($\Delta\tau$) ranging

between 0 and 7 MPa, and peaks at 1.2 MPa and 4 - 5 MPa, with a valley around 3 MPa. The wet, Pf10 and Pf150 experiments have primary peaks at 0.4 - 0.8 MPa, slightly (0.6 - 0.8 MPa) smaller than the dry experiment. The wet experiment has a medium peak at $\Delta\tau$ of 3 - 4 MPa, and the Pf10 experiment has also a medium peak at 4 -5 MPa, which is absent in the event distribution of the Pf150 experiment. Above a stress drop $\Delta\tau$ of 6 MPa, the dry experiment has only few events, while the Pf10 experiment shows a diminishing number of events from 7 MPa onward. By contrast, the wet experiment has an additional peak around $\Delta\tau$ of 7.4 MPa and the Pf150 experiment also has a peak around $\Delta\tau$ of 7.0 MPa. The wet and Pf150 have a similar 'cut-off' stress drop around 10 MPa, although the wet experiment also have a few events at ~11 MPa.

As mentioned earlier, I estimated accurate slip velocity data for each stress drop by processing the 5 MHz sampled shear stress data using Eq.7.6 and with the self-adjusted low pass filter (see also appendix II). Maximum slip velocity (V_{max}) of each event is taken for statistical analysis (Fig. 7.8b). All 4 experiments show two maxima in their PDFs, one at 10^{-2} to 10^{-1} mm/s and another one at $10^{1.5}(\sim 30)$ to $10^{2.5}(\sim 300)$ mm/s. All experiments show a lack of events with a V_{max} between 10^{-1} to 10^{1} mm/s.

Generally, I find an enhanced probability for slip events with a V_{max} up to one or two orders of magnitude larger than the load-point velocity (0.006 mm/s), which I define here as "slow slip events". The presence of a pore fluids shifts the velocities of these slow slip events to smaller values (Fig. 7.8b). In this slow slip regime (V_{max} from 0.01 to 1 mm/s in Fig. 7.8b), I find that the Pf10 and Wet experiments show a similar pattern, but an increase to 150 MPa (Pf150) significantly increased the probability of slow slip events.

The higher probability of slow slip of experiment Pf150 in Fig. 7.8b is coincident with a larger proportion of small stress drops (Fig. 7.8a). To further investigate the relationship between slip velocity and stress drop, I plot one as a function of the other for the four experiments separately in Fig. 7.9.

For slower maximum slip rate ($V_{max} < 1$ mm/s), I find that the V_{max} increases exponentially with stress drop (insets in Fig. 7.9), with a rate that slightly varies over the experiments. In this slip rate regime, piston acceleration is small. Assuming quasi-steady state sliding, the evolution of the RSF state variable θ is small, which gives $\frac{d\theta}{dt} \approx 0$, and then, $\frac{1}{V} \approx \frac{\theta}{D_c}$, so that Equation.7.1 becomes simplified to:

$$\mu_{ss} = \mu_0 + (a-b)ln(\frac{V}{V_0}) \tag{7.8}$$

Based on Equation.7.8, the following relation between slip velocity V and friction drop $\Delta\mu$ ($\mu - \mu_0$) and shear stress drop can be obtained.

$$V = V_0 \cdot e^{(-\frac{\Delta\mu}{(a-b)})} = V_0 \cdot e^{(-\frac{\Delta\tau}{\sigma_n^e f f \cdot (a-b)})} \tag{7.9}$$

This shows that slip velocity V is an exponential function of stress drop $\Delta\tau$. Thus, an exponential function has been introduced, to fit the data set.

$$v = v_0 \cdot e^{c\Delta\tau}; \quad [\Delta\tau < \Delta\tau_s] \tag{7.10}$$

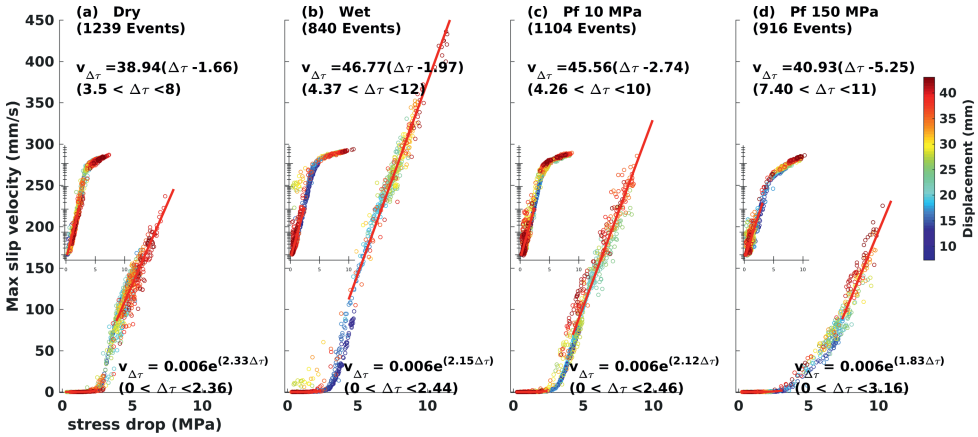

Figure 7.9: Maximum slip velocity (V_{max}) of each stress drop event as a function of stress drop magnitude. Exponential and linear curves are fitted with least square minimization. Inset in each subplot is the same data plotted in linear-log scale. Color of each dot indicates the displacement at the time of the event.

A larger c means a faster increase of slip rate with increasing stress drop. After a least square regression for the slip velocity interval [0.006 mm/s, 1 mm/s] for displacement smaller than 20 mm (red straight line in the inset of Fig. 7.8a - d), I obtain $c = 2.33, 2.15, 2.12, 1.83$ for the Dry, Wet, Pf10, and Pf150 experiments, respectively. The decrease in c from dry to high pore pressure, indicates a slower increase of slip rate (at this slow slip regime). Based on Eq.7.9 and Eq.7.11, $(a-b)$ can be obtained. Specifically $(a-b) \approx -0.0072, -0.0077, -0.0078, -0.0091$ for the four experiments. Note that $(a-b)$ becomes slightly more negative with water involved. At wet condition and with a pore pressure of 10 MPa (Pf10) $(a-b)$ are near identical. While increasing pore pressure to 150 MPa (Pf150) makes $(a-b)$ become significantly more negative.

As the assumption of steady state is not valid during stick slip, I performed a series of simulations to verify our estimated $(a-b)$ evolution with pore pressure. The program is coded by Van den Ende (2020) using the equation of motion for a spring-slider system with single degree of freedom plus radiation damping and rate and state friction (Rice, 1993). In each set of simulations, the ratio of k/k_c (Eq.7.5), is increased to close to one by changing the value of k to simulate the emergence of slow slip events. Simulation results (Fig. 7.10) show that the dominant parameter that controls the slope of V_{max} vs. friction drop is $(a-b)$, and that a more negative $(a-b)$ produces a smaller slope, which is consistent with our estimate. Note that in the simulations constant values of $(a-b)$ and d_c were assumed, while in reality these are likely to change during the experiment (Scuderi et al., 2017). Therefore, the absolute values of $(a-b)$ obtained from our estimation (using Eq.7.9 and c) are not reliable, since the assumption of constant state is not valid. However, the different slopes (c) for the different experiments shown in Fig. 7.9 do indicate a decrease in $(a-b)$ with increasing pore pressure to 150 MPa.

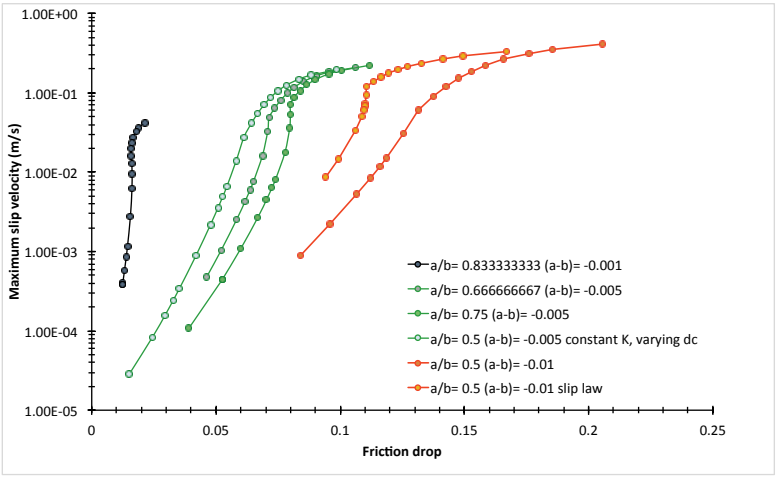

Figure 7.10: Evolution of V_{max} vs. friction drop, from stick slips simulation.

For larger stress drops in Fig. 7.9, beyond the quasi-steady (quasi-stable) sliding regime (V > 10 ~ 20 mm/s), slip velocity gradually transform to a linear dependence on stress drop. For V > ~100 mm/s, the relation between stress drop and V_{max} becomes linear for all four experiments. Here, I define this linear regime (V > ~100 mm/s) as the fast slip regime, during which inertia starts to play a role in limiting the slip rate (He et al., 2003). A linear function:

$$v = g(\Delta\tau + d); \quad [\Delta\tau > \Delta\tau_d] \tag{7.11}$$

is applied to fit the curves with a least square regression. I obtained g= 38.94, 46.87, 45.56, 40.93 and d=-1.66, -1.97, -2.74, -5.25 MPa for the dry, wet, Pf10 and Pf150 experiments, respectively. The variation in g is relatively small, and they are even similar under wet and 10 MPa conditions. The decrease in d with increasing pore pressure suggests a lower slip rate for high pore pressure, for a given stress drop. In other words, a larger stress drop is required to produce fast slip in the experiments with high pore pressure (Pf150).

7.3.4 Shear stiffness changes with pore pressure

As shown in previous studies (Leeman et al., 2016; Scuderi et al., 2017) and via equation 7.5, shear stiffness is an important parameter for controlling slip stability. Fig. 7.11 shows that the peaks in the PDFs of the shear stiffness values obtained from figures.7.4 to 7.7 are different for the four different experiments. First, the presence of water lowers the average stiffness (apparatus stiffness + sample stiffness) from 148 (dry) to 137 MPa/mm (wet). At the same time, an increase in pore pressure is accompanied with an increase in average stiffness, from 137 MPa/mm to 150 MPa/mm to 163 MPa/mm for the wet, Pf10 and Pf150 experiments, respectively. This trend is consistent with the dependence of slip velocity on stress drop in the fast slip regime (Fig. 7.9). Here, slip velocity increased slightly from dry to wet

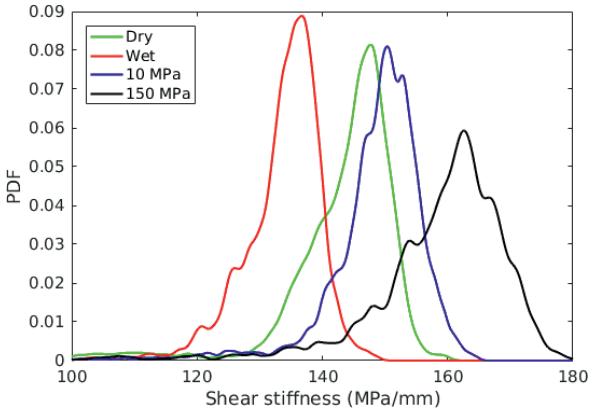

Figure 7.11: Probability density function of shear stiffness.

conditions, and then continuously decreased with pore pressure, suggesting that the shear stiffness variation might play a key role in controlling variable slip rates (V_{max}) at least in the fast slip regime. It is difficult to quantitatively compare the changes in stiffness with changes in slip velocity because the other parameters in equation 7.5, namely $(a - b)$ and d_c are likely to vary between experiments as well.

7.3.5 Sample volume and normal stress changes during the seismic cycle

Sample shortening (layer thinning) is observed in all 4 experiments, relative to the thickness at the start of shearing. The total amount of shortening at a displacement of 43 mm is 194, 201, 239, 244 μm for the dry, wet, Pf10 and Pf150 experiments, respectively (Fig. 7.12d). In general, this layer thinning is the combined result of material loss via extrusion through small gaps between the confining rings and the pistons, and porosity decrease via shear-enhanced compaction involving grain breakage, hence size reduction and grain rearrangement/repacking. Superimposed on long-term sample shortening, I observe co-seismic shortening and inter-seismic dilatation in all 4 experiments (Fig. 7.12b).

'Co-seismic' shortening or layer thinning is variable and has the maximum value in the wet experiment at around 1.5 μm or 0.15 - 0.2% for a layer thickness of 800 - 1000 μm. In Fig. 7.12f, axial displacements occurring during slip events are plotted as a function of the stress drop. Although the data show significant scatter, there are clear trends, with sample thinning correlating with stress drop. In addition, the dry and wet experiments show more sample shortening than the Pf10 and Pf150 experiments.

During the 'interseismic periods' dilatation is observed and this follows corresponding trend, highest in the wet and dry experiments and lowest in the experiments with pore fluid pressure Fig. 7.12b. The rate of dilatation often increases towards the end of the interseismic period, accompanied by "yield" and a subsequent roll-over in shear stress.

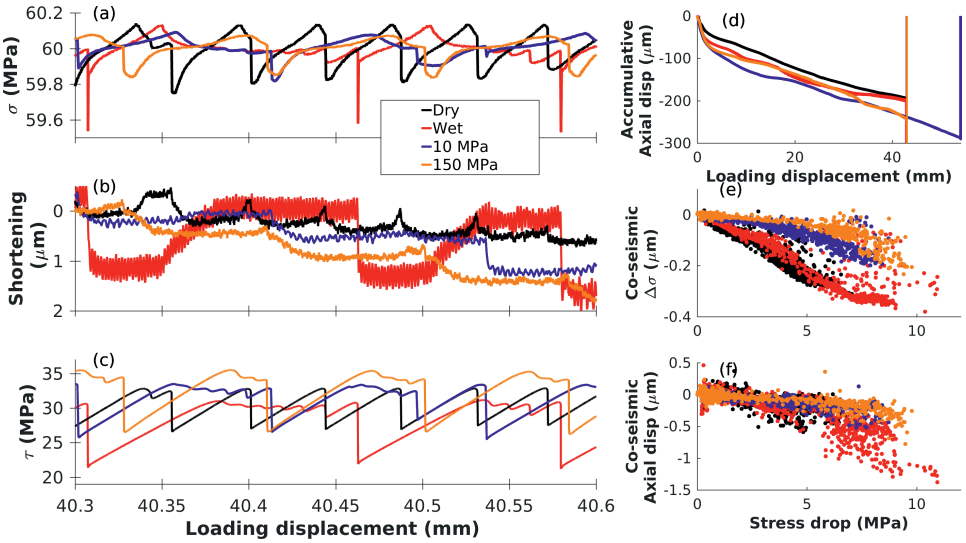

Figure 7.12: Axial displacement and normal stress in all experiments. (a) Detail of the record of normal stress, (b) Shortening during the same displacement interval as (a), (c) Shear stress during the same displacement interval as (a). (d) Axial displacement (=shortening) as a function of load-point displacement over the entire duration of the experiments. (e) Co-seismic normal stress change as a function of shear stress drop for all identified slip events. (f) Co-seismic axial displacements as a function of stress drop, where a negative number indicates compaction.

Normal stress is under high accuracy servo-control by the Instron loading frame, and only small fluctuations are observed on long time scales. However, small but clear drops in normal stress accompany co-seismic sample shortening. For example, alongside the ~1.5 μm shortening observed in the wet experiment at 40.46 mm displacement, I observe a decrease in normal stress of ~0.5 MPa (0.83%) (Fig. 7.12a, b), demonstrating failure of the servo-control system to fully buffer rapid changes in sample thickness. Note that the sample shortening data was not corrected for elastic deformation.

7.4 Results from acoustic emission data

As described in the methods section, acoustic emissions are recorded by a 1 MHz piezoelectric sensor at 5 MHz sampling rate at 16 bit resolution with a range ±2.5 V with a noise level of maximum 10 mV. In Fig. 7.13, I present representative examples of stress drop events from the Pf150 experiment, and their associated AE records, falling in 2-second windows around the maximum slip velocity. Event No.72 (Fig. 7.13a) is indicated by the red box in Fig. 7.3b at a displacement of ~13.8 mm. It is a fast slip event, with maximum slip rate of ~40 mm/s and a stress drop of ~5.5 MPa (bottom panel of Fig. 7.13a). Accompanied with this stress drop, I can identify a low frequency (few kHz) AE signal, but a high frequency AE signal is absent. Another

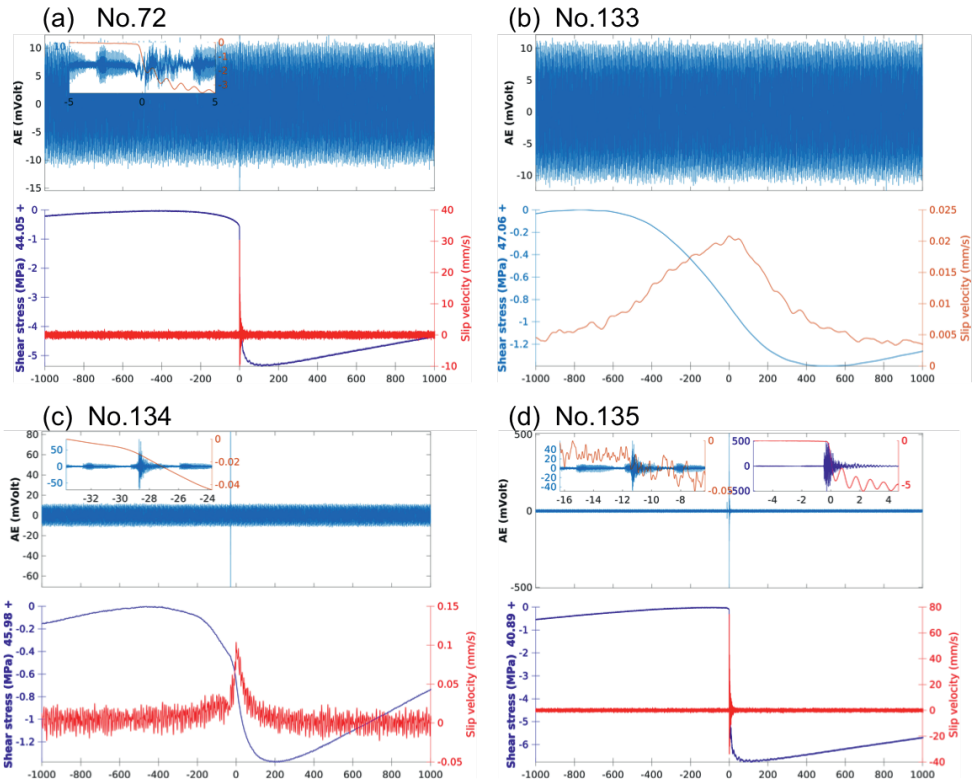

Figure 7.13: Stress drop events and associated AE recordings. X axis is time with unit of millisecond. Zero time is defined at the moment of maximum slip velocity. (a) event No.72, shown in the red box in Fig. 7.3b. (b,c,d) event No.133,134,135 are 3 successive events annotated in Fig. 7.3c. Note that tremor-like high frequency signal, for example the high frequency signal in the insets of (a), are noise from the servo-controlled fluid pump.

clear character of the AE signal in event No.72 is the negative first onset (inset in Fig. 7.13a). A manual check of other low frequency AE signals, I find that they all show negative first onset.

Event No.135 presented in Fig. 7.13d, is an event at slightly larger displacement (~16.24 mm), with a slightly larger stress drop ~7 MPa and higher slip rate ~70 mm/s. In contrast to event No.72, I observed a significant high frequency (maximum ~1 MHz) in AE signals, with a co-seismic signal that has a maximum amplitude of ~ 500 mV. A small precursory AE (amplitude ~40 mV) occurs, which can be associated with a visible stress drop of ~0.01 MPa.

Event 133 and 134 in Fig. 7.13b and c, are two slow slip events before the fast slip event No.135. The stress drops of these two events are similar, ~1.3 MPa, with different but both small slip rates (0.02 vs. 0.1 mm/s). Neither of them has notable AE signal around the maximum slip rate. However, event No.134 has a noticeable high frequency precursory signal located 29 ms before the moment of maximum slip

rate (Inset in Fig. 7.13c). This AE can be associated with the first acceleration of slip starting at ~ −30 ms. Similar to event No.134, high frequency AE signals are found accompanying visible acceleration of slip, while oscillation of slow slip type, without clear acceleration, such as event No.133 in Fig. 7.13, are accompanied with hardly any AE signal.This clearly indicates that fast slip acceleration is a necessary condition for generating high frequency AE.

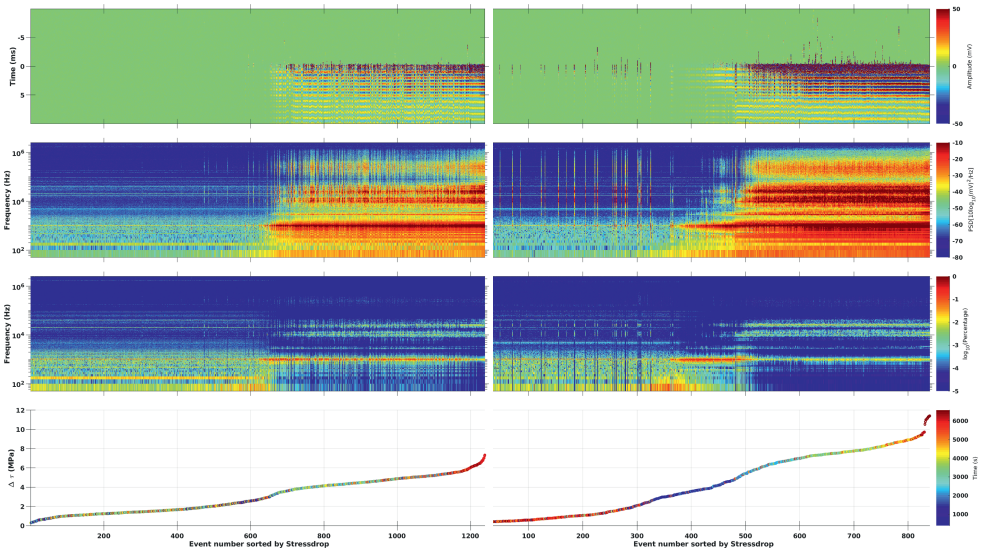

Figure 7.14: u802 dry

Figure 7.15: u803 wet

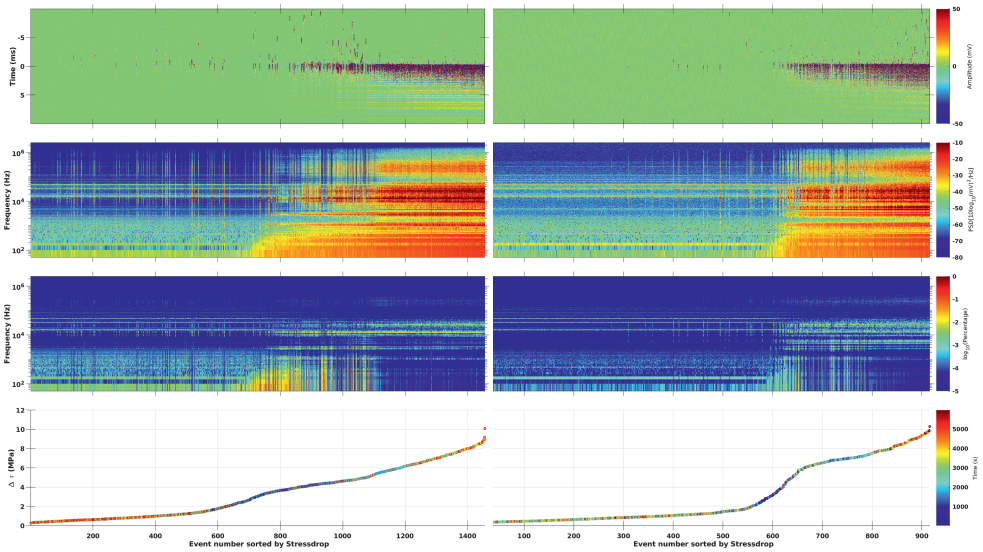

Figure 7.16: u812 10 MPa

Figure 7.17: u804 150 MPa

Figures 7.14 - 7.17: (a) Segments of acoustic recording from the 1 MHz sensor, 0 ms referring to the timing of maximum slip rate. (b) Power spectrum density (PSD) of each segment in (a). (c) Energy frequency distribution of each segment. All four panels have event number on the x-axis, which is sorted by stress drop (d).

In Figures 7.14 to 7.17, I show stress drop events (bottom panel) and associated acoustic sensor recordings (top panel). The acoustic signals are presented for the interval -10 to 10 ms, where 0 ms is defined as the time of maximum slip velocity, and the color scale represents AE signal amplitude (amplitudes are saturated in the plot to emphasize signal duration and small amplitude events). A Fourier transform is applied to each of the 20 ms recordings, and power spectrum densities (PSDs) are presented in the second panel with a logarithmic frequency scale.

Generally in Figures 7.14 to 7.17, I see longer signal duration (panels a), higher energy (panels b) AE signals associated with larger stress drop (panels d). In all four experiments, I observe that in the small stress drop regime ($\Delta\tau < 2.5\ MPa$), most recordings do not exceed the noise level of ~10 mV, while there are some events that are accompanied with acoustic emissions. As stress drop increases, I can distinguish stable frequency bands for each experiment (specific frequencies are identified in Fig. 7.18).In panels c of each figure, I show the relative energy contributions from the different frequencies for each event. This clearly shows that the energy distribution is a function of stress drop (panel d) and ongoing displacement (color scale in panel d), and varies between experiments.

Taking the wet experiment as an example (Fig. 7.15), for event numbers 300 to 400 ($\Delta\tau$ = 2 ~ 3 MPa), there is a first increase in energy density at a frequency as low as 100 Hz. Note that the event number here is sorted according to stress drop and not time or displacement. From event numbers 350 to 500 ($\Delta\tau$ = 3 ~ 5 MPa), there is a significant increase in the 1 kHz signal which dominates the acoustic signal spectrum, while higher frequency signals are mostly absent. From event 500 ($\Delta\tau$ > 5 MPa) onwards, the events fall in the fast slip regime and the signal energy spectrum does not show major changes. Similar trends can be observed in the other experiments, with slightly different transitions. The appearance of the low frequency (100s to 1000s Hz) signal seems to indicate a transition from slow to fast slip.

In order to further compare the AE frequency content between the four experiments, in Fig. 7.18, I present the averaged PSDs, for events that have high frequency signal (50 kHz high passed signal with amplitude larger than 100 mV). The differences in frequency bands between experiments are significant below 50 kHz. At the same time, between 50 kHz to 1 MHz, the PSD curves have the same trends, although the PSD values are not the same. The dry and wet experiments have nearly-identical frequency distribution of the AE signal, except for a generally lower amplitude at dry condition, due to smaller stress drop. Significantly higher PSD values are observed at low frequency range (around 1000 Hz) for the dry and wet conditions, compared with Pf10 and Pf150.

The broad band sensitivity (although not flat) of our AE sensor with a good coverage of signal from 100 Hz to 1 MHz covers elastic deformation over a wide range of scales. In order to investigate the elastic energy from local deformation event, I apply a 50 kHz high pass filter to AE recordings (± 1 s around each stress drop). I then project each AE amplitude (represented by colored dots) to its associated stress drop

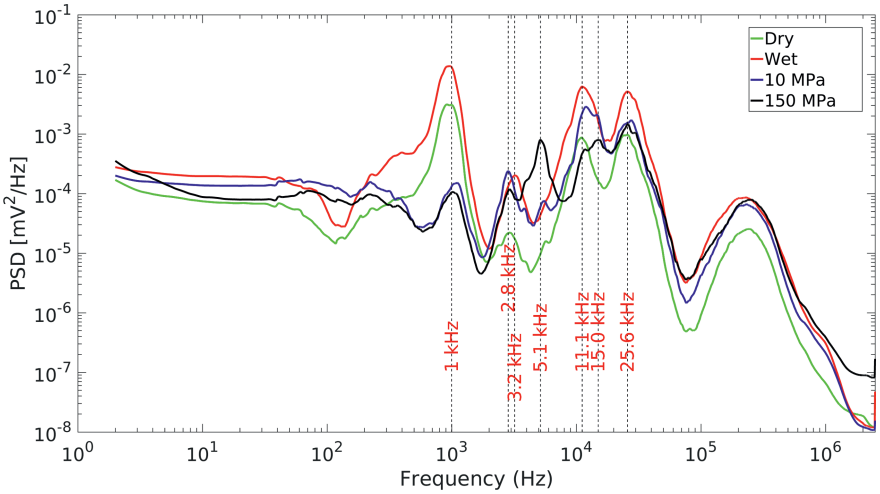

Figure 7.18: Averaged power spectrum densitities (PSDs) of stress drop events with amplitude (50 kHz high passed) larger than 100 mV.

event for each experiment, taking the maximum amplitude of each stress drop event, resulting in Fig. 7.19. Not surprisingly, in general, a larger stress drop is more likely to be accompanied by a larger AE amplitude. At the same time, clear patterns in AE amplitude with displacement are observed in all four experiments. We find AE amplitudes are generally low during the transitional periods, even though stress drops are large at the later part of these periods (for example, at displacement around 13 mm in the Pf150 experiment). We also find a large number of inter-seismic slow slip events with notable AE signal, for instance at a displacement of 30 to 35 mm at Pf150. These events occur more often at larger displacement, and are observed in wet and fluid pressurized experiments but are very rare under dry conditions.

Based on Fig. 7.19, a list of the proportion of slow slip events with an AE (50 kHz high pass filtered) that have amplitude > 10 mV, is presented in Table.7.2, without distinguishing transitional- or inter-seismic- slow slip events. The total number of slow slip events of each experiment is also listed.

Table 7.2: Portion of slow slip events (V_{max} <1 mm/s) with AE amplitude larger than 10 mV

	Dry	Wet	10 MPa	150 MPa
SSE No.	520	270	747	595
Percentage AE (±1 s)>10 mV	2.5	7.2	11.5	14.5

7.5 Particle size distribution data

The average particle size distributions for each experiment are presented in Fig. 7.20, with the color area indicating one standard deviation.

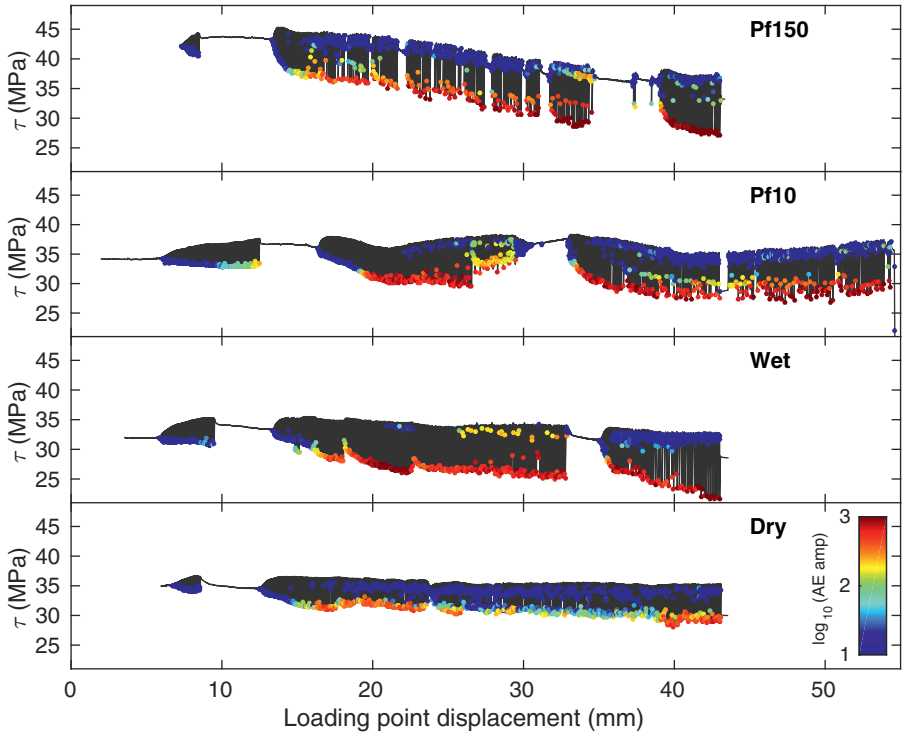

Figure 7.19: High frequency AE signals associated with stress drop events. Each colored dot represents the maximum AE amplitude from each stress drop events within a window of ±1 s around the maximum slip velocity.

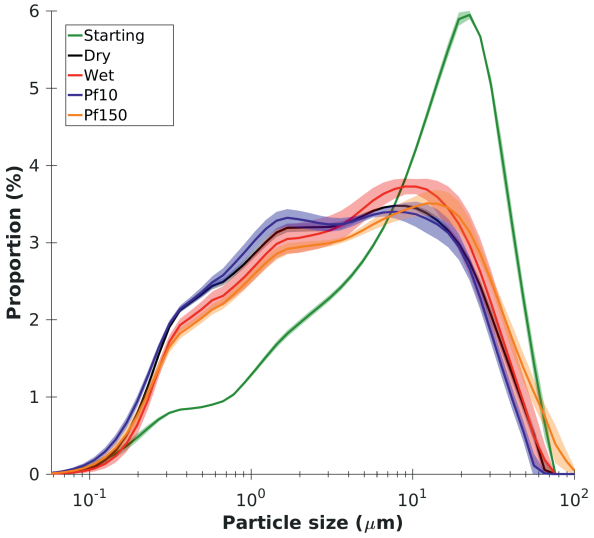

Figure 7.20: Particle size distribution of all experimental samples and the starting material, obtained using a Malvern laser diffraction particle size analyzer.

Generally, I observe similar trends of particle size distribution over the 4 experiments. Compared with the starting material, the proportion of small particles (0.2 to 6 μm) increases and the proportion of large particles (10 to 60 μm) decreases.

Focusing on the small particle regime (< 6 μm), Fig. 7.20 shows that the Pf10 experiment(blue curve) has the largest proportion of particles in this size range, which is likely due to the longer slip displacement applied in this experiment (Fig. 7.3). The second highest is the dry experiment (black curve), followed by the wet experiment (red), and finally the Pf150 experiment (orange). The opposite trend is found for particle size larger than 10 μm. Note, however, that the differences are rather small, and that the volume of material measured is only ~ 5$\%$ of the total volume of each sample and that some clumping of particles might have occurred (which is likely the reason for the presence of larger than initial sizes in experiment Pf150).

7.6 Discussion

7.6.1 Macroscopic transitions in slip behavior

I performed rotary shear experiments on simulated quartz fault gouges at room temperature, a constant sliding rate of 6 $\mu m/s$ and at a constant effective normal stress of 60 MPa. I investigated the influence on slip behaviour and associated acoustic emissions of varying pore fluid conditions from dry to wet(1 atmosphere) and of using pore water pressures Pf of 10 MPa and 150 MPa. All experiments showed transitions from stable sliding to slow slip events to fast slip events. The large shear strains (γ) reached in these experiments allowed me to collect data on 800 to 1200 slip events in each experiment and make meaningful comparisons between the four experiments.

Previous experiments on fine-grained quartz gouge at 100% humidity conditions have shown that the transitions from stable sliding to slow slip to fast slip are a function of applied normal stress, system stiffness as well as accumulated displacement, see Leeman et al. (2016) and Scuderi et al. (2017). These authors showed that the transition from stable sliding to slow slip to stick-slip can be directly related to the stability criterion (Eq.7.5 and Eq.7.4). Higher effective normal stress results in a smaller value of K and thus more unstable slip. Scuderi et al. (2017) performed microstructural analyses of fault gouge samples sheared to variable amounts of displacement (shear strains) and showed that deformation becomes more localized, concomitant with a decrease in the value of d_c and a decrease in $(a-b)$, which decreases K and promotes unstable slip. A similar decrease in d_c with accumulated displacement was observed by Marone & Kilgore (1993).

In line with the results of Leeman et al. (2016) and Scuderi et al. (2017), I observed a continuous transition from stable sliding, via slow slip, to fast slip, which started at displacements of ~6 mm. This transition is presumably due to a similar localization process as in the work by Scuderi et al. (2017). The localization of shear deformation causes a decrease in $(a-b)$ (more negative) and d_c, which causes more unstable behaviour through a reduction in K. However, in our experiments, fast stick-slips disappear again after a displacement increment of 2 - 7 mm (Fig. 7.3a),

which suggests a delocalization of shear that is associated with an increase in $(a-b)$ and d_c. This resembles the results of Beeler et al. (1996), although these authors did not give an explanation for the delocalization of slip. The reverse transitions from stick slip to stable sliding occur often after a 'yielding' of shear stress. At larger displacement, reversal transitions still occur over a short displacement interval, with the exception of an obvious gradual transition at a displacement of 30 mm in the Pf10 experiment.

The difference in the experimental results presented here versus those of Scuderi et al. (2017) do not have a simple physical explanation, but it is likely that the higher shear strain reached in our experiments and the variation in slip velocity across the width of the annulus play a role. For a thickness of 0.8 to 1 mm, we reached total strain γ>40, which is much larger than Scuderi et al. (2017) who imposed 20 mm slip on 2.5 mm thick samples. I observe no systematic trends in the number of transitions or the displacements at which they occur as a function of the presence of pressurized water, but do note that more visible transitions occur in the Pf150 experiment than in the others, which indicates that Pf150 is closer to the stable condition.

Besides slow slips during the transition period between stable and unstable behaviour ("transitional slow slip"), I observe another type of slow slip event (Fig. 7.3d), which often occurs at the end of interseismic periods. The "interseismic slow slip events" observed in our experiments fall on the same slip rate vs. stress drop curves as the transitional slows slips, and without showing clear clustering (Fig. 7.9), indicating a similar value of $(a-b)$.

Taking a closer look at the stress drop curves characterizing these two types of slow slip, the two types look mostly similar with a simple and smooth acceleration and deceleration phase, without an observable AE signal, for instance, event No.133 in Fig. 7.13c. The statistic analysis of AE signal also shows that slow slips are mostly devoid of high frequency AE. In Fig. 7.19, it is shown that small and slow slip events are mostly devoid of high frequency AE (blue dots). However, there is a proportion of interseismic slow slip events that are accompanied by clear AE signal (light dots). I manually checked these interseismic slow slip event and associated AE and find that most of them have multiple phases of acceleration and deceleration (less smooth) during the stress drop. Additionally, the AEs are not necessarily generated at the moment of fast slip rate (event No 134 in Fig. 7.13c). The occurrence of AE suggests that interseismic slow slip events occasionally trigger part of the fault to slip faster locally, whereas transitional slow slip hardly trigger any smaller scale localized faster slip.

7.6.2 The effects of pore fluid pressure on unstable slips

All experiments were performed at constant Terzaghi effective normal stress while the pore fluid conditions were varied. The data clearly indicate that solely varying pore pressure has an effect on the slip rate of unstable slip events (both slow and fast ones).

In the fast slip regime(V_{max} > 20 mm/s), a significant decrease of the slip rate is observed with increasing pore pressure, for a given stress drop. For slow slips (V_{max} < 1 mm/s), I observed a similar trend, although the difference is smaller.

Dilatant strengthening has been suggested by Segall et al. (2010) as a possible mechanism for promoting slow slips in the presence of a pore fluid pressure. Dilatancy during accelerating slip can cause a transient decrease in pore pressure which leads to a transient increase in effective normal stress which can effectively slow down instabilities. This mechanism was also suggested to be active in experiments on fault gouges by French & Zhu (2017), Ougier-Simonin & Zhu (2015), and Xing et al. (2019). In the experiments described here, co-seismic slip rate was lower (especially fast-slip) at high pore pressure, which might indicate a role of dilatancy strengthening. However, a few lines of evidence suggest that dilatancy strengthening was not important in our experiments. First, in all four experiments, although sample dilatation is observed in our local LVDT data, it precedes co-seismic slip. By contrast, during the co-seismic slip phase, I only observe sample shortening (Fig. 7.12e). Second, porosity of the bulk gouge layer is not expected to be very low but is probably >15%, as is also evident from the observation that most of the samples disaggregated upon disassembly of the piston set. Porosity in the localized slip zone might be lower, but due to its small thickness (< 100 μm, see Scuderi et al., 2017) the fluid diffusion distance to the porous bulk layer is short, of the order of 50 μm (half the thickness), meaning that any pore fluid decrease during dilatation would be rapidly compensated by fluid flow. Therefore, it is highly unlikely that dilatancy strengthening could explain the slip velocity variations with pore pressure in my experiments.

To investigate the potential role of stiffness ratio k/k_c, I performed an estimate of $(a-b)$ from slow slip events and find that $(a-b)$ slightly decreases with increasing pore pressure, which means fault friction becomes more unstable at high pore pressure. Smaller co-seismic compaction (i.e. sample thinning / shortening) has also been observed at high pore pressure, which seems to support a more localized (potentially unstable) deformation. At the same time, I observe that loading stiffness k increases with increasing pore pressure, which has a stabilizing effect on slip (equation 7.5).

Based on the stability criterion ($K = k/k_c < 1$), both a decrease of k_c or an increase of k can promote slow slip. The observed k_c, as a function of $(a-b)$ and d_c, increases with pore pressure, but our observations suggest that the increase of k is more important than the increase in k_c. Note also that the values of $(a-b)$ and d_c are likely to change during slip due to localization and delocalization (Beeler et al., 1996; Scuderi et al., 2017) and that the estimate I obtained for $(a-b)$ is for the slow slip regime. An increase in the value of $(a-b)$ with increasing pore pressure at constant effective normal stress has been reported earlier by Den Hartog & Spiers (2013) for mixtures of quartz and muscovite and by Niemeijer & Collettini (2014) for a carbonate-bearing natural fault gouge, albeit at elevated temperatures and for positive values of $(a-b)$.

In addition to differences in the slow slip phase, as suggested by Scuderi et al. (2017), dynamic weakening mechanisms, such as flash heating, or thermal pressurization (i.e pore fluid pressurization caused by frictional heating) might occur during fast slip. In the experiments reported here, although co-seismic slip distance is generally small (10 - 100 μm), maximum slip rates reach 0.3 m/s. Water compressibility reduces slightly with increasing pore pressure (Fine & Millero, 1973),

particularly considering the possibility of small amounts of trapped air, but a lower compressibility would lead to more efficient weakening (and thus acceleration) as a result of compaction during fast slip, which is opposite to what is observed. The viscosity of water does not change much with pressure at room temperature conditions, but changes considerably at elevated temperatures (Schmelzer et al., 2005). At 100 °C, a change in pore pressure from 10 to 100 MPa results in a 8% increase in viscosity and at 200 °C this increase is 14%. High velocity experiments with different viscosity fluids have shown that weakening occurs over a larger distance when fluids with higher viscosity are used (Cornelio et al., 2019; Cornelio et al., 2020). This suggests that high pressure conditions in our experiments might reduce the efficiency of dynamic weakening mechanisms of "elastodynamic lubrication" as proposed by Cornelio et al. (2019), slowing down the slip.

7.6.3 Acoustic emissions: Source and the role of pore pressure

In my experiments, I observe a large difference in the frequency content of the AE between dry, wet (unpressurized) and pressurized experiments (Pf10 and Pf150). The main difference is that the dry and wet (unpressurized) experiments show that more acoustic energy is released in the frequency band around 1 kHz (Fig. 7.18)than in the pressurized experiments. The AE sensor is mostly sensitive to vertical displacement and the records are mostly vertically propagating P waves, whose source are co-seismic movement. This suggests that co-seismic vertical movement (compaction) is most likely generating low frequency AE signals around 1 kHz. Additional evidence comes from the consistent negative voltage first motion which might indicate a consistent traction force on the sensor and an implosion (compaction) on the sample, since a compressive force would give a positive onset, as shown in the drop ball test in the Appendix III.

The signal energy for the four experiments (Wet (10^{-2}) > Dry(5×10^{-3}) > Pf10 (10^{-4})> Pf150 (9×10^{-5}), Fig. 7.18) fits well with the trends seen in co-seismic sample compression (shortening/thinning) and normal stress change (Fig. 7.12e, f). However, a 1 kHz signal has a wavelength of around 5 m, which is beyond the size of the apparatus, it might be influenced by the changes in surrounding fluid conditions. The correlation between low frequency AE and co-seismic volume changes suggest low frequency AE is a sensitive way of measuring these changes. Our low frequency AE data thus also suggest less co-seismic sample shortening in the higher pore pressure experiments.

If low frequency AEs are generated from apparatus-scale elastic deformation, it seems likely that high frequency (50 kHz - 1 MHz) AEs are from localized (microscopic) elastic wave release, which can be interpreted to be localized slip and cracking events. The role of grain scale cracking is potentially small, since the results show that high frequency AE signals are absent at small displacement, where more grain size reduction (cracking) is likely occurring (Scuderi et al., 2017). Thus, I propose that our high frequency AE signals are generated mainly from localized slip patches, due to heterogeneity along the fault gouge. Furthermore, assuming rupture propagation speed equal to S velocity at sample as 2000 m/s, for a corner frequency 300 kHz, we obtain a slip patch size of 6 mm. Although large variations have been found in the low frequency part of AE signal, at high frequency, I did not

observe systematic frequency distribution differences between the experiments (Fig. 7.18). This might suggest that the source of high frequency AEs is less variable over our experiments and thus that pore pressure has less effect on localized slip in our observed frequency band of 50 kHz to 1 MHz.

7.6.4 Slow slip events and acoustic emissions

The present AE signal analysis (Fig. 7.19) has shown that in general AE signal amplitude increases with stress drop, which is consistent with previous work by Korkolis (2019) with glass beads. Moreover, I see that the accumulated displacement has a significant footprint on the signal amplitude. This is mainly due to the absence of high frequency signals during slow- and fast-slip events in the transition phase from stable to unstable slip stability (panels b in Figs.7.4 - 7.7). One hypothesis that could lead to this behaviour is that the fault gouge is more homogeneous, during this type of transition, and thus does not host localized slip patches or else the patches are too small to generate detectable AE signals. Microstructural analysis by Scuderi et al. (2017) does show that internal Y-shear patch size grows with increasing shearing strain. The absence of high frequency signals could suggest that transitional slow slip of the type observed here, which is presumably due to less localized slip, might provide a mechanism for producing slow slip events without tremors, while the transitional 'fast' slip might provide a mechanism for low frequency earthquakes (LFEs) and very low frequency earthquakes (vLFEs) in immature fault zones in shallow subduction zones (Obara & Ito, 2005).

At larger displacement (for instance $x > 15$ mm at the Pf150 experiment), I observe high frequency AE signals generated by interseismic slow slip. This phenomenon might be explained by the contribution from localized slip patches in the shear zone that do not rupture the entire fault. This kind of slow slip accompanied with AE might be an analogue of deep episodic tremors and slip (ETS) frequently observed in subduction zones around the world (Obara et al., 2004; Rogers & Dragert, 2003; Wallace et al., 2016). At the same time, the AE signals in the slow slip events in my experiments are not as continuous as natural tectonic tremors, which might be due to the small size of the sample.

7.7 Conclusions

In this chapter, I reported the results of rotary shear experiments on simulated quartz fault gouges performed at room temperature, at a constant effective normal stress of 60 MPa and at a constant load-point velocity of 6 $\mu m/s$. Pore fluid conditions applied to the sample were varied from dry to wet to pressurized with water at 10 and 150 MPa. The large shear strains that are achieved in the rotary shear configuration, allowed acquisition of data on a large number of slip events, including their acoustic signature. In all experiments, I observe a transition with accumulated displacement from stable sliding to slow slip to fast slip. We defined slow slip events at these transitional period as transitional slow slip events. In addition, reverse transitions back to periods of stable sliding were observed in all experiments. These reverse transitions occur over smaller displacements than transitions from stable to unstable

sliding.

On the basis of previous work by Beeler et al. (1996) and Scuderi et al. (2017), I interpret these transitions and reverse transitions to be the result of a continuous evolution in fault slip localization and delocalization, respectively. More transitions are observed in the Pf = 150 MPa experiment over similar amounts of total fault displacement, which suggests that high pore pressure promotes stable sliding or inhibits continuous instability.

Besides transitional slow slip events, I observed inter-seismic slow slip events after a displacement of at least 15 mm in our experiments. Inter-seismic slow slip occurs at the end of the stick phase of each seismic cycle and often gradually evolves into a fast slip event. Inter-seismic slow slip events exist in our four experiments with peak slip velocity smaller than 1 mm/s. The presence of a high pore pressure promotes inter-seismic slow slip events, compared to wet (unpressurized) condition. Inter-seismic slow slip events and transitional slow slip events are found to be mostly similar, but some differences exist in terms of their acoustic signature. Transitional slow slip events in the experiments are all silent, i.e. without visible AE, while a portion (10-15$\%$ for wet and pressurized conditions, ~2$\%$ for dry condition) of inter-seismic slow slip events are accompanied by AE. This observation suggests an interaction between whole-fault scale inter-seismic slow slip and small scale (few mm) localized slip, which might provide a mechanism for explaining natural episodic slip and tremor.

Another observation from the AE signal in the transitional period from stable to slow slip to fast slip, is that even fast slip events (with slip velocity ~ 40 mm/s in the example in Fig. 7.13a) are devoid of high frequency AE. These events are accompanied with low frequency signals between 100 to 1000s Hz. These 'fast' events, which seem like catastrophic events on the macroscopic scale but lack significant size of localized deformation (as evidenced by the lack of high frequency AE), might be analogous to low frequency earthquakes (LFEs) and very low frequency earthquakes (vLFEs) occurring in nature.

Using a quantitative analysis of stress drop and slip rate, I found that larger stress drops during unstable events are characterized by larger slip rate. In the slow sip rate regime, in our case V_{max} < ~10 mm/s, stress drop and slip rate are log-linearly related. The relation gradually transforms to linear,beyond a slip rate of ~10 mm/s. For V_{max} > ~100 mm/s, slip velocity is linearly proportional to stress drop. Simulations using the equation of motion and rate and state friction for variable values of K produced a comparable evolution of the stress drop vs. slip velocity relations. Comparing the slip rate of the four experiments, I found that for a given stress drop, the maximum slip rate is smaller at higher pore pressure.

I conclude that in the present experiments, although at room temperature and with simplified mineralogy of only quartz, slow slip behaviour is promoted by high pore fluid pressure at constant effective normal stress, relative to fully unstable slip which conversely tends to be inhibited at high pore fluid pressure. This indicates an additional role of pore pressure besides just lowering the Terzaghi effective stress. With increasing pore pressure, I found a decrease in the estimated $(a-b)$ from slow slip events (V_{max} < 1 mm/s), a decrease in co-seismic (fast slip) sample shortening and a decrease in low frequency AE, which all suggest that high pore pressure

promotes more localized slip. At the same time, I observed an increase in shear stiffness, which is likely the dominant effect promoting slow slip events and inhibiting continuous instability, based on the stability criterion. However, the cause of these effects (high pore pressure promote localization and increase shear stiffness) in quartz gouges remains unresolved for the moment. Low frequency AE signals occur around 1 kHz, which are likely generated from co-seismic sample shortening (compaction) and their amplitude decreases with increasing pore pressure. High frequency AE signals (50 kHz to 1 MHz) which are explained as small scale localized slip, have similar frequency content in the four experiments, which indicates small scale slip is less affected by pore pressure in this frequency band, for quartz gouge at room temperature.

7.8 Appendix I - Apparent shear stress rate and slip velocity

Shear stress rate (MPa/s) is defined as the time derivative of shear stress on the sample. Since measurements are not possible directly on the sample, the response of apparatus is unavoidably involved. Following the simplified sketch in Fig .7.21, I have

$$f_s = k_2 d_2 - m_2 a_2 = k_1 d_1 - m_1 a_1 \tag{7.12}$$

and

$$F_M = k_2 d_2 \tag{7.13}$$

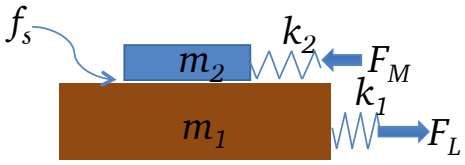

Figure 7.21: Sketch model of the loading and measuring system of the ring shear apparatus.

Here f_s is friction between m_1 and m_2, and both the loading side and resisting side have a compliance $1/k_1$ and $1/k_2$. F_L is the loading force, and F_M is the measured force at the resisting side. Since f_s can not be measured directly, I measured the apparent shear stress as:

$$\tau_m \equiv \frac{F_M}{A} \tag{7.14}$$

Here A is the surface area between the two masses m_1 and m_2. Taking the derivative of τ_m to loading displacement x, I have:

$$\frac{\partial \tau_m}{\partial x} = \frac{1}{A}\frac{\partial F_M}{\partial x} = \frac{1}{A} k_2 \frac{\partial d_2}{\partial x} \tag{7.15}$$

In the stick periods, i.e. when the sample is approximately locked, there is only elastic deformation in the system and I can obtain an apparent shearing stiffness

k =130~150 MPa/mm (Fig. 7.4 and Fig. 7.7), since the change of load-point displacement can be obtained from: $\delta(x) = V_L \cdot \delta t$ and

$$k \equiv \frac{1}{A} k_2 \frac{\partial d_2}{\partial x} \tag{7.16}$$

The apparent shear stress rate can be defined as:

$$\dot{\tau_m} \equiv \frac{1}{A}\frac{\partial F_M}{\partial t} = \frac{k_2}{A}\frac{\partial d_2}{\partial t} = \frac{k_2}{A}\frac{\partial d_2}{\partial x}\frac{\partial x}{\partial t} = k\frac{\partial x}{\partial t} \tag{7.17}$$

From the above two equations, I obtain a relative sliding velocity (V_s) for the sample relative to the rotating (bottom) piston.

$$V_s \equiv \frac{\partial x}{\partial t} = \frac{\dot{\tau_m}}{k} \tag{7.18}$$

The real shear stress rate on the sample is

$$\dot{\tau} \equiv \frac{\partial f_s}{A\partial t} = \dot{\tau_m} - \frac{1}{A} m_2 \frac{\partial a_2}{\partial t} \tag{7.19}$$

When the sample is sliding stably or quasi-statically, a_2 is close to 0 and $\dot{\tau} = \dot{\tau_m}$. During fast slip, the inertial term is not negligible, thus I have overestimated the shear stress rate.

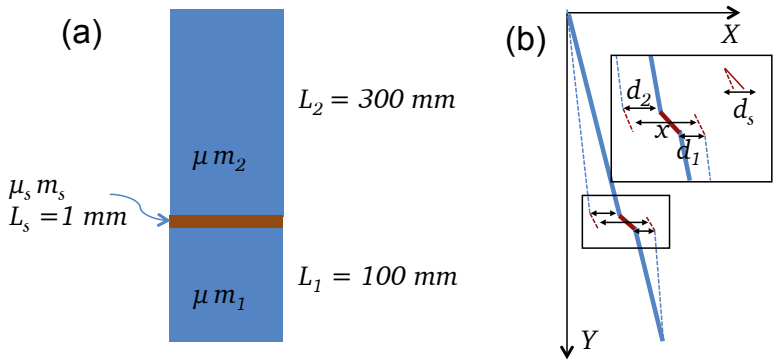

Figure 7.22: Sketch model of the shearing deformation of the ring shear apparatus.

Assuming ma is a small term, I can calculate a at the load point from the second derivative of F_M. This calculation shows that a is approximately ~5 m^2/s for even the largest event. Assuming a_2 is similar to a, and m_2 is ~30 kg, the term is $m_2 a_2$ (~150 N), which is much smaller than F_M which is ~8000 N. So I can conclude that even during fast slip, the apparent shear stress is equal to shear stress on the sample. Assuming shear deformation mainly on the two pistons and the sample. shear strain on the upper piston is

$$e_2 = d_2/L_2;\ e_1 = d_1/L_1;\ e_s = d_s/L_s;\ \mu = 80GPa;\ \mu_s = 8GPa; \tag{7.20}$$

If I assume

$$\tau^{max} \approx 40MPa \tag{7.21}$$

then the maximum elastic shear deformation on sample: $d_s^{max} \approx 5\mu m$. The average shear stiffness $k \approx 1/400 \cdot \mu = 200$ MPa/mm which is in the same order of magnitude as our measured results, but slightly larger, which suggests other parts of apparatus are also involved in the elastic deformation.

7.9 Appendix II - Slip rate calculation for each stress drop event

The sample slip rate is determined from stress drop rate and system stiffness (Eq.7.17). However, the measured signals are always accompanied with electronic noise. Moreover, due to the large variation in slip rate, the measured signal frequency content varies over each event. For instance, a small and slow slip has a low frequency signal around 10s to 100s Hz, for these events, high frequency recordings are noise and would produce an overestimate of the derivative of shear stress, due to the noise level that increases significantly with increasing frequency (Fig. 7.23).

For each stress drop event, I determine its signal (stress rate) frequency range and then based on that, I applied a frequency filter. In order to identify signal from noise, I first take a 20 second window that contains no visible stress drops to calculate stress drop rate, and then obtained its smoothed power spectrum density (PSD). For each stress drop event, $\dot{\tau}$ and the PSD are calculated at a 2 second window. The PSD from the stress drop events are then compared with the PSD of noise, presented in Fig. 7.23. A fast event as demonstrated here, has a near flat PSD at lower frequency range and has a sharp cut-off above the oscillation frequency (~1 kHz). A low pass filter is then applied to prevent an overestimate of $\dot{\tau}$. The corner frequency of the low pass filter is two times larger than the first cross-over frequency of the signal with the PSD of the noise as shown in Fig. 7.23.

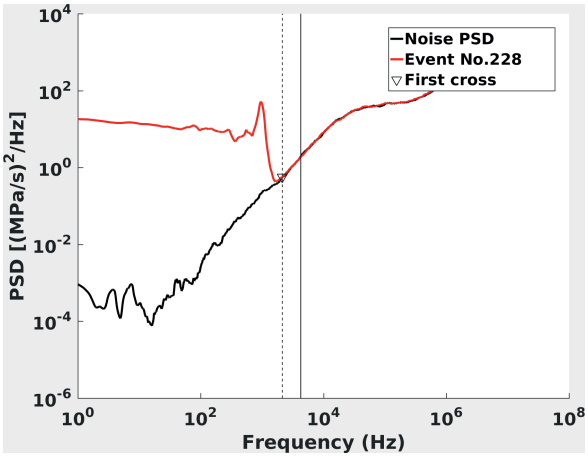

Figure 7.23: Stress drop event signal frequency range comparing with noise

7.10 Appendix III - Drop ball test

Positive amplitude first onsets are obtained from drop ball tests for both the low frequency signal generated by a steel ball with a diameter of 12 mm and the high frequency signal by a 2 mm diameter steel ball, which means a displacement pointing downward is the positive direction of our sensor.

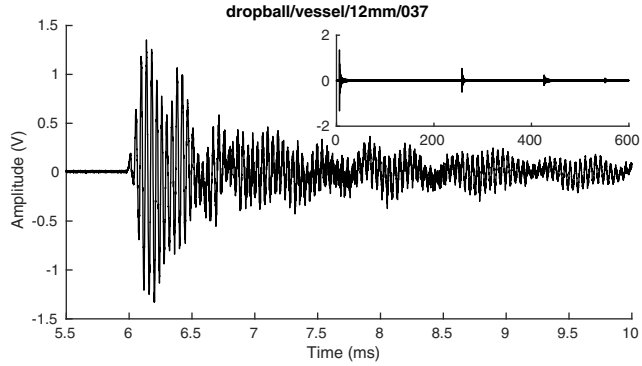

Figure 7.24: Drop ball test with sensors mounted on the bottom of the vessel. A 12 mm stainless steel ball was dropped to the bottom piston guided by a glass tube.

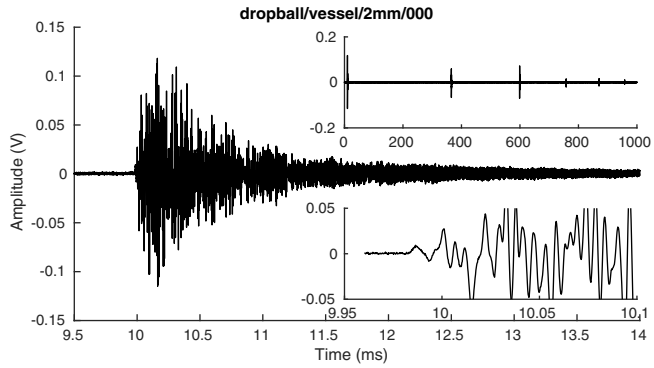

Figure 7.25: Drop ball test with a 2 mm stainless steel ball.

Chapter 8

Conclusions and suggestions for future research

This thesis presents results of seismic and experimental studies to improve our understanding of the induced seismicity of the Groningen gas field. The aim of the seismic studies was to develop methods for time-lapse monitoring of subsurface variations with borehole geophone array data. These subsurface variations are caused by reservoir compaction due to gas depletion and can be associated to induced seismicity. The experimental study was aimed at understanding potential pore pressure effects on fault slip and slip stability. Since fluids are commonly present in natural faults, this study can contribute to the understanding of both induced and natural earthquakes.

To monitor the Groningen subsurface, I analysed recordings of a deep borehole geophone array and found abundant signals that could be used for in-situ subsurface imaging and time-lapse monitoring. I first applied the method of ambient noise interferometry to determine the seismic structure along the geophone array. Then I adapted the method so that it could be applied to isolated train signals. Their high frequency content provided a velocity structure with higher accuracy and their regular occurrence allowed time-lapse monitoring of P wave travel times. Furthermore, I developed a method analogous to the receiver function technique that is commonly used in global seismology to retrieve P-to-S converted waves from the reservoir overburden. When applied to deep borehole data, it allows imaging of the overburden structure without installing additional receivers.

To investigate the pore pressure effects on earthquake slip, I performed experiments simulating slip using synthetic quartz gouge, measured mechanical and 'seismic' signals, and applied systematic analyses.

The main findings and conclusions are reviewed below and they are followed by suggestions for future research.

8.1 Main conclusions

8.1.1 Noise and seismic signals at 3 km depth

I started this research by investigating the noise distributions of deep borehole geophone array data in Groningen (chapter 2). I calculated the power spectrum density distributions and found that most of the ambient seismic noise was present in the frequency band of a few Hz to approximately 40 Hz. From more detailed analyses in the time-frequency domain (spectrograms), I found abundant noise signals that are clearly related to human activity. They mostly appear during daytime and have temporal patterns that can be associated with working hours. Regularly occurring signals with very similar characteristics were generated by nearby passing trains. These are the signals that were later used in chapters 4 to 6.

I also identified waves that travel along the geophone array with a propagation speed of approximately 1500 m/s. The origin of these so-called fluid waves is not completely clear, but their speed and high frequency content (up to 1000 Hz) suggest that they propagate predominantly within the water column of the borehole. These fluid waves have been used in chapter 4 to detect potential geophone displacements.

Earthquake seismograms for events at various distances were also investigated. Seismograms of earthquakes at distances from a few hundreds to thousand km have

simple and clear near vertically propagating P and S waves that can potentially be used for reflection imaging of the structure between the geophone array and the surface.

8.1.2 P and S velocity structure from noise interferometry

In chapter 3 I showed that it is feasible to determine the P and S velocity structure of the reservoir from the noise data recorded by the geophone array. For this, I used the method of interferometry by cross-correlation with some additional processing to obtain optimal results. The P velocity model in the reservoir was obtained with high accuracy, and it matched the sonic log data very well. Although the accuracy of the S velocity model is somewhat lower, it was possible to determine an azimuthal anisotropy of approximately 4% with a WNW-ESE fast direction. This fast direction roughly corresponds to the direction of maximum horizontal stress but also to the paleo-stress direction. Because of their similarity, it is not possible to unambiguously relate the inferred anisotropy to one of the two stress directions.

8.1.3 Temporal changes in P wave travel time from train noise

I used the isolated signals of nearby passing trains to once more determine the P and S velocity structure along the geophone array in chapter 4. The inter-geophone travel times, now obtained by deconvolution interferometry, could be measured with significantly higher accuracy than before because the train signals contain higher frequencies than the ambient noise.

The accuracy of the travel time measurements, the repeatability of the train signals and their frequent occurrence (~9000 trains in 5 months) enabled time-lapse monitoring of the reservoir. I found that the long-term travel time changes associated with reservoir compaction are small. The inter-geophone travel times decrease by less than 30 μs for each of the two 5-month periods analyzed, while the standard deviation of the measurements is around 10 μs. It is remarkable that these changes are much smaller than reported in the literature from 4D seismics (0.1 - 1.5 ms per year), whereas my measurements have a significantly higher accuracy. I did not detect short-term travel time variations related to rock property changes caused by local earthquakes.

8.1.4 'Receiver functions' applied to train noise

The high accuracy of the time-lapse P wave travel time measurements encouraged me to continue working with the train signals. Inspired by the receiver function method that has been widely used to image crustal and upper mantle discontinuities using teleseismic earthquakes recorded by surface receivers, I implemented a similar strategy to the train signals in chapter 5. I renamed the horizontal-to-vertical deconvolution technique HZdecon for this different setting with noise sources at the surface and receivers at depth. With the HZdecon method, I retrieved several P-to-S converted waves and traced them to interfaces from the reservoir up to ~1 km depth. I demonstrated that HZdecon can be used for passive time-lapse monitoring of the overburden, that is, from the near surface down to the depth of the receivers.

8.1.5 Distant effects of drilling

The most striking discovery presented in this thesis is that of P wave travel time changes associated with the drilling of a new borehole at 4.5 km distance. The results from both noise interferometry and HZdecon consistently indicate a P velocity increase around the gas water contact (GWC) of the sandstone reservoir suggesting a temporary rise of the GWC. Additional evidence is provided by the simultaneous decrease in the ambient noise level recorded below the GWC. The rise of the GWC at the observation well is linked to pressure variations at the drilling well through pore pressure diffusion. I also revisited the Midlaren earthquake swarm of 2009 which is associated to the drilling of another well in the Groningen field. Both cases require a high pore pressure diffusivity to explain the rapid effects (a day to a few days) for the distances over which they occur (4 - 5 km). Their setting further suggests that faults in the Groningen subsurface may act as effective conduits of pore pressure diffusion. It is evident that faults should be properly mapped prior to drilling to prevent them from being drilled, causing pressure variations that can generate induced earthquakes even at large distance.

8.1.6 Pore pressure slows down slip rate at constant effective normal stress

Episodic slow slip events have been discovered in subduction zones. Since they release elastic energy and transfer stress, slow slip events are important for understanding earthquakes and fault behaviour in general. In chapter 7, I investigated pore pressure effects on experimental fault slip using simulated fault gouges of quartz powder. Results from four experiments at constant effective normal stress and constant loading velocity at room temperature, with varying fluid pressure have been reported. In the experiments, I observed a wide spectrum of slip rates, from few micron/s to near 0.5 m/s, with variable stress drops. I observed clear trends of a higher probability of low slip velocity with increasing pore pressure. The experiments show that slow slips are promoted by solely increasing pore pressure, without decreasing effective normal stress. Pore pressure changes in these experiments induce gouge property changes, such as an increase in shear stiffness and the degree of localization. The microscale mechanism that leads to these changes is unknown at this point and further research is needed.

8.2 Suggestions for further research

In this thesis, I presented methods to monitor the Groningen gas reservoir with passive seismic data recorded by a deep borehole geophone array and I conducted some of the first experiments to investigate pore pressure effects on unstable slips. The work leaves behind a number of limitations and unsolved problems, and also raised a number of new questions. They are listed below.

The seismic monitoring period that I have studied was limited. A study that would cover the full 3 year period of the deep borehole recordings may provide better insights into the effects of reservoir compaction or overburden deformation on changes in the seismic signature of the reservoir and the overburden.

In the data that I analyzed, I did not find variations in seismic velocity that could be associated to local earthquakes. Such variations have been observed in other studies, but for different settings or for larger magnitude earthquakes (Brenguier et al., 2008; Nakata & Snieder, 2011; Niu et al., 2008; Obermann et al., 2019). I think it is still worthwhile to search for earthquake related seismic velocity variations, for instance for the M_L=3.4 Zeerijp earthquake of 2018 recorded by the geophone array in borehole ZRP-2 at 2.3 km distance.

In chapter 2 I showed seismograms of a M=5.4 deep focus earthquake in the Fiji island region. The first P wave arrival and its surface reflection are clearly visible. It is remarkable that the high frequencies, a few Hz, generated by this earthquake are well recorded by the deep borehole geophones at 144° distance. In this study, I chose to use train signals to image the reservoir and overburden because of their high frequency content and their regular occurrence, both crucial for detailed monitoring. Here, I propose that high frequency P waves from teleseismic earthquakes can be used for larger scale crustal monitoring.

In this thesis (chapter 4 and 5), I have shown that isolated train signals are stable noise sources that can provide high-resolution time-lapse measurements of P and S wave travel times and of P-to-S converted waves in the Groningen gas field. However, the methods can be applied more widely. They can be used in other deep borehole settings, for instance for permanent reservoir monitoring (Behm, 2016), near surface monitoring (Nakata & Snieder, 2011) and for fault zone monitoring of, for instance, the Chelongpu fault (Hillers et al., 2014) or the San Andreas fault (Lellouch et al., 2019). The accuracy of fault zone monitoring by noise interferometry (Brenguier et al., 2019) may be improved by applying it to isolated train signals. For regions where trains signals are not available, I suggest searching for other repetitive noise sources such as machines or wind turbines (Jagt, 2017; Van Der Vleut, 2019).

In my experimental studies, inter-seismic slow slips exist in all four experiments and are influenced by pore pressure, suggesting pore-pressure dependent variations in the localization-delocalization process which is constantly evolving during the experiments. Microphysical mechanisms that might explain these transitions are not explored in this thesis, while it is potentially an important phenomenon that could be linked with slow slip and tremors. It might help to establish links between slow and fast slip and how one can trigger the other.

In the experiments with quartz gouge, I observe that pore pressure has an effect on fault slip and slip stability, the experiments were done under room temperature condition, whereas experiments with more realistic temperature, pore pressure and normal stress, can help to quantitatively improve the understanding of fault slip, both in the case of induced seismicity such as in Groningen as well as in natural settings, such as in subduction zones. Frequency-dependent acoustic emission events were observed in the experiments. The links to natural silent earthquakes and regular earthquakes are only qualitatively suggested. AE with slow slip events are suggested as an mechanism of ETS, while the AE signals in our experiments are not as continuous as tectonic tremors. To address these questions, an up-scaling from experiment slips to real fault settings is needed, which might be done through numerical simulation or larger scale experiments (Wu & McLaskey, 2019; Zhuo et

al., 2018).

Furthermore, in our experiments, we obtained rate state friction parameter $(a-b)$ from statistical analysis, and with the assumption of a steady-state which is not valid for stick slips. Thus, a more novel method is needed to obtain a better estimation of friction law parameters to constrain the critically of the system.

References

Adam, L., M. Batzle & I. Brevik (2006), Gassmann's fluid substitution and shear modulus variability in carbonates at laboratory seismic and ultrasonic frequencies, *Geophysics*, vol. 71, no. 6, F173–F183, DOI: 10.1190/1.2358494.

Akbar, M., I Vasconcelos, W Zhou & H Paulssen (2018), Subsurface reflection response estimation at Groningen by seismic interferometry using deep borehole data, in: *Extended abstract of 80th EAGE Conference and Exhibition 2018*.

Aki, K. (1957), Space and time spectra of stationary stochastic waves, with special reference to microtremors, *Bulletin of the Earthquake Research Institute*, vol. 35, pp. 415–456.

Audet, P., M. G. Bostock, N. I. Christensen & S. M. Peacock (2009), Seismic evidence for overpressured subducted oceanic crust and megathrust fault sealing, *Nature*, vol. 457, no. 7225, pp. 76–78, DOI: 10.1038/nature07650.

Bakulin, A. & R. Calvert (2006), The virtual source method: Theory and case study, *Geophysics*, vol. 71, no. 4, SI139–SI150.

Bath, M & R. Stefánsson (1966), SP conversion at the base of the crust, *Annals of Geophysics*, vol. 19, no. 2, pp. 119–130.

Beeler, N., T. Tullis, M. Blanpied & J. Weeks (1996), Frictional behavior of large displacement experimental faults, *Journal of Geophysical Research: Solid Earth*, vol. 101, no. B4, pp. 8697–8715.

Behm, M. (2016), Feasibility of borehole ambient noise interferometry for permanent reservoir monitoring, *Geophysical Prospecting*, vol. 65, pp. 563–580.

Behm, M., G. M. Leahy & R Snieder (2014), Retrieval of local surface wave velocities from traffic noise–an example from the La Barge basin (Wyoming), *Geophysical Prospecting*, vol. 62, no. 2, pp. 223–243.

Bensen, G., M. Ritzwoller, M. Barmin, A. Levshin, F Lin, M. Moschetti, N. Shapiro & Y Yang (2007), Processing seismic ambient noise data to obtain reliable broad-band surface wave dispersion measurements, *Geophysical Journal International*, vol. 169, no. 3, pp. 1239–1260.

Beroza, G. C. & S. Ide (2011), Slow Earthquakes and Nonvolcanic Tremor, *Annual Review of Earth and Planetary Sciences*, vol. 39, no. 1, pp. 271–296, DOI: 10.1146/annurev-earth-040809-152531.

Blanpied, M. L., D. A. Lockner & J. D. Byerlee (1995), Frictional slip of granite at hydrothermal conditions, *Journal of Geophysical Research*, DOI: 10.1029/95jb00862.

Boait, F. C., N. J. White, M. J. Bickle, R. A. Chadwick, J. A. Neufeld & H. E. Huppert (2012), Spatial and temporal evolution of injected CO2 at the Sleipner Field, North Sea, *Journal of Geophysical Research: Solid Earth*, vol. 117, no. B3, DOI: 10.1029/2011JB008603.

Bostock, M. G., A. A. Royer, E. H. Hearn & S. M. Peacock (2012), Low frequency earthquakes below southern Vancouver Island, *Geochemistry, Geophysics, Geosystems*, DOI: 10.1029/2012GC004391.

Botev, Z. I., J. F. Grotowski, D. P. Kroese, et al. (2010), Kernel density estimation via diffusion, *The Annals of Statistics*, vol. 38, no. 5, pp. 2916–2957.

Boulton, C., D. E. Moore, D. A. Lockner, V. G. Toy, J. Townend & R. Sutherland (2014), Frictional properties of exhumed fault gouges in DFDP-1 cores, Alpine Fault, New Zealand, *Geophysical Research Letters*, vol. 41, no. 2, pp. 356–362, DOI: 10.1002/2013GL058236.

Bourne, S., S. Oates, J Van Elk & D Doornhof (2014), A seismological model for earthquakes induced by fluid extraction from a subsurface reservoir, *Journal of Geophysical Research: Solid Earth*, vol. 119, no. 12, pp. 8991–9015.

Brace, W. & J. Byerlee (1966), Stick-slip as a mechanism for earthquakes, *Science*, vol. 153, no. 3739, pp. 990–992.

Brenguier, F., P. Boué, Y. Ben-Zion, F. Vernon, C. Johnson, A. Mordret, O. Coutant, P.-E. Share, E. Beaucé, D. Hollis & T. Lecocq (2019), Train traffic as a powerful noise source for monitoring active faults with seismic interferometry, *Geophysical Research Letters*, vol. 46, no. 16, pp. 9529–9536, DOI: 10.1029/2019GL083438.

Brenguier, F., M. Campillo, C. Hadziioannou, N. Shapiro, R. M. Nadeau & E. Larose (2008), Postseismic relaxation along the San Andreas fault at Parkfield from continuous seismological observations, *Science*, vol. 321, no. 5895, pp. 1478–1481.

Caffagni, E., D. Eaton, M. Van der Baan & J. P. Jones (2015), Regional seismicity: A potential pitfall for identification of long-period long-duration events, *Geophysics*, vol. 80, no. 1, A1–A5, DOI: 10.1190/geo2014-0382.1.

Candela, T., B. Wassing, J. ter Heege & L. Buijze (2018), How earthquakes are induced, *Science*, vol. 360, no. 6389, pp. 598–600, DOI: 10.1126/science.aat2776.

Cannon, M. & P. Kole (2018), The first year of distributed strain sensing (DSS) monitoring in the Groningen gas field, *NAM report*, no. SR.17.009342.

Chen, Q.-f., L. Li, G. Li, L. Chen, W.-t. Peng, Y. Tang, Y. Chen & F.-y. Wang (2004), Seismic features of vibration induced by train, *Acta Seismologica Sinica*, vol. 17, no. 6, pp. 715–724, DOI: 10.1007/s11589-004-0011-7.

Cheng, C., T. Bodin, B. Tauzin & R. M. Allen (2017), Cascadia subduction slab heterogeneity revealed by three-dimensional receiver function Kirchhoff migration, *Geophysical Research Letters*, vol. 44, no. 2, pp. 694–701.

Chester, F. M. (1994), Effects of temperature on friction: Constitutive equations and experiments with quartz gouge, *Journal of Geophysical Research*, vol. 99, no. B4, p. 7247, DOI: 10.1029/93JB03110.

Claerbout, J. F. (1968), Synthesis of a layered medium from its acoustic transmission response, *Geophysics*, vol. 33, no. 2, pp. 264–269.

Cornelio, C., E. Spagnuolo, G. Di Toro, S. Nielsen & M. Violay (2019), Mechanical behaviour of fluid-lubricated faults, *Nature Communications*, DOI: 10.1038/s41467-019-09293-9.

Cornelio, C., F. X. Passelègue, E. Spagnuolo, G. Di Toro & M. Violay (2020), Effect of Fluid Viscosity on Fault Reactivation and Coseismic Weakening, *Journal of Geophysical Research: Solid Earth*, DOI: 10.1029/2019JB018883.

Crotwell, H. P., T. J. Owens & J. Ritsema (1999), The TauP Toolkit: Flexible seismic travel-time and ray-path utilities, *Seismological Research Letters*, vol. 70, no. 2, pp. 154–160.

Das, I. & M. D. Zoback (2013), Long-period, long-duration seismic events during hydraulic stimulation of shale and tight-gas reservoirs — Part 1: Waveform characteristics, *GEOPHYSICS*, vol. 78, no. 6, KS97–KS108, DOI: 10.1190/geo2013-0164.1.

De Jager, J. & C. Visser (2017), Geology of the Groningen field - An overview, *Netherlands Journal of Geosciences*, vol. 96, no. 5, s3–s15, DOI: 10.1017/njg.2017.22.

De Waal, J., A. Muntendam-Bos & J. Roest (2015), Production induced subsidence and seismicity in the Groningen gas field - can it be managed?, *Proceedings of the International Association of Hydrological Sciences*, vol. 372, pp. 129–139.

Dempsey, D. & J. Suckale (2017), Physics-based forecasting of induced seismicity at Groningen gas field, the Netherlands, *Geophysical Research Letters*, vol. 44, no. 15, pp. 7773–7782.

Den Hartog, S. A. (2013), Frictional behaviour of megathrust fault gouges under in-situ subduction zone conditions, PhD thesis, Utrecht Univeristy.

Den Hartog, S. & C. Spiers (2013), Influence of subduction zone conditions and gouge composition on frictional slip stability of megathrust faults, *Tectonophysics*, vol. 600, pp. 75–90, DOI: 10.1016/j.tecto.2012.11.006.

Den Hartog, S., A. Niemeijer & C. Spiers (2012), New constraints on megathrust slip stability under subduction zone P - T conditions, *Earth and Planetary Science Letters*, vol. 353-354, pp. 240–252, DOI: 10.1016/j.epsl.2012.08.022.

Dieterich, J. H. (1978), Time-dependent friction and the mechanics of stick-slip, in: *Rock friction and earthquake prediction*, Springer, pp. 790–806.

– (1979), Modeling of rock friction: 1. Experimental results and constitutive equations, *Journal of Geophysical Research: Solid Earth*, vol. 84, no. B5, pp. 2161–2168.

DINOloket (2020), Data and Information on the Dutch Subsurface, https://www.dinoloket.nl/en/nomenclature-deep.

Dost, B., F. Goutbeek, T. van Eck & D. Kraaijpoel (2012), Monitoring induced seismicity in the North of the Netherlands: status report 2010, *KNMI Scientific report*.

Dost, B., E. Ruigrok & J. Spetzler (2017), Development of seismicity and probabilistic hazard assessment for the Groningen gas field, *Netherlands Journal of Geosciences*, vol. 96, no. 5, s235–s245.

Draganov, D, X Campman, J Thorbecke, A Verdel & K Wapenaar (2009), Reflection images from ambient seismic noise, *Geophysics*, vol. 74, A63–67.

Draganov, D, K Heller & R Ghose (2012), Monitoring CO_2 storage using ghost reflections retrieved from seismic interferometry, *International Journal of Greenhouse Gas Control*, vol. 11, S35–S46.

Dragert, H., K. Wang & T. S. James (2001), A silent slip event on the deeper Cascadia subduction interface, *Science*, vol. 292, no. 5521, pp. 1525–1528.

Fine, R. A. & F. J. Millero (1973), Compressibility of water as a function of temperature and pressure, *The Journal of Chemical Physics*, DOI: 10.1063/1.1679903.

Fokker, E. & E. Ruigrok (2019), Quality parameters for passive image interferometry tested at the Groningen network, *Geophysical Journal International*, vol. 218, no. 2, pp. 1367–1378.

French, M. E. & W. Zhu (2017), Slow fault propagation in serpentinite under conditions of high pore fluid pressure, *Earth and Planetary Science Letters*, DOI: 10.1016/j.epsl.2017.06.009.

Fuchs, F. & G. Bokelmann (2018), Equidistant spectral lines in train vibrations, *Seismological Research Letters*, vol. 89, no. 1, pp. 56–66, DOI: 10.1785/0220170092.

Galetti, E., A. Curtis, B. Baptie, D. Jenkins & H. Nicolson (2017), Transdimensional Love-wave tomography of the British Isles and shear-velocity structure of the East Irish Sea Basin from ambient-noise interferometry, *Geophysical Journal International*, vol. 208, no. 1, pp. 36–58.

Gassmann, F (1951), Über die Elastizität poröser Medien (on elasticity of porous media) Vierteljahrsschrift der Naturforschenden Gesellschaft in Zürich, *Zürich*, vol. 96, pp. 1–23.

Gent, H. W. van, S. Back, J. L. Urai, P. A. Kukla & K. Reicherter (2009), Paleostresses of the Groningen area, the Netherlands - Results of a seismic based structural reconstruction, *Tectonophysics*, vol. 470, no. 1, pp. 147–161.

Gerstoft, P., P. M. Shearer, N. Harmon & J. Zhang (2008), Global P, PP, and PKP wave microseisms observed from distant storms, *Geophysical Research Letters*, vol. 35, no. 23.

GFZ (2020), GEOFON Earthquake Information Service - Earthquake Bulletin, https://geofon.gfz-potsdam.de/old/eqinfo/form.php.

Gomberg, J., J. L. Rubinstein, Z. Peng, K. C. Creager, J. E. Vidale & P. Bodin (2008), Widespread triggering of nonvolcanic tremor in California, *Science*, vol. 319, no. 5860, pp. 173–173.

Grechka, V. & Y. Zhao (2012), Microseismic interferometry, *The Leading Edge*, vol. 31, no. 12, pp. 1478–1483.

Gu, J. C., J. R. Rice, A. L. Ruina & S. T. Tse (1984), Slip motion and stability of a single degree of freedom elastic system with rate and state dependent friction, *Journal of the Mechanics and Physics of Solids*, DOI: 10.1016/0022-5096(84)90007-3.

Guglielmi, Y., F. Cappa, J. P. Avouac, P. Henry & D. Elsworth (2015), Seismicity triggered by fluid injection-induced aseismic slip, *Science*, DOI: 10.1126/science.aab0476.

Hatchell, P. & S. Bourne (2005), Rocks under strain: Strain-induced time-lapse time shifts are observed for depleting reservoirs, *The Leading Edge*, vol. 24, no. 12, pp. 1222–1225.

Havskov, J. & G. Alguacil (2004), Instrumentation in earthquake seismology, vol. 358, Springer.

He, C., T.-f. Wong & N. M. Beeler (2003), Scaling of stress drop with recurrence interval and loading velocity for laboratory-derived fault strength relations, *Journal of Geophysical Research: Solid Earth*, vol. 108, no. B1, DOI: 10.1029/2002JB001890.

Hettema, M. H., B. Jaarsma, B. M. Schroot & G. C. Van Yperen (2017), An empirical relationship for the seismic activity rate of the Groningen gas field, *Netherlands Journal of Geosciences*, vol. 96, no. 5, s149–s161, DOI: 10.1017/njg.2017.18.

Hillers, G., M. Campillo & K.-F. Ma (2014), Seismic velocity variations at TCDP are controlled by MJO driven precipitation pattern and high fluid discharge properties, *Earth and Planetary Science Letters*, vol. 391, pp. 121–127, DOI: 10.1016/j.epsl.2014.01.040.

Hillers, G., S. Husen, A. Obermann, T. Planès, E. Larose & M. Campillo (2015), Noise-based monitoring and imaging of aseismic transient deformation induced by the 2006 Basel reservoir stimulation, *Geophysics*, vol. 80, no. 4, KS51–KS68.

Hirose, H., K. Hirahara, F. Kimata, N. Fujii & S. Miyazaki (1999), A slow thrust slip event following the two 1996 Hyuganada earthquakes beneath the Bungo Channel, southwest Japan, *Geophysical Research Letters*, DOI: 10.1029/1999GL010999.

Hofman, R, E Ruigrok, B Dost & H Paulssen (2017), A shallow seismic velocity model for the Groningen area in the Netherlands, *Journal of Geophysical Research*, vol. 122, DOI: 10.1002/2017JB014419.

Hol, S., A. van der Linden, S. Bierman, F. Marcelis & A. Makurat (2018), Rock physical controls on production-induced compaction in the Groningen field, *Scientific reports*, vol. 8, no. 1, pp. 1–13.

Huang, H., P. Wang, N. Mi, Z. Huang, M. Xu, L. Wang, H. Li & D. Yu (2014), Lateral variations of the mantle transition zone structure beneath eastern China, *Bulletin of the Seismological Society of America*, vol. 104, no. 3, pp. 1533–1539, DOI: 10.1785/0120130315.

Hunfeld, L., A. Niemeijer & C. Spiers (2017), Frictional properties of simulated fault gouges from the seismogenic Groningen gas field under in situ P-T-chemical conditions, *Journal of Geophysical Research: Solid Earth*, vol. 122, no. 11, pp. 8969–8989, DOI: 10.1002/2017JB014876.

Inbal, A., T. Cristea-Platon, J.-P. Ampuero, G. Hillers, D. Agnew & S. Hough (2018), Sources of long-range anthropogenic noise in southern California and implications for tectonic tremor detection, *Bulletin of the Seismological Society of America*, vol. 108, no. 6, pp. 3511–3527, DOI: 10.1785/0120180130.

International Seismological Centre (2020), On-line Bulletin, https://doi.org/10.31905/D808B830.

Ito, Y., R. Hino, M. Kido, H. Fujimoto, Y. Osada, D. Inazu, Y. Ohta, T. Iinuma, M. Ohzono, S. Miura, M. Mishina, K. Suzuki, T. Tsuji & J. Ashi (2013), Episodic slow slip events in the Japan subduction zone before the 2011 Tohoku-Oki earthquake, *Tectonophysics*, DOI: 10.1016/j.tecto.2012.08.022.

Jagt, L. (2017), Characterizing seismic signals from wind farms in Groningen, *Guided research, Utrecht University*.

Jagt, L., E. Ruigrok & H. Paulssen (2017), Relocation of clustered earthquakes in the Groningen gas field, *Netherlands Journal of Geosciences*, vol. 96, no. 5, s163–s173.

Kaproth, B. M. & C. Marone (2013), Slow earthquakes, preseismic velocity changes, and the origin of slow frictional stick-slip, *Science*, DOI: 10.1126/science.1239577.

KNMI (2020), KNMI - Aardbevingscatalogus, https://www.knmi.nl/kennis-en-datacentrum/dataset/aardbevingscatalogus.

Kole, P. (2015), In-situ compaction measurements using gamma ray markers, *NAM report*, no. EP201506209302.

Komatitsch, D., J. Ritsema & J. Tromp (2002), The spectral-element method, Beowulf computing, and global seismology, *Science*, vol. 298, no. 5599, pp. 1737–1742, DOI: 10.1126/science.1076024.

Komatitsch, D., G. Erlebacher, D. Göddeke & D. Michéa (2010), High-order finite-element seismic wave propagation modeling with MPI on a large GPU cluster, *Journal of Computational Physics*, vol. 229, no. 20, pp. 7692–7714, DOI: 10.1016/j.jcp.2010.06.024.

Korkolis, E. (2019), Rotary shear experiments on glass bead aggregates: Stick-slip statistics and parallels with natural seismicity, PhD thesis, Utrecht University.

Kortekaas, M. & B. Jaarsma (2017), Improved definition of faults in the Groningen field using seismic attributes, *Netherlands Journal of Geosciences*, vol. 96, no. 5, s71–s85.

Langston, C. (1979), Structure under Mount Rainier, Washington, inferred from teleseismic body waves, *Journal of Geophysical Research*, vol. 84, no. B9, pp. 4749–4762, DOI: 10.1029/JB084iB09p04749.

Larose, E., T. Planes, V. Rossetto & L. Margerin (2010), Locating a small change in a multiple scattering environment, *Applied Physics Letters*, vol. 96, no. 20, DOI: 10.1063/1.3431269.

Leeman, J. R., D. M. Saffer, M. M. Scuderi & C. Marone (2016), Laboratory observations of slow earthquakes and the spectrum of tectonic fault slip modes, *Nature Communications*, DOI: 10.1038/ncomms11104.

Lellouch, A, S Yuan, Z Spica, B Biondi & W. Ellsworth (2019), Seismic velocity estimation using passive downhole distributed acoustic sensing records–examples from the San Andreas Fault Observatory at Depth, *Journal of Geophysical Research: Solid Earth*.

Lin, F.-C., M. H. Ritzwoller, Y. Yang, M. P. Moschetti & M. Fouch (2011), Complex and variable crustal and uppermost mantle seismic anisotropy in the western United States, *Nature Geoscience*, vol. 4, pp. 1239–1260.

Lin, Y.-Y., K.-F. Ma & V. Oye (2012), Observation and scaling of microearthquakes from the Taiwan Chelungpu-fault borehole seismometers, *Geophysical Journal International*, DOI: 10.1111/j.1365-246X.2012.05513.x.

Linde, A. T., M. T. Gladwin, M. J. Johnston, R. L. Gwyther & R. G. Bilham (1996), A slow earthquake sequence on the San Andreas fault, *Nature*, vol. 383, no. 6595, pp. 65–68.

Liu, Y. & J. R. Rice (2005), Aseismic slip transients emerge spontaneously in three-dimensional rate and state modeling of subduction earthquake sequences, *Journal of Geophysical Research: Solid Earth*, vol. 110, no. B8.

Liu, Y. & J. R. Rice (2007), Spontaneous and triggered aseismic deformation transients in a subduction fault model, *Journal of Geophysical Research*, vol. 112, no. B9, B09404, DOI: 10.1029/2007JB004930.

MacBeth, C., A. Kudarova & P. Hatchell (2018), A semi-empirical model of strain sensitivity for 4D seismic interpretation, *Geophysical Prospecting*, vol. 66, no. 7, pp. 1327–1348.

MacBeth, C., M.-D. Mangriotis & H. Amini (2019), Post-stack 4D seismic time-shifts: Interpretation and evaluation, *Geophysical Prospecting*, vol. 67, no. 1, pp. 3–31.

Marone, C. & B. Kilgore (1993), Scaling of the critical slip distance for seismic faulting with shear strain in fault zones, *Nature*, vol. 362, no. 6421, pp. 618–621.

Maxwell, S. (2011), Microseismic hydraulic fracture imaging: The path toward optimizing shale gas production, *The Leading Edge*, vol. 30, no. 3, pp. 340–346, DOI: 10.1190/1.3567266.

Miyazawa, M., R. Snieder & A. Venkataraman (2008), Application of seismic interferometry to extract P-and S-wave propagation and observation of shear-wave splitting from noise data at Cold Lake, Alberta, Canada, *Geophysics*, vol. 73, no. 4, pp. D35–D40.

Nakata, N. & R. Snieder (2011), Near-surface weakening in Japan after the 2011 Tohoku-Oki earthquake, *Geophysical Research Letters*, vol. 38, no. 17, pp. 1–5, DOI: 10.1029/2011GL048800.

Nakata, N. & R. Snieder (2012), Estimating near-surface shear wave velocities in Japan by applying seismic interferometry to KiK-net data, *Journal of Geophysical Research: Solid Earth*, vol. 117, no. B1.

Nakata, N., R. Snieder, T. Tsuji, K. Larner & T. Matsuoka (2011), Shear wave imaging from traffic noise using seismic interferometry by cross-coherence, *Geophysics*, vol. 76, no. 6, SA97–SA106, DOI: 10.1190/geo2010-0188.1.

NAM (2016), Study and data acquisition plan induced seismicity in Groningen - Winningsplan 2016, *NAM report*, no. EP201604200072.

NAM (2018), Assessment of subsidence based on production scenario "Basispad Kabinet", *NAM report*.

– (2019a), Monitoring local seismicity with deep downhole arrays - Summary report of 60 months of monitoring in 5 Groningen wells, *NAM report*.

– (2019b), Seismic monitoring Groningen field deep downhole arrays - synthesis report 2013-2018, *NAM report*.

NAM (2020a), Diepte van aardbevingen, https://www.nam.nl/feiten-en-cijfers/diepte-van-aardbevingen.html.

NAM (2020b), NAM interactieve kaart, https://nam-feitenencijfers.data-app.nl/geotool/nam.html.

NAM (2020), Review and update of: Study and data acquisition plan induced seismicity in Groningen - Update post-winningsplan 2016, *NAM report*.

Niemeijer, A. R. & C. Collettini (2014), Frictional Properties of a Low-Angle Normal Fault Under In Situ Conditions: Thermally-Activated Velocity Weakening, *Pure and Applied Geophysics*, DOI: 10.1007/s00024-013-0759-6.

Niemeijer, A., C. Spiers & C. Peach (2008), Frictional behaviour of simulated quartz fault gouges under hydrothermal conditions: Results from ultra-high strain rotary shear experiments, *Tectonophysics*, DOI: 10.1016/j.tecto.2008.09.003.

Niemeijer, A., C. Boulton, V. Toy, J. Townend & R. Sutherland (2016), Large-displacement, hydrothermal frictional properties of DFDP-1 fault rocks, Alpine Fault, New Zealand: Implications for deep rupture propagation, *Journal of Geophysical Research: Solid Earth*, vol. 121, no. 2, pp. 624–647.

Niu, F., P. Silver, T. Daley, X. Cheng & E. Majer (2008), Preseismic velocity changes observed from active source monitoring at the Parkfield SAFOD drill site, *Nature*, vol. 454, no. 7201, pp. 204–208, DOI: 10.1038/nature07111.

NLOG (2020), Borehole - Data - HGZ-01, https://www.nlog.nl/nlog/requestData/nlogp/allBor/metaData.jsp?tableName=BorLocation&id=382607703.

Obara, K. (2002), Nonvolcanic deep tremor associated with subduction in southwest japan, *Science*, vol. 296, no. 5573, pp. 1679–1681.

Obara, K. & Y. Ito (2005), Very low frequency earthquakes excited by the 2004 off the Kii peninsula earthquakes: A dynamic deformation process in the large accretionary prism, *Earth, Planets and Space*, vol. 57, no. 4, pp. 321–326.

Obara, K., H. Hirose, F. Yamamizu & K. Kasahara (2004), Episodic slow slip events accompanied by non-volcanic tremors in southwest Japan subduction zone, *Geophysical Research Letters*, vol. 31, no. 23, pp. 1–4, DOI: 10.1029/2004GL020848.

Obermann, A., T. Planès, E. Larose & M. Campillo (2019), 4-D Imaging of Subsurface Changes with Coda Waves: Numerical Studies of 3-D Combined Sensitivity Kernels and Applications to the Mw 7.9, 2008 Wenchuan Earthquake, *Pure and Applied Geophysics*, vol. 176, no. 3, pp. 1243–1254, DOI: 10.1007/s00024-018-2014-7.

Okazaki, K. & I. Katayama (2015), Slow stick slip of antigorite serpentinite under hydrothermal conditions as a possible mechanism for slow earthquakes, *Geophysical Research Letters*, vol. 42, no. 4, pp. 1099–1104, DOI: 10.1002/2014GL062735.

Olivier, G, F Brenguier, M Campillo, P Roux, N. Shapiro & R Lynch (2015), Investigation of coseismic and postseismic processes using in situ measurements of seismic velocity variations in an underground mine, *Geophysical Research Letters*, vol. 42, no. 21, pp. 9261–9269.

Ougier-Simonin, A. & W. Zhu (2013), Effects of pore fluid pressure on slip behaviors: An experimental study, *Geophysical Research Letters*, vol. 40, no. 11, pp. 2619–2624, DOI: 10.1002/grl.50543.

– (2015), Effect of pore pressure buildup on slowness of rupture propagation, *Journal of Geophysical Research: Solid Earth*, DOI: 10.1002/2015JB012047.

Paulssen, H. & D. De Vos (2017), Slab remnants beneath the Baja California peninsula: Seismic constraints and tectonic implications, *Tectonophysics*, vol. 719-720, From continental to oceanic rifting in the Gulf of California, pp. 27 –36, DOI: https://doi.org/10.1016/j.tecto.2016.09.021.

Peacock, S. M. & K. Wang (1999), Seismic consequences of warm versus cool subduction metamorphism: Examples from southwest and northeast Japan, *Science*, vol. 286, no. 5441, pp. 937–939.

Peterson, J. R. (1993), Observations and modeling of seismic background noise, tech. rep., US Geological Survey.

Phinney, R. A. (1964), Structure of the Earth's crust from spectral behavior of long-period body waves, *Journal of Geophysical Research*, vol. 69, no. 14, pp. 2997–3017.

Pijnenburg, R., B. Verberne, S. Hangx & C. Spiers (2018), Deformation behavior of sandstones from the seismogenic Groningen gas field: Role of inelastic versus elastic mechanisms, *Journal of Geophysical Research: Solid Earth*, vol. 123, no. 7, pp. 5532–5558.

– (2019), Inelastic deformation of the Slochteren sandstone: Stress-strain relations and implications for induced seismicity in the Groningen gas field, *Journal of Geophysical Research: Solid Earth*, vol. 124, no. 5, pp. 5254–5282.

Plourde, A. P., M. G. Bostock, P. Audet & A. M. Thomas (2015), Low-frequency earthquakes at the southern Cascadia margin, *Geophysical Research Letters*, vol. 42, no. 12, pp. 4849–4855, DOI: 10.1002/2015GL064363.

Poli, P., M. Campillo, H Pedersen & L. W. Group (2012), Body-wave imaging of Earth's mantle discontinuities from ambient seismic noise, *Science*, vol. 338, pp. 1063–1065.

Quiros, D. A., L. D. Brown & D. Kim (2016), Seismic interferometry of railroad induced ground motions: body and surface wave imaging, *Geophysical Journal International*, vol. 205, no. 1, pp. 301–313.

Reid, H. F. (1910), The Mechanics of the Earthquake, The California Earthquake of April 18, 1906: Report of the State Earthquake Investigation Commission, Vol.2, Carnegie Institution of Washington, Washington, D.C.

Rice, J. R. (1993), Spatio-temporal complexity of slip on a fault, *Journal of Geophysical Research*, vol. 98, no. B6, p. 9885, DOI: 10.1029/93JB00191.

Ridder, S. de, B. Biondi & R. Clapp (2014), Time-lapse seismic noise correlation tomography at Valhall, *Geophysical Research Letters*, vol. 41, no. 17, pp. 6116–6122.

Rogers, G. & H. Dragert (2003), Episodic tremor and slip on the Cascadia subduction zone: The chatter of silent slip, *Science*, vol. 300, no. 5627, pp. 1942–1943.

Romijn, R. (2017), Groningen velocity model 2017 - Groningen full elastic velocity model, *NAM report*.

Rondenay, S., G. Abers & P. van Keken (2008), Seismic imaging of subduction zone metamorphism, *Geology*, vol. 36, no. 4, cited By 129, pp. 275–278, DOI: 10.1130/G24112A.1.

Rubinstein, J. L., M. La Rocca, J. E. Vidale, K. C. Creager & A. G. Wech (2008), Tidal modulation of nonvolcanic tremor, *Science*, vol. 319, no. 5860, pp. 186–189.

Ruigrok, E., X. Campman & K. Wapenaar (2012), Basin delineation with a 40-hour passive seismic record, *Bulletin of the Seismological Society of America*, vol. 102, no. 5, pp. 2165–2176.

Ruina, A. (1983), Slip instability and state variable friction laws, *Journal of Geophysical Research: Solid Earth*, vol. 88, no. B12, pp. 10359–10370.

Samuelson, J., D. Elsworth & C. Marone (2009), Shear-induced dilatancy of fluid-saturated faults: Experiment and theory, *Journal of Geophysical Research*, vol. 114, no. B12, B12404, DOI: 10.1029/2008JB006273.

Schmelzer, J. W. P., E. D. Zanotto & V. M. Fokin (2005), Pressure dependence of viscosity, *The Journal of Chemical Physics*, vol. 122, no. 7, p. 074511, DOI: 10.1063/1.1851510.

Scholz, C. & T Engelder (1976), Role of asperity indentation and ploughing in rock friction, *Int. J. Rock Mech. Min. Sci*, vol. 13, pp. 149–154.

Schuster, G. (2009), Seismic interferometry, ISBN: 9780511581557, DOI: 10.1017/CBO9780511581557.

Scuderi, M. M., C. Collettini, C. Viti, E. Tinti & C. Marone (2017), Evolution of shear fabric in granular fault gouge from stable sliding to stick slip and implications for fault slip mode, *Geology*, vol. 45, no. 8, pp. 731–734, DOI: 10.1130/G39033.1.

Segall, P., A. M. Rubin, A. M. Bradley & J. R. Rice (2010), Dilatant strengthening as a mechanism for slow slip events, *Journal of Geophysical Research: Solid Earth*, vol. 115, no. B12.

Sens-Schönfelder, C. & T. Eulenfeld (2019), Probing the in situ Elastic Nonlinearity of Rocks with Earth Tides and Seismic Noise, *Phys. Rev. Lett.* Vol. 122, 13, p. 138501, DOI: 10.1103/PhysRevLett.122.138501.

Shapiro, N. M., M. Campillo, L. Stehly & M. H. Ritzwoller (2005), High-resolution surface-wave tomography from ambient seismic noise, *Science*, vol. 307, no. 5715, pp. 1615–1618.

Shapiro, N. M., M. Campillo, E. Kaminski, J. P. Vilotte & C. Jaupart (2018), Low-Frequency Earthquakes and Pore Pressure Transients in Subduction Zones, *Geophysical Research Letters*, DOI: 10.1029/2018GL079893.

Shapiro, S. A., E. Rothert, V. Rath & J. Rindschwentner (2002), Characterization of fluid transport properties of reservoirs using induced microseismicity, *Geophysics*, vol. 67, no. 1, pp. 212–220.

Sheley, D. & G. T. Schuster (2003), Reduced-time migration of transmitted PS waves, *GEOPHYSICS*, vol. 68, no. 5, pp. 1695–1707, DOI: 10.1190/1.1620643.

Shelly, D. R., G. C. Beroza & S. Ide (2007), Non-volcanic tremor and low-frequency earthquake swarms, *Nature*, vol. 446, no. 7133, p. 305.

Silver, P. G., T. M. Daley, F. Niu & E. L. Majer (2007), Active source monitoring of cross-well seismic travel time for stress-induced changes, *Bulletin of the Seismological Society of America*, vol. 97, no. 1B, pp. 281–293, DOI: 10.1785/0120060120.

Smith, T., C. Sondergeld & C. Rai (2003), Gassmann fluid substitutions: A tutorial, *Geophysics*, vol. 68, no. 2, pp. 430–440, DOI: 10.1190/1.1567211.

Snieder, R. (2004), Extracting the Green's function from the correlation of coda waves: A derivation based on stationary phase, *Physical Review E*, vol. 69, no. 4, DOI: 10.1103/PhysRevE.69.046610.

Snieder, R. & E. Larose (2013), Extracting Earth's elastic wave response from noise measurements, *Annual Review of Earth and Planetary Sciences*, vol. 41, pp. 183–206.

Snieder, R., J. Sheiman & R. Calvert (2006), Equivalence of the virtual-source method and wave-field deconvolution in seismic interferometry, *Physical Review E*, vol. 73, no. 6, p. 066620.

Snieder, R., M. Miyazawa, E. Slob, I. Vasconcelos & K. Wapenaar (2009), A comparison of strategies for seismic interferometry, *Surveys in Geophysics*, vol. 30, no. 4-5, pp. 503–523.

Spetzler, J. & B. Dost (2017), Hypocentre estimation of induced earthquakes in Groningen, *Geophysical Journal International*, vol. 209, no. 1, pp. 453–465.

Spica, Z. J., N. Nakata, X. Liu, X. Campman, Z. Tang & G. C. Beroza (2018), The ambient seismic field at Groningen gas field: An overview from the surface to reservoir depth, *Seismological Research Letters*, vol. 89, no. 4, pp. 1450–1466, DOI: 10.1785/0220170256.

Stauble, A. J. & G. Milius (1970), Geology of Groningen gas field, Netherlands, *Geology of Giant Petroleum Fields*, vol. 14, ed. by Halbouty, M. T., pp. 359–369.

Takagi, R., K. Nishida, Y. Aoki, T. Maeda, K. Masuda, M. Takeo, K. Obara, K. Shiomi, M. Sato & K. Saito (2015), A single bit matters: Coherent noise of seismic data loggers, *Seismological Research Letters*, vol. 86, no. 3, pp. 901–907.

Talwani, P., L. Chen & K. Gahalaut (2007), Seismogenic permeability, ks, *Journal of Geophysical Research: Solid Earth*, vol. 112, no. B7.

The Engineering Toolbox (2020), The engineering toolbox, `www.engineeringtoolbox.com/water-dynamic-kinematic-viscosity-d_596.html`.

Thomas, A. M., R. M. Nadeau & R. Bürgmann (2009), Tremor-tide correlations and near-lithostatic pore pressure on the deep San Andreas fault, *Nature*, vol. 462, no. 7276, pp. 1048–1051.

Trampert, J., M. Cara & M. Frogneux (1993), SH propagator matrix and Qs estimates from borehole- and surface-recorded earthquake data, *Geophysical Journal International*, vol. 112, no. 2, pp. 290–299.

Tromp, J., D. Komatitsch & Q. Liu (2008), Spectral-element and adjoint methods in seismology, *Communications in Computational Physics*, vol. 3, no. 1, pp. 1–32.

Vaezi, Y. & M. van der Baan (2015), Interferometric assessment of clamping quality of borehole geophones, *Geophysics*, vol. 80, no. 6, WC89–WC98.

Van den Ende, M. (2020), PyRSF is a rate-and-state friction (RSF) modelling package written in Python, `https://github.com/martijnende/PyRSF`.

Van Der Vleut, B. C. M. (2019), Characterizing the seismic signal of individual wind turbines in the Borgsweer area, *Master thesis, Utrecht University*, DOI: `https://dspace.library.uu.nl/handle/1874/383284`.

Van Eijs, R. (2015), Neotectonic stresses in the Permian Slochteren formation of the Groningen field, *NAM report*, no. EP201510210531.

Van Thienen-Visser, K. & J. Breunese (2015), Induced seismicity of the Groningen gas field: History and recent developments, *The Leading Edge*, vol. 34, no. 6, pp. 664–671.

Van Weers, J. (2019), Hypocenter relocation in Groningen using the double-difference method, *MSc thesis, Utrecht University*.

Vasconcelos, I., P. Sava & H. Douma (2010), Nonlinear extended images via image-domain interferometry, *Geophysics*, vol. 75, no. 6, SA105–SA115.

Vinnik, L. (1977), Detection of waves converted from P to SV in the mantle, *Physics of the Earth and planetary interiors*, vol. 15, no. 1, pp. 39–45.

Wallace, L. M., S. C. Webb, Y. Ito, K. Mochizuki, R. Hino, S. Henrys, S. Y. Schwartz & A. F. Sheehan (2016), Slow slip near the trench at the Hikurangi subduction zone, New Zealand, *Science*, vol. 352, no. 6286, pp. 701–704, DOI: `10.1126/science.aaf2349`.

Wang, K. & A. M. Tréhu (2016), Invited review paper: Some outstanding issues in the study of great megathrust earthquakes - The Cascadia example, *Journal of Geodynamics*, DOI: `10.1016/j.jog.2016.03.010`.

Wang, T., X. Song & H. H. Xia (2015), Equatorial anisotropy in the inner part of Earth's inner core from autocorrelation of earthquake coda, *Nature Geoscience*, vol. 8, no. 3, pp. 224–227.

Wapenaar, K. & J. Fokkema (2006), Green's function representations for seismic interferometry, *Geophysics*, vol. 71, no. 4, SI33–SI46.

Wapenaar, K., D. Draganov, R. Snieder, X. Campman & A. Verdel (2010), Tutorial on seismic interferometry: Part 1 - Basic principles and applications, *Geophysics*, vol. 75, no. 5, 75A195–75A209.

Weaver, R. L. & O. I. Lobkis (2005), Fluctuations in diffuse field-field correlations and the emergence of the Green's function in open systems, *Journal of the Acoustical Society of America*, vol. 117, no. 6, pp. 3422–3439.

Wegler, U. & C Sens-Schönfelder (2007), Fault zone monitoring with passive image interferometry, *Geophysical Journal International*, vol. 168, no. 3, pp. 1029–1033.

Wei, S., J. P. Avouac, K. W. Hudnut, A. Donnellan, J. W. Parker, R. W. Graves, D. Helmberger, E. Fielding, Z. Liu, F. Cappa & M. Eneva (2015), The 2012 Brawley swarm triggered by injection-induced aseismic slip, *Earth and Planetary Science Letters*, DOI: 10.1016/j.epsl.2015.03.054.

Willacy, C., E. Van Dedem, S. Minisini, J. Li, J.-W. Blokland, I. Das & A. Droujinine (2019), Full-waveform event location and moment tensor inversion for induced seismicity, *Geophysics*, vol. 84, no. 2, KS39–KS57, DOI: 10.1190/geo2018-0212.1.

Willacy, C., E. van Dedem, S. Minisini, J. Li, J. W. Blokland, I. Das & A. Droujinine (2018), Application of full-waveform event location and moment-tensor inversion for Groningen induced seismicity, *The Leading Edge*, vol. 37, no. 2, pp. 92–99.

Wu, B. S. & G. C. McLaskey (2019), Contained Laboratory Earthquakes Ranging From Slow to Fast, *Journal of Geophysical Research: Solid Earth*, vol. 124, no. 10, pp. 10270–10291, DOI: 10.1029/2019JB017865.

Xiao, X., M. Zhou & G. T. Schuster (2006), Salt-flank delineation by interferometric imaging of transmitted P- to S-waves, *GEOPHYSICS*, vol. 71, no. 4, SI197–SI207, DOI: 10.1190/1.2209550.

Xing, T., W. Zhu, M. French & B. Belzer (2019), Stabilizing Effect of High Pore Fluid Pressure on Slip Behaviors of Gouge-bearing Faults, *Journal of Geophysical Research: Solid Earth*, DOI: 10.1029/2019jb018002.

Xu, L., S. Rondenay & R. D. van der Hilst (2007), Structure of the crust beneath the southeastern Tibetan Plateau from teleseismic receiver functions, *Physics of the Earth and Planetary Interiors*, vol. 165, no. 3-4, pp. 176–193.

Yang, Y., H. Hung & D. Chang (2003), Train-induced wave propagation in layered soils using finite/infinite element simulation, *Soil Dynamics and Earthquake Engineering*, vol. 23, no. 4, pp. 263–278, DOI: 10.1016/S0267-7261(03)00003-4.

Yehya, A., Z. Yang & J. Rice (2018), Effect of Fault Architecture and Permeability Evolution on Response to Fluid Injection, *Journal of Geophysical Research: Solid Earth*, vol. 123, no. 11, pp. 9982–9997, DOI: 10.1029/2018JB016550.

Zecevic, M., G. Daniel & D. Jurick (2016), On the nature of long-period long-duration seismic events detected during hydraulic fracturing, *GEOPHYSICS*, vol. 81, no. 3, KS113–KS121, DOI: 10.1190/geo2015-0524.1.

Zhang, H. L., B. L. Wang, J. Y. Ning & Y. M. Li (2019), Interferometry imaging using high-speed-train induced seismic waves, *Chinese J. Geophys. (in Chinese)*, vol. 62, no. 6, pp. 2321–2327, DOI: 10.6038/cjg2019M0676.

Zhou, W. & H. Paulssen (2019), Travel time changes in the Groningen gas reservoir by train noise interferometry of borehole data, in: *Extended abstracts of 81th EAGE Conference and Exhibition 2019*, European Association of Geoscientists & Engineers, pp. 1–5, DOI: 10.3997/2214-4609.201900671.

– (2020), Compaction of the Groningen gas reservoir investigated with train noise, *Manuscript submitted for publication*.

Zhou, W. & H. Paulssen (2017), P and S velocity structure in the Groningen gas reservoir from noise interferometry, *Geophysical Research Letters*, vol. 44, no. 23.

Zhuo, Y.-Q., P. Liu, S. Chen, Y. Guo & J. Ma (2018), Laboratory Observations of Tremor - Like Events Generated During Preslip, *Geophysical Research Letters*, vol. 45, no. 14, pp. 6926–6934, DOI: 10.1029/2018GL079201.

Samenvatting

Het Groningse gasveld in Nederland is één van de grootste onder land gesitueerde gasvelden ter wereld. Vanaf het begin van productie in 1963 is het Groningse aardgas een belangrijke energiebron voor Nederland geweest en daarmee heeft het een significante bijdrage geleverd aan de Nederlandse economie. Vanaf de jaren '90 zijn er echter steeds meer problemen met geïnduceerde seismiciteit veroorzaakt door de gaswinning. Hoewel de aardbevingen relatief kleine magnitudes hebbben ($M_L \leq 3.6$), veroorzaken ze schade aan de merendeels bakstenen huizen. Dit hangt samen met het feit dat de aardbevingen relatief ondiep zijn en met de zachte sedimenten in de ondergrond.

De seismiciteit is gerelateerd aan compactie van het reservoirgesteente door de afname van de gasdruk. Compactie van het poreuze reservoirgesteente veroorzaakt veranderingen in de nomaal- en schuifspanningen langs oude, bestaande breuken. Hierdoor kan er beweging langs de breuk plaatsvinden, waarbij er seismische energie in de vorm van aardbevingen kan vrijkomen. Voor het seismisch risico in Groningen is het is daarom van belang om compactie te monitoren.

Er wordt aangenomen dat een verhoogde poriëndruk de effectieve normaalspanning vermindert en daarmee langzame breukbeweging bevordert ten opzichte van snelle (aardbevings)breukbeweging, maar er zijn weinig studies die onderzocht hebben hoe veranderingen in poriëndruk de breukbeweging kan beïnvloeden. Omdat de poriëndruk van het Groningse gasveld in de loop van de tijd is afgenomen, is het belangrijk om de effecten van poriëndruk op het breukgedrag te begrijpen.

De twee doelen die in dit proefschrift behandeld worden zijn de in-situ monitoring van de seismische eigenschappen van het reservoir en het effect van poriëndruk op breukbeweging.

Voor de in-situ monitoring van de seismische eigenschappen in de ondergrond van Groningen heb ik seismische ruis geanalyseerd die geregistreerd is door een array van geofoons in een diep boorgat (hoofdstuk 2). Ik heb tevens methodes onderzocht om met deze seismische ruis de ondergrond in kaart te brengen (hoofdstuk 3, 4, 5). Seismische interferometrie en HZdecon, een nieuwe door mij ontwikkelde methode, is toegepast op ruis die veroorzaakt is door treinen. Hiermee is een indrukwekkende nauwkeurigheid verkregen van de seismische eigenschappen van de ondergrond. Er is een afname van de seismische looptijden in het reservoir gedetecteerd, oplopend tot enkele tientallen microseconden in 2015. Dit wijst op een klein effect van compactie, maar de metingen zijn van dezelfde grootte als de onzekerheid. Hoewel de

in-situ waarneming van compactie in deze studie niet overtuigend is, kan de nieuw ontwikkelde methode ook worden toegepast op een langere registratieduur voor een beter resultaat. Tevens kan de methode toegepast worden op andere reservoirs met een grotere compactie.

Terwijl de gemeten effecten van compactie klein zijn, zijn er opvallend grote effecten die geassocieerd worden met boorwerkzaamheden van een put op 4,5 km afstand. De observaties en de interpretatie hiervan worden gepresenteerd in hoofdstuk 6. Diverse waarnemingen wijzen op een stijging van het waterpeil in het reservoir nabij de observatieput gedurende het boren van de nieuwe put. De verandering van het waterniveau wordt gerelateerd aan de verandering van de poriëndruk als gevolg van overdruk tijdens het boren.

In hoofdstuk 7 wordt onderzocht hoe de condities van vloeistofporiëndruk het schuifgedrag van breuken beïnvloeden. Mechanische data en akoestische emissies zijn verkregen voor meer dan 500 instabiele bewegingen of “laboratorium aardbevingen” per experiment. De experimenten suggereren dat een verandering van poriëndruk, bij gelijkblijvende effectieve normaalspanning, een groot effect kan hebben op de stabiliteit van de breukbeweging.

Acknowledgments

First of all, I am grateful to Andrea Tommasi for initializing the ITN-CREEP project, and to my promoter Chris Spiers, co-promoters Hanneke Paulssen and André Niemeijer for giving me the chance to work on this PhD position. I also want to acknowledge the committee members Prof. Elisa Tinti, Prof. Jeannot Tremport, Prof. Mike Kendall, Prof. Christina Thomas and Prof. Läslo Evers for taking time to evaluate this work.

It is a long journey for this PhD, longer and tougher than I thought. I would not have finished this book without the greatest help from my two supervisors: Hanneke Paulssen and André Niemeijer, and supports from my amazing colleagues in the Seismology group and the HPT lab.

Hanneke, you have taken care of my research in great detail and have made sure that I did not work too roughly, as I would always do to pursue a quick result. You are smart, enthusiastic in this study and always helpful. I can not remember how many times I have knocked on your door and discussed all those puzzles we found in Groningen, how many times I have delayed you in the office and let your husband wait for you for supper. I have been so lucky to work with you.

André, you are just as good a supervisor as Hanneke, while you are in a different style. You let me explore in the lab and helped me, as I needed. I felt sorry that this thesis went a bit away from our original plan and I had less time working in the lab. But eventually, I am happy that we managed to have these interesting experiments after many failures. I hope you are happy as well.

The time spending in the Seismology group is full of fun. In the 'olden' days, when we were still in the van Unnik building, it was my great pleasure to have friends and colleagues like you: Denise, Suzanne Atkins, Maria, Nienke, Agnieszka, Sahar, Nesli, Su, Simon, Haorui, Lisanne, Haydar, Yanadet, Laura, Andrew, Elmer, Ivan, Arwen, Jeannot, Theo, Arie, Jacqueline, Kabir and Henk. Then we moved to the modern Vening Meinesz building, and new talented colleagues joined in the group: Ashim, Janneke, David, Leon, Henry, Runa, Loes, Annemijn, Eldert, Rhys and Thomas. The group has grown and changed, with people coming and going, but its characteristic continues and I appreciate all of you who made my life in the group cheerful. Especially thanks to Haorui and David as roommates for providing me with a good environment during the period of writing this thesis.

In the HPT lab, Besides André and Chris, Jianye and Evangelos have afforded me help on friction experiments and acoustic emissions, and I learned a lot from them.

Yuntao has involved in useful discussion among experiments and seismology topics. Ronald has pointed out the overlapping of ZRP-3 drilling with my seismic observation. Peter Fokker is interested in this study and kindly offered his calculating of pore pressure propagation. Tim, Peter and their colleagues have helped on understanding wellbore behaviour. Gerard has designed and made the acoustic emission (AE) assembly that is used in Chapter 7. My experiments are on the ring shear machine that is based on support and maintain by Gert, Emert, Thony, Gerard, Floris and Han. Magda has helped me a lot with administration. Beside that, I want to thank you all: Chris, Magda, Hans, Colin, Suzanne Hangx, Andre, Chen, Tim, Bart, Yuntao, Maartje, Ronald, Luuk, Loes Buijze, Mariska, Martijn, Piercalo, Casper, Miao, Rose, Sabine, Elisenda, Dawin, Hadi, Jeroen, Aditya, Anastasia, Chien-Cheng, Taka, Annika, Marcel, Mark and Tanmaya for making this lab a family like cosy place.

Elmer has brought me the opportunity to do internship in KNMI, and made sure that my data processing was correct. I was pleasant to work with colleagues: Filex, Janneke de Laat, Mathijs, Pieter, Läslo, Jelle, Janneke van Ginkel, Kees, Jesper, Bernald, Elske, Reinoud, Olivier, Gert-Jan and many others.

I also would like to thank my colleagues at Bristol University. Mike, Sarah, Philipp, Thomas Loriaux, Tan, Jessica , Adam and many others who gave me warm welcome in Bristol and made my study there joyful. Philipp guided me on the use of SPECFEM2D. James Verdon kindly provided his software for microseismic and anisotropy analysis.

This PhD project has been funded by the European Union's Horizon 2020 research and innovation program under the Marie Sklodowska-Curie grant agreement No 642029 - ITN CREEP. I am thankful to all CREEP early-career researchers: Manuel Thieme, Casper Sinn, Piercalo Giacomel, Giacomo Pozzi, Linfeng Ding, Elenora van Rijsingen, Gianluca Gerardi, Nicolo Sgareva, Lucan Mameri, Gabriel Meyer, Angelo Pisconti, Beatriz Martinez Montesinos, Philipp Prasse, Thomas Loriaux, Jana Schierjott and Simon Preuss.

Remco Roijm and NAM are acknowledged for introducing and providing the deep borehole seismic data which contributed to most of this thesis. Steve Oates, Clemens Visser, Jan van Elk, Gerbrand Krol, Jenena Tomic, Assaf Mar-Or and Sander Hol kindly offered very fruitful discussions.

Master students Xiuying Chen, Muhammad Akbar, Eva Arwert and Maurits Beudeker have subsequently worked on the deep borehole dataset with innovative approaches, which are also helpful for me. Other friends and colleagues in Utrecht are also thanked: Yue Zhao, Rob Hovers, Matt, Meng Li, Yvonne, Denise, Kangming Xu, Li Lin, Zijun Wang, Donglong Fu, Ming Zhang, Jie Sheng, Robin, Lisa, Jessica, Marian Heijboer and many others.

Overall, it is a treasury experience for me to get to know all of you, which has made me rich in a sense.

最后要感谢我的家人们。爸爸妈妈、陈英、倩和悠宜，谢谢你们的支持和陪伴，才使得我顺利地完成这本论文。

Curriculum Vitae

Wen Zhou (周文)

18 Sep 1988	Born in Ningxiang County, Hunan province, China
	Education
	PhD candidate
2015 - 2020	Utrecht University
	Utrecht, The Netherlands
Mar-Jun 2018	University of Bristol
	Bristol, UK
	MSc
2012 - 2015	Nanjing University
	Nanjing, China
	BSc
2008 - 2012	Guilin University of Technology
	Guilin, China
	Internships
Sep-Dec 2017	Royal Netherlands Meteorological Institute (KNMI)
	De Bilt, The Netherlands
Jan 2014 -	Geophysical Research Institute at SINOPEC
Mar 2015	Nanjing, China

Utrecht University
Faculty of Geosciences
Department of Earth Sciences

Since the start of production in 1963, natural gas from the Groningen field has been an important source of energy and contributed significantly to the Dutch economy. However, since the 1990s, there have been increased incidences of induced earthquakes related to reservoir compaction caused by gas extraction and associated pore pressure reduction. In this EU-funded PhD project, I investigated if changes in the physical properties of the sandstone reservoir rock can be detected using seismic monitoring methods. In addition, I conducted laboratory experiments on sandstone to investigate the effects of pore pressure on the stability of simulated faults that cut the sandstone reservoir.

I used deep borehole recordings of seismic noise produced by human activity, such as passing trains, over two 5-month periods. Employing seismic wave interferometry, I was able to determine variations in wave speed in the reservoir with a very high accuracy around the single borehole studied. I found small increases in seismic wave speed that might be related to compaction of the reservoir during the two periods of data acquisition. Furthermore, I detected a temporary change in the level of the gas-water interface associated with drilling operations at 4.5 km distance from the borehole. I did not find any effects of earthquakes on wave speeds in the reservoir. However, my experiments suggest that the decrease in gas pressure that causes reservoir compaction also promotes unstable earthquake slip on faults, as opposed to quiet fault motion.

ISSN 2211-4335